

**IMAGE RESOLUTION ANALYSIS: A NEW, ROBUST  
APPROACH TO SEISMIC SURVEY DESIGN**

A Dissertation

by

CONSTANTINOS TZIMEAS

Submitted to the Office of Graduate Studies of  
Texas A&M University  
in partial fulfillment of the requirements for the degree of

DOCTOR OF PHILOSOPHY

May 2004

Major Subject: Geophysics

IMAGE RESOLUTION ANALYSIS: A NEW, ROBUST  
APPROACH TO SEISMIC SURVEY DESIGN

A Dissertation

by

CONSTANTINOS TZIMEAS

Submitted to Texas A&M University  
in partial fulfillment of the requirements  
for the degree of

DOCTOR OF PHILOSOPHY

Approved as to style and content by:

---

Richard L. Gibson, Jr.  
(Chair of Committee)

---

Joel S. Watkins  
(Member)

---

Mark E. Everett  
(Member)

---

Akhil Datta-Gupta  
(Member)

---

Richard L. Carlson  
(Head of Department)

May 2004

Major Subject: Geophysics

## ABSTRACT

Image Resolution Analysis: A New, Robust  
Approach to Seismic Survey Design. (May 2004)

Constantinos Tzimeas, B.S., Aristotle University of Thessaloniki, Greece;  
M.S., University of Leeds, U.K.

Chair of Advisory Committee: Dr. Richard L. Gibson, Jr.

Seismic survey design methods often rely on qualitative measures to provide an optimal image of their objective target. Fold, ray tracing techniques counting ray hits on binned interfaces, and even advanced 3-D survey design methods that try to optimize offset and azimuth coverage are prone to fail (especially in complex geological or structural settings) in their imaging predictions. The reason for the potential failure of these commonly used approaches derives from the fact that they do not take into account the ray geometry at the target points.

Inverse theory results can provide quantitative and objective constraints on acquisition design. Beylkin's contribution to this field is an elegant and simple equation describing a reconstructed point scatterer given the source/receiver distribution used in the imaging experiment. Quantitative measures of spatial image resolution were developed to assess the efficacy of competing acquisition geometries. Apart from the source/receiver configuration, parameters such as the structure and seismic velocity also influence image resolution. Understanding their effect on image quality, allows us to better interpret the resolution results for the surveys under examination.

A salt model was used to simulate imaging of target points located underneath and near the flanks of the diapir. Three different survey designs were examined. Results from these simulations show that contrary to simple models, near-offsets do not always produce better resolved images than far-offsets. However, consideration of decreasing signal-to-noise ratio revealed that images obtained from the far-offset experiment are degrading faster than the near-offset ones.

The image analysis was performed on VSP field data as well as synthetics generated by finite difference forward modeling. The predicted image resolution results were compared to measured resolution from the migrated sections of both the field data and the synthetics. This comparison confirms that image resolution analysis provides as good a resolution prediction as the prestack Kirchhoff depth migrated

section of the synthetic gathers. Even in the case of the migrated field data, despite the presence of error introducing factors (different signal-to-noise ratios, shape and frequency content of source wavelets, etc.), image resolution performed well exhibiting the same trends of resolution changes at different test points.



To Georgia-Danaë

## ACKNOWLEDGMENTS

I would like to thank my advisor, Dr. Richard Gibson, Jr., for his guidance and support all these years. His brilliance always set the scientific bar high enough for us to keep struggling. His demeanor and teaching though, made it reachable. It is an honor for me to have met and worked with him. But first and foremost, it is an honor to call him and his family friends. I would also like to thank the other committee members, Drs. Mark Everett, Datta-Gupta, and Joel Watkins for their support. I would especially like to thank Drs. Terry Spencer and Mark Everett for allowing me to work for them prior to my advisor's coming.

To my fellow research group members, Kyoung-Jin Lee, Hung-Liang Lai, Pablo Buenafama, and Seung Yoo, a special thanks for sharing not only the computer lab resources but also ideas, worries and hopes. I will miss you (and your questions)! I would like to express my sincere appreciation and friendship to former A&M students, Veit Matt and Sung Hwan Yuh who did not forget me back in College Station and kept encouraging me. I would also like to thank John Priest for all the fruitful conversations I benefited from. A big thanks to Michele Beal for the numerous letters she had to prepare for me. I will fondly remember Javier Perez's cheerful attitude.

My Greek friends were always there for me when I needed help or entertainment. I would not have seen this through without them. I would like to extend my love and deepest admiration to my parents, Dimitri and Eleni, and sister, Giota, who supported me in any imaginable way. I promise, I will visit soon!

My wife, Neta, and daughter, Georgia-Danaë were the ones who kept me going for the last three dark years that we had to be apart. I miss you dearly and hope to make it up to you. This dissertation is dedicated to your patience and endurance. My deepest appreciation and gratitude go to my parents-in-law for all their sacrifices.

Finally, I would like to thank the Gas Research Institute for their partial financial support of the project under contract 5096-210-3781 under the guidance of Iraj Salehi. OPEX, for providing the field data, Green Mountain Geophysics (GMG/AXIS) for their collaboration and donation of the MESA/GRIP packages. Baker Atlas and Landmark Graphics Corp. generously provided the Seislink and ProMAX processing packages respectively.

I received funding (scholarships and fellowships) from Fulbright, Conoco Inc., Phillips Petroleum Co., SEG and the department of Geology & Geophysics, Texas

A&M University. I would like to thank them all. Without their financial support it would have been impossible for me to complete my studies.

## TABLE OF CONTENTS

		Page
ABSTRACT	.....	iii
DEDICATION	.....	v
ACKNOWLEDGMENTS	.....	vi
TABLE OF CONTENTS	.....	viii
LIST OF TABLES	.....	xi
LIST OF FIGURES	.....	xii
CHAPTER		
I	INTRODUCTION	1
	1.1 Image resolution analysis: An alternative to conventional illumination analyses	2
	1.2 Background theory	5
II	METHOD DEVELOPMENT	11
	2.1 Introduction	11
	2.2 Image resolution measures	11
	2.2.1 Scatter plots	12
	2.2.2 Space domain images	15
	2.2.3 Standard deviation	19
	2.2.4 Smoothness	24
	2.3 Examples of the effects of acquisition geometry on spatial resolution	28
	2.4 Comparison of image resolution prediction to migration	36
	2.5 Conclusions	41
III	METHOD SENSITIVITY ANALYSIS	42
	3.1 Introduction	42

CHAPTER	Page	
3.2	Zero-offset versus common-offset acquisition geometries: Their significance in image resolution . . . . .	43
3.3	Effects of the background model on spatial resolution . . . . .	51
3.3.1	The homogeneous, half space model . . . . .	53
3.3.2	The flat interface model . . . . .	54
3.3.3	The Gaussian models . . . . .	58
3.3.3.a	Multipathing . . . . .	61
3.4	The role of signal-to-noise ratio in image resolution . . . . .	64
3.5	Conclusions . . . . .	65
IV	EFFICACY ASSESSMENT OF COMPETING 3-D ACQUISITION DESIGNS OVER A SALT DOME MODEL . . . . .	69
4.1	Introduction . . . . .	69
4.2	Resolution and acquisition geometry in homogeneous media: Multi-offset versus single-offset surveys. . . . .	70
4.3	Survey design for a salt dome model . . . . .	74
4.3.1	Subsalt imaging . . . . .	81
4.3.2	Subsalt imaging: Improving a problematic marine acquisition by incorporating VSP data . . . . .	94
4.3.3	Salt flank imaging: Surface data . . . . .	98
4.3.4	Resolution and S/N ratio . . . . .	102
4.3.5	Salt flank imaging: VSP data . . . . .	107
4.4	Discussion and conclusions . . . . .	111
V	APPLICATION OF IMAGE RESOLUTION ANALYSIS TO VSP FIELD DATA . . . . .	115
5.1	The 1998 acquisition survey . . . . .	115
5.2	VSP data processing . . . . .	120
5.2.1	Pre-processing phase . . . . .	120
5.2.2	First arrival travel time picking . . . . .	120
5.2.3	Phase matching . . . . .	125
5.2.4	Velocity analysis . . . . .	128
5.2.5	Wavefield separation . . . . .	133
5.3	VSP migration and image resolution analysis . . . . .	137
5.3.1	Image resolution analysis . . . . .	139
5.3.2	Image resolution: Migrated synthetics vs image resolution analysis . . . . .	144

CHAPTER	Page
5.3.3	Image resolution: Migrated field data vs im- age resolution analysis . . . . . 148
5.4	Conclusions . . . . . 152
VI	CONCLUSIONS . . . . . 153
6.1	Future work . . . . . 155
REFERENCES	. . . . . 157
VITA	. . . . . 164

**LIST OF TABLES**

TABLE		Page
3.1	Physical properties of the two layers used in evaluating the effects of the background model on spatial resolution and their representative lithologies (Gardner et al., 1974; Meckel and Nath, 1977). . . .	52
5.1	Simple descriptive statistics for the three different travel time picking approaches. All listed results are in ms. . . . .	124

## LIST OF FIGURES

FIGURE	Page	
1.1	<p>A) Fold diagram for the split-spread seismic experiment. If used as a resolution indicator, fold predicts equally good resolution for all points lying within the distances of 3 and 4 km irrespectively of depth. B) Relative standard deviation curves for a series of scattering points at two different depth levels (500 and 2000 m). C) Depth profile of relative standard deviation for scattering points underneath the center of the seismic array. In general, the standard deviation measure predicts changes of image resolution not only laterally but vertically as well. . . . .</p>	4
1.2	<p>Schematic illustration of the wavenumber vector described by equation (1.8). The wavenumber vector that represents the portion of the wavenumber domain resolved by data acquired by the illustrated source/receiver pair is the bold vector, the sum of the two vectors tangent to the ray paths at the image point. The oppositely directed wavenumber vector is also included in the wavenumber domain (Beylkin et al., 1985). . . . .</p>	9
2.1	<p>Homogeneous model used to demonstrate the effectiveness of the proposed image resolution measures. The seismic array is 3 km long consisting of 31 sources and 61 receivers evenly spaced every 100 and 50 m respectively. Note that the image area of interest extends laterally beyond the edges of the seismic array. . . . .</p>	13
2.2	<p>Wavenumber scatter plots for three scattering plots underneath the center of the seismic array of Figure 2.1. From top to bottom, their depths are 200, 500 and 4000 m. Note that the wavenumber vector aperture decreases continuously with depth. . . . .</p>	14
2.3	<p>A) Ricker-type source wavelet used in the seismic experiments of this chapter and B) its amplitude spectrum. Its dominant frequency is 30 Hz. The dots denote the sampling increments in both time (2 ms) and frequency (<math>\approx 7.8</math> Hz) for the discrete Fourier Transform of 64 samples. . . . .</p>	16



FIGURE	Page
2.4	Gray-scale wavenumber plots for three scattering points underneath the center of the seismic array of Figure 2.1. From top to bottom, their depths are 200, 500 and 4000 m. The source wavelet was taken into account in generating these wavenumber vector density plots. Compare to Figure 2.2. . . . . 17
2.5	Spatial images of the same three imaging points as in Figures 2.2 and 2.4. Note that the best overall resolved point lies at the depth of 500 m although its wavenumber vector aperture (Figure 2.4) is smaller than that of the shallower point (200 m). . . . . 20
2.6	A) Relative standard deviation curves for a series of scattering points at the depth of 2 km. Distance denotes the lateral displacement of the point relative to the center of the array. Different curves denote different number of declinational bins used to compute the relative standard deviation. B) Relative standard deviation curves for the same points. Different curves denote different number of radial bins used to compute the relative standard deviation. Note that while the relative standard deviation curves are sensitive to the number of declinational bins used to compute them, they are almost independent of the number of radial bins. . . . 23
2.7	Relative standard deviation map for a grid of scattering points covering the image area of Figure 2.1. The smaller standard deviation values, thus, the better overall resolved points, occur beneath the center of the seismic array at depths around 500 m. . . . . 24
2.8	A) Gridded ( $3 \times 3$ ) image region. B) and C) Masks used to compute the components of the gradient at $z_5$ in the $x$ and $y$ directions respectively. D) and E) An alternative scheme: the Sobel edge operator masks. The advantage of using a larger mask size is that errors are reduced by local averaging. . . . . 26
2.9	Relative smoothness map for a grid of scattering points covering the image area of Figure 2.1. The smaller smoothness values, thus, the better overall resolved points, occur beneath the center of the seismic array at depths around 500 m. . . . . 27

FIGURE	Page
2.10	The same homogeneous model and image area as in Figure 2.1. The seismic array is still 3 km long but a gap of 1 km is introduced at the center of the array. The live sources and receivers are reduced from 31 to 20 and 61 to 40 respectively. . . . . 28
2.11	Relative standard deviation map for a grid of scattering points covering the image area of Figure 2.10. The best resolved points are shifted from the center of the seismic array sideways due to the gap introduced in the seismic array. (Compare to Figure 2.7). . . 30
2.12	Relative smoothness map for a grid of scattering points covering the image area of Figure 2.10. The best resolved points are shifted from the center of the seismic array sideways due to the gap introduced in the seismic array. (Compare to Figure 2.9). . . . 31
2.13	Gray-scale wavenumber plots for the three scattering plots underneath the center of the seismic array of Figure 2.10. From top to bottom, their depths are 200, 500 and 4000 m. The effects of the introduced gap in the array are clear (compare to Figure 2.4). . . . . 32
2.14	Spatial images of the same three imaging points corresponding to the wavenumber vector plots of Figure 2.13. The introduction of the gap in the array has rendered the effective aperture much smaller resulting in worse resolved points (compare to the spatial images obtained by the full array, in Figure 2.5). In addition to that, the concentration of the wavenumber vectors along certain directions is manifested in the highly accentuated image artifacts. . . 33
2.15	Depth profiles of relative standard deviation underneath the center of three seismic arrays with different lengths. Note that the longer the array, the deeper the best resolved point is. Moreover, the slope of the curves decreases with increasing array length, indicating that the longer arrays manage to better image larger ranges of depth. . . . . 34

FIGURE	Page
2.16	Spatial images of scattering points at different depths and different array lengths. From left to right, columns correspond to array lengths of 3, 5 and 7 km. Note that the best resolved points occur at larger depths with longer array lengths. Additionally, by comparing the last two rows of the figure, it becomes clear that longer arrays are capable of better resolving larger image areas. . . . . 35
2.17	Schematic of the laterally heterogeneous model used in the comparison of the image resolution prediction to prestack phase shift migration. The background velocity is 4 km/s while the reservoir is characterized by alternating bands of 4.42 km/s and 4.89 km/s. . . . . 37
2.18	Top: Zero-offset synthetic seismograms. Note the diffraction hyperbolas whose apexes are located at the boundaries between the strong and weak reflecting reservoir bands. Bottom: The same data after the phase shift migration. . . . . 38
2.19	RMS amplitude curves of the reflection event around a reservoir band boundary. The dotted curve denotes the RMS amplitudes before the migration and the solid, the RMS amplitudes after. The increase of resolution after the migration is obvious. . . . . 39
2.20	The spatial image for a scattering point 5 m off the reservoir band boundary. The predicted horizontal resolution is around 70 m and is in good agreement with the resolution indicated by the RMS amplitude curve after the migration (Figure 2.19). . . . . 40
3.1	A) The zero-offset geometry. B) The 1 km common-offset geometry. The source and receiver locations are such that the midpoint locations coincide with those of the zero-offset experiment. Rays from the first source ( $S_1$ ) to a scattering point and back to the corresponding receiver ( $R_1$ ) are shown. The scattering point is located at the depth of 500 m and lies underneath the center of the midpoint line. . . . . 45
3.2	A) Wavenumber vector plot of the scattering point at the depth of 500 m for the zero-offset geometry. B) Wavenumber vector plot (black points) of the same scatterer for the 1 km common-offset geometry. The plot is superimposed over A) (red dots) for easier comparison of their relative wavenumber space coverage. . . . . 46

FIGURE	Page
3.3	A) Spatial image of the scattering point at the depth of 500 m for the zero-offset geometry. B) Spatial image of the same point for the 1 km common-offset geometry. The image resolution deteriorates in the case of the common-offset configuration. . . . . 47
3.4	Horizontal and vertical resolution curves for both the zero- and common-offset geometries and the scattering point at the depth of 500 m. The maximum amplitudes of all curves are normalized to 1. The common-offset configuration results in an overall worse resolution. The same behavior was also predicted by the wavenumber vector plots of Figure 3.2. . . . . 48
3.5	A) Spatial image of the scattering point at the depth of 2000 m for the zero-offset geometry. B) Spatial image of the same point for the 1 km common-offset geometry. For distant scatterers, the two geometries provide, for all practical purposes, the same overall resolution. . . . . 49
3.6	Horizontal and vertical resolution curves for both the zero- and common-offset geometries and the scattering point at the depth of 2000 m. The maximum amplitudes of all curves are normalized to 1. As the scatterer's distance from the source/receiver array increases, the two geometries result in practically the same resolution (compare to Figure 3.4). . . . . 50
3.7	Family of curves defined by equation (3.2). The solid blue and red lines describe the formation interfaces for the two diapir models. The graph is presented with vertical (depth) axis exaggeration. . . . 52
3.8	On-scale representation of the models under examination. The acquisition line and imaging point are centered above and below the structures respectively. Lithological interfaces from all the reviewed models are shown. . . . . 53

FIGURE	Page
3.9	A) Wavenumber vector plot and B) corresponding spatial image for the imaging point of Figure 3.8. The background velocity of the homogeneous medium was 3500 m/s. (Compare with Figure 3.10.) In A), only the wavenumber vectors corresponding to the frequency component of 30 Hz are shown. These vectors along with the dashed lines delineate the covered portion of the wavenumber vector domain. . . . . 54
3.10	A) Wavenumber vector plot and B) corresponding spatial image for the imaging point of Figure 3.8. The velocity of the homogeneous medium was 4500 m/s. (Compare with Figure 3.9.) . . . . . 55
3.11	Initial value raytracing results for the flat interface model. Since the velocity increases with depth, the rays bend away from the normal to the interface. . . . . 56
3.12	Initial value raytracing results for the flat interface model. Since the velocity decreases with depth, the rays bend towards the normal to the interface. . . . . 56
3.13	A) Wavenumber vector plot and B) corresponding spatial image for the imaging point of Figure 3.8. The velocity increases across the flat interface from 3.5 to 4.5 km/s. In A), only the wavenumber vectors corresponding to the frequency component of 30 Hz are shown. . . . . 57
3.14	A) Wavenumber vector plot and B) corresponding spatial image for the imaging point of Figure 3.8. The velocity decreases across the flat interface from 4.5 to 3.5 km/s. In A), only the wavenumber vectors corresponding to the frequency component of 30 Hz are shown. . . . . 57
3.15	A) Wavenumber vector plot and B) corresponding spatial image for the imaging point of Figure 3.8. The velocity still increases across the flat interface but the medium where the scatterer lies is now assumed to be 3.5 km/s. In A), only the wavenumber vectors corresponding to the frequency component of 30 Hz are shown. . . . . 58

FIGURE	Page
3.16	Initial value raytracing results for the steep Gaussian model. Since the velocity increases with depth, the ray aperture widens. Notice that due to the structure, rays converge and diverge significantly. . . . . 59
3.17	Initial value raytracing results for the steep Gaussian model. Since the velocity decreases with depth, the ray aperture becomes narrow. Notice that due to the structure, ray triplication is evident. . . . . 59
3.18	Initial value raytracing results for the gentle Gaussian model. Since the velocity increases with depth, the ray aperture widens. . . . . 60
3.19	Initial value raytracing results for the gentle Gaussian model. Since the velocity decreases with depth, the ray aperture becomes narrow. . . . . 60
3.20	Spatial resolution for the image point from Figure 3.8. The left column displays results for the models with increasing velocity with depth; the right column is for the models with decreasing velocity with depth. The uppermost pair of figures shows the results for the flat interface model and are identical to the corresponding images in Figures 3.13B and 3.14B. . . . . 62
3.21	A) One-way traveltime and B) corresponding amplitude curves for the steep Gaussian model with decreasing velocity with depth. The red highlighted curves satisfy the minimum traveltime criterion of selecting the rays that were used in the image resolution analysis. . . . . 63
3.22	Amplitude curves against horizontal distance. For both the gently and steeply dipping Gaussian models, amplitudes are greater when the velocity increases with depth. . . . . 65
3.23	Spatial resolution for the image point from Figure 3.8 with the flat interface. The left column displays results for increasing velocity with depth; the right column is for the model with decreasing velocity with depth. The uppermost pair of figures shows the results for an infinite S/N ratio. Notice the loss of resolution as the noise level increases from top to bottom. . . . . 66

FIGURE	Page
3.24	Spatial resolution for the image point from Figure 3.8 with the gentle Gaussian interface. The left column displays results for increasing velocity with depth; the right column is for the model with decreasing velocity with depth. The uppermost pair of figures shows the results for an infinite S/N ratio. Notice the loss of resolution as the noise level increases from top to bottom. . . . . 67
4.1	Acquisition geometry for Figures 4.2, 4.3, and 4.4. The symbols mark station locations at which both sources and receivers were located on the free surface. Sources occupied each station, and active receivers were located at all 81 stations for each shot. . . . . 71
4.2	Wavenumber-domain images of the point scatterer at the test point in Figure 4.1. (A) Zero-offset result for collocated source-receiver at $(x, z) = (1000, 0)$ in Figure 4.1. (B) Result obtained using all source and receiver locations in Figure 4.1. . . . . 72
4.3	Space-domain images of the point scatterer at the test point in Figure 4.1. Fourier transforms of the wavenumber-domain images in Figure (4.2). (A) Zero-offset result for collocated source-receiver at $(x, z) = (1000, 0)$ in Figure 4.1. (B) Result obtained using all source and receiver locations in Figure 4.1. . . . . 73
4.4	(A) Wavenumber- and (B) space-domain images of the scatterer at the test point using a zero-offset acquisition geometry. Resolution is better than for the multioffset geometry (Figure 4.3B). These images are obtained by considering zero-offset source-receiver pairs located at each of the 81 stations in Figure 4.1. . . . . 75
4.5	Perspective view of the salt model used for testing survey design. A small, thin feeder stock can be observed near the center of the model on the front side of the image. The salt thickness is negligible outside of the dome and the feeder stock. . . . . 76

FIGURE	Page
4.6	Marine acquisition geometry used to compute image resolution for the salt dome model (Figure 4.5). The elliptical outline in the center indicates the approximate location and shape of the salt structure beneath the experiment. The station locations correspond to a single-cable geometry, and the hypothetical ship sailed in the vertical direction, firing in the region from $y = 6$ to $y = 11$ km. Since the receivers are towed behind the boat, there are stations outside of the total source region. . . . . 78
4.7	Circular/radial land acquisition geometry used to compute image resolution for the salt dome model (Figure 4.5). The elliptical outline in the center indicates the approximate location and shape of the salt structure beneath the experiment. This geometry is based on that used in the field experiment described by Constance et al. (1999). This figure shows only the locations of every fifth source along the concentric source line circles for clarity. . . . . 79
4.8	Orthogonal land acquisition geometry used to compute image resolution for the salt dome model (Figure 4.5). The elliptical outline in the center indicates the approximate location and shape of the salt structure beneath the experiment. . . . . 80
4.9	Example of receiver patches for the circular/radial (Top) and orthogonal (Bottom) land acquisition geometries used to compute image resolution for the salt dome model (Figure 4.5). The locations of the associated sources which define these particular templates are also indicated. . . . . 82
4.10	Subsalt resolution obtained using the acquisition geometries in Figures 4.6 and 4.7. Each figure shows the point scatterer images predicted for a depth of 4 km in a region underlying the center of the salt dome. (A) Near offsets, marine acquisition geometry. (B) Far offsets, marine acquisition geometry, (C) Near offsets, circular/radial acquisition geometry. . . . . 83



FIGURE	Page
4.11	Subsalt resolution obtained using the acquisition geometries in Figures 4.7 and 4.8. Each figure shows the point scatterer images predicted for a depth of 4 km in a region underlying the center of the salt dome. (A) Near offsets, circular/radial acquisition geometry (repeated from Figure 4.10C). (B) Near offsets, orthogonal acquisition geometry. . . . . 84
4.12	A perspective view of the salt model at a 45° angle with respect to the $x$ - and $y$ -axes and the screening effect of the salt body on the seismic rays emanating from a subsalt imaging point. For clarity, rays only of a single azimuth value are displayed. . . . . 85
4.13	Wavenumber vector plots for an imaging point centered beneath the salt diapir. Only the near offsets of the marine geometry were considered. The coverage of the wavenumber vector $k_x$ - $k_y$ plane (top) reflects the acquisition geometry. The asymmetric coverage of the $k_x$ - $k_z$ plane (bottom) is due to the feeder stock towards the negative $k_x$ -axis. . . . . 86
4.14	Wavenumber vector plot for an imaging point centered beneath the salt diapir. The near offsets of the circular/radial land acquisition geometry provide a better coverage of the wavenumber vector $k_x$ - $k_y$ plane compared to either the near- or the far-offsets of the marine geometry. . . . . 87
4.15	Comparison of ray paths for near- (above) and far-offset (below) pairs in the marine acquisition geometry (Figure 4.6) for the point beneath the center of the salt dome. Only rays for several lines near the center of the survey are displayed for clarity. The predicted image resolution is better for the far-offset geometry because the wavenumber vectors include a larger aperture, as shown by the correspondingly larger ray aperture at the image point. . . . . 89
4.16	Subsalt resolution obtained using the acquisition geometries in Figures 4.6, 4.7 and 4.8. Each figure shows the relative standard deviation measure predicted for a depth of 4 km in a region underlying the center of the salt dome. (A) Near offsets, marine acquisition geometry. (B) Near offsets, circular/radial acquisition geometry, (C) Near offsets, orthogonal acquisition geometry. . . . . 90

FIGURE	Page
4.17	Subsalt resolution obtained using the acquisition geometries in Figures 4.6, 4.7 and 4.8. Each figure shows the smoothness measure predicted for a depth of 4 km in a region underlying the center of the salt dome. (A) Near offsets, marine acquisition geometry. (B) Near offsets, circular/radial acquisition geometry, (C) Near offsets, orthogonal acquisition geometry. . . . . 91
4.18	Subsalt resolution obtained using the acquisition geometries in Figures 4.6, 4.7 and 4.8. Each figure shows the error (in %) between the relative standard deviation measures predicted by the orthogonal acquisition survey and (A) the marine acquisition geometry or (B) the circular/radial acquisition geometry. (For plots of the relative standard deviation measures, see Figure 4.16.) . . . . 92
4.19	Subsalt resolution obtained using the acquisition geometries in Figures 4.6, 4.7 and 4.8. Each figure shows the error (in %) between the smoothness measures predicted by the orthogonal acquisition survey and (A) the marine acquisition geometry or (B) the circular/radial acquisition geometry. (For plots of the smoothness measures, see Figure 4.17.) . . . . . 93
4.20	Narrow marine acquisition geometry used to compute image resolution for the salt dome model (Figure 4.5). The elliptical outline in the center indicates the approximate location and shape of the salt structure beneath the experiment. The station locations correspond to a single-cable geometry, and the hypothetical ship sailed in the vertical direction, firing in the region from $y = 6$ to $y = 11$ km. Since the receivers are towed behind the boat, there are stations outside of the total source region. For comparison, the extended marine acquisition geometry of Figure 4.6 is also shown (shaded stations). . . . . 95
4.21	Subsalt resolution obtained using the acquisition geometry in Figure 4.20. Each figure shows the point scatterer images predicted for a depth of 4 km in a region underlying the center of the salt dome. (A) Near offsets. (B) Far offsets. (C) All offsets. . . . . 97

FIGURE	Page	
4.22	Subsalt resolution obtained using the acquisition geometry in Figure 4.20. Each figure shows the spatial images predicted for a scatterer located directly beneath the center of the salt at the depth of 4 km. (A) Near offsets, marine acquisition geometry. (B) VSP1 (receiver in well 1). (C) VSP2 (receiver in well 2). . . . .	99
4.23	Subsalt resolution obtained using the acquisition geometry in Figure 4.20. Each figure shows the spatial images predicted for a scatterer located directly beneath the center of the salt at the depth of 4 km. (A) Combined near offsets and VSP1. (B) Combined near offsets and VSP2. (C) Combined near offsets and both VSP's. . . . .	100
4.24	Locations of four points located near the salt dome at a depth of 2 km. The points are used to assess salt flank imaging potential of the marine and two land acquisition geometries (Figures 4.6, 4.7 and 4.8). . . . .	101
4.25	Spatial resolution for the four salt flank image points in Figure 4.24. Only the near offsets from the marine acquisition geometry were used. . . . .	103
4.26	Spatial resolution for the four salt flank image points in Figure 4.24. Only the far offsets from the marine acquisition geometry were used. . . . .	104
4.27	Spatial resolution for the four salt flank image points in Figure 4.24, using the near offsets from the circular/radial land acquisition geometry. . . . .	105
4.28	Spatial resolution for the four salt flank image points in Figure 4.24, using the near offsets from the orthogonal land acquisition geometry. . . . .	106

FIGURE	Page
4.29	Spatial resolution for the salt flank image point A from Figure 4.24 for different S/N ratios (SNR). The left column displays results for the far offsets from the marine geometry; the right column is for the near offsets from the circular/radial land survey. The uppermost pair of figures shows the results for perfect, noise-free data and are identical to the corresponding images in Figure 4.26 and 4.27. . . . . 108
4.30	VSP acquisition geometry used to compute image resolution for the salt dome model (Figure 4.5). For comparison, the circular/land acquisition geometry of Figure 4.7 is also shown (shaded stations). . . . . 109
4.31	Spatial images of the scattering point under examination using sources along line 135. (A) Dominant frequency of source signal is 30 Hz. (B) Dominant frequency of source signal is 90 Hz. . . . . 110
4.32	Spatial images of the scattering point under examination. Predicted image using (A) sources along line 135 (repeated from Figure 4.31B), and (B) sources along line 225. . . . . 111
4.33	Spatial images of the same scattering point as in Figure 4.32. Predicted image using (A) sources along both lines (135 and 225), and (B) all sources within the sector defined by lines 110 and 250. . . . . 112
5.1	Map view of seismic source, surface receiver and populated borehole locations used in the simultaneous surface/VSP acquisition. . . . . 117
5.2	Only the Northern half (black dots) of the total source spread of the combined surface/VSP survey was recorded by the 3-C receivers in the two wells. The open circles indicate the sources that comprised the NW-SE line under further examination (see also, Figure 5.4). . . . . 118
5.3	Common shot gathers along a NW-SE line through the well (Figure 5.4). A) Near offset gather (source/well separation = 160 m). B) Mid offset gather (source/well separation = 2156 m). C) Far offset gather (source/well separation = 4356 m). . . . . 119

FIGURE	Page
5.4	Detailed map view of the NW-SE line sources and their position relative to the well. The labels (A,B,C) refer to the shot gathers shown in Figure 5.3. . . . . 121
5.5	Travel times for the two nearest offset shot gathers to the NW of the well. The discrepancies between the relative picked travel times (solid lines) and the cross-correlation time lags (circles) for the greater relative travel times are attributed to the different response of the deeper receivers. The arrows indicate the transition point between different types of receivers. . . . . 126
5.6	A typical shot gather with the first arrivals aligned. The signal character change between shallow (traces 1 to 40) and deep (traces 41 to 65) receivers and its effects on later events is very clear. . . . . 127
5.7	The same shot gather as in Figure 5.6 after phase and time correction. Notice the improvement on the continuity of the two events at the time of 100 and 700 ms (marked with arrows). . . . . 129
5.8	Schematic explaining the variables involved in the correction of travel time for the source's non-zero offset. After the correction is applied, the travel times simulate a check-shot survey. . . . . 130
5.9	Interval velocity graph simulating the velocity field at the well location. The one-dimensional velocity profile indicates a gradual velocity increase with depth. . . . . 131
5.10	The different gradient models as inferred from the velocity analysis of the nearest-offset shot gather (Figure 5.9). The one- and two-gradient models (black and blue lines) are the least-square fit curves to the interval velocities. For the shallower part of the model, additional constraints were applied to ensure the velocity continuity at depth and velocities greater than 1.5 km/s at the surface (red lines). . . . . 132
5.11	Proposed velocity models along the NW-SE seismic line. (A) The result of travelttime inversion of a single-gradient initial velocity model. (B) Layered model resulted from the velocity analysis of the surface seismic data. . . . . 134

FIGURE	Page
5.12	The difference between the two velocity fields of Figure 5.11. Since tomographic results are reliable only in the area defined by the two rays (black lines) and the free surface, the “log-like” realizations of the velocity difference at the well and an arbitrary location are confined within this region. . . . . 135
5.13	Separated up-going wavefields using (A) median and (B) $f$ - $k$ filtering techniques. Observing their difference (C), it becomes readily obvious that median filtering allowed some of the down-going energy with different slope than the first arrival to “leak” into the up-going wavefield record. (D) The original shot gather data, representing the total wavefield. . . . . 138
5.14	Spatial image of a scatterer located 200 m away from the well in the downdip direction. The shot gathers that contribute to the image correspond to the 7 sources lying on the same side of the well as the test point itself. . . . . 140
5.15	The spatial image of the same point as in Figure 5.14. The 4 shots in the updip direction (i.e., lying on the opposite side of the well than the test point) also contributed to the imaging of the scatterer. The improvement of the spatial wavefield sampling is translated to a better resolved image of the imaging point. . . . . 141
5.16	Predicted vertical resolution (in m) of a series of test points. All 11 shots contributed in the imaging. On the far right of the model, the compressional velocities of each layer are denoted (in km/s). . . . 142
5.17	Predicted vertical resolution (in m) of a series of test points. Only the 7 shots in the downdip direction contributed in the imaging. On the far right of the model, the compressional velocities of each layer are denoted (in km/s). . . . . 143
5.18	Migrated section of all 11 synthetic gathers. The layer model used in both the forward model and the migration is overlaid for comparison reasons. . . . . 145

FIGURE	Page
5.19	Migrated section of only the 7 downdip synthetic gathers. Compared to Figure 5.18, it shows that neglecting the updip gathers affects mainly the updip portions of the imaged reflectors. The layer model used in both the forward model and the migration is overlaid for comparison reasons. . . . . 146
5.20	Raytracing reveals that downdip gathers are exclusively responsible for imaging the dowdip portion of the interfaces, covering some of the updip portions as well (red lines). On the other hand, updip gathers manage to image portions of the reflectors (blue lines) in the updip direction further away from the well. . . . . 147
5.21	Comparison of the predicted vertical resolution (black circles) to the measured resolution from the migrated synthetic gathers (red circles). All 11 gathers were considered in both approaches. . . . . 148
5.22	Migrated section of only the 7 downdip shot gathers of the field data. The layer model used in the migration is overlaid for comparison reasons. . . . . 150
5.23	Comparison of the predicted vertical resolution (black circles) to the measured resolution from the migrated field gathers (red circles). The 7 gathers in the downdip direction from the well were considered in both approaches. . . . . 151

## CHAPTER I

### INTRODUCTION

Design of 3-D seismic surveys can seek optimizations with several different objectives. For example, an initial survey in a new field might seek to provide an optimal image over a large range of depths and lateral positions to locate hydrocarbon reserves. On the other hand, in a more mature area, the goal might be to target a single reservoir with the most economical and precise image for only one unique, laterally constrained location in the subsurface. A third potential scenario could be the design of a survey for time-lapse seismic projects. In this case, the survey should be designed to not only yield an effective image of the reservoir, but to also provide complimentary results to the earlier data sets. In addition, any differences in resolution or image quality should be quantified, if possible.

Seismic survey design, however, is often a relatively qualitative procedure and cannot address the aforementioned issues. Simple ray tracing methods provide one technique for obtaining some quantitative input by measuring binning along target interfaces. Although fold calculation is important in predicting whether a good signal to noise ratio can be obtained using a particular survey geometry, it is rather misleading as an “illumination” measure because it does not incorporate any ray geometry information. For example, consider a case where a point of interest exhibits high fold but all rays are predominantly in the same direction. Structural or geological complexities might be the cause of such extreme behavior. Although the fold is high, the point will be poorly resolved since it is illuminated from a very narrow range of angles.

Results from inverse theory, on the other hand, can provide important constraints on acquisition design that are truly quantitative and objective. Based on Beylkin’s approach to spatial image resolution estimation (Beylkin, 1984; Beylkin, 1985), this research seeks to develop an accurate and objective way to assessing the effectiveness of any given acquisition geometries. Our main criterion will be the image resolution

---

This dissertation follows the style and format of Geophysics.



one can obtain at the target area using a particular acquisition geometry.

### 1.1 Image resolution analysis: An alternative to conventional illumination analyses

Conventional seismic survey design procedures tend to apply simple, qualitative analyses to compare various competing survey designs or to assess variations of image quality for a specific survey. The simplest procedure is to simply compute fold using the source/receiver geometry, completely neglecting Earth structure and wave propagation effects. Other illumination analyses seek to not only optimize fold coverage but also azimuth and/or offset distribution (Cordson et al., 2000). An even better approach is that proposed by Slawson et al. (1994; see also Slawson et al., 1995), who suggested a model-based 3-D acquisition design to incorporate structural complexities and velocity variations into an accurate common reflection point (CRP) binning analysis for a more realistic representation of the imaging capabilities of the proposed acquisition geometry. This method can easily identify regions of poor or no CRP bin coverage, thus facilitating the modification and subsequent improvement of the acquisition survey design under examination. However, the CRP coverage analysis still neglects the ray geometries at reflection points, counting only the total number of ray reflection points at a specific location. Therefore, these procedures do not directly produce information that can be used for *quantitative* analysis of spatial resolution of the seismic surveys.

Here, as an example, we consider a simple, one layer homogeneous 2D earth model to clearly demonstrate the limitations of the fold as an illumination measure even in cases where structural and/or geological settings are not challenging as far as imaging is concerned. The survey under consideration was a split-spread, consisting of 41 sources, spaced every 50 m for a total source array length of 2 km. Each source was recorded in 20 receivers on each side of the source. The receiver spacing was also 50 m. According to the fold diagram (Figure 1.1A) for CDP bins of 25 m, illumination is best when the fold is 20 and tapers off at both edges of the survey. This behavior of the fold is independent of the depth of the horizon. Therefore, fold suggests equal illumination for a range of horizontal distances (3 to 4 km) at any depth. The standard deviation measure is one of the tools we developed to quantitatively assess the seismic image resolution, and is discussed in detail in chapter II. The standard deviation curves of

Figure 1.1B, exhibit different behavior predicting that the best illuminated point is right in the middle of the array. Any lateral displacement would result in less resolved points. The rate of this resolution deterioration clearly depends on the depth of the points as this is demonstrated by the two curves. Figure 1.1C shows the resolution predictions for a series of points beneath the center of the array in different depths. The image resolution decreases with depth, an intuitive reasonable result. The reason for this discrepancy between the fold and the proposed method lies in the fact that the image resolution measures account for the ray geometry (direction) whereas the fold does not. When a point of interest is at greater depths (or laterally displaced off the center of the array), rays cluster together and the range of angle of incidence becomes smaller, decreasing this way the effective aperture. Therefore, the point is illuminated from fewer different angles leading to a resolution that is poorer than that of a point at shallower depths (or near the center of the array).

Fold analysis can still be used to determine whether a particular experiment can improve signal to noise ratio and provides some qualitative indication about illumination. However, we showed that even in simple cases, relying on fold measures only can be misleading. More sophisticated techniques where more parameters (azimuth, offset) are taken into account are prone to the same errors when complex structures are considered. Tzimeas and Gibson, Jr. (1999) also considered the case of a more complex 3D salt model with the target being a subsalt planar surface. According to the fold analysis, the area directly underneath the salt structure should have been better illuminated. This prediction was in total contradiction to typical subsalt images and the result of severe ray focusing due to the salt diapir.

From the above, it immediately becomes apparent that *quantitative* measures of seismic image resolution can be very helpful in designing optimal acquisition geometries. In the following chapters, we develop several such measures, compare them to other methods and apply them to several synthetic models as well as field datasets.

More specifically, in chapter II, we discuss in detail the development of the quantitative image resolution measures of standard deviation, smoothness, wavenumber vector scatter plots and spatial images. We validate one against the others by considering simple 2D acquisition geometries. Moreover, we compare their image resolution prediction to an independent imaging method, namely the Kirchhoff prestack migration.

Chapter III considers factors other than the acquisition geometry that can affect

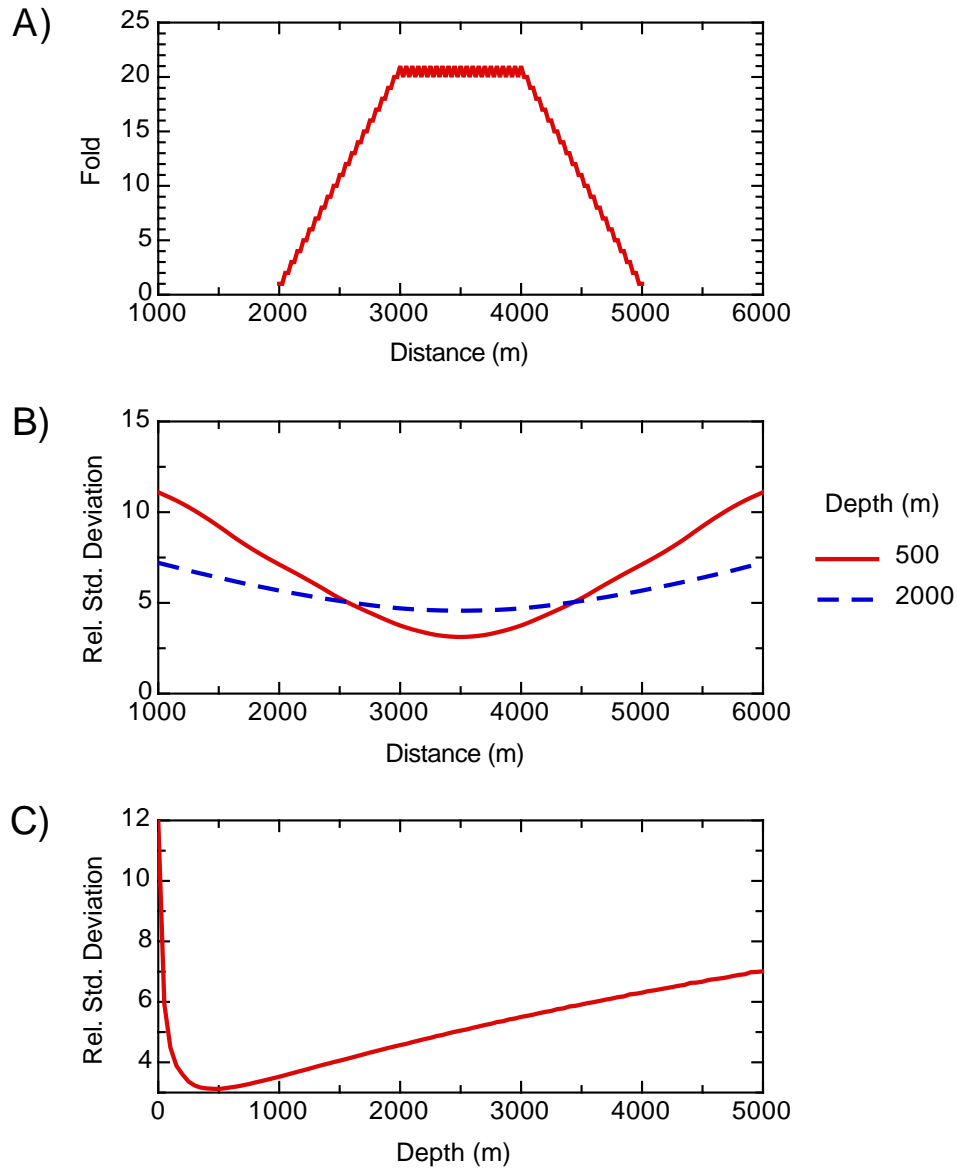


Fig. 1.1. A) Fold diagram for the split-spread seismic experiment. If used as a resolution indicator, fold predicts equally good resolution for all points lying within the distances of 3 and 4 km irrespectively of depth. B) Relative standard deviation curves for a series of scattering points at two different depth levels (500 and 2000 m). C) Depth profile of relative standard deviation for scattering points underneath the center of the seismic array. In general, the standard deviation measure predicts changes of image resolution not only laterally but vertically as well.

spatial image resolution. We demonstrate that understanding how the structure and velocity of a given model, as well as signal-to-noise ratio influence the spatial resolution predictions of the proposed method, is an important parameter in interpreting the results correctly and better assessing the effectiveness of the examined acquisition geometry.

In chapter IV, we apply the proposed image resolution analysis to a 3D salt dome. We compare the ability of three competing acquisition designs to resolve targets underneath and adjacent to the salt body. In addition to this comparison, we examine the conditions under which a narrow marine geometry’s resolving capability can benefit from a simultaneous Vertical Seismic Profiling (VSP).

Finally, in chapter V, we apply our method to a VSP field dataset. The VSP data are processed and prestack depth migrated. We compare the predicted spatial resolution of our image analysis to the migrated images.

## 1.2 Background theory

Seismic survey design procedures usually depend on simple, qualitative analyses to examine antagonistic survey designs or evaluate image resolution variations for a particular geometry. A typical study may specify source and receiver geometries, choose a reference earth model and then perform ray tracing. The ray tracing results are typically analyzed only in terms of fold, or illumination. This type of analysis can provide some useful insights, such as detecting regions of the subsurface that are not imaged by the experiment. However, as was clearly demonstrated in the example of the previous section, this information can be difficult to utilize for *quantitative* analyses.

On the other hand, it is possible to obtain a more quantitative result using inversion theory. Inverse methods are broadly classified into (1) operator-based approaches such as migration, and (2) model-based approaches such as travel-time tomography. Operator-based inversion methods estimate model parameters directly from the observed data using a specified mathematical model for wave propagation. An example of operator-based inversion for improved survey design is given by Gibson, Jr. et al. (1994). They performed a modeling study to design a source configuration which could be used to collect VSP data suitable for 3-D elastic Kirchhoff migration. In contrast, Barth and Wunsch (1990) applied a model-based optimization. They attempted

to estimate the optimal distribution of shots and receivers for an ocean acoustic tomographic experiment. The inverse problem was given in the form  $\mathbf{G}\mathbf{m} = \mathbf{d}$  where  $\mathbf{G}$  is the design matrix,  $\mathbf{m}$  are the desired slowness values and  $\mathbf{d}$  is the data. In general, the appropriate objective criterion depends on the goals of the survey, but they found a useful result by requiring the smallest singular value of  $\mathbf{G}$  to be as large as possible. They perturbed the source and receiver distribution using simulated annealing until the smallest singular value was maximized.

Beylkin (1984; 1985) and Beylkin et al. (1985) made an important contribution to this field of study by demonstrating that the spatial resolution of seismic imaging can be computed using these ray tracing results. Specifically, he showed that the geometry of ray paths from source and receiver to a subsurface image point, along with the source signal bandwidth, controls the maximum resolution that can be obtained. Therefore, a much more detailed and useful analysis of resolution can be obtained with comparatively little numerical effort. This approach allows a direct estimation of the spatial resolution length, which in turn can be used to estimate error in the size and distribution of reservoir features. Likewise, distortions in seismic images by ray bending and focusing are easily detected and can be included in interpretation.

The approach to estimating spatial resolution of seismic experiments was obtained by applying the Generalized Radon Transform to the acoustic scattering problem. The scattered waves are described using the single scattering (Born) approximation, and the inverse algorithm applies ray methods to compute the traveltimes and amplitudes of waves travelling from source to image point and back to the receiver. This approach, and similar methods for elastic media, have been described in a number of references (e.g., Beylkin et al., 1985; Beylkin, 1985; Beylkin and Burridge, 1990).

First, the forward problem can be linearized in the form:

$$u_{total}(\xi, \eta, t) = u_{in}(\xi, \eta, t) + \delta u(\xi, \eta, t), \quad (1.1)$$

where the total scalar displacement field  $u_{total}$  for a source at location  $\eta$  and receiver location  $\xi$  is expressed as the sum of incident and scattered fields.

The linearized equation for the frequency domain field  $\delta u(\xi, \eta, \omega)$ , assuming a fixed source location  $\eta$ , is the Born approximation

$$\delta u(\xi, \eta, \omega) = -\omega^2 \int_{\mathcal{X}} G(\xi, \mathbf{x}, \omega) f(\mathbf{x}) u_{in}(\eta, \mathbf{x}, \omega), \quad (1.2)$$

where  $f(\mathbf{x})$  is the perturbation to a smoothly varying background index of refraction  $n_o(\mathbf{x})$  such that the total index is given by  $n^2(\mathbf{x}) = n_o^2(\mathbf{x}) + f(\mathbf{x})$ . Analogous expressions can be written for the elastic problem (Beylkin and Burridge, 1990). The inversion problem is to develop a scheme to estimate the unknown perturbations  $f(\mathbf{x})$ , given observations of data  $\delta u(\xi, \eta, \omega)$ .

The general form of the solution for this integral equation for the estimated solution  $f_{est}(\mathbf{x})$  is

$$f_{est}(\mathbf{x}) = 2Re \int_{Dx_{rcv}} \int_0^\infty M(\xi, \eta, \mathbf{x}, \omega) \delta u(\xi, \eta, \omega) d\xi d\omega, \quad (1.3)$$

where  $Re$  indicates the real part of the result and  $Dx_{rcv}$  indicates the region of the Earth's surface occupied by receivers.  $M(\xi, \eta, \mathbf{x}, \omega)$  is a kernel that provides the inverse solution. If, as usual, there are multiple source positions, there will be an additional integral over source position in this solution (Beylkin et al., 1985). The exact form of the kernel depends on the medium (i.e., elastic or acoustic) and other assumptions, but a typical first step is to utilize ray methods to simulate wave propagation in the background medium with known index of refraction  $n_o(\mathbf{x})$ .

For the acoustic inversion problem, the frequency domain ray theoretical Green's functions for the incident wavefield is

$$G^{in}(\eta, \mathbf{x}, \omega) = -A^{in}(\mathbf{x}, \eta) e^{i\omega\phi^{in}(\mathbf{x}, \eta)}, \quad (1.4)$$

where the phase, or travelttime, function is  $\phi^{in}(\mathbf{x}, \eta)$  and the amplitude is  $A^{in}(\mathbf{x}, \eta)$ . Similarly, the scattered wave Green's function is

$$G^{sc}(\xi, \mathbf{x}, \omega) = -A^{sc}(\mathbf{x}, \xi) e^{i\omega\phi^{sc}(\mathbf{x}, \xi)}. \quad (1.5)$$

An explicit solution of the integral equation using the Generalized Radon Transform was presented by Beylkin (1985) (see also Beylkin et al., 1985, equation 2.2):

$$M(\xi, \eta, x, \omega) = -\frac{1}{16\pi^3} \frac{e^{-i\omega[\phi^{sc}(\mathbf{x}, \xi) + \phi^{in}(\mathbf{x}, \eta)]}}{A^{sc}(\mathbf{x}, \xi) A^{in}(\mathbf{x}, \eta)} h(\mathbf{x}, \xi, \eta). \quad (1.6)$$

The factor  $h(\mathbf{x}, \xi, \eta)$  is a Jacobian of a specific coordinate transformation, which can be related to a mapping from the pair  $\omega, \xi$  to a vector  $\mathbf{k}$  that is a wavenumber vector discussed further below. In this kernel, the amplitude factors in the denominator cancel out the amplitude of the incident wavefield and Green's function in equation (1.2).

The numerator includes the total traveltime from the source  $\eta$  to image point  $\mathbf{x}$  and from the image point to the receiver location  $\xi$ .

Beylkin (1985) (see also Beylkin et al., 1985) proved that the estimated space domain image of the point scatterer  $f_{est}(\mathbf{x})$  can (up to a smooth error) be expressed as

$$f_{est}(\mathbf{x}) = \frac{1}{(2\pi)^3} \int_{D_x} F(\mathbf{k}) e^{-i\mathbf{x}\cdot\mathbf{k}} d\mathbf{k}. \quad (1.7)$$

The point scatterer is represented by the function  $f(\mathbf{x})$  and its Fourier transform is  $F(\mathbf{k})$ , where  $\mathbf{k}$  is the wavenumber vector. Function  $f(\mathbf{x})$  is assumed to be real implying that both  $\mathbf{k}$  and  $-\mathbf{k}$  are mapped in the Fourier space. The domain of integration,  $D_x$ , is the key to understanding the spatial resolution.  $D_x$ , unlike conventional Fourier transforms, does not extend to infinity. Instead, this domain is controlled by the source/receiver acquisition geometry. For a specific point  $\mathbf{x}$  in the subsurface, the wavenumber values that are included in the image domain are obtained from the following relationship:

$$\mathbf{k} = \omega [\nabla\tau(\mathbf{x}, \eta) + \nabla\tau(\mathbf{x}, \xi)]. \quad (1.8)$$

Here  $\omega$  is the frequency,  $\mathbf{x}$  is the image point,  $\eta$  is the location of a source point, and  $\xi$  is the location of a receiver. The function  $\tau$  is simply the ray-theoretical travel time for the ray connecting the indicated two points. It follows that the gradient of this travel time function,  $\nabla\tau(\mathbf{x}, \eta)$ , is the slowness vector along the ray. In other words, it is the vector parallel to the ray at the image point  $\mathbf{x}$ , with magnitude equal to  $1/v$ ,  $v$  being the seismic velocity at the point. Therefore, the image wavenumber vector resulting from a specific source/receiver pair is simply the sum of the slowness vectors along the rays from both source and receiver down to the image point, weighted by frequency (Figure 1.2). The wavenumber domain image of the scatterer is the total set of wavenumber domain points computed for all source/receiver pairs using equation (1.8). Clearly, the more restricted the region of the surface occupied by sources and receivers, the more restricted will be the range of the wavenumber domain that is covered in this Fourier integral and the worse the reconstruction of the image  $f_{est}(\mathbf{x})$ . Some initial applications of this approach were made by Miller et al. (1989) and von Seggern (1991), though they did not directly consider the implications for survey design.

This approach to inversion and resolution is based on the Born approximation for scattered acoustic waves (equation 1.2); in this framework, it is most natural to

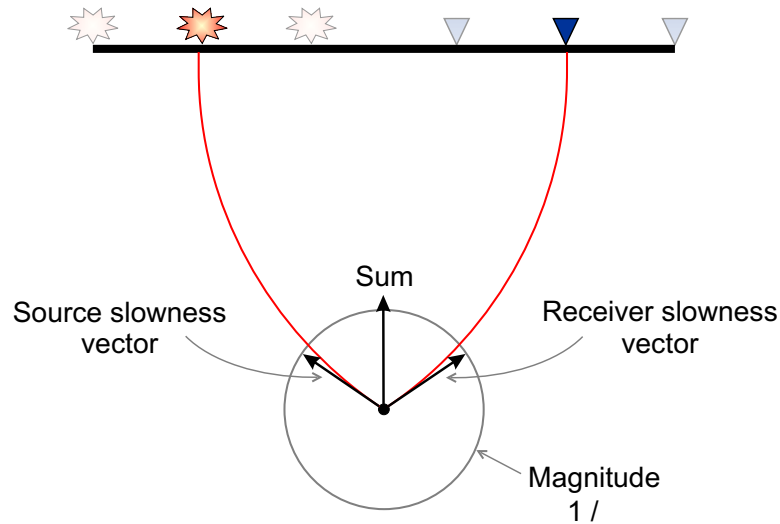


Fig. 1.2. Schematic illustration of the wavenumber vector described by equation (1.8). The wavenumber vector that represents the portion of the wavenumber domain resolved by data acquired by the illustrated source/receiver pair is the bold vector, the sum of the two vectors tangent to the ray paths at the image point. The oppositely directed wavenumber vector is also included in the wavenumber domain (Beylkin et al., 1985).

consider the Earth model as discretized into individual volume elements that can be modeled as point scatterers. This is the viewpoint that we will adopt below, but there are alternatives. For example, it is possible to describe the forward model for the scattered wavefield as reflections from interfaces. Bleistein (1987) developed such a solution based on “Kirchhoff data”. Since the data are explicitly described as reflections from interfaces, it is natural to develop an inversion for angle-dependent reflection coefficient. This approach has been expanded in other papers (e.g., Bleistein, 1989; de Hoop and Bleistein, 1997). Because these inversion schemes rely on reflections from interfaces, valid ray paths must satisfy Snell’s law, and this therefore restricts that range of wavenumber vectors computed using equation (1.8) to those normal to the interface.

The importance of Beylkin’s equation [equation (1.8)] coming from the Generalized Radon Transform, lies in the fact that we are able to estimate spatial image resolution by performing relatively simple forward computations. In contrast, migration schemes which can also provide estimates of image resolution, are indeed imaging/inversion methods and thus, more expensive (time and resource consuming). There are definite similarities with the classical inverse problem ( $\mathbf{Gm} = \mathbf{d}$  where  $\mathbf{G}$  is



the data kernel,  $\mathbf{m}$  the model parameter matrix, and  $\mathbf{d}$  the observed data) where the model resolution matrix  $\mathbf{R}$  can be expressed as  $\mathbf{R} = \mathbf{G}\mathbf{G}^{-\mathbf{g}}$ . Here,  $\mathbf{G}^{-\mathbf{g}}$  is the generalized inverse matrix (Menke, 1984). Therefore, the resolution matrix is a function of the data kernel only and can be computed without conducting the experiment. However, if we needed to formulate the spatial resolution prediction problem in the same way, the ray-theoretical traveltime data would not suffice. Similar to the imaging problem, it would be necessary to obtain additional information (for example, amplitudes). It would, therefore, become as expensive to perform the image resolution analysis as a migration scheme.

## CHAPTER II

### METHOD DEVELOPMENT

#### 2.1 Introduction

Beylkin (1984; 1985) and Beylkin et al. (1985) demonstrated through the equations (1.7) and (1.8) that the spatial resolution of seismic imaging can be computed using the forward modeling results of ray tracing. The most important factor that controls the maximum image resolution that can be theoretically obtained is the distribution of the sources and receivers which determine the domain of integration  $D_x$  of equation (1.7) and are used in a seismic experiment. Therefore, we can use these equations, especially equation (1.8), to help us design acquisition geometries that provide good image quality at specific subsurface targets (e.g., reservoirs, subsalt structures etc.).

In this chapter, we discuss the measures we developed and used for quantitative assessment of the seismic image quality. We also demonstrate that the resolution predictions do in fact provide a good measurement of spatial resolution by comparing them to spatial images obtained by prestack migration methods. We finally show how the image resolution provides a better criterion in acquisition design than others conventionally used in the petroleum industry.

#### 2.2 Image resolution measures

The point scatterer representation as stated in equation (1.7), provides an excellent means of predicting spatial resolution. The wavenumber domain image of the scatterer is the total set of wavenumber vectors computed for all source/receiver pairs using equation (1.8). This theoretical result is used in our method to assess variations in image quality for different acquisition geometries. However, working in the wavenumber domain as this result is presented, can be hard relate to image quality. Therefore, we developed a series of resolution measures on which we rely to compare the effectiveness of competing acquisition designs.

In the following subsections, we describe each resolution measure, the motivation

behind its development and its advantages and disadvantages.

### 2.2.1 Scatter plots

Wavenumber vectors can be computed using equation (1.8). A first approach to quantitatively assess the resolution of a point scatterer is by directly plotting the wavenumber vector plots (Miller et al., 1989; von Seggern, 1991). Recalling that the wavenumber domain representation of a point scatterer is a constant value of one, it is clear that we can consider such a scatter plot as a filtered version of a point scatterer. The best resolved (illuminated) point scatterer using a particular acquisition pattern would be the one whose wavenumber vector plot exhibits the most uniform coverage of the wavenumber domain.

A simple, homogeneous model with a compressional velocity  $v_p = 2$  km/s and a simple linear source/receiver array will be used throughout the resolution measure sections (Figure 2.1). The source array consists of 31 sources spaced every 100 m for a total length of 3 km ( $x$  coordinate ranges from -1500 to 1500 m). The receiver array is denser (61 receivers spaced every 50 m) and occupies the same physical space as the source array. Signals from each source were recorded at all 61 receivers. In Figure 2.2, we show wavenumber domain images of 3 point scatterers at three different depths (200, 500 and 4000 m from top to bottom), underneath the center of the array. The plotted wavenumber vectors correspond to a range of frequencies from 5 to 60 Hz with an increment of 2.5 Hz.

Although such a representation of the wavenumber domain coverage is insightful, it has obvious shortcomings originating from the fact that the wavenumber vectors are plotted in discrete increments of frequency. Simulating real seismic experiments requires considering the effects of a source wavelet with a certain bandwidth and amplitude spectrum. We accomplish that in the wavenumber domain by applying a Cartesian binning scheme — bin size is chosen according to the sampling theorem (Bracewell, 1986) — and weighting the contribution of each wavenumber vector in a particular Cartesian bin by the amplitude of the source spectrum at the corresponding frequency. For all the examples in this chapter, a Ricker-type seismic wavelet with a dominant frequency of 30 Hz was used (Figure 2.3). The resulting wavenumber domain images are shown in Figure 2.4. Note that the gray-scale images better indicate that although the aperture of the scattering points decrease with depth, there

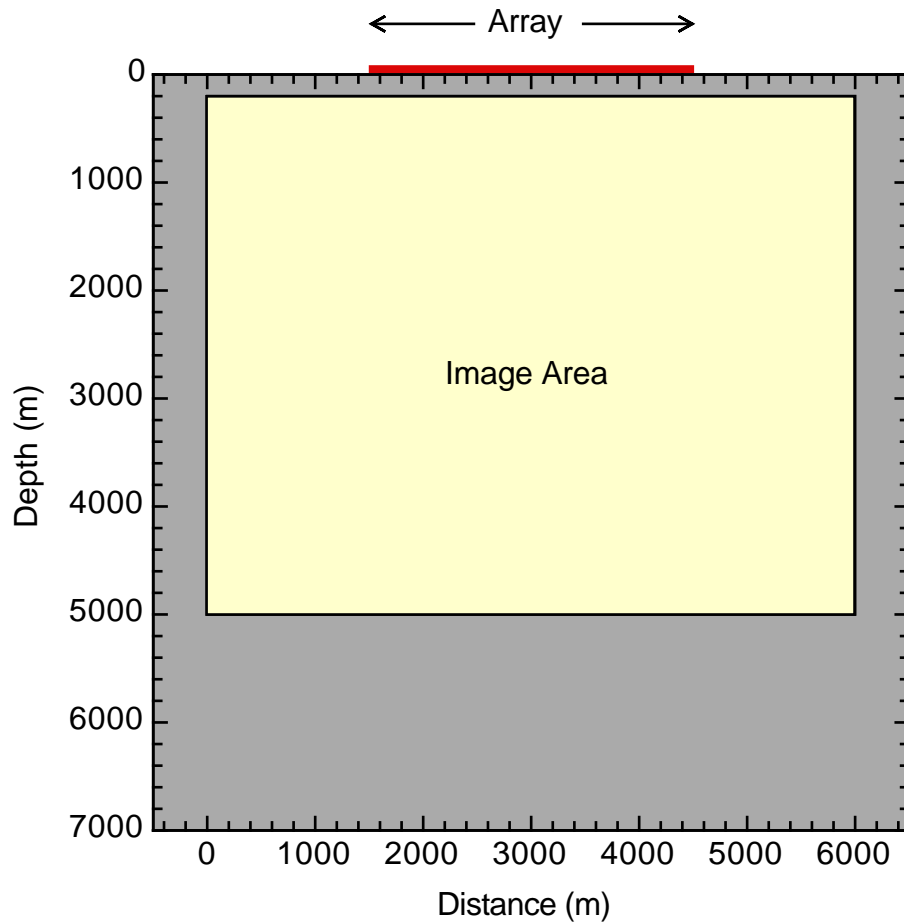


Fig. 2.1. Homogeneous model used to demonstrate the effectiveness of the proposed image resolution measures. The seismic array is 3 km long consisting of 31 sources and 61 receivers evenly spaced every 100 and 50 m respectively. Note that the image area of interest extends laterally beyond the edges of the seismic array.

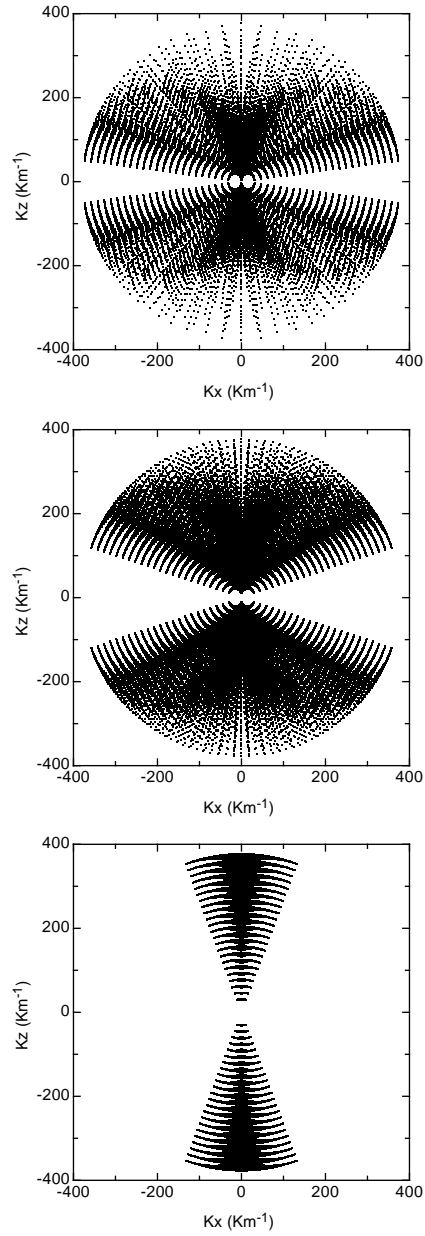


Fig. 2.2. Wavenumber scatter plots for three scattering plots underneath the center of the seismic array of Figure 2.1. From top to bottom, their depths are 200, 500 and 4000 m. Note that the wavenumber vector aperture decreases continuously with depth.

is an optimum depth at which the wavenumber domain is more smoothly and evenly “sampled” in all directions. Specifically, the wavenumber domain representation of the scattering points at depths of 200 and 4000 m exhibit a preferred direction along which most of the wavenumber vectors point. This direction is nearly horizontal and vertical, respectively, meaning that the seismic image resolution is going to be much better along these directions than any other. On the other hand, the coverage of the wavenumber domain for the scattering point at the depth of 500 m lacks the strong wavenumber vector alignment along certain directions. Therefore, despite the fact that its wavenumber domain aperture is smaller than that of the scattering point at the depth of 200 m ( $143^\circ$  against  $165^\circ$ ), the scattering point is expected to be better resolved.

Although such an approach is direct and very straightforward, its limitation becomes apparent when we need to image and assess the quality of the imaging of a large portion of the subsurface, as is usually the case with surface surveys. The wavenumber vector plots are generally three-dimensional and their visualization requires the use of appropriate software. Therefore, their use in image resolution assessment for a large volume of the subsurface would not only be very intensive in terms of computer resources but also impractical since one would have to compare a huge amount of three-dimensional information. For this reason, we developed two scalar image resolution measures, namely, the standard deviation and smoothness measures which are based on simple statistical or mathematical principles. These measures are further discussed in the following sections.

### 2.2.2 Space domain images

By applying an inverse Fourier transform to the wavenumber domain image of a point scatterer associated with a particular acquisition geometry, one can compute the spatial image of the scatterer. We implemented the transform step using a modern, high speed FFT library named “Fastest Fourier Transform in the West” (FFTW) developed in the Laboratory for Computer Science at MIT (Frigo and Johnson, 1998; Frigo, 1999). The source code for this library is free and is distributed under a GNU license. Not only does the library allow optimized, rapid FFT computations, but it also does not restrict array sizes to be a power of two. This allows a more flexible and natural implementation of the algorithms and conserves memory by avoiding zero

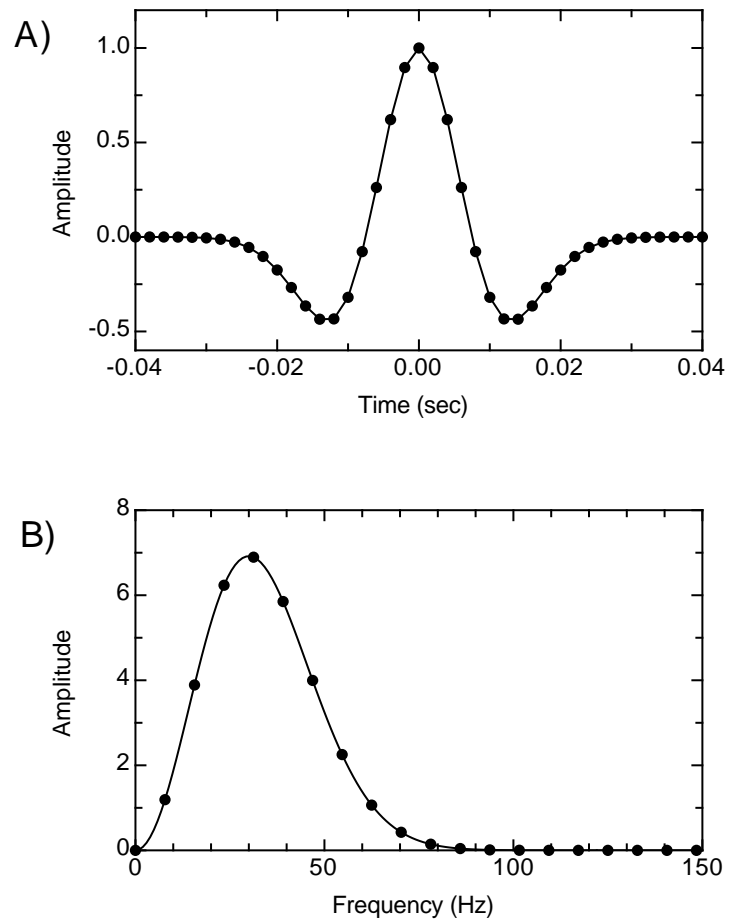


Fig. 2.3. A) Ricker-type source wavelet used in the seismic experiments of this chapter and B) its amplitude spectrum. Its dominant frequency is 30 Hz. The dots denote the sampling increments in both time (2 ms) and frequency ( $\approx 7.8$  Hz) for the discrete Fourier Transform of 64 samples.

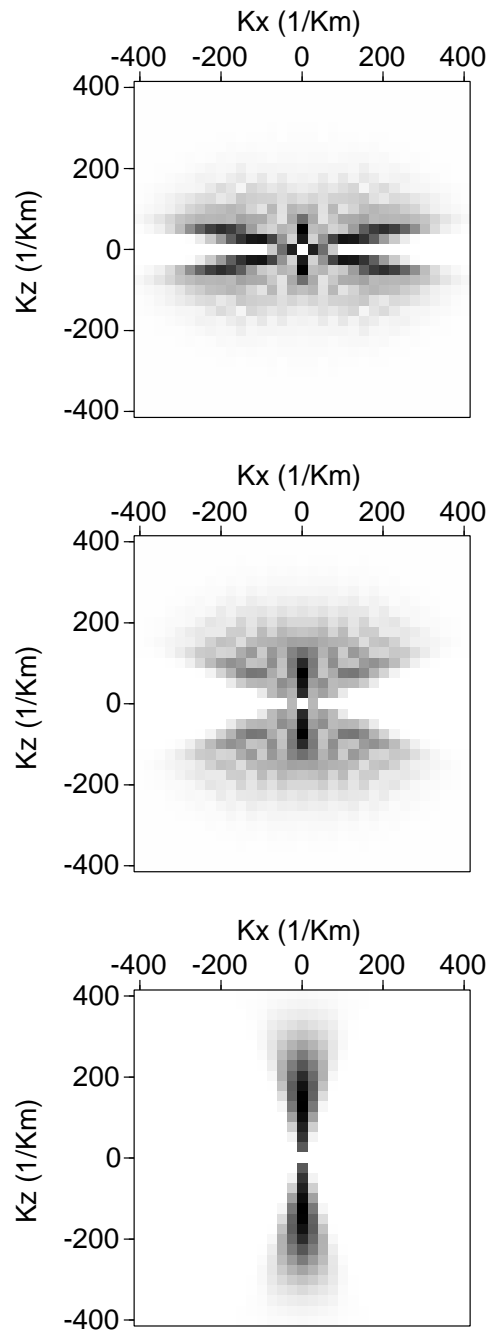


Fig. 2.4. Gray-scale wavenumber plots for three scattering points underneath the center of the seismic array of Figure 2.1. From top to bottom, their depths are 200, 500 and 4000 m. The source wavelet was taken into account in generating these wavenumber vector density plots. Compare to Figure 2.2.



padding, which is an important consideration in three-dimensional analyses. The results are very important since they can be directly used to measure the resolution of a given point by simply measuring its dimensions in any desired direction.

Several practical considerations arise in implementing the inverse Fourier transform of the wavenumber domain image. For example, the Cartesian spatial bin size and the size of the grid must be user defined in order to simplify use of the code for a typical user. Specifically, it is most natural for the typical seismologist to specify a discretization interval and an image space region in kilometers or meters, rather than specifying an area of wavenumber space. We therefore set the bin size in wavenumber domain automatically based on the space domain image defined by the user and making sure the Nyquist sampling criterion is not violated (Bracewell, 1986). For instance, if a spatial image of size  $X = 250$  m and lattice spacing  $dx = 2.0$  m is requested by the user, the sampling interval  $dk$  and maximum acceptable value  $k_{max}$  are calculated internally according to the equations:

$$k_{max} = k_{Nyq} = \frac{1}{2dx} = 0.25 \text{ m}^{-1}, \quad (2.1)$$

$$dk = \frac{2k_{max}}{N} = 0.004 \text{ m}^{-1}, \quad (2.2)$$

where  $N = X/dx = 125$  is the number of samples in both spatial and wavenumber domains.

An analysis of the space domain images corresponding to hypothetical point scatterers provides a more direct estimate of resolution than the scatter plots of wavenumber points. The size of the image is a direct measurement of the resolution, since it reveals the volume across which information about a single subsurface point is distributed. It is also more effective because the user can compute the images for a number of points of interest in an image volume and then superpose the results. For example, if the user is studying resolution at points along a horizontal surface beneath a complex structure, it would be straightforward to specify a grid of points at 0.5 km intervals in the  $x$  and  $y$  directions. The resulting individual images would be superposed into a single block of data that could be visualized just like a conventional three-dimensional seismic data set, and the variations in size of the images would directly indicate the variations in resolution.

Figure 2.5 depicts the spatial images of the three scattering points whose wavenumber vector plots are shown in Figure 2.4. Although one would expect the resolution to be constantly decreasing with depth, there seems to be an optimum depth at which the overall resolution of the scattering points reaches its maximum. This counter-intuitive result was explained in detail in the previous section (2.2.1). The spatial images merely show the same behavior as the scatter plots with the additional benefit of enabling us to assign specific values to the resolution in any wanted direction. Thus, we measure the horizontal and vertical resolution of the scattering point at the depth of 200 m to be approximately 33 and 110 m respectively, whereas the corresponding resolutions are 45 and 52 m for the scattering point at the depth of 500 m. The shallower point also suffers from strong image artifacts, the result of the clustering of the wavenumber vectors along the edges of the aperture (top of Figure 2.4). The same artifacts are more subdued in the case of the scattering point at the depth of 500 m. Finally, the target at the depth of 4000 m is the worst resolved of all three considered points. It exhibits particularly low horizontal resolution, the result of a narrow wavenumber vector aperture, where all vectors tend to become parallel to the  $kz$  axis.

### 2.2.3 Standard deviation

Both wavenumber vector plots and spatial images are difficult to apply when studying large volumes of image points. An ideal measure would replace the three-dimensional data produced by these methods with a single scalar value that would indicate the image quality. This way, a large portion of the subsurface can be easily displayed and its image quality can be easily assessed.

We generated such a measurement by considering the properties of point scatterers. A perfectly imaged point scatterer would have a uniform illumination from all directions, so that the wavenumber vectors computed using equation (1.8) would fill all wavenumber space. The best acquisition geometry would produce a perfectly smooth and even coverage of the wavenumber domain. The uniformity of the wavenumber vectors can be easily measured by the standard deviation statistic,

$$s = \sqrt{\frac{\sum_{i=1}^n (y_i - \bar{y})^2}{n - 1}} = \sqrt{\frac{1}{n - 1} \left[ \sum_{i=1}^n y_i^2 - \frac{(\sum_{i=1}^n y_i)^2}{n} \right]}. \quad (2.3)$$

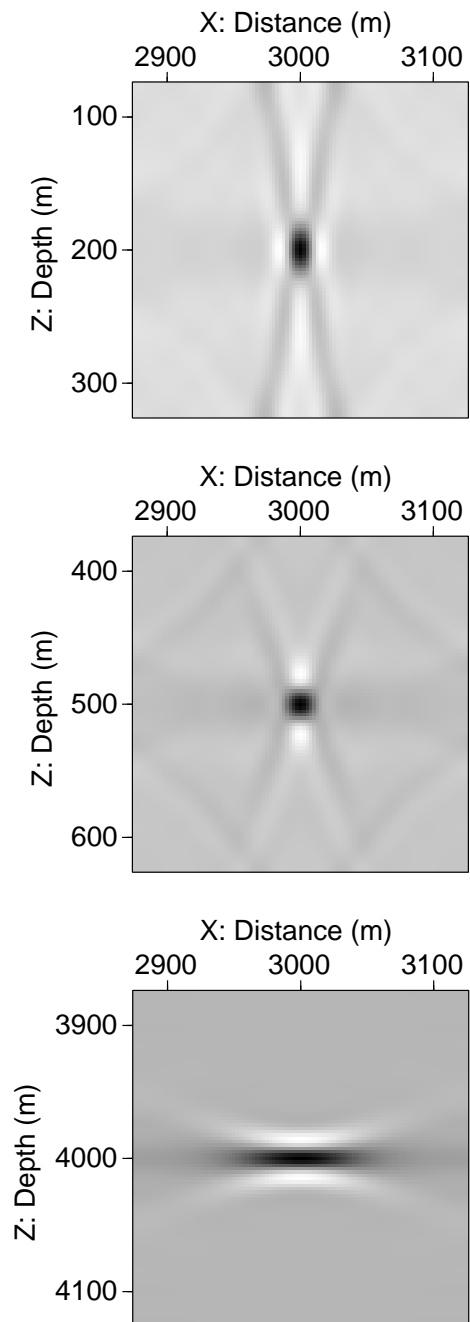


Fig. 2.5. Spatial images of the same three imaging points as in Figures 2.2 and 2.4. Note that the best overall resolved point lies at the depth of 500 m although its wavenumber vector aperture (Figure 2.4) is smaller than that of the shallower point (200 m).

The implementation requires a binning of the wavenumber domain and a tabulation of how many vectors lie in each bin, at which point the standard deviation of the resulting tabulations is computed. A point that is well resolved shows a small standard deviation in contrast to a poorly resolved point, which exhibits relatively high standard deviation.

The choice of a binning scheme was investigated and spherical coordinates (declinational, azimuthal and radial) were eventually chosen since this scheme is most similar to the natural distribution of the wavenumber vectors, which radiate from a common origin for a point scatterer. The implementation requires that vectors be transformed from Cartesian to spherical coordinates. Additional coding effort was required to carefully account for vectors located on bin boundaries, since a careless binning generated standard deviation values that were artificially high. In such cases, wavenumber vectors were equally distributed to all bins sharing the boundary on which they happened to lie.

An important point for correctly using the method is that when wavenumber domain coverage has to be computed for different acquisition geometries with different numbers of sources and receivers, the standard deviation measure has to be normalized by the mean (a relative standard deviation). This is because the changes in standard deviation are proportional to the number of the wavenumber vectors, which in turn is proportional to the product of the number of sources and receivers.

The number of bins in both the azimuthal and declinational directions must be large enough in order to enable the standard deviation measure to successfully “sense” the wavenumber aperture changes as a scattering point changes position (laterally and vertically). Figure 2.6A illustrates the behavior of the relative standard deviation for a suite of calculations with different numbers of declinational bins. The seismic array is the same as described earlier in the chapter (see Figure 2.1). The scattering point lies at a depth of 2000 m and is initially underneath the center of the array (distance: 0 m). As it moves laterally, the wavenumber vector aperture decreases gradually. However, the relative standard deviation curves with the small number of declinational bins fail to predict this gradual change in aperture. The fluctuations in the curve denoting the computed relative standard deviation with only four declinational bins is the result of the wavenumber vectors lying successively on two, three, two and eventually one (flat portion of the curve) declinational bins. On the other hand, a sufficiently large number of bins ( $\geq 48$ ) exhibit the expected smooth change in aperture. Moreover,

since they all converge, there seems to be an optimal choice of number of bins i.e. not too small, so it predicts the right behavior of aperture changes and not too large, so that it conserves computer memory. For this particular example and all subsequent ones of this chapter, we chose to use 64 declinational bins. In general 3-D experiments, an analogous search for the optimal number of azimuthal bins should be conducted. In this example it was not necessary because a linear source/receiver array was used and only scattering points lying in the vertical plane defined by the array were examined.

On the other hand, the standard deviation measure is not as sensitive to the number of radial bins. This is because the radial direction is the direction along which a wavenumber vector corresponding to a particular source/receiver pair, is scaled by frequency. As long as the frequency range remains the same for the specific experiment in its entirety, the effect of the number of radial bins on the computation of the standard deviation resembles that of a scaling factor. Of course, even if a source with a consistent frequency content is used throughout the experiment, the earth acts as a low pass filter gradually attenuating high frequencies with distance traveled by the seismic waves (see chapter VI, section 6.1). Figure 2.6B illustrates the behavior of the relative standard deviation for different numbers of radial bins for the same acquisition geometry and same scattering points as in Figure 2.6A. The number of declinational and azimuthal bins were kept constant. The relative standard deviation curves cluster together for scattering points lying below the seismic array and they only gradually deviate from each other for points that lie beyond its edges. However, they all exhibit the same general behavior and the preference of an optimal number of radial bins is not as clear as in the case of the declinational (and azimuthal) bins. If conserving computer memory is also under consideration, then the choice is apparently a single radial bin.

The advantage of a scalar image resolution measure such as the standard deviation becomes more obvious when one is interested in examining a large image area like the one in Figure 2.1. It is very straightforward to produce a relative standard deviation plot for a grid of scattering points. Figure 2.7 shows the standard deviation plot for the acquisition geometry of Figure 2.1. The best illuminated points lie directly underneath the center of the array at a depth of approximately 500 m. The scattering points that were used to generate the plot, were arranged in 25 rows spaced every 200 m. Each row consisted of 301 scattering points spaced every 20 m. In general,

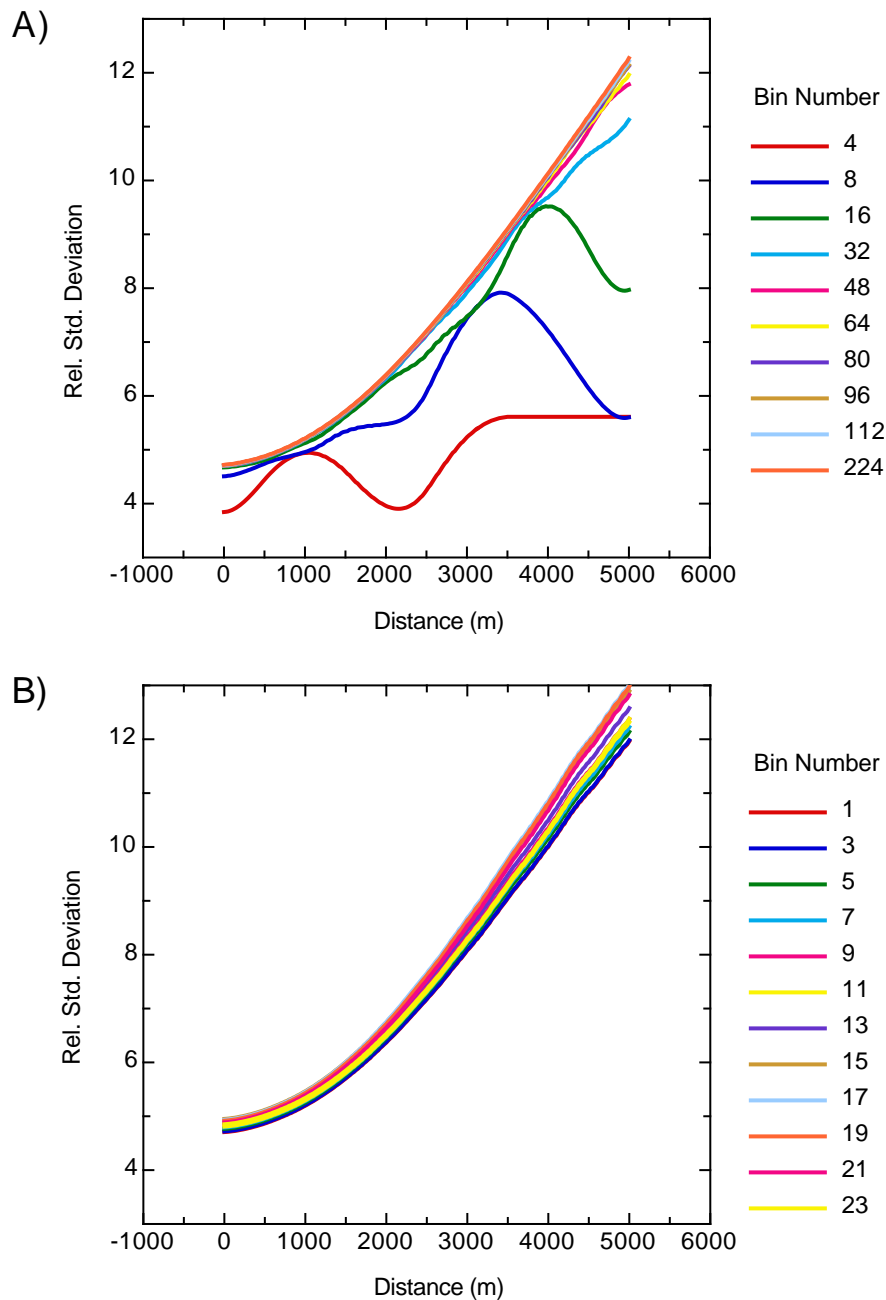


Fig. 2.6. A) Relative standard deviation curves for a series of scattering points at the depth of 2 km. Distance denotes the lateral displacement of the point relative to the center of the array. Different curves denote different number of declinational bins used to compute the relative standard deviation. B) Relative standard deviation curves for the same points. Different curves denote different number of radial bins used to compute the relative standard deviation. Note that while the relative standard deviation curves are sensitive to the number of declinational bins used to compute them, they are almost independent of the number of radial bins.

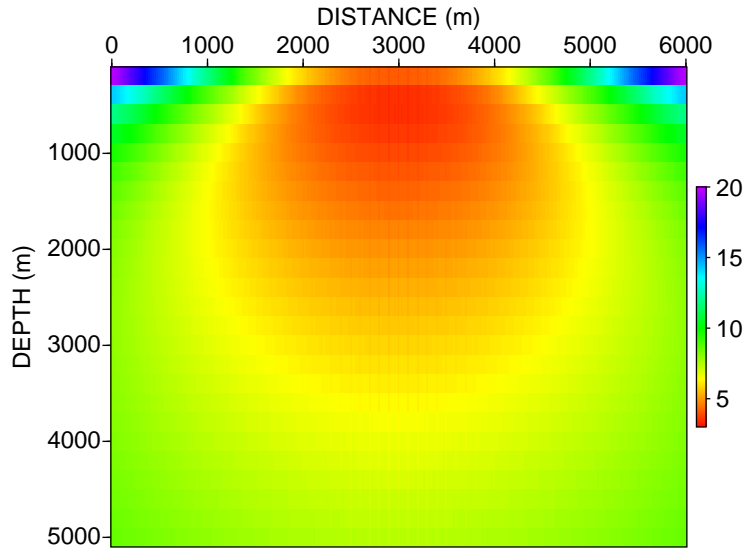


Fig. 2.7. Relative standard deviation map for a grid of scattering points covering the image area of Figure 2.1. The smaller standard deviation values, thus, the better overall resolved points, occur beneath the center of the seismic array at depths around 500 m.

resolution decreases not only with depth but also with the lateral displacement of the imaging points from the center of the array. In contrast to the standard deviation plot, it would be very difficult to visualize the three-dimensional spatial images for all the scattering points ( $\approx 7500$ ).

#### 2.2.4 Smoothness

Considering the properties of Fourier Transform, we can infer that the wider and smoother the distribution of the wavenumber vectors for a particular scattering point, the more spike-like is its corresponding spatial image. Specifically, the smoother the distribution of the wavenumber vectors, the less prominent the artifacts of the spatial image are (e.g., Figure 2.5) resulting in a better quality image. The appeal of such an indicator of image quality is that smoothness, like standard deviation, is also a scalar, unitless quantity. In digital image processing, smoothness is an important quantity in detecting the presence of an edge in an image (Gonzalez and Woods, 1992; Shi and Huifang, 2000). From vector analysis, it is well known that the gradient  $\nabla f$  of

a three-dimensional image  $f(x, y, z)$  points in the direction of the maximum rate of change of  $f$  at  $(x, y, z)$ . The scalar magnitude of the gradient, equals:

$$\begin{aligned} |\nabla f| &= \left[ \left( \frac{\partial f}{\partial x} \right)^2 + \left( \frac{\partial f}{\partial y} \right)^2 + \left( \frac{\partial f}{\partial z} \right)^2 \right]^{1/2} \\ &= [G_x^2 + G_y^2 + G_z^2]^{1/2}. \end{aligned} \quad (2.4)$$

In our implementation, we followed the approach of Gonzalez and Woods (1992) who use as a smoothness measure of the entire image the sum of the square of the magnitude of the gradient at each pixel. The use of the square of the magnitude instead of the magnitude itself is just for practical reasons i.e., for saving an extra operation per image pixel. An alternative approximate computation of the magnitude of the gradient which was not considered but is even more easier to implement, is:

$$|\nabla f|_{appr} = |G_x| + |G_y| + |G_z|. \quad (2.5)$$

The computation of the partial derivatives  $\partial f/\partial x$ ,  $\partial f/\partial y$  and  $\partial f/\partial z$  may be also implemented in digital form in several ways (for further discussion, see Gonzalez and Woods (1992)). We chose to implement their computation by using a simple central difference scheme. Figure 2.8 shows schematically how the derivatives at a center point,  $z_5$ , of a two-dimensional (for simplicity) region of  $3 \times 3$  pixels are computed. More specifically, they are:

$$\begin{aligned} G_x^2 &= \left( \frac{z_6 - z_4}{2dk_x} \right)^2, \\ G_y^2 &= \left( \frac{z_8 - z_2}{2dk_y} \right)^2, \end{aligned} \quad (2.6)$$

where the  $z$ 's denote the number of wavenumber vectors that happen to fall into a particular pixel and  $dk_x$  and  $dk_y$  are the sampling intervals in the wavenumber space as they were defined in equation (2.2), in the  $x$  and  $y$  directions respectively. The scheme can be easily extended to accommodate three-dimensional images.

As in the case of the standard deviation measure, when the smoothness measure has to be computed for different acquisition geometries, it has to be normalized by the product of the number of sources and receivers available in each experiment. In fact,



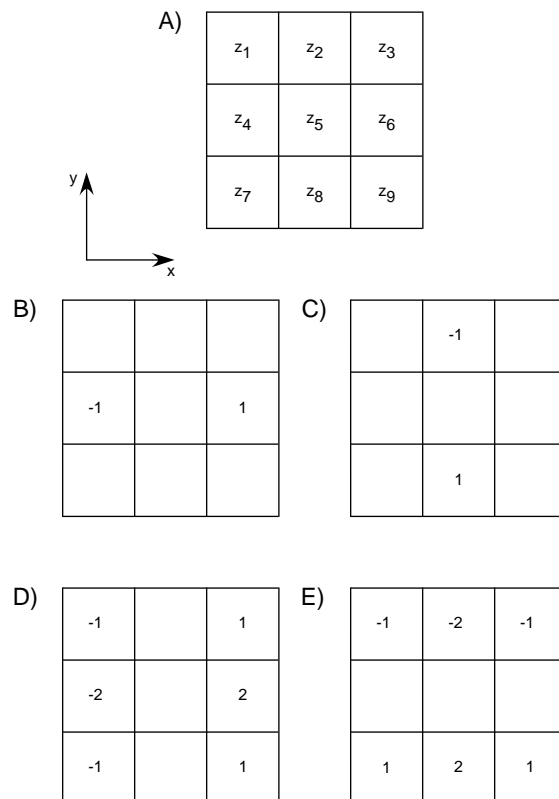


Fig. 2.8. A) Gridded ( $3 \times 3$ ) image region. B) and C) Masks used to compute the components of the gradient at  $z_5$  in the  $x$  and  $y$  directions respectively. D) and E) An alternative scheme: the Sobel edge operator masks. The advantage of using a larger mask size is that errors are reduced by local averaging.

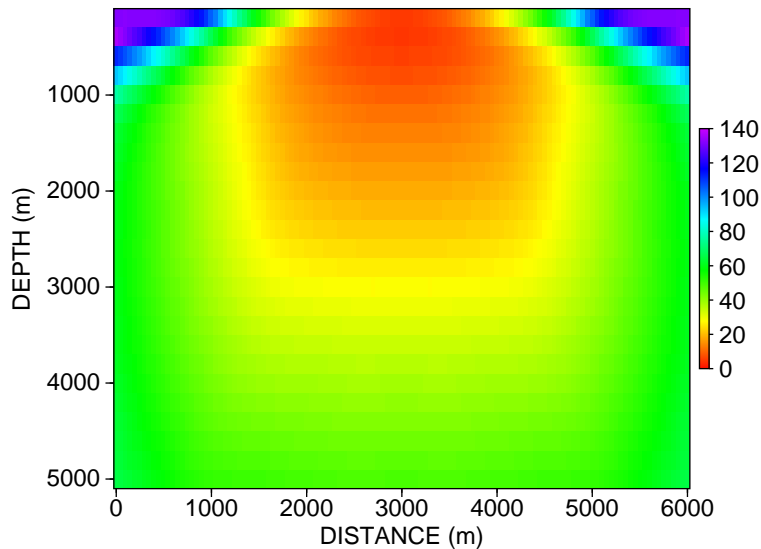


Fig. 2.9. Relative smoothness map for a grid of scattering points covering the image area of Figure 2.1. The smaller smoothness values, thus, the better overall resolved points, occur beneath the center of the seismic array at depths around 500 m.

since the square of the magnitude of the gradient is computed for each pixel of the wavenumber domain, the relative smoothness is computed by dividing the smoothness by the square of the source/receiver product.

An additional calibration is needed if the user requests different spatial image sizes and lattice spacings for different acquisition designs since these parameters will internally affect the number of pixels in each each direction of the wavenumber space as well as the sampling interval (see discussion in the subsection 2.2.2).

Figure 2.9 shows the relative smoothness plot that corresponds to the model of Figure 2.1. The scattering points used to generate the plot were arranged in 25 rows and 121 columns. Their vertical spacing was 200 m, and the horizontal 50 m every 200 m. The best image quality is predicted for the scattering points underneath the center of the array, at the depth of approximately 500 m. Overall, the relative smoothness exhibits a behavior similar to the equivalent relative standard deviation plot (Figure 2.7).

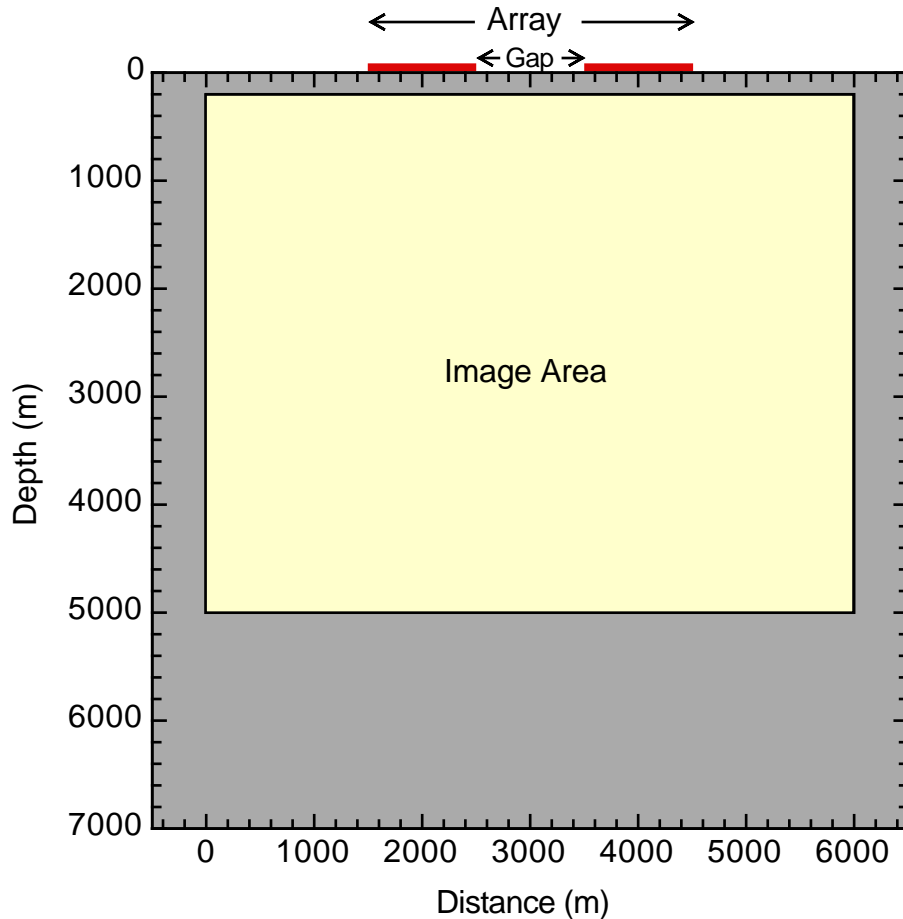


Fig. 2.10. The same homogeneous model and image area as in Figure 2.1. The seismic array is still 3 km long but a gap of 1 km is introduced at the center of the array. The live sources and receivers are reduced from 31 to 20 and 61 to 40 respectively.

### 2.3 Examples of the effects of acquisition geometry on spatial resolution

In this chapter, we will limit ourselves to homogeneous models with 2D array geometries. This is to simplify and thus render the interpretation of all image resolution measures more comprehensible.

We start with a variation of the geometry considered in Figure 2.1. We now suppose that an obstacle (e.g., a lake or a platform) prevents the deployment of sources and receivers for a significant portion of the initial seismic array (Figure 2.10). More specifically, the gap is approximately 1 km and is located in the center of the initial array. As a result, only two thirds of the initial sources and receivers are available.

Figure 2.11 is the relative standard deviation map for the image area of Fig-

ure 2.10. The figure is plotted on the same scale as the relative standard deviation map of Figure 2.7 in order to facilitate their direct comparison. It readily becomes clear that the introduction of the gap in the array results in the decrease of the resolution everywhere in the image area. The best resolved points are no longer located underneath the center of the array but are symmetrically displaced towards the live portions of the array. The relative smoothness map (Figure 2.12) supports these observations with its distribution of smoothness values closely resembling that of the standard deviation map (compare to Figure 2.9). However, it exhibits weak, radially distributed, directions of high and low values of smoothness. This is thought to be the result of the cartesian binning of the wavenumber vectors (as opposed to the spherical binning used for the standard deviation measure). One way to alleviate the side effects of the cartesian binning on the smoothness measure, would be to use the Sobel scheme of computing the gradient components which also has an averaging/smoothing effect on the calculations than the simplistic central difference scheme that was used (compare Figures 2.8D and 2.8E to Figures 2.8B and 2.8C respectively).

Of course, the ultimate means of assessing the effects of the two different surveys, is by examining the wavenumber vector plots (Figure 2.13) and their corresponding spatial images (Figure 2.14). Comparing these to the wavenumber vector plots (Figure 2.4) and spatial images (Figure 2.5) that correspond to the full array of Figure 2.1, we confirm the detrimental effect of the gap in the image resolution of the scattering points under examination. The image artifacts are even more prominent, which adds to the overall loss of resolution in certain directions.

Next, we considered the effects of the array length on the imaging of the target area. In addition to the original full array of Figure 2.1 which has a length of 3 km, two new arrays of length 5 and 7 km were examined. The source and receiver spacings were kept the same for all three arrays (100 and 50 m respectively). The total number of possible source/receiver pairs increases approximately from 1891 to 5151 to 10011 as the array becomes longer.

Figure 2.15 depicts the depth profiles of the relative standard deviation beneath the center of the three arrays. The minimum value of the relative standard deviation curves (denoting the best resolved point along the depth profile) occurs at increasingly larger depths for increasingly longer arrays. In particular, the minima occur at the depths of 500, 800 and 1100 m for the arrays with length of 3, 5 and 7 km respectively.

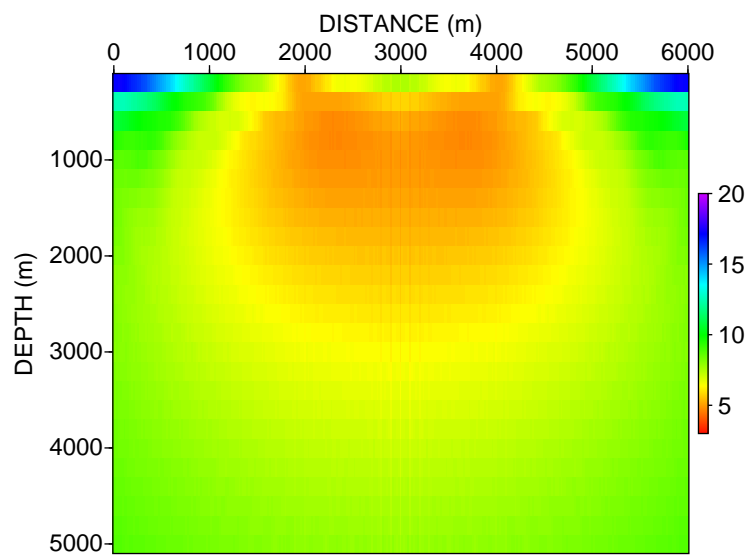


Fig. 2.11. Relative standard deviation map for a grid of scattering points covering the image area of Figure 2.10. The best resolved points are shifted from the center of the seismic array sideways due to the gap introduced in the seismic array. (Compare to Figure 2.7).

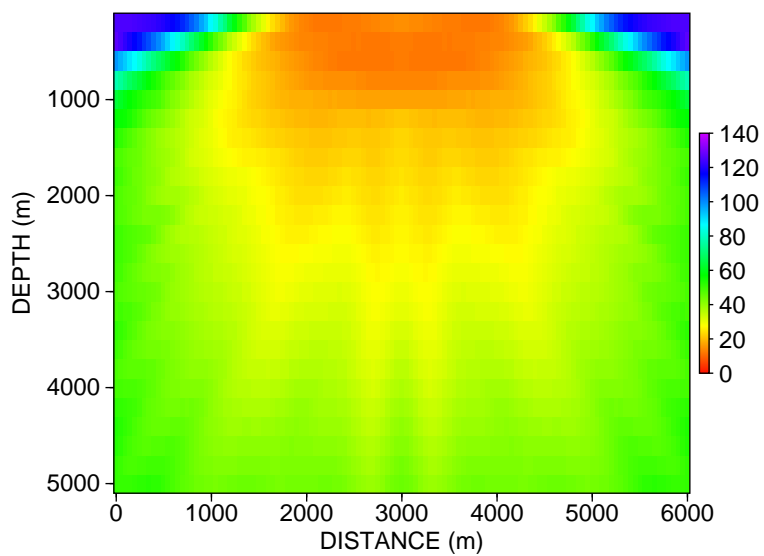


Fig. 2.12. Relative smoothness map for a grid of scattering points covering the image area of Figure 2.10. The best resolved points are shifted from the center of the seismic array sideways due to the gap introduced in the seismic array. (Compare to Figure 2.9).

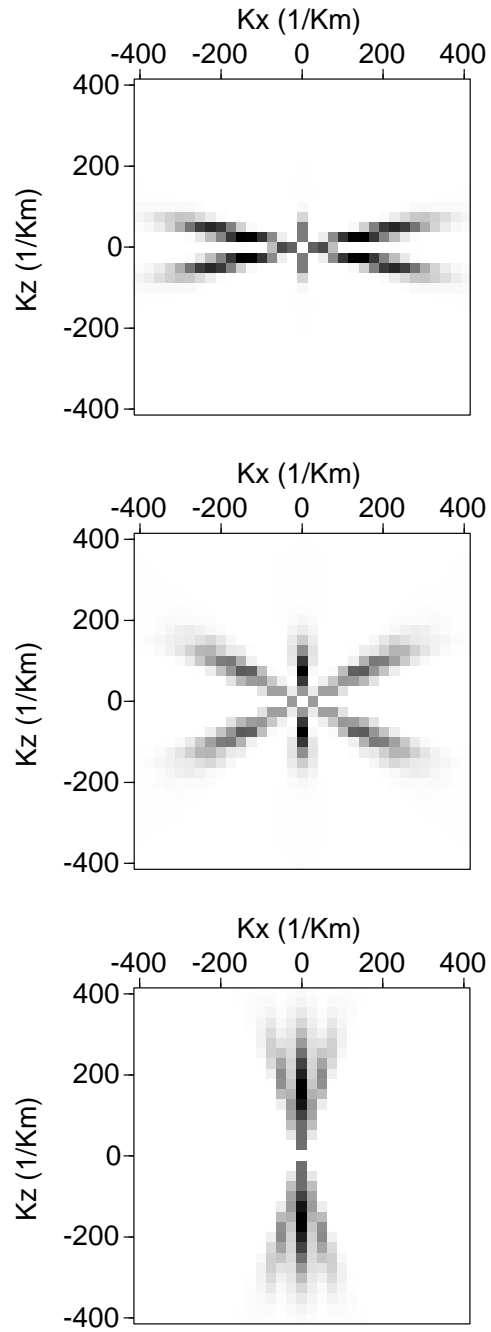


Fig. 2.13. Gray-scale wavenumber plots for the three scattering plots underneath the center of the seismic array of Figure 2.10. From top to bottom, their depths are 200, 500 and 4000 m. The effects of the introduced gap in the array are clear (compare to Figure 2.4).

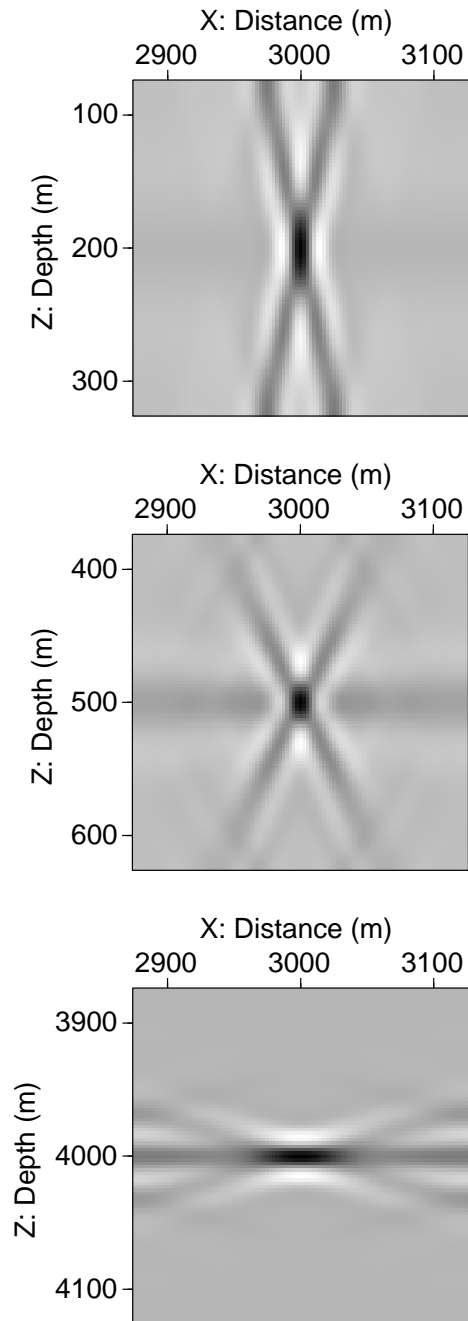


Fig. 2.14. Spatial images of the same three imaging points corresponding to the wavenumber vector plots of Figure 2.13. The introduction of the gap in the array has rendered the effective aperture much smaller resulting in worse resolved points (compare to the spatial images obtained by the full array, in Figure 2.5). In addition to that, the concentration of the wavenumber vectors along certain directions is manifested in the highly accentuated image artifacts.



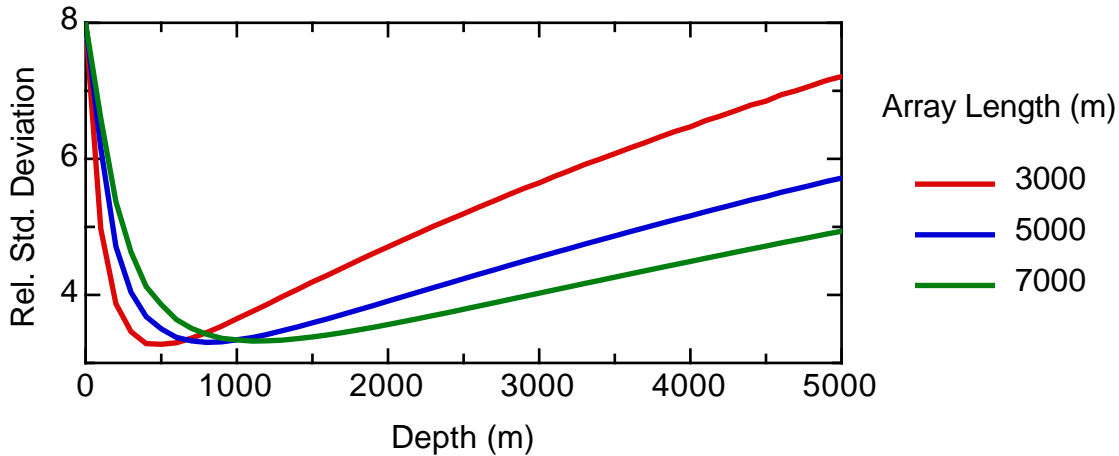


Fig. 2.15. Depth profiles of relative standard deviation underneath the center of three seismic arrays with different lengths. Note that the longer the array, the deeper the best resolved point is. Moreover, the slope of the curves decreases with increasing array length, indicating that the longer arrays manage to better image larger ranges of depth.

Moreover, the slope of the curves becomes less for longer arrays, indicating that the longer the array, the more capable of better resolving larger regions of the image space.

Figure 2.16 shows a series of spatial images at different depths for the three arrays in consideration arranged in three columns. Each column corresponds to an array of different length (with increasing length from left to right). Carefully examining these points, we note that indeed the best overall resolved point for each array, lies at increasingly larger depth with increasing array length. These points seem to be equally (or close to equally) resolved in all directions. Points at smaller depths are better resolved horizontally than vertically (horizontal to vertical resolution ratio aspect  $< 1.0$ ) whereas, points at greater depths are better resolved vertically than horizontally (horizontal to vertical resolution ratio aspect  $> 1.0$ ).

The points at shallow depths such as those at the depth of 200 m (first row of Figure 2.16) are better overall resolved for the shorter array (also evident in Figure 2.15). This result can be explained by the fact that for the longer arrays, a larger portion of the total number of wavenumber vectors clusters around the horizontal ( $kz$  axis). Therefore, the wavenumber domain spectrum of the scattering point is even more heavily biased in the horizontal direction, thus the poorer vertical resolution.

On the other hand, points below the best overall resolved point, are better re-

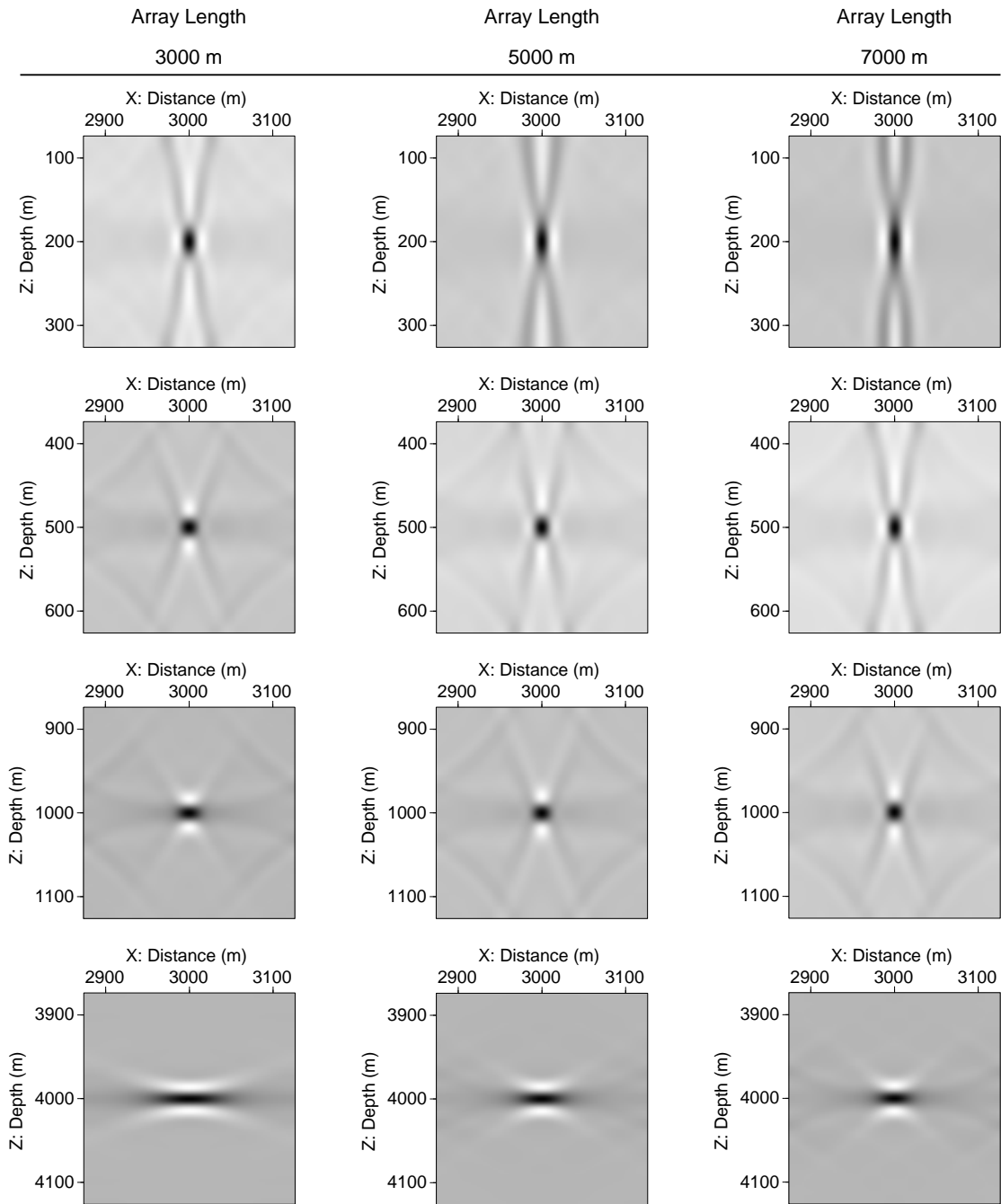


Fig. 2.16. Spatial images of scattering points at different depths and different array lengths. From left to right, columns correspond to array lengths of 3, 5 and 7 km. Note that the best resolved points occur at larger depths with longer array lengths. Additionally, by comparing the last two rows of the figure, it becomes clear that longer arrays are capable of better resolving larger image areas.

solved for the longer array (for example, fourth row of Figure 2.15). This can be more easily explained by considering the aperture of the wavenumber vectors which is larger for the longer array for points at any particular depth.

## 2.4 Comparison of image resolution prediction to migration

Another important task in the development of the proposed method was to demonstrate that the resolution predictions do in fact provide a good measurement of spatial resolution. On unmigrated data, the limiting factor determining the horizontal resolution is the Fresnel zone. Of course, when real data are concerned, other factors (signal/noise ratio, spatial sampling, etc.) also affect the resolution. Therefore, the Fresnel zone is taken as a theoretical measure of the best feasible resolution. On the other hand, the process of migration collapses the Fresnel zone, and migrated sections exhibit increased (sub-Fresnel) image resolution (Yilmaz, 1987; Sheriff and Geldart, 1995). Here, we use a prestack migration method to compare our resolution measures. Whether or not the two methods produce the same or at least similar results comprises the strongest criterion of the feasibility of the method.

We first compute synthetic seismograms for a laterally heterogeneous model of a hydrocarbon reservoir (Figure 2.17). This model contains a reservoir that is 0.010 km thick, and 0.6 km by 4.0 km in the horizontal directions  $x$  and  $y$  respectively. A horizontal velocity heterogeneity is introduced in the form of alternating bands of high and low  $P$ -wave velocity compared to the surrounding medium. Specifically, the material above and below the reservoir has a velocity of 4 km/s, while the reservoir velocities are 4.42 km/s and 4.89 km/s. Normal incidence reflection coefficients are calculated to be approximately 0.05 and 0.1. This model is simple but relevant. Many reservoirs are thin compared to a seismic wavelength, and by modeling the velocity contrasts, we can assess how accurately a seismic experiment might image this target.

The numerical modeling applied a ray-Born method, a rapid, approximate solution for seismic wavefields scattered in weakly inhomogeneous, three-dimensional media (Beydoun and Mendes, 1989; Gibson, Jr. et al., 1993). The Born approximation predicts the amplitudes of scattered waves from perturbations to a background model. We implemented a numerical solution by assuming that this background model is relatively smooth so that a ray theoretical solution is valid. In our case, the model is homogeneous, and ray solutions will certainly be adequate. We also spec-

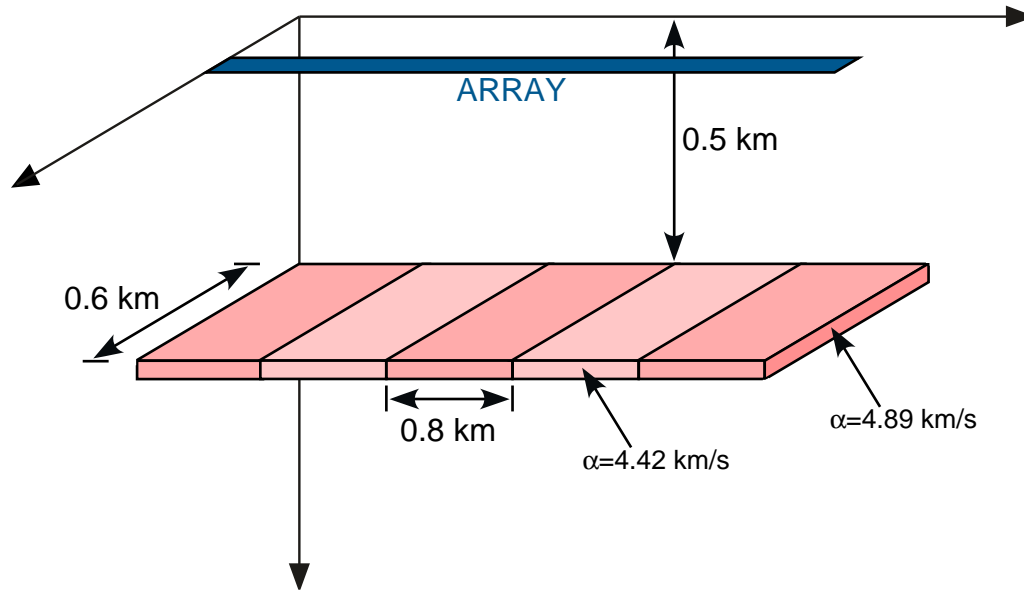


Fig. 2.17. Schematic of the laterally heterogeneous model used in the comparison of the image resolution prediction to prestack phase shift migration. The background velocity is 4 km/s while the reservoir is characterized by alternating bands of 4.42 km/s and 4.89 km/s.

ified a source wavelet with a dominant frequency of 30 Hz (Figure 2.3), so that the wavelength in the background material is 0.133 km. This wavelength is much longer than the reservoir layer thickness, and the Born approximation will be accurate, even though velocity contrasts are somewhat large (Beydoun and Tarantola, 1988).

The source/receiver array was located along the thick, blue line in Figure 2.17. The top of Figure 2.18 displays synthetic seismograms computed using a zero-offset array with source/receiver pairs located every 0.01 km along the free surface. The corresponding data after migration using a phase shift algorithm (Gazdag, 1978) are shown on the bottom of Figure 2.18. The boundaries between high and low velocity portions of the reservoir are seen more clearly — are better resolved — in the migration image, which is not surprising. To better quantify these results, we computed RMS amplitudes of the reservoir reflection event for these data (Figure 2.19). The increase in resolution after migration is clear. The resolution prediction for the zero-offset model predicts that a point scatterer will be smeared to a width of approximately 70 m, which closely matches the distance across which the boundary of the high and low velocity regions is smeared (Figure 2.20; compare to Figure 2.19).

Therefore, the image resolution analysis is as a valid approach to determining the

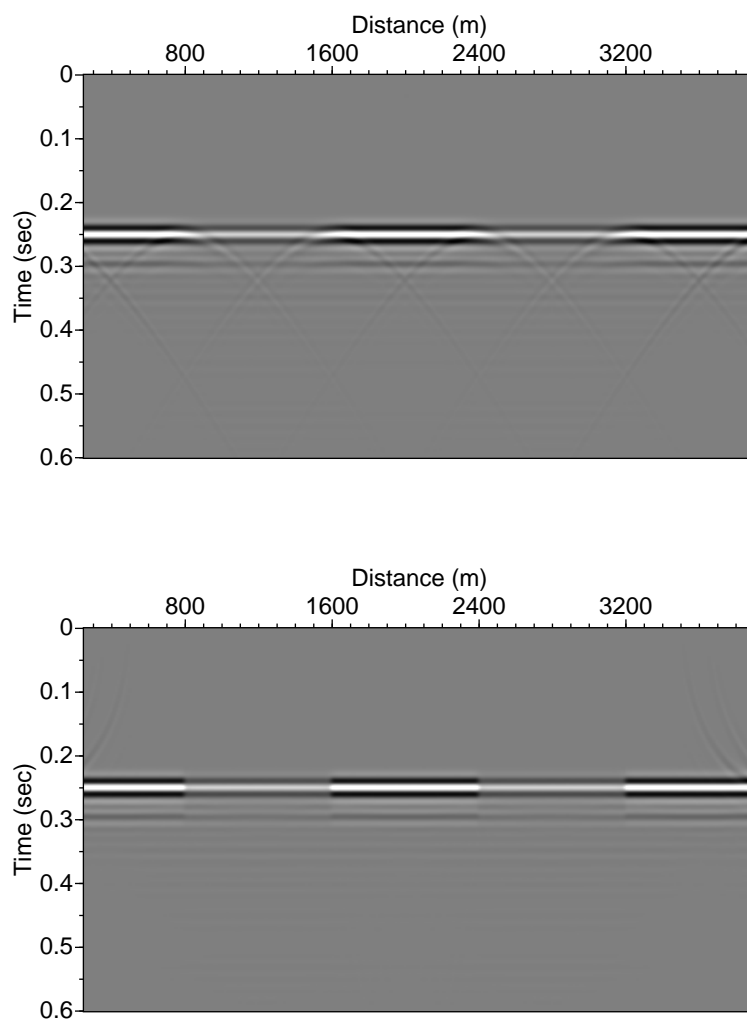


Fig. 2.18. Top: Zero-offset synthetic seismograms. Note the diffraction hyperbolas whose apexes are located at the boundaries between the strong and weak reflecting reservoir bands. Bottom: The same data after the phase shift migration.

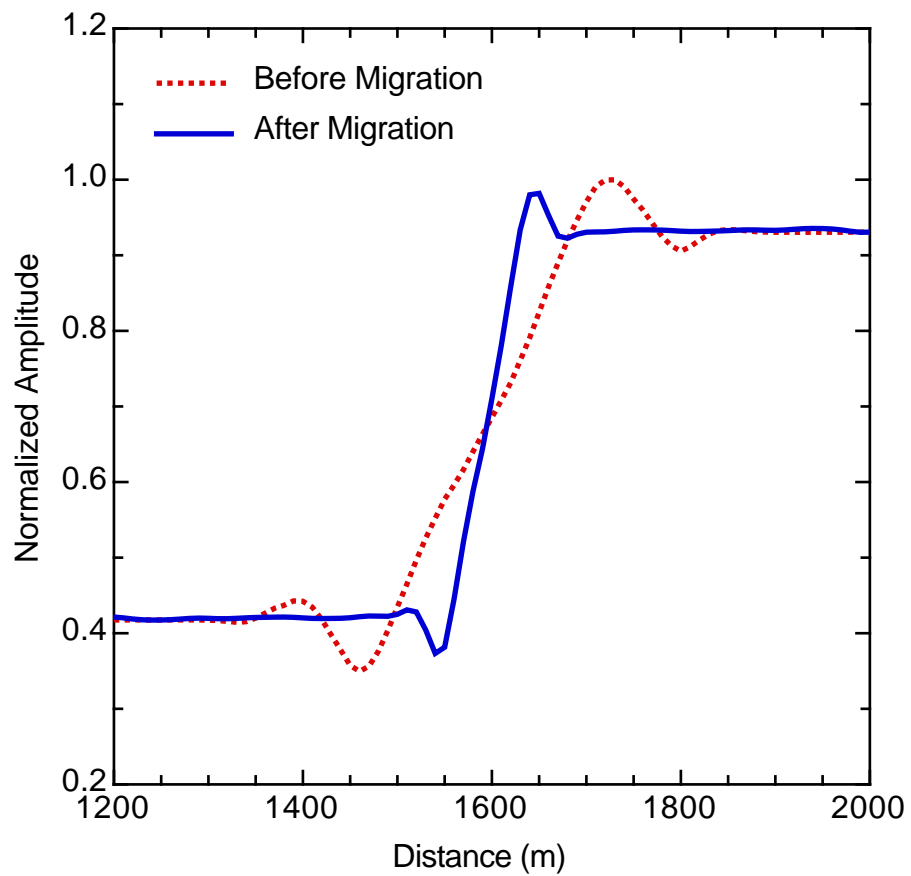


Fig. 2.19. RMS amplitude curves of the reflection event around a reservoir band boundary. The dotted curve denotes the RMS amplitudes before the migration and the solid, the RMS amplitudes after. The increase of resolution after the migration is obvious.

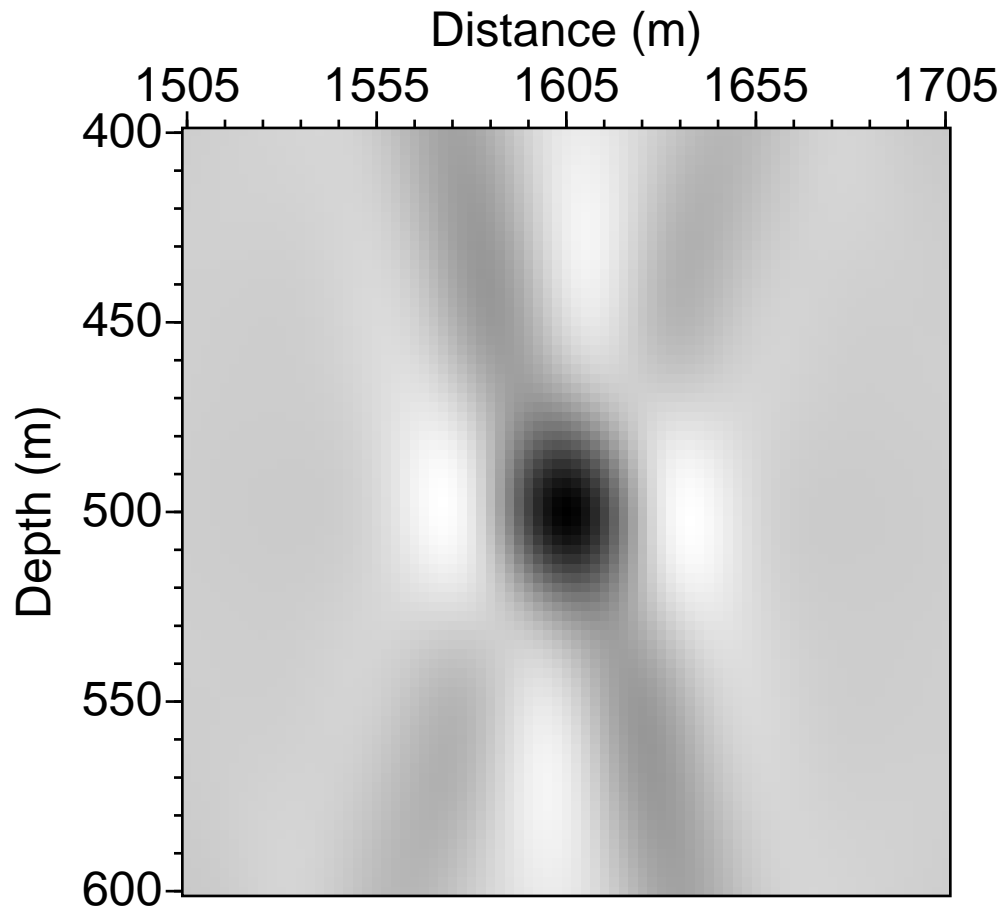


Fig. 2.20. The spatial image for a scattering point 5 m off the reservoir band boundary. The predicted horizontal resolution is around 70 m and is in good agreement with the resolution indicated by the RMS amplitude curve after the migration (Figure 2.19).

resolution of target points as is the prestack migration. The benefit of the proposed analysis lies in the fact that it is not as resource intensive, and thus is much cheaper than migration itself. Additionally, since it essentially provides the response of scattering points with a given acquisition geometry, one could use the image resolution analysis as a preliminary step to better understand migration outputs (migrated images) and gain confidence in using the right migration parameters (such as velocities).

## 2.5 Conclusions

We demonstrated that all the proposed measures based on Beylkin's theory can reliably assess whether a target area is efficiently imaged by a given acquisition geometry. The two scalar measures, i.e., the relative standard deviation and relative smoothness, are very useful tools in assessing the image quality of large target areas. However, the user should always keep in mind that these measures indicate the overall achievable resolution at any imaging point. It is not possible for example, to draw any conclusions for the resolution along particular directions. Nonetheless, it is possible to modify the smoothness measure in such a way that it is only calculated for a subset of the original 3-D image. This sub-image can be chosen so that it corresponds to the particular direction in question.

On the other hand, the three dimensional wavenumber vector plots and spatial images, are better suited for cases where a closer examination of the theoretically achievable resolution is needed. In those cases, the spatial images provide us with a quantitative measure of resolution in any wanted direction. Their disadvantage is that they require a lot of computer resources, and the simultaneous examination or even display of many scattering points becomes cumbersome due to their 3-D nature.

We also showed that the image resolution analysis gives similar results as the prestack migration methods. Considering the minimal overburden (i.e., the calculation of wavenumber vectors from the ray tracing results) required by the image resolution analysis, renders it cheap compared to any prestack migration scheme. It can, therefore, be used as a precursor step to migration or even instead of it if one's need is to just assess the effectiveness of an acquisition geometry on the imaging of specific targets.



## CHAPTER III

### METHOD SENSITIVITY ANALYSIS

#### 3.1 Introduction

The factors that affect the seismic resolution have been extensively discussed in the literature. Such factors include the wavelet's frequency and phase spectrum. Berkhout (1973) proved that of all one-sided (i.e., causal) functions, the minimum-phase signal has the minimum length. Schoenberger (1974) relaxed the restriction of dealing only with one-sided signals arguing that the seismic signal processing can be designed to produce either one-sided or two-sided signals. He showed that a zero-phase (two-sided) signal corresponding to the same amplitude spectrum as a minimum-phase signal has an even smaller length (see also, Berkhout, 1974). Moreover he demonstrated that seismograms generated with zero-phase input signals are also better indicators of reflection time (and thus, reflector depth) and reflector spacing.

Kallweit and Wood (1982) examined the different criteria of resolution, namely, the Rayleigh, Ricker (1953) and Widess (1973) criteria. They concluded that temporal resolution depends on the highest terminal frequency of a broadband wavelet, provided that its bandwidth is at least two octaves. The bandwidth of at least two octaves is required because it results in waveforms with reduced side-lobe amplitudes (compared to central-lobe amplitude) and ringiness (Knapp, 1990). Vermeer (1999) stated that spatial resolution, as a direct extension of these results, is controlled by the maximum wavenumber. In fact, this is an obvious consequence of Beylkin's equation [equation (1.8)]. The largest coverage of the wavenumber space (thus, the highest spatial resolution) is obtained when the wavenumber vectors' magnitudes achieve their greatest value. It is easily shown that this occurs in zero-offset configurations. Therefore, zero-offset acquisition geometries can be considered to provide the best image resolution compared to any common-offset designs. In this chapter, we examine the validity of this statement and indicate its limitations.

Other factors affecting spatial resolution can be easily identified using Beylkin's equations. These are the background velocity at the imaging point, the frequency

of the signal and the direction of the traveltimes gradients from the imaging point to both the source and the receiver. These gradients, obtained numerically by ray tracing, depend not only on the source/receiver configuration of the experiment but also on the background model. In this chapter, we closely examine the effects of the background model (velocity and structure) on the spatial resolution.

### 3.2 Zero-offset versus common-offset acquisition geometries: Their significance in image resolution

We have previously showed that the larger the coverage of the wavenumber space, the better the spatial resolution. The wavenumber space coverage is determined by considering the wavenumber vectors corresponding to all possible source/receiver pairs of a given acquisition geometry. Recall that Beylkin's equation [equation (1.8)] expresses the wavenumber vector as the vectorial sum of the slowness vectors along the rays from both source and receiver down to the image point (weighted by frequency). Alternatively, it is:

$$\mathbf{k} = \omega [\nabla\tau(\mathbf{x}, \mathbf{s}) + \nabla\tau(\mathbf{x}, \mathbf{r})] = \mathbf{k}_s + \mathbf{k}_r, \quad (3.1)$$

where  $\mathbf{k}_s$  and  $\mathbf{k}_r$  are the source and receiver contributions to the wavenumber vector  $\mathbf{k}$  which is mapped into the wavenumber space. By maximizing the magnitude of the wavenumber vectors, one can achieve the largest coverage of the wavenumber space, thus, the best spatial resolution. From equation (3.1), it is readily seen that the maximum magnitude of  $\mathbf{k}$  is obtained when the vectors  $\mathbf{k}_s$  and  $\mathbf{k}_r$  coincide, i.e., when a zero-offset geometry is used.

In order to compare the resolving capability of a zero-offset geometry to a common-offset one, we considered two acquisition geometries, both consisting of 41 sources and 41 receivers equally spaced every 25 m. Therefore, the total source and receiver array lengths were equal to 1 km. In the first case (Figure 3.1A), the source and receiver arrays coincided to generate the zero-offset experiment. In the second case (Figure 3.1B), the arrays were offset to simulate a 1 km common-offset experiment. However, their locations were chosen in such a way that the midpoint locations were identical to the ones for the zero-offset experiment. Although a common-offset of 1 km may seem extreme for source/receiver array lengths of 1 km, it was chosen

to accentuate the differences between the two geometries and it should not detract from the analysis.

In both cases, a homogeneous medium with compressional velocity  $v_p = 2.5$  km/s was used. Moreover, the source wavelet (with dominant frequency of 30 Hz) was kept identical for both cases (as well as for all subsequently examined ones throughout this chapter). This enables us to attribute any changes in the image resolution to the acquisition geometry and/or the location of the imaging point.

First, we consider an imaging point at the relatively shallow depth of 500 m. The point lies underneath the center of the midpoint line for both the zero- and common-offset configurations. For the zero-offset geometry, the rays from the source to the point and from the point to the receiver are coincident. Therefore, the corresponding wavenumber vectors  $\mathbf{k}_s$  and  $\mathbf{k}_r$  being tangential to the rays at the imaging point, are also coincident. Their vectorial sum,  $\mathbf{k}$ , takes on its maximum possible magnitude. Moreover, as shown in Figure 3.1A, the maximum angle between all possible wavenumbers  $\mathbf{k}$  and the vertical is  $45^\circ$ , rendering the total aperture of wavenumbers covering the wavenumber domain equal to  $90^\circ$ .

For the common-offset geometry, the rays from the source to the point and from the point to the receiver are not coincident anymore. Thus, the resulting wavenumbers obtain a magnitude less than the maximum. The magnitudes vary with different source/receiver positions across the array. For the most distant source/receiver pair (i.e., either the couple  $S_1/R_1$  or  $S_{41}/R_{41}$  in Figure 3.1B), the angle between the wavenumber and the vertical is approximately  $32^\circ$ . Therefore, the total wavenumber aperture is  $\approx 64^\circ$ .

Figure 3.2 shows the wavenumber vector plots for the two cases. The plots show vectors that correspond to a frequency range of 5 to 30 Hz in increments of 2.5 Hz for clarity purposes. It is obvious that both the wavenumber vectors' magnitudes and coverage aperture in the common-offset experiment are smaller than in the zero-offset one. Additionally, the varying magnitude of the wavenumber vectors in the case of the common-offset experiment is clearly demonstrated (Figure 3.2B), since the wavenumber vectors do not lie on perfectly circular arcs like they do in the zero-offset case (compare to Figure 3.2A). In particular, the magnitude of the vectors obtains its smallest value along the Kz-axis. This is simply because the vector along the Kz-axis is the resultant of vectors  $\mathbf{k}_{s21}$  and  $\mathbf{k}_{r21}$  and the angle between them takes its maximum value ( $90^\circ$ ) than any other  $\mathbf{k}_{sX}/\mathbf{k}_{rX}$  combination, with X being the station

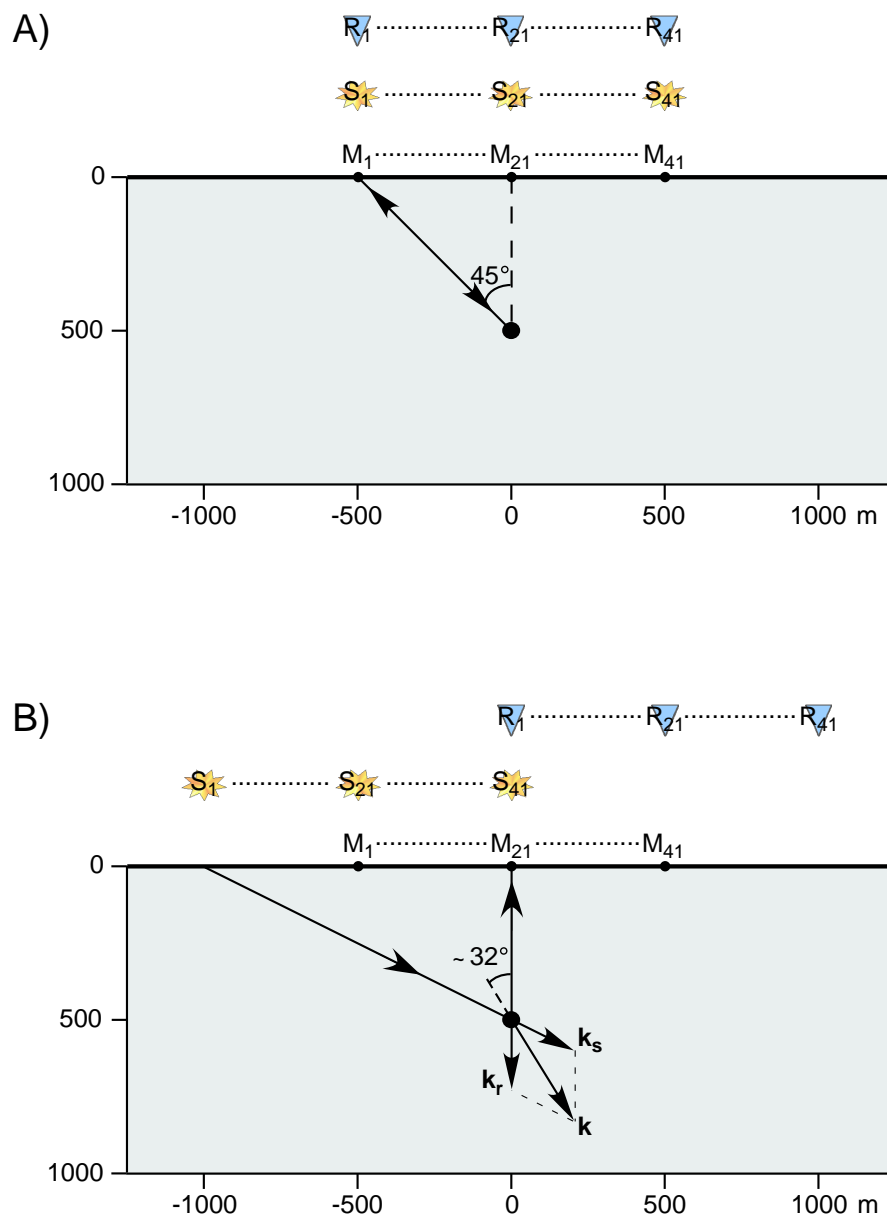


Fig. 3.1. A) The zero-offset geometry. B) The 1 km common-offset geometry. The source and receiver locations are such that the midpoint locations coincide with those of the zero-offset experiment. Rays from the first source ( $S_1$ ) to a scattering point and back to the corresponding receiver ( $R_1$ ) are shown. The scattering point is located at the depth of 500 m and lies underneath the center of the midpoint line.

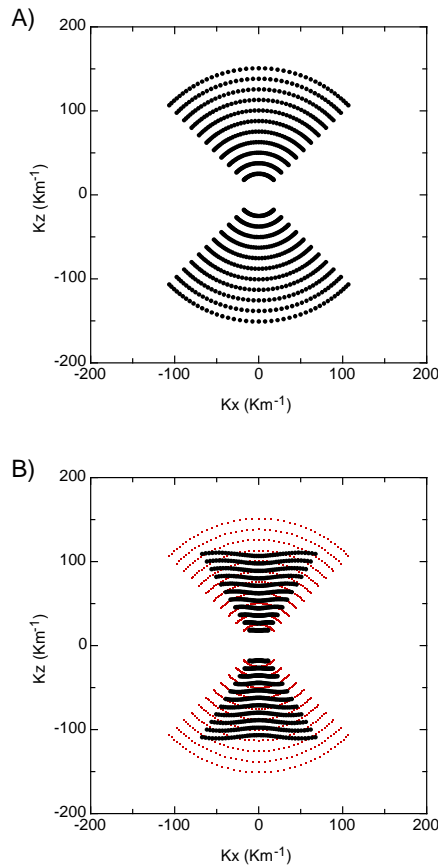


Fig. 3.2. A) Wavenumber vector plot of the scattering point at the depth of 500 m for the zero-offset geometry. B) Wavenumber vector plot (black points) of the same scatterer for the 1 km common-offset geometry. The plot is superimposed over A) (red dots) for easier comparison of their relative wavenumber space coverage.

index, here  $X \in [1, 41]$  (see Figure 3.1B). We can interpret this as a negative effect of the common-offset geometry on the image resolution in all directions. This negative effect, however, is particularly severe in the vertical direction.

On the other hand, the difference in the wavenumber vector apertures is located towards the horizontal axis,  $K_x$ , of the wavenumber vector domain. Therefore, one could suggest that the lack of wider aperture in the common-offset experiment has a negative effect predominantly on the horizontal image resolution. Of course, both the magnitude and aperture factors act synergistically in reducing the overall image resolution in the common-offset geometry.

In Figure 3.3 the spatial images of the scattering point for both geometries are presented. As predicted by the wavenumber vector plots (Figure 3.2), the image resolution provided by the zero-offset geometry (Figure 3.3A) is much better compared

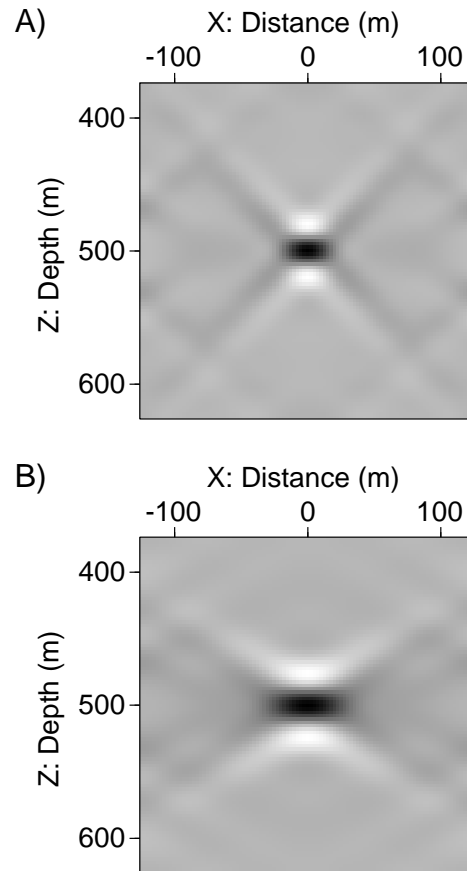


Fig. 3.3. A) Spatial image of the scattering point at the depth of 500 m for the zero-offset geometry. B) Spatial image of the same point for the 1 km common-offset geometry. The image resolution deteriorates in the case of the common-offset configuration.

to the resolution that the common-offset geometry (Figure 3.3B) provide.

In order to closer examine the resolution differences of Figures 3.3A and 3.3B in horizontal and vertical directions, we extracted their amplitudes along these directions (Figure 3.4). The maximum amplitudes of all curves used in this figure and any other similar ones thereof, were normalized to 1 in order to facilitate their comparison. The shapes of the horizontal (solid lines) and vertical (dashed lines) resolution curves confirm von Seggern's (1991) (see also, Vermeer, 1999) statement that for surface only recorded data, the imaging response in the vertical direction resembles the shape of the source wavelet, whereas in the horizontal direction takes the shape of a Gaussian spatial wavelet.

Comparing the horizontal and vertical resolution curves for the zero-offset ge-

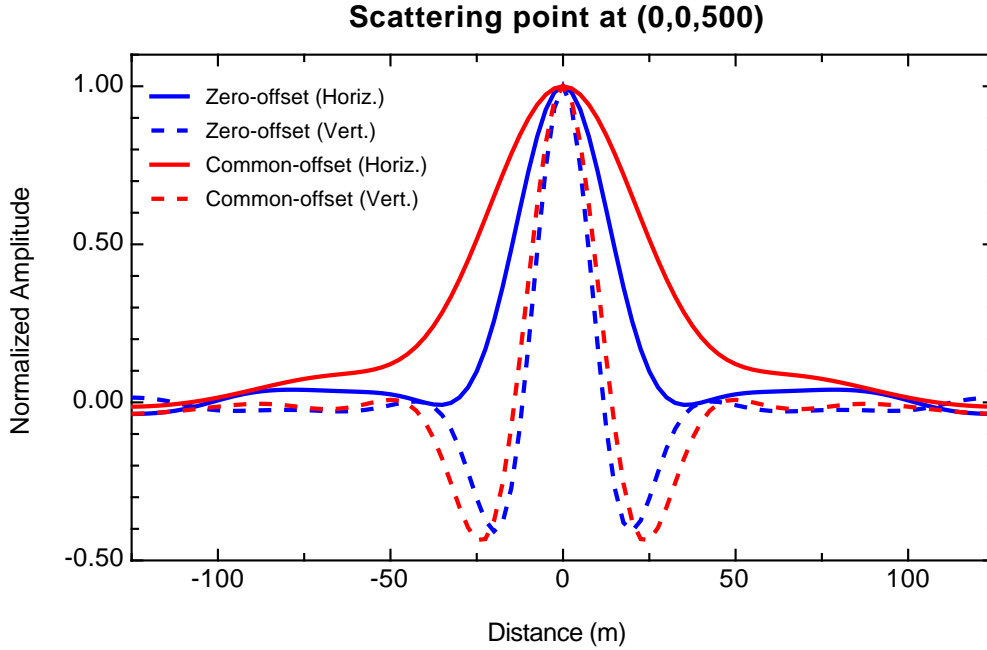


Fig. 3.4. Horizontal and vertical resolution curves for both the zero- and common-offset geometries and the scattering point at the depth of 500 m. The maximum amplitudes of all curves are normalized to 1. The common-offset configuration results in an overall worse resolution. The same behavior was also predicted by the wavenumber vector plots of Figure 3.2.

ometry (blue lines) to the respective ones of the common-offset geometry (red lines), it becomes apparent that the image resolution of the common-offset configuration worsens in both directions, especially in the horizontal.

Next, we let the distance between the scattering point and the acquisition arrays increase by moving the scatterer to the depth of 2000 m. This, by simple geometrical reasoning, makes the wavenumber vector apertures smaller for both geometries. In fact, the aperture for the zero-offset geometry becomes  $\approx 28^\circ$  and the aperture for the common-offset geometry becomes  $\approx 27^\circ$ . Similarly, the magnitudes of the wavenumber vectors  $\mathbf{k}$  for the common-offset configuration approach those of the zero-offset configuration because the angles between their constituent vectors  $\mathbf{k}_s$  and  $\mathbf{k}_r$  are drastically reduced. In conclusion, the coverage of the wavenumber vector domain for the two geometries become similar as the scattering point comes further apart from the source/receiver arrays. In the limit, where the scatterer's distance from the acquisition arrays is infinite, the coverage for both geometries would be exactly the same.

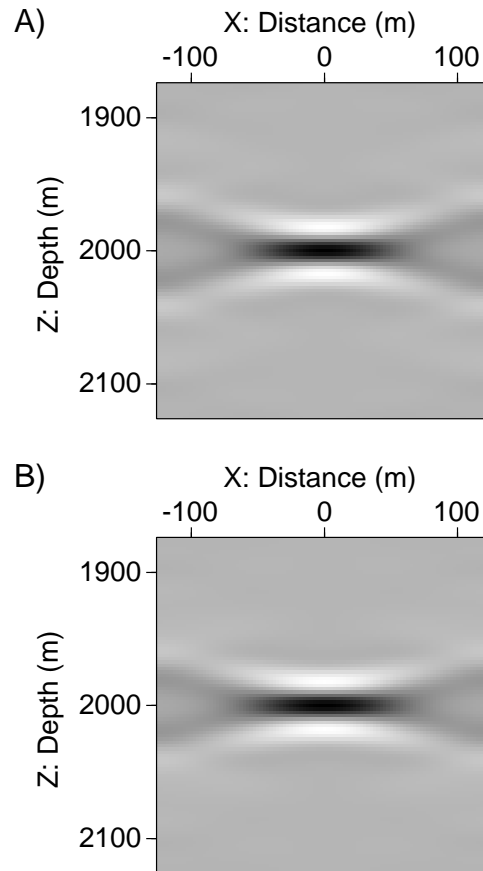


Fig. 3.5. A) Spatial image of the scattering point at the depth of 2000 m for the zero-offset geometry. B) Spatial image of the same point for the 1 km common-offset geometry. For distant scatterers, the two geometries provide, for all practical purposes, the same overall resolution.

The spatial images of the scattering point at the depth of 2000 m for the zero- and common-offset configurations are shown in Figures 3.5A and 3.5B respectively. The differences in resolution between them are so small that is very hard to set them apart. For that, once more we resort to display the horizontal and vertical resolution curves (Figure 3.6). It becomes apparent that even the horizontal resolution (solid lines) that showed a significant difference when the scattering point was located at the depth of 500 m (Figure 3.4), is now comparable. Therefore, for all practical purposes the two geometries produce the same spatial images. Of course, the depth at which this happens is not fixed but relative to the length of the acquisition array because this is what essentially dictates the wavenumber vector aperture (at least in the simple case where a homogeneous medium is considered).



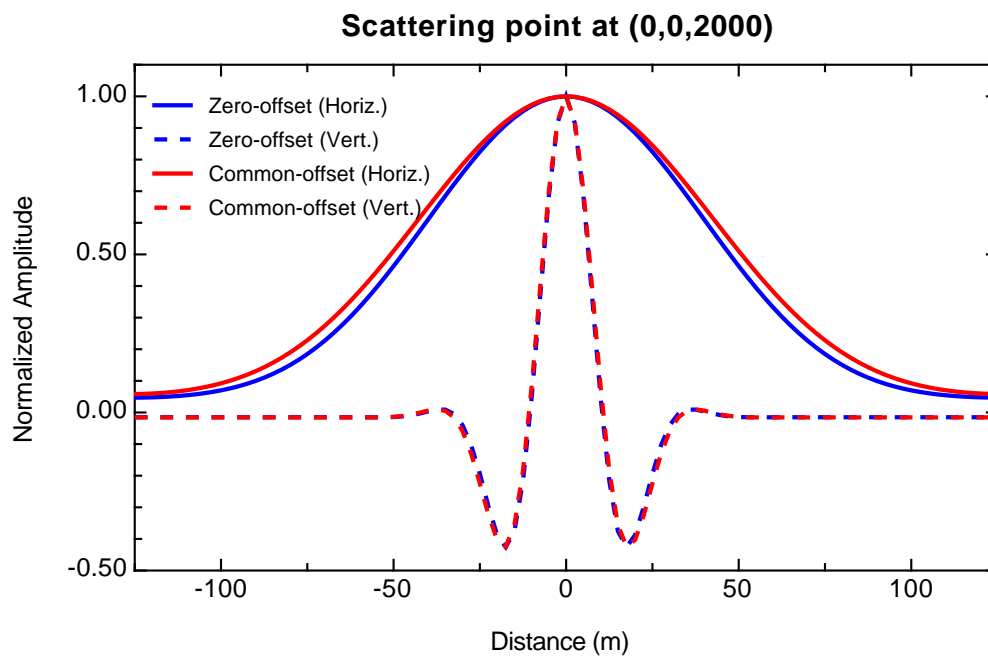


Fig. 3.6. Horizontal and vertical resolution curves for both the zero- and common-offset geometries and the scattering point at the depth of 2000 m. The maximum amplitudes of all curves are normalized to 1. As the scatterer's distance from the source/receiver array increases, the two geometries result in practically the same resolution (compare to Figure 3.4).

From the previous analysis, we infer that the statement that zero-offset experiments provide us with the best possible resolution may be true in theory but in practice, we need to closer examine its limitations. Factors such as the depth of the target point (relative to the acquisition array length) from the source/receiver arrays and the magnitude of the source/receiver offset play a very important role in whether or not a zero-offset geometry is going to produce a better resolved image over a common-offset one. In addition to these factors examined in this section, it is possible that lateral velocity inhomogeneities affect the wavenumber vector domain coverage in an unpredictable way. One such example, a salt-dome model, we consider in the next chapter (Chapter IV).

### 3.3 Effects of the background model on spatial resolution

In order to examine the effects of the background model (velocity and structure) on spatial resolution, we considered four models: a homogeneous half space, a homogeneous flat layer with thickness of 3 km over a half space and two diapir-like structures of the same height but one considerably wider than the other. The interfaces of the two “bulging” models can be mathematically expressed by the Gaussian function:

$$3000 - 500e^{-(x-8500)^2/2\sigma^2}, \quad (3.2)$$

where  $\sigma$  is the standard deviation which controls the geometry of the structure i.e., its width. Therefore, the smaller the standard deviation, the steeper the flanks of the interface. Figure 3.7 shows a family of interfaces defined by different values of standard deviation. We chose the end members of these interfaces (blue and red solid lines) to investigate the effects of the structure on spatial resolution.

The compressional velocity and density of the two layers involved in the models were chosen so that a significant acoustical impedance would occur across their interface. Their values are summarized in Table 3.1.

All the models were built to be 2.5-D with the structures remaining constant along the  $x$ -axis. This symmetry allowed us to consider a 2-D acquisition geometry, reducing, hence, the computational effort with little loss of generality. For all four different models, a single seismic acquisition line was simulated. 221 stations were placed symmetrically over the structures, equally spaced every 50 m. Thus, the total length of the line was 11 km. 220 sources (all 221 stations except for the first)

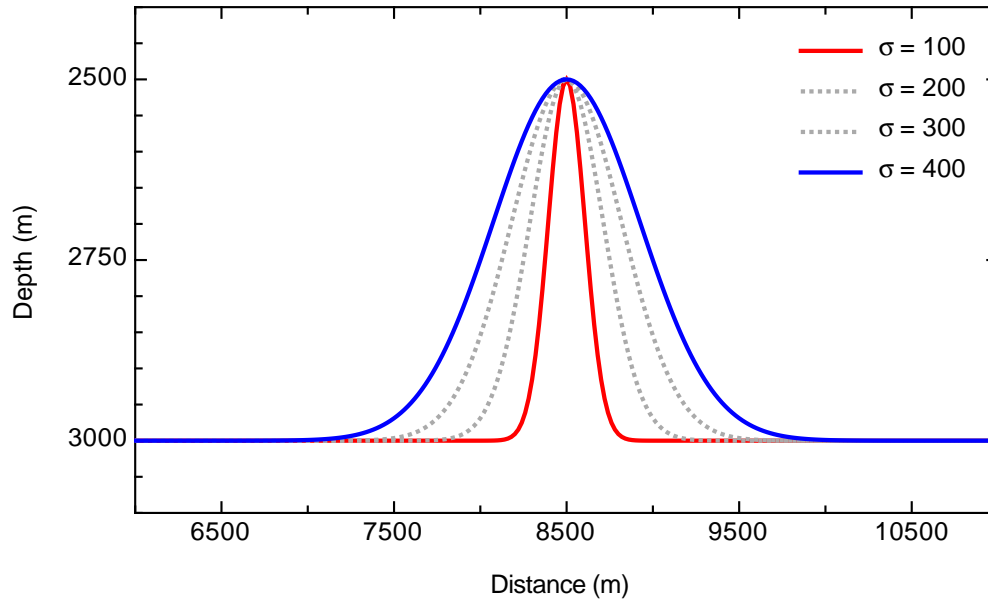


Fig. 3.7. Family of curves defined by equation (3.2). The solid blue and red lines describe the formation interfaces for the two diapir models. The graph is presented with vertical (depth) axis exaggeration.

Table 3.1. Physical properties of the two layers used in evaluating the effects of the background model on spatial resolution and their representative lithologies (Gardner et al., 1974; Meckel and Nath, 1977).

P-Velocity ( $m/s$ )	Density ( $g/cm^3$ )	Acoustic Impedance ( $m/s * g/cm^3$ )	Representative Lithology
3500.0	2.3	$8.05 \cdot 10^3$	Shale/Sandstone
4500.0	2.1	$9.45 \cdot 10^3$	Salt

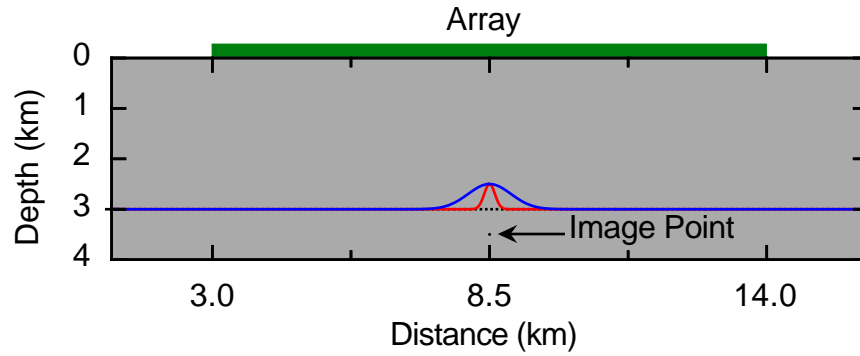


Fig. 3.8. On-scale representation of the models under examination. The acquisition line and imaging point are centered above and below the structures respectively. Lithological interfaces from all the reviewed models are shown.

were recorded in a gradually increasing number of receivers on one side of the source until the maximum number of 60 was reached. Thereafter, the number of recording receivers per source remained constant. Consequently, the nearest offset was 50 m while the farthest was 3000 m with the total recorded traces to reach the number of 11430. The imaging point was placed underneath the apex of the diapir-like structures at a depth of 3500 m. Figure 3.8 illustrates the relative positions of the seismic line, the structures, and the image point.

### 3.3.1 The homogeneous, half space model

The first model we considered was the trivial homogeneous half space. The rays are just straight lines joining the imaging point to all possible stations (sources and receivers). We simulated the experiment twice, contemplating the physical properties for the two media described in Table 3.1. As stated previously, the wavenumber vector magnitudes are inversely proportional to the velocity of the background medium [equations (1.8) and (3.1)]. It is, therefore, not surprising that the wavenumber vector domain is better covered in the case of the lower velocity (3500 m/s) medium instead of the faster (4500 m/s). Moreover, according to the similarity theorem (Bracewell, 1986), the expansion of the wavenumber vectors by a factor of  $\alpha = 4500/3500$  (28.5% increase) results in a compressed spatial image by a factor of  $\alpha^{-1}$  i.e., a decrease of  $\approx 22\%$ . Figures 3.9 and 3.10 show the coverage of the wavenumber vector domain (left) and the resulting spatial image (right) for the same imaging point in the 3500 and 4500 m/s half space medium respectively. For clarity reasons, the wavenumber

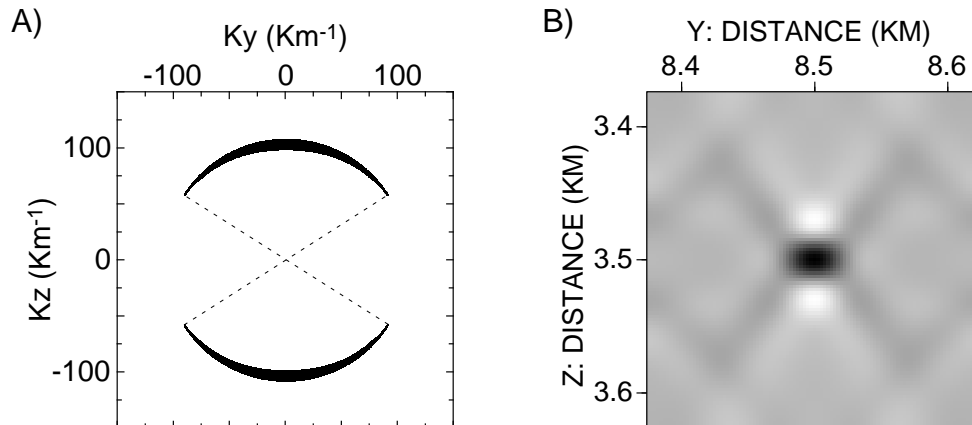


Fig. 3.9. A) Wavenumber vector plot and B) corresponding spatial image for the imaging point of Figure 3.8. The background velocity of the homogeneous medium was 3500 m/s. (Compare with Figure 3.10.) In A), only the wavenumber vectors corresponding to the frequency component of 30 Hz are shown. These vectors along with the dashed lines delineate the covered portion of the wavenumber vector domain.

vector plots depict only the vectors which correspond to frequencies of 30 Hz. The area defined by those vectors and the dashed lines (Figure 3.9) should also be considered covered. The same stands for all consecutive wavenumber vector plots of this chapter.

If one needs to calculate the effect of a different velocity for the medium enclosing the image point, it is very straightforward to achieve without repeating the raytracing. A simple scaling of the once computed wavenumber vectors (either by raytracing or, in the case of the homogeneous model, just by simple geometrical reasoning) and a Fourier transform suffice to generate the new spatial image. Following this reasoning, we scaled the wavenumber vectors of the high velocity medium to simulate the experiment of the low velocity medium. The resulting wavenumber vector plots and the corresponding spatial images were identical to those obtained by performing the ray tracing independently (Figure 3.9). We will use this approach in the next sections where more complicated models are considered.

### 3.3.2 The flat interface model

Next in the series of models we examined was the flat interface model. The interface was placed at the depth of 3 km with the scatterer lying 500 m below it. We allowed the velocities across the interface to either increase (from 3.5 to 4.5 km/s) or decrease (from 4.5 to 3.5 km/s). Since there is a significant velocity contrast across the in-

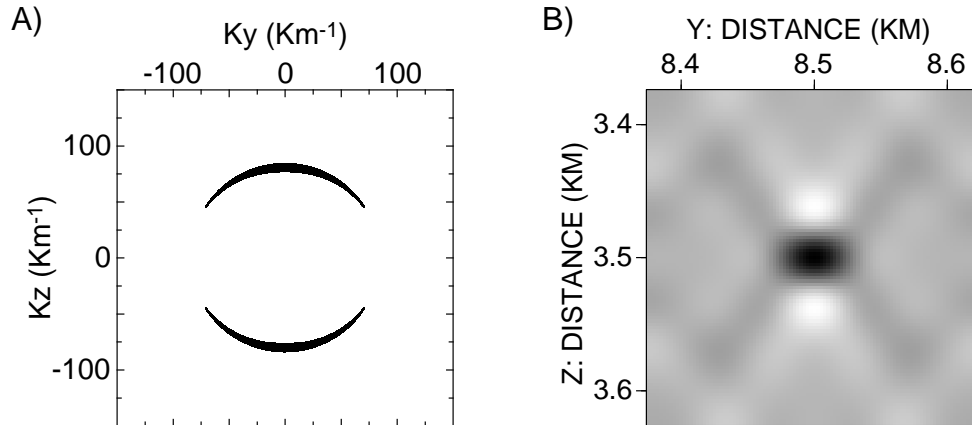


Fig. 3.10. A) Wavenumber vector plot and B) corresponding spatial image for the imaging point of Figure 3.8. The velocity of the homogeneous medium was 4500 m/s. (Compare with Figure 3.9.)

terface, a rather severe ray-bending should occur. Figures 3.11 and 3.12 show the raytracing results for the two cases. Apart from the significant bending of the rays, one can easily infer that compared to the homogeneous model considered earlier, the ray apertures become larger when the velocity increases with depth and smaller when it decreases. Figures 3.13 and 3.14 show the wavenumber vector domain coverage (left) and the corresponding spatial images (right) of the test point for increasing and decreasing velocities with depth respectively. The wide aperture of wavenumber vectors of Figure 3.13A results into an almost equally resolved point in all directions (Figure 3.13B). On the other hand, the wavenumber vectors of Figure 3.14A have greater amplitudes and are more concentrated around the  $K_z$ -axis. This results into an image which exhibits stronger artifacts but is better resolved in the vertical direction.

Compensating for the difference in the velocity of the medium where the test point lies, corrects the wavenumber vector magnitude difference between the two cases. Figure 3.15 shows the wavenumber vector coverage (left) and the resulting spatial image (right) of the scatterer of the increasing velocity model after a velocity scaling was applied to simulate a test point lying in a medium of 3.5 km/s. The magnitudes of the wavenumber vectors resemble those of the model with decreasing velocity with depth (compare Figures 3.15A and 3.14A). However, the effects of the increasing versus decreasing velocity with depth are still present and expressed by the difference of the wavenumber vector apertures. The spatial image of this hypothetical

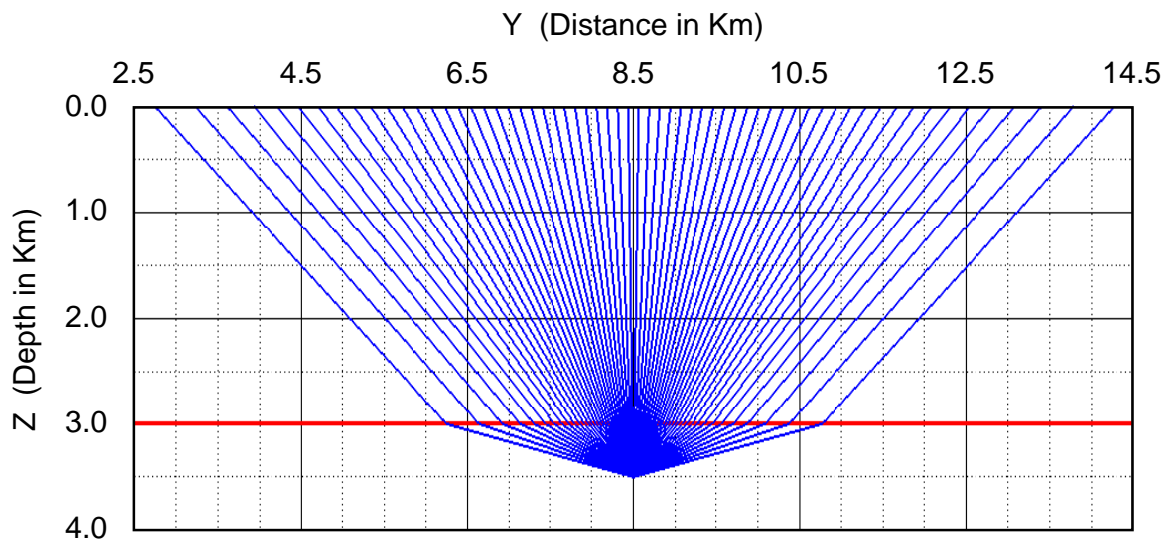


Fig. 3.11. Initial value raytracing results for the flat interface model. Since the velocity increases with depth, the rays bend away from the normal to the interface.

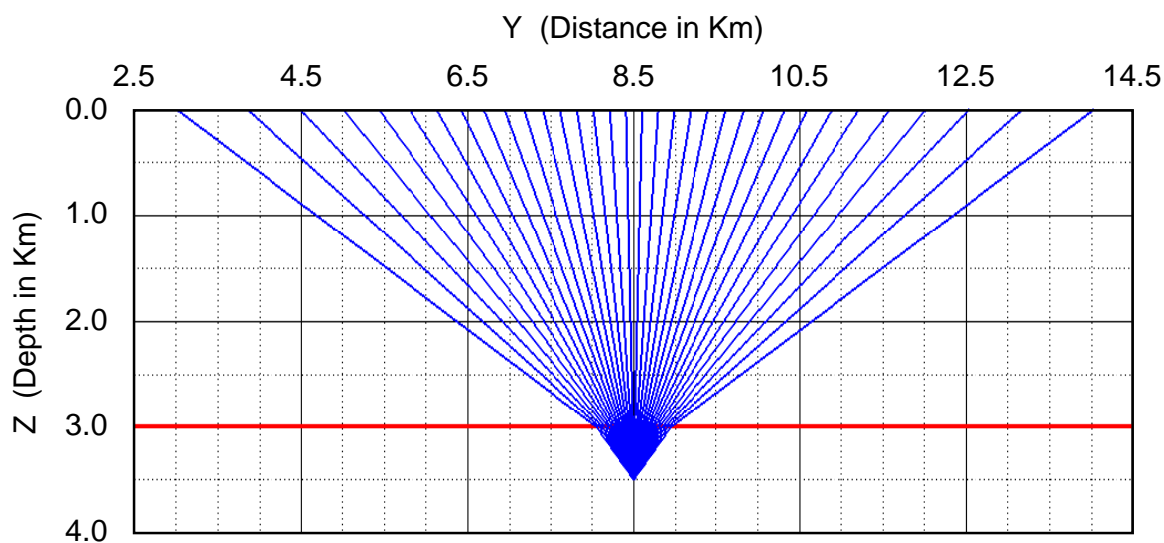


Fig. 3.12. Initial value raytracing results for the flat interface model. Since the velocity decreases with depth, the rays bend towards the normal to the interface.

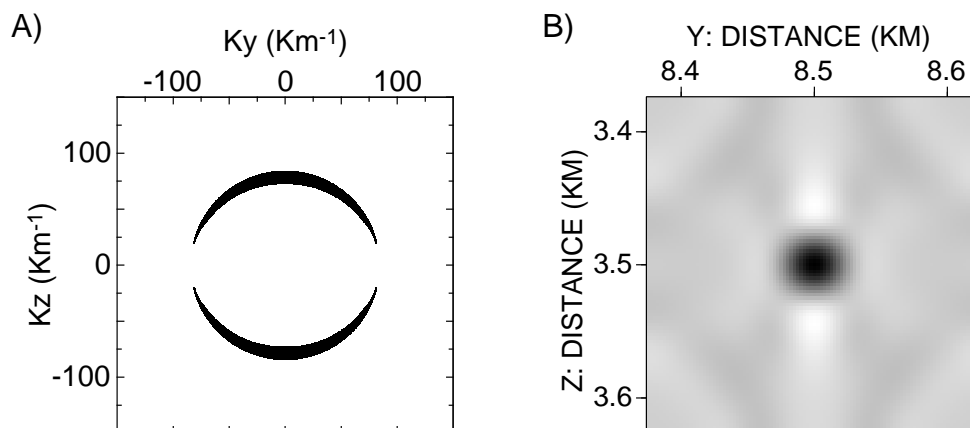


Fig. 3.13. A) Wavenumber vector plot and B) corresponding spatial image for the imaging point of Figure 3.8. The velocity increases across the flat interface from 3.5 to 4.5 km/s. In A), only the wavenumber vectors corresponding to the frequency component of 30 Hz are shown.

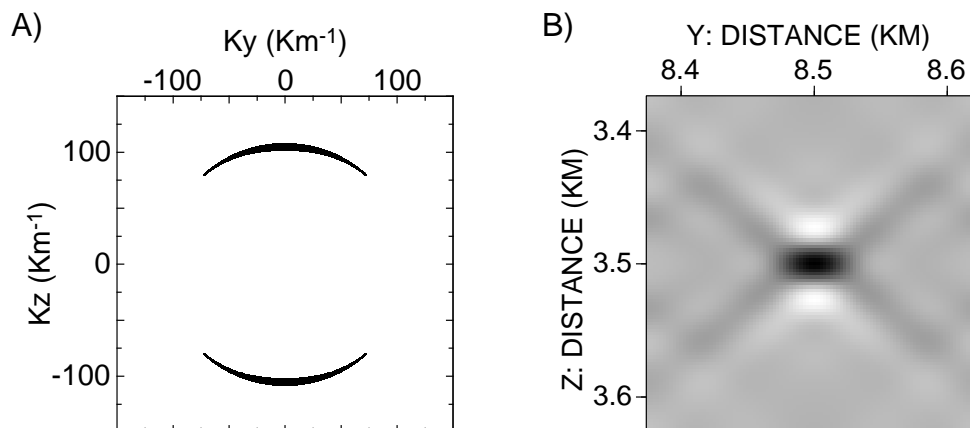


Fig. 3.14. A) Wavenumber vector plot and B) corresponding spatial image for the imaging point of Figure 3.8. The velocity decreases across the flat interface from 4.5 to 3.5 km/s. In A), only the wavenumber vectors corresponding to the frequency component of 30 Hz are shown.



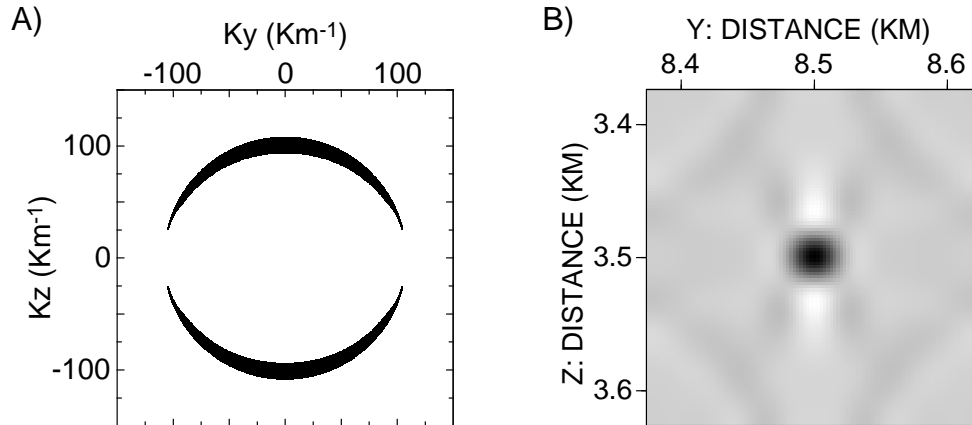


Fig. 3.15. A) Wavenumber vector plot and B) corresponding spatial image for the imaging point of Figure 3.8. The velocity still increases across the flat interface but the medium where the scatterer lies is now assumed to be 3.5 km/s. In A), only the wavenumber vectors corresponding to the frequency component of 30 Hz are shown.

model, i.e., one with increasing velocity with depth but with low velocities overall, exhibits the best resolution of all the examined models so far (Figure 3.15B).

### 3.3.3 The Gaussian models

The final set of experiments performed in order to better understand the effects of background model (velocity and structure) on spatial image resolution were the two diapir-like structures described in detail in the beginning of section 3.3 (see also, Figure 3.7). Again, velocity was allowed to either increase or decrease with depth, alternating values of 3.5 and 4.5 km/s (as in all previous models).

Figures 3.16, 3.17, 3.18 and 3.19 depict the raytracing results for all 4 possible cases. Consistent with the previous results, ray apertures become wide or narrow in the cases of increasing and decreasing velocity with depth respectively. Due to the large length of the acquisition line, the apertures are practically the same for all models (flat and diapir-like structures) with increasing velocity with depth (compare Figures 3.11, 3.16 and 3.18). The same holds for the apertures of all models with decreasing velocity with depth (compare Figures 3.12, 3.17 and 3.19). However, the distribution of the rays (and consecutively, the corresponding wavenumber vectors) is different in each case. Therefore, only very subtle differences in the spatial images are expected.

The spatial images resulted from the image resolution analysis in the cases of the

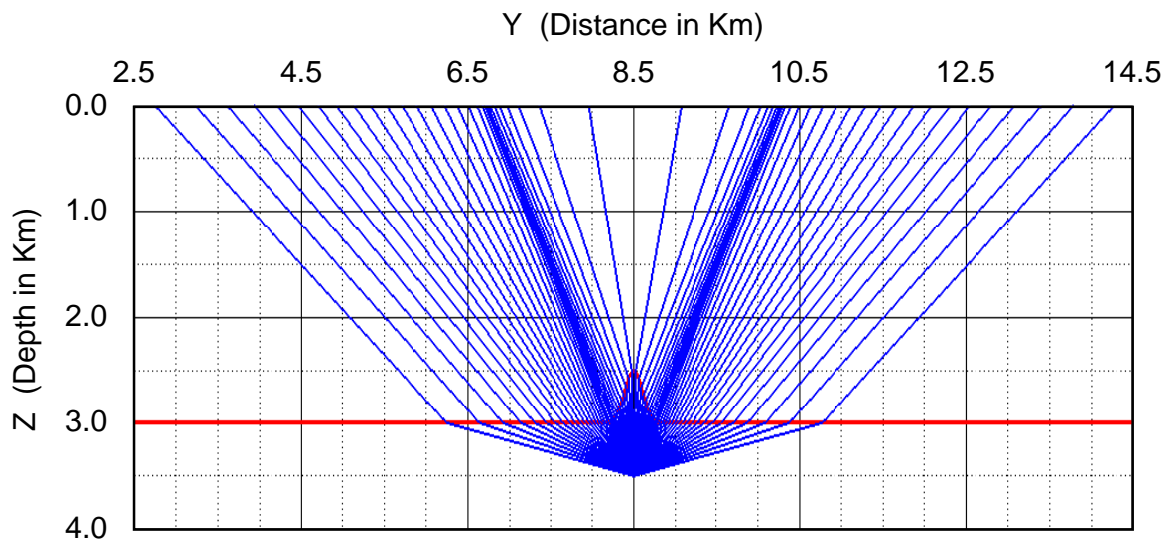


Fig. 3.16. Initial value raytracing results for the steep Gaussian model. Since the velocity increases with depth, the ray aperture widens. Notice that due to the structure, rays converge and diverge significantly.

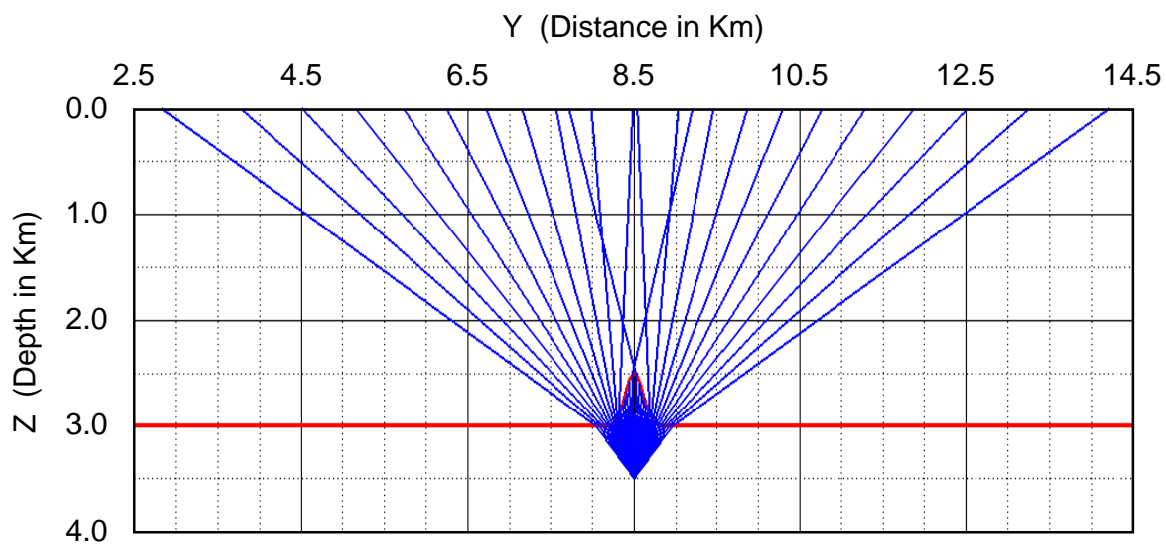


Fig. 3.17. Initial value raytracing results for the steep Gaussian model. Since the velocity decreases with depth, the ray aperture becomes narrow. Notice that due to the structure, ray triplication is evident.

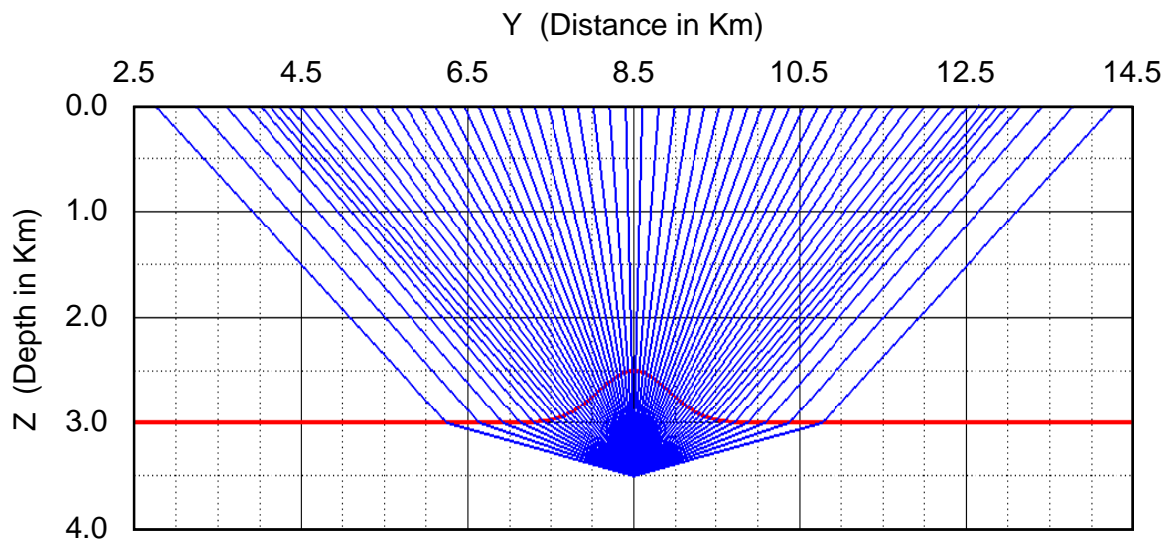


Fig. 3.18. Initial value raytracing results for the gentle Gaussian model. Since the velocity increases with depth, the ray aperture widens.

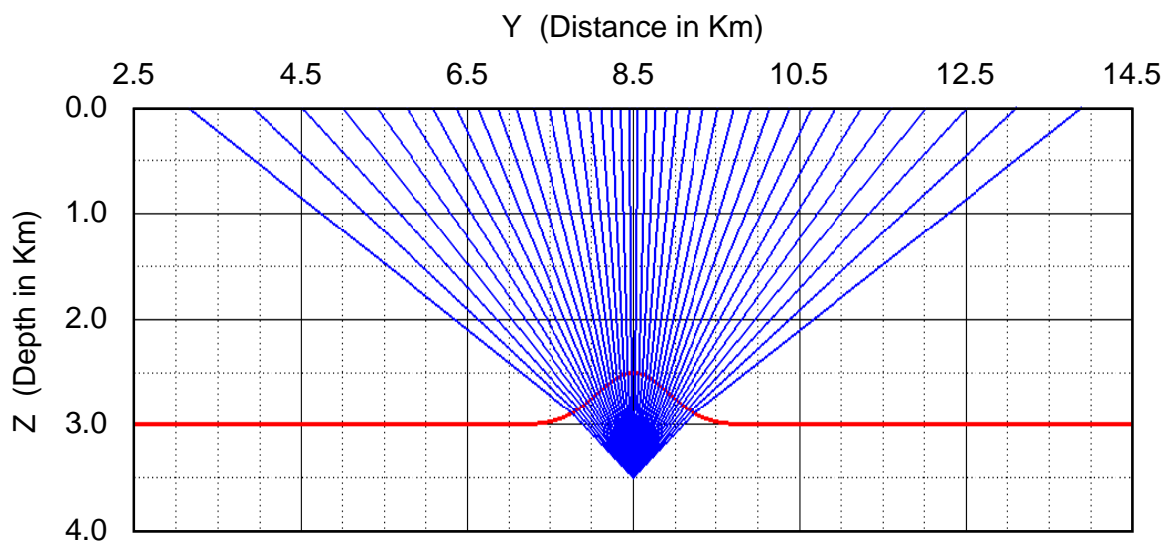


Fig. 3.19. Initial value raytracing results for the gentle Gaussian model. Since the velocity decreases with depth, the ray aperture becomes narrow.

gentle and steep Gaussian models are shown in Figure 3.20. The images of the flat interface model are repeated from Figures 3.13B and 3.14B for comparison reasons. The left column of the figure corresponds to models with increasing velocity with depth (i.e., wide ray and wavenumber vector apertures). Similarly, the right column corresponds to models with decreasing velocity with depth (i.e., narrow apertures). There is very little change in image resolution along each column. However, as the structure becomes steeper (from top to bottom), image artifacts start to develop. These artifacts seem to be more prominent in the models with the decreasing velocity. The fact that the images change so little when considering these different structures, is of course, the outcome of the very long acquisition line that allows the ray (and wavenumber) apertures to be consistent in all models.

### 3.3.3.a Multipathing

In complex media, multi-pathing is very common. In this case, in order to correctly evaluate the Kirchhoff integral for the prestack depth migration (PDM), one needs to sum over all branches of the multi-valued traveltime function. However, the cost of doing this is currently prohibitive, especially for the 3-D PDM. Therefore, if not all the branches of the multi-valued traveltime field can be used, we must choose which ones we should use. Traditionally, the first-arrival times are used because they can be easily and efficiently computed, for example, by solving the eikonal equation (Vidale, 1988; Vidale, 1990; van Trier and Symes, 1991).

Apart from the first arrival traveltimes, other selection criteria have been recently proposed. Geoltrain and Brac (1993) using the Marmousi 2-D model (Versteeg and Grau, 1991), demonstrated that, wherever existed, later arrivals contained most of the wavefield energy and proposed the use of the traveltime of the most energetic event as a selection rule (see also, Thierry et al., 1999). The traveltime associated with the ray with the shortest physical length, is an alternative selection criterion (Moser, 1994; Nichols et al., 1998). Its advantages lie on the fact that ray travel path is a first-order attribute of the ray tracing method (unlike the amplitude) and it is more stable (based solely on Fermat's principle). Stieglitz (2001) introduced a new selection criterion, the maximum angular aperture (MAA), where, from the multi-valued operator, the branch with the greatest aperture about the image point is selected. The MAA selection criterion can be directly tied to our spatial image

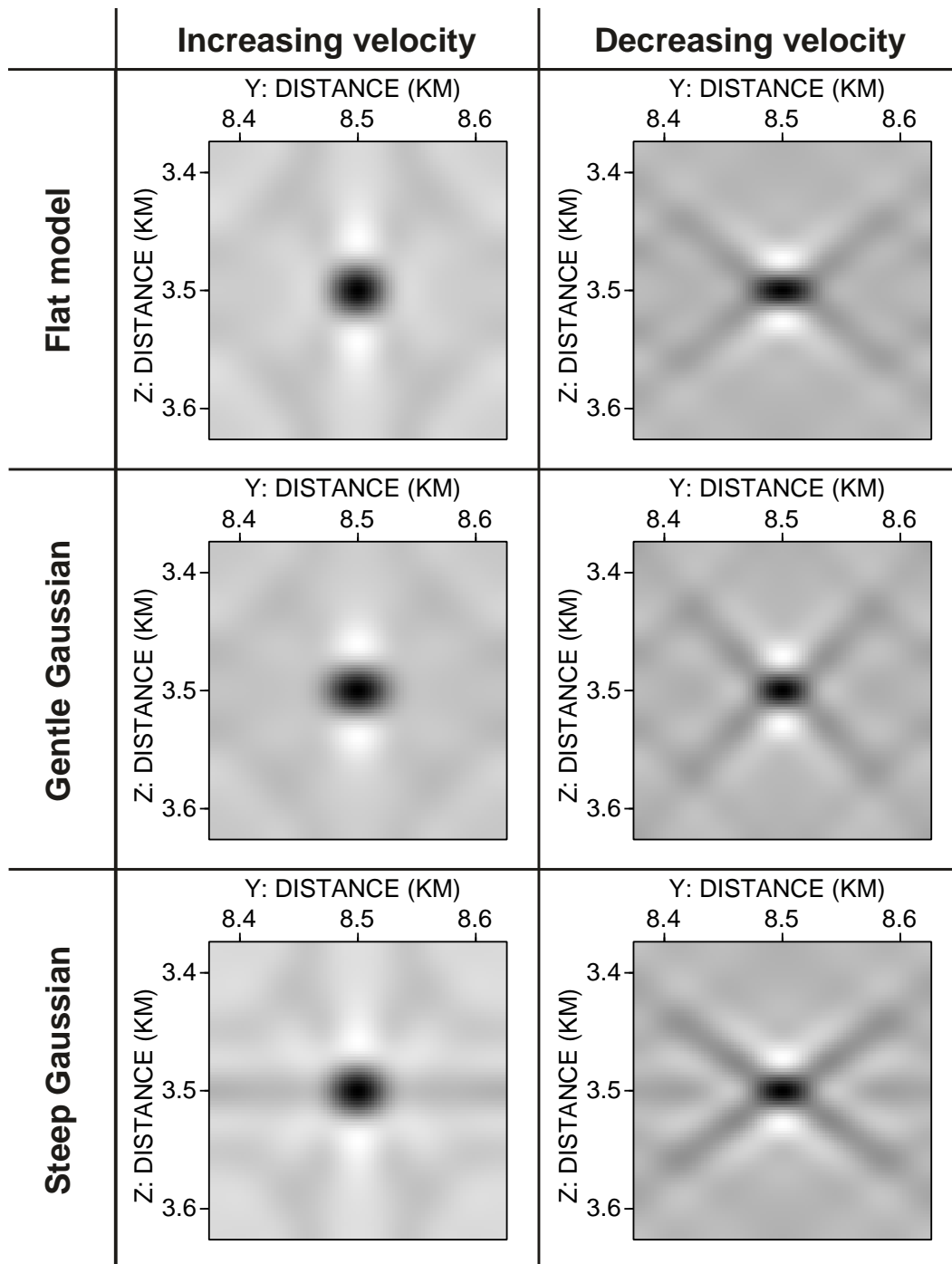


Fig. 3.20. Spatial resolution for the image point from Figure 3.8. The left column displays results for the models with increasing velocity with depth; the right column is for the models with decreasing velocity with depth. The uppermost pair of figures shows the results for the flat interface model and are identical to the corresponding images in Figures 3.13B and 3.14B.

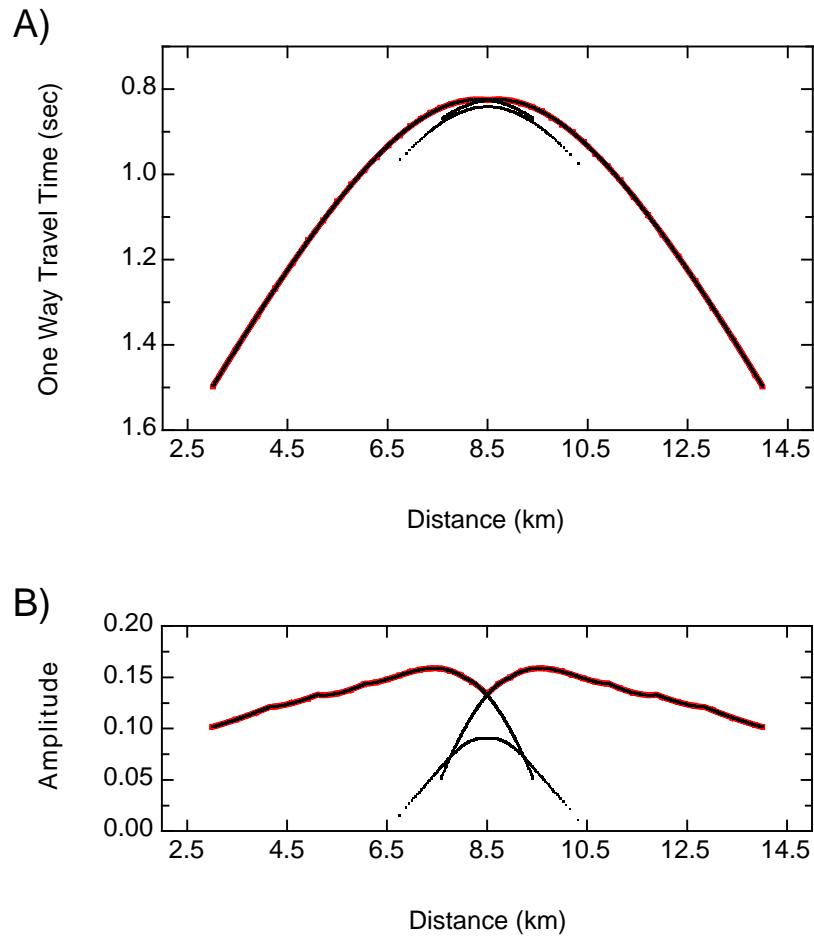


Fig. 3.21. A) One-way traveltime and B) corresponding amplitude curves for the steep Gaussian model with decreasing velocity with depth. The red highlighted curves satisfy the minimum traveltime criterion of selecting the rays that were used in the image resolution analysis.

resolution analysis and our criterion to evaluate competing acquisition geometries (Gibson, Jr. and Stieglitz, 2001).

Even in the simple cases of the Gaussian models examined here, multi-pathing is evident (Figure 3.17). To comply with the simpler and widely used single-valued operators, we needed to be able to choose a ray with a particular attribute wherever multiple choices were available. Consequently, we implemented the selection rules of the first arrival (minimum traveltime) and most energetic (maximum amplitude). From this section on, whenever multiple arrivals occur, it is implied that the minimum traveltime criterion was applied. Figure 3.21 clearly indicates that in the case of the steep diapir model, multipathing is present. Figure 3.21A is the one-way travel time

from the test point to the surface stations. In the center of the seismic line, multiple time curve branches are evident and are the result of wave-folding or, equivalently, ray-crossing (Figure 3.17). Figure 3.21B shows the corresponding amplitude curves. The red highlighted parts of the curves denote the chosen minimum traveltimes (and corresponding amplitudes) used in the image resolution analysis.

### 3.4 The role of signal-to-noise ratio in image resolution

All of the spatial images shown to this point indicate the theoretically achievable resolution using this particular acquisition geometry. We assumed for example, that the signal-to-noise ratio in all cases was infinite. However, we can indirectly examine the effect of noise level on resolution by accepting into the image resolution analysis rays that satisfy an amplitude criterion, i.e., if the computed amplitude that corresponds to a ray trajectory from a source to the image point and back to a receiver is more than a threshold amplitude value, we allow the corresponding wavenumber vector to contribute to the imaging of the point. (For further discussion on the proposed signal-to-noise approach see the relevant section of Chapter IV).

Since all raytracing results (Figures 3.11, 3.12, 3.16, 3.17, 3.18 and 3.19) shown in this chapter were calculated using the same increment in ray take-off angles, the relative spacing of the rays is a good indication of the expected recorded amplitudes since ray focusing and defocusing are described by the geometrical spreading factor (Aki and Richards, 1980). Examining those figures carefully, one can infer that in all cases, amplitudes associated with models whose velocity decreases with depth are lower than those in the respective models with increasing velocity. Figure 3.22 shows the amplitude of the one-way traveled rays for the Gaussian models, confirming the validity of the previous statement.

Figures 3.23 and 3.24 display the spatial images for the flat interface (Figure 3.23) and the gently dipping Gaussian (Figure 3.24) models. The left columns of both figures correspond to increasing velocity with depth whereas the right columns refer to decreasing velocity with depth. The noise level increases from top to bottom. It becomes apparent that the spatial resolution decreases more rapidly in those models that lower amplitudes were recorded i.e., the ones with the decreasing velocity with depth. In addition to that, each structure behaves differently, filtering out wavenumber vectors of different directions as noise level increases. The result of this preferen-

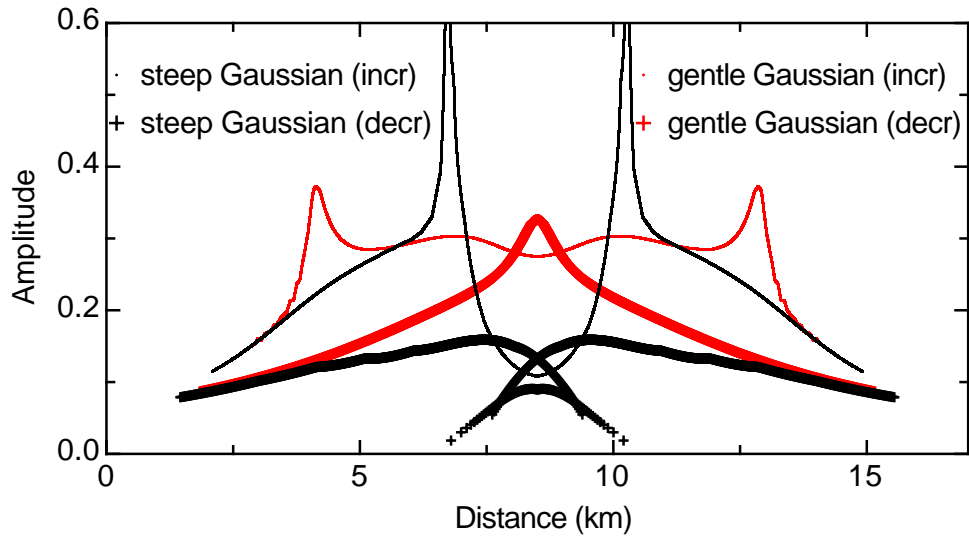


Fig. 3.22. Amplitude curves against horizontal distance. For both the gently and steeply dipping Gaussian models, amplitudes are greater when the velocity increases with depth.

tial filtering of wavenumber vectors, is the worsening of spatial resolution in different directions (compare the high noise level images of the gently dipping Gaussian model with increasing velocity of Figure 3.24 and the flat interface model of Figure 3.23).

### 3.5 Conclusions

In this chapter we established how the proposed image resolution method depends on factors that are not explicitly described by Beylkin's equation [equation (1.8)], or to be more precise, are lumped into the domain of integration  $D_x$  of equation (1.7). First, we confirmed that zero-offset experiments provide, in general, better image resolution than common-offset ones, as readily derived from Beylkin's equation. However, the location of the image point relative to the acquisition array, is an important parameter that we have to take a closer look at before we unconditionally accept such a statement. By considering simple geometrical arguments, we showed that common-offset experiments can provide spatial image resolution comparable to zero-offset.

Next, we considered the effects of velocity and structure on image resolution. In simple homogeneous half space models, it is unambiguous that not only can the effect of velocity be predicted but also be quantitatively assessed. However, when



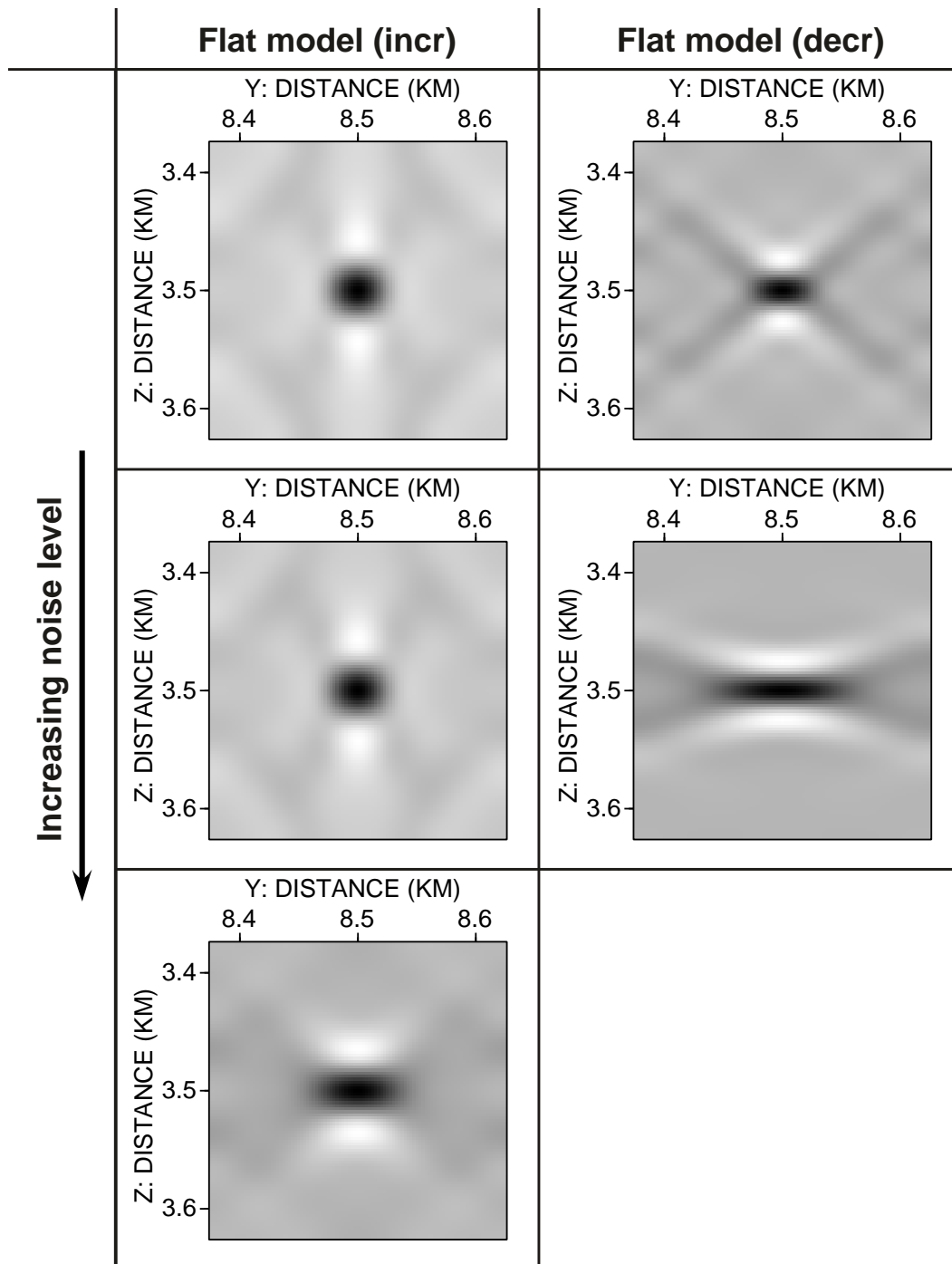


Fig. 3.23. Spatial resolution for the image point from Figure 3.8 with the flat interface. The left column displays results for increasing velocity with depth; the right column is for the model with decreasing velocity with depth. The uppermost pair of figures shows the results for an infinite S/N ratio. Notice the loss of resolution as the noise level increases from top to bottom.

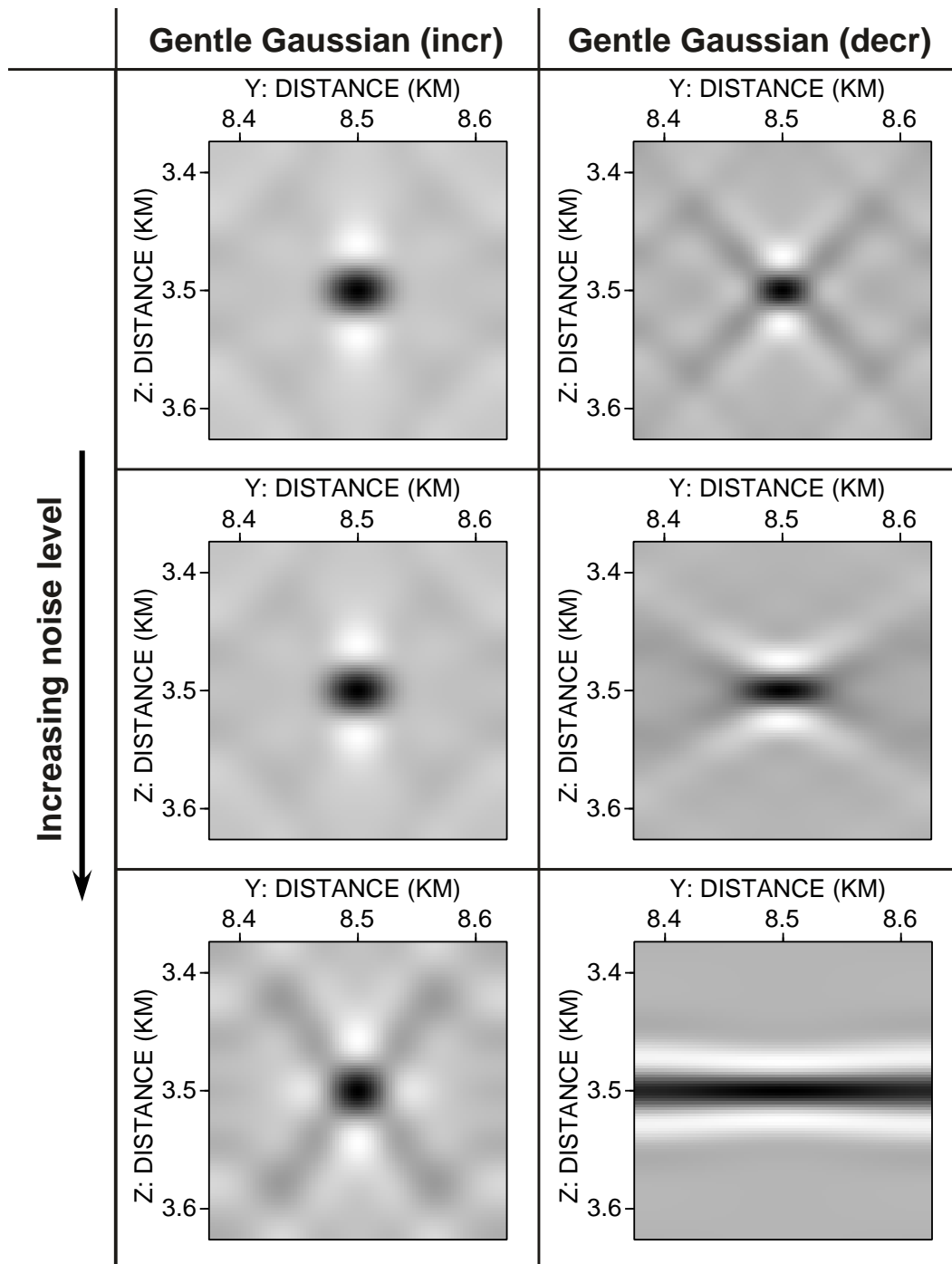


Fig. 3.24. Spatial resolution for the image point from Figure 3.8 with the gentle Gaussian interface. The left column displays results for increasing velocity with depth; the right column is for the model with decreasing velocity with depth. The uppermost pair of figures shows the results for an infinite S/N ratio. Notice the loss of resolution as the noise level increases from top to bottom.

a structure, as simple as a flat interface, is introduced above the image point, one has to consider not only the velocity of the medium that surrounds the point (as is explicitly stated in Beylkin's equation) but the velocities of all the media that a ray traverses, from a source to the point, and back to a receiver. Moreover, we showed that the order of velocities in a sequence of media is also important. We established that the most favorable scenario for good image resolution is a model where velocities increase with depth and have overall small values.

Finally, different structure models seemed to provide comparable spatial images as long as they were compared to models of the same velocity order (either increasing or decreasing with depth). This was most likely due to the great length of the acquisition line. However, when we introduced noise into the image resolution analysis, and started increasing its level, the different effects of each structure on image resolution were revealed. Overall, one can still say that structures with increasing velocity with depth are more stable in high noise environments, providing image resolution that deteriorates slower than in structures with decreasing velocity with depth. However, the directions in which spatial resolution decreases as noise level increases, are dependent not only on the order of the velocity but the shape of the interface as well.

This analysis provided important insights in our understanding of factors affecting spatial resolution. If one seeks to obtain good imaging of a target area, it is imperative to incorporate velocity, target location and possible structure of overlying strata into the design of an acquisition geometry.

## CHAPTER IV

### EFFICACY ASSESSMENT OF COMPETING 3-D ACQUISITION DESIGNS OVER A SALT DOME MODEL

#### 4.1 Introduction

Seismic survey design must take into account many different factors, including economic considerations as well as practical constraints such as those introduced by features such as lakes or rivers on land or drilling platforms in marine settings<sup>1</sup>. One of the most important issues is clearly to adjust the acquisition geometry to optimize the seismic images of the target reservoir formations. For example, Maldonado and Hussein (1994) suggest that a concentric circle source-receiver layout may produce better images near salt domes than some simpler designs. In the preceding chapters (Chapters II and III), simple examples for homogeneous geologic models illustrate the wavenumber and space-domain images and how they depend on simple 2-D acquisition geometries. Here, we apply the approach to a 3-D model of a salt dome structure that causes significant ray-bending effects. These results present a significant advance over previous work, which typically considers only relatively simple geologic structures (e.g., von Seggern, 1994; Vermeer, 1999). Because of the complex wave propagation properties, resolution predictions are less intuitive. Furthermore, we compare the resolution for a marine geometry with results for a radial survey geometry based on a joint surface seismic/vertical seismic profiling (VSP) survey recently conducted in the onshore Gulf Coast area as well as a more conventional orthogonal survey. The efficacy of these different survey designs is also assessed in conjunction with decreasing S/N ratios.

---

<sup>1</sup>Part of this chapter is reprinted with permission from "Quantitative measures of image resolution for seismic survey design" by R. L. Gibson, Jr. and C. Tzimeas, 2002. *Geophysics*, **67**, 1844-1852. Copyright 2002 by the Soc. of Expl. Geophys.

## 4.2 Resolution and acquisition geometry in homogeneous media: Multi-offset versus single-offset surveys.

The resolution analysis is easily illustrated for homogeneous media, where the ray-paths are obviously straight lines connecting source or receiver and the image point. While such examples may seem trivial, they provide very important insights that are broadly applicable to acquisition over geologic models with gentle structure where raypath bending is minimal, since small changes in ray directions result in only small perturbations to the wavenumber vectors computed with equation (1.8) or equation (3.1).

For example, Figure 4.2 compares the wavenumber-domain images for a single zero-offset, vertical incidence source-receiver pair and for the surface array shown in Figure 4.1. The surface array consists of 81 sources and coincident receivers, spaced every 50 m for a total length of 2 km. All shots are fired into all receivers. The rays for the single source-receiver pair are vertical, so the corresponding wavenumber vector is vertical (Figure 4.2A). On the other hand, the array includes raypaths with a larger aperture, so a much larger portion of the wavenumber domain is illuminated (Figure 4.2B).

Transforming these images back to the space domain yields the predicted migration images of the point scatterer (Figure 4.3). The vertical wavenumber vector transforms to a horizontal, planar image (Figure 4.3A), while the multioffset experiment produces a comparatively well-resolved image of the point scatterer (Figure 4.3B). Migrations of synthetic data computed for the multioffset experiment produce an image that is indistinguishable from Figure 4.3B, confirming the accuracy of the image prediction. On the other hand, the migration of data from the single source-receiver pair will be the well-known half-circle imaging impulse response. The Beylkin formula [equation 1.7] yields information only on the Fourier wavenumber domain components that are resolved at a specific image point, so it instead produces the plane-wave component (Figure 4.2A).

For this simple geometry, the best spatial resolution is theoretically obtained with an array of zero-offset source-receiver pairs, since the slowness vectors for the source and receiver rays coincide and their vector sum will be a maximum (e.g., Vermeer, 1999). When we repeat the calculations for the geometry of the preceding example using only a zero-offset receiver for each of the 81 sources, the resolution

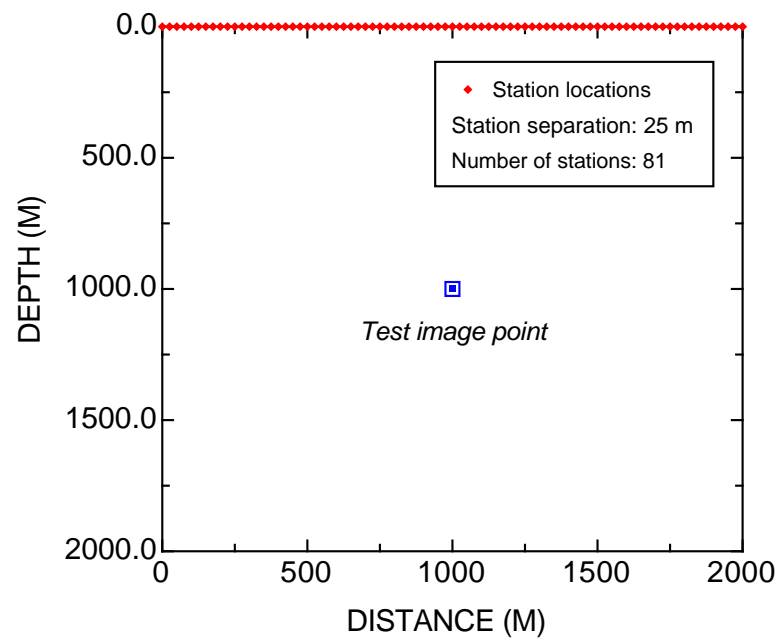


Fig. 4.1. Acquisition geometry for Figures 4.2, 4.3, and 4.4. The symbols mark station locations at which both sources and receivers were located on the free surface. Sources occupied each station, and active receivers were located at all 81 stations for each shot.

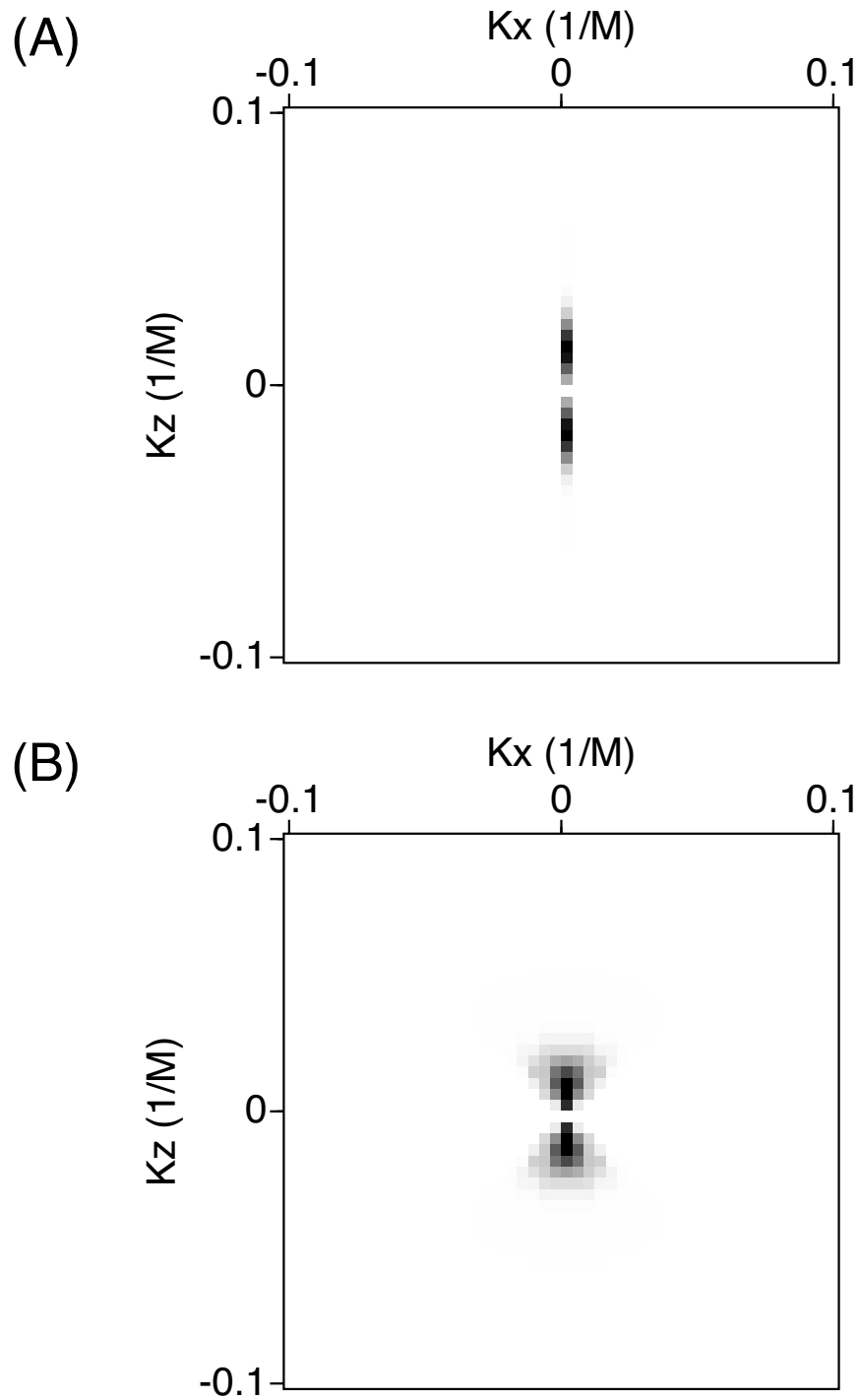


Fig. 4.2. Wavenumber-domain images of the point scatterer at the test point in Figure 4.1. (A) Zero-offset result for collocated source-receiver at  $(x, z) = (1000, 0)$  in Figure 4.1. (B) Result obtained using all source and receiver locations in Figure 4.1.

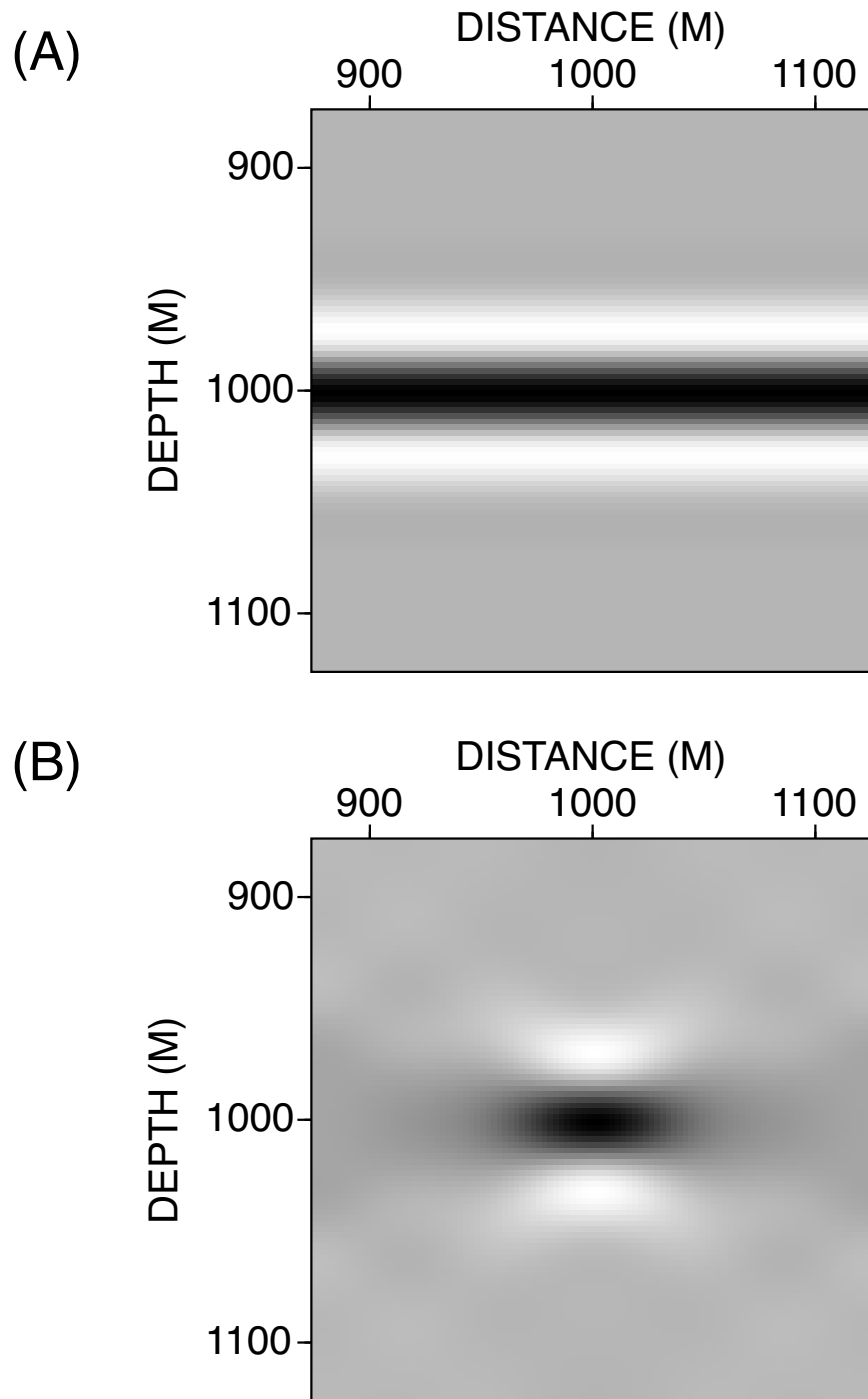


Fig. 4.3. Space-domain images of the point scatterer at the test point in Figure 4.1. Fourier transforms of the wavenumber-domain images in Figure (4.2). (A) Zero-offset result for collocated source-receiver at  $(x, z) = (1000, 0)$  in Figure 4.1. (B) Result obtained using all source and receiver locations in Figure 4.1.



improves over the image obtained using a multioffset array (Figure 4.4). Since the array has exactly the same total length for both cases, the aperture of directions occupied in the wavenumber domain is the same. However, the wavenumber vectors in the zero-offset model are all the same length, and the only reason the amplitudes vary in Figure 4.4A is because of the binning that occurs in Cartesian coordinates. In practice, the increase in S/N ratio will likely compensate for the degradation in resolution obtained using the idealized model.

Whether a single-fold, zero-offset data set can practically provide the best possible resolution compared to any other single-fold, common-offset set depends on the actual acquisition geometry, geologic model and location of target point (see further discussion in 3.2). It is well established however, that combining redundant subsets (such as common-midpoint gathers or multi-offset data) in prestack migration, decreases the subsurface image resolution (Bleistein, 1987; Levin, 1998; Vermeer, 1999). It is, therefore, desirable when examining the ability of a particular acquisition survey to resolve a target point, to analyze the data in “nonredundant data subsets” (Levin, 1998) or “minimal data sets” (Padhi and Holley, 1997; Vermeer, 1999). Padhi and Holley (1997) define a minimal data set as “*the smallest amount of data that can adequately image a reflector (or at least a reasonable piece of one)*”. In such minimal data sets, all traces which usually are described in terms of four coordinates (two source and two receiver coordinates, assuming constant elevation coordinates) lie on a 2-D plane of this 4-D space. Examples of such data sets are the common-offset subsets of an ideal (no cable feathering) marine geometry, a cross spread geometry and a single shot into an areal receiver distribution. In the following analyses, we adopted the approach of minimal data sets (by examining common offset subsets) in order to assess the resolving power of competing acquisition geometries. This is not to say however, that multi-offset (multi-fold) data sets cannot be used. They would simply yield images that would be equivalent to some average of all single-fold data.

### 4.3 Survey design for a salt dome model

While the preceding results provide general insight into the types of resolution that will be obtained for acquisition in areas with minimal geologic structure, a complete calculation of rays is required for more complex models, and results may be difficult to predict prior to computation. As an example, we consider a model of a salt

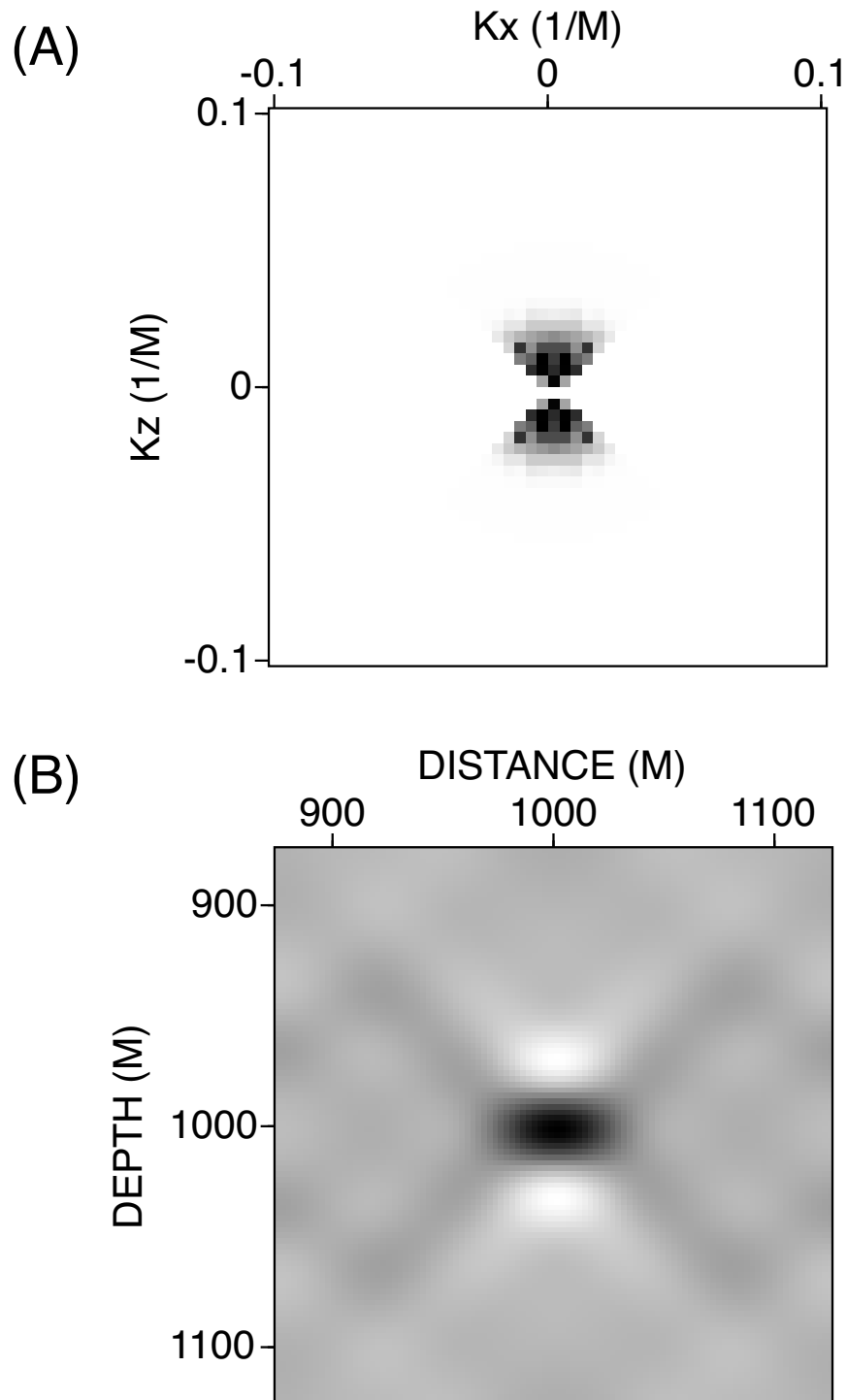


Fig. 4.4. (A) Wavenumber- and (B) space-domain images of the scatterer at the test point using a zero-offset acquisition geometry. Resolution is better than for the multioffset geometry (Figure 4.3B). These images are obtained by considering zero-offset source-receiver pairs located at each of the 81 stations in Figure 4.1.

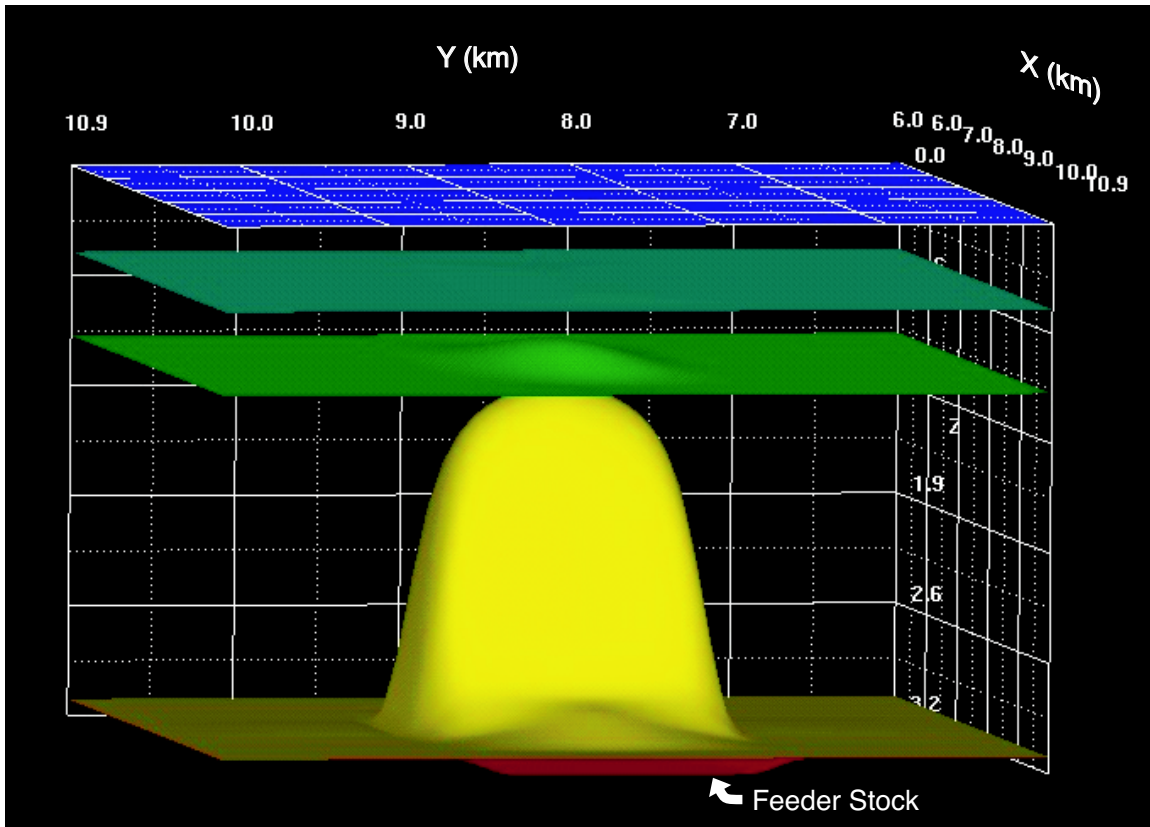


Fig. 4.5. Perspective view of the salt model used for testing survey design. A small, thin feeder stock can be observed near the center of the model on the front side of the image. The salt thickness is negligible outside of the dome and the feeder stock.

dome structure (Figure 4.5). The layers in this model each have a constant velocity with increasing values of 1.7, 2.2, and 3.0 km/s. The salt is also homogeneous, with a higher velocity than the surrounding layers (4.5 km/s). While most of the salt is contained within a tall, cylindrical structure, there is also a thin, horizontal component representing a feeder stock on one side.

To consider the influence of acquisition geometry on imaging near and beneath the salt structure in the model, we consider three very different types of acquisition. The first geometry corresponds to a simple marine experiment with a single towed cable (Figure 4.6). The total configuration includes 75 parallel lines, with source and receiver in-line spacing of 50 m and cross-line spacing of 150 m. The cable is 3 km long, with 60 receivers to record each shot. The nearest offset receiver is located 50 m

from the source. All of the source positions are located in a rectangular area above the salt dome, while receiver positions naturally extend outside this region since the cable always trails the boat.

The geometry of the area occupied by all stations was designed to provide a similar aperture and total number of source-receiver pairs as used in the second geometry, a land acquisition pattern based on a field experiment used for imaging a salt structure in the Gulf of Mexico region (Constance et al., 1999). This survey geometry included sources located along circles with radii increasing in increments of 330 m, while receivers were located along radially directed lines every  $10^\circ$ . At larger distances from the center of the experiment, additional receiver lines were inserted to maintain uniform data coverage. The shorter infill receiver lines were inserted halfway between the complete lines, creating a spacing of  $5^\circ$  at large offsets. Source spacing was 50 m along the circles, and in-line receiver spacing was also 50 m. During field data recording, receivers within a  $90^\circ$  wedge were active when sources located in the center  $10^\circ$  arc of the wedge were detonated. This geometry is displayed in Figure 4.7, which shows a decimated set of source positions for clarity.

The circular/radial land geometry and the simple marine geometry present a rather extreme contrast in designs. To better compare competing land geometries, we also examined an orthogonal land survey geometry that matched the aperture and total number of source-receiver pair criteria of the two previously mentioned geometries. It consisted of 34 source and 34 receiver lines, orthogonal to each other. The source and receiver line intervals were 360 m, with sources and receivers spaced every 60 m (Figure 4.8). All sources were recorded into receiver patches that were 108 receivers by 16 receiver lines. The aspect ratio of each receiver patch was 84%, providing a wide azimuth distribution.

Figure 4.9 shows an example of the receiver patches and associated sources for both the circular/radial and orthogonal geometries. It can be readily seen that for the circular/radial geometry, the number of active receivers per shot remains constant throughout the survey. In the orthogonal geometry however, it is in the designer's discretion whether or not to roll-on/off stations or lines. Roll-on and roll-off refers to the procedure of recording with partial patches when shot points get near the edges of a 3-D survey (Cordson et al., 2000).

Geometries similar to the circular/radial one have been suggested as effective designs for high-quality imaging near salt structures since they have a symmetry that

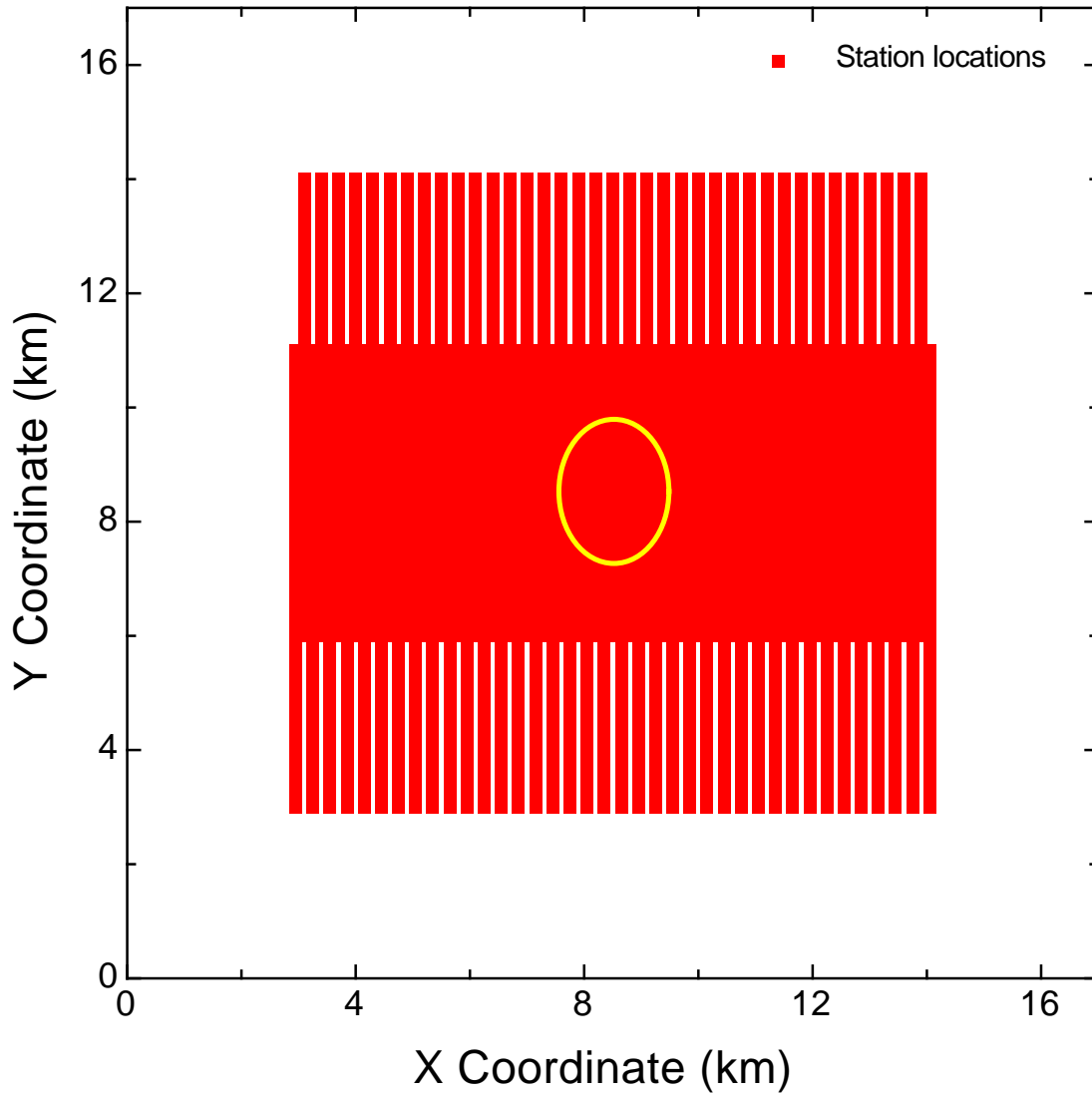


Fig. 4.6. Marine acquisition geometry used to compute image resolution for the salt dome model (Figure 4.5). The elliptical outline in the center indicates the approximate location and shape of the salt structure beneath the experiment. The station locations correspond to a single-cable geometry, and the hypothetical ship sailed in the vertical direction, firing in the region from  $y = 6$  to  $y = 11$  km. Since the receivers are towed behind the boat, there are stations outside of the total source region.

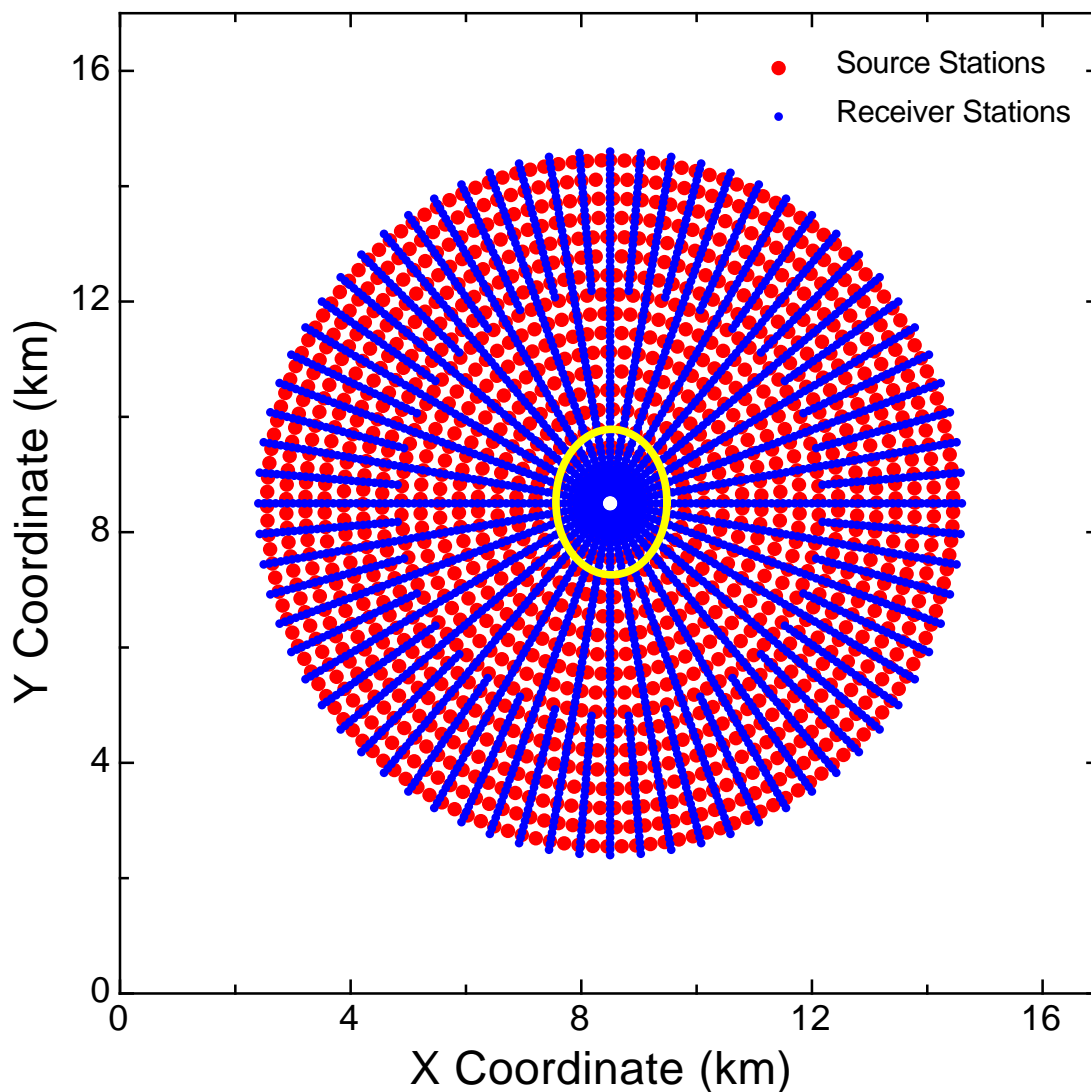


Fig. 4.7. Circular/radial land acquisition geometry used to compute image resolution for the salt dome model (Figure 4.5). The elliptical outline in the center indicates the approximate location and shape of the salt structure beneath the experiment. This geometry is based on that used in the field experiment described by Constance et al. (1999). This figure shows only the locations of every fifth source along the concentric source line circles for clarity.

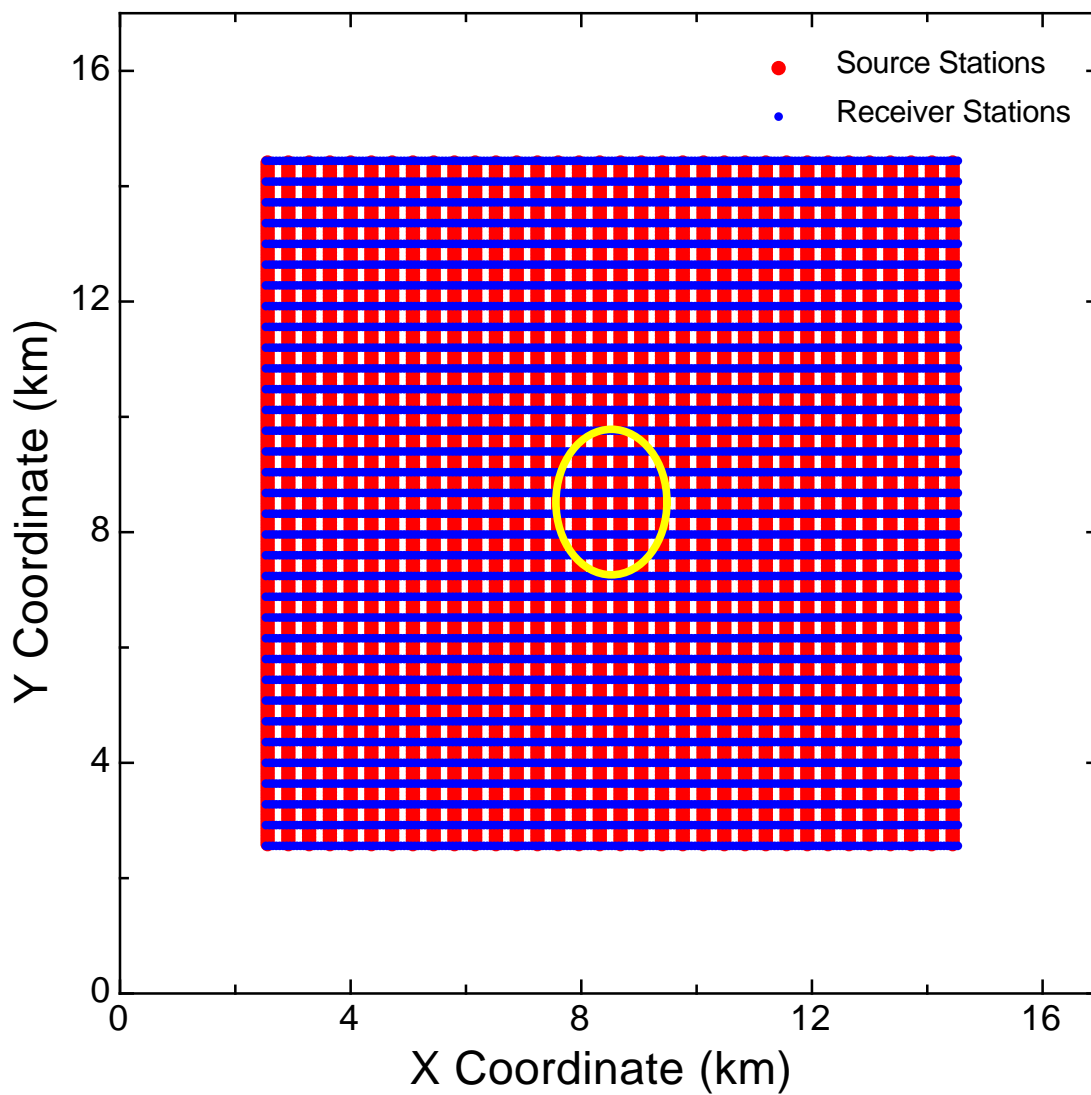


Fig. 4.8. Orthogonal land acquisition geometry used to compute image resolution for the salt dome model (Figure 4.5). The elliptical outline in the center indicates the approximate location and shape of the salt structure beneath the experiment.

is similar to that of the hypothetical structure and should provide fairly uniform illumination (e.g., Maldonado and Hussein, 1994). Our calculations therefore test whether this suggestion is correct and also show the potential differences in image quality between the very different land and marine geometries.

### 4.3.1 Subsalt imaging

The first imaging target we consider is a horizon at a depth of 4 km, which is several hundred meters beneath the salt dome (Figure 4.5). Specifically, we consider a grid of image points extending over a rectangular region from  $x = 7$  to  $x = 10$  and from  $y = 6$  to  $y = 11$ , with point scatterers located at intervals of 0.3 km. A perfect image would produce a single pixel at each location, but the acquisition geometries and band-limited data instead yield smeared images with different degrees of resolution (Figures 4.10 and 4.11). An additional limiting factor in this case is the salt body itself which, for certain imaging points, generates large shadow zones obstructing seismic energy to be recorded. Figure 4.12 displays the screening effect of the salt body on the seismic energy realized by seismic rays starting at an imaging point deeper than the base of the salt. Figure 4.13 depicts the wavenumber vector plots for an imaging point centered beneath the salt, with coordinates  $(x, y, z) = (8.5, 8.5, 4.0)$ . The wavenumber vectors were generated by considering only the near offsets of the marine geometry (solid red square of Figure 4.6). Their distribution in the  $k_x$ - $k_y$  plane reflects the geometry with which they were acquired whereas the asymmetric coverage of the  $k_x$ - $k_z$  is the result of the asymmetry of the salt (feeder stock towards the negative  $k_x$ -axis). A comparison of the wavenumber vector distribution in the  $k_x$ - $k_y$  plane for the same imaging point but different acquisition geometries, is shown in Figure 4.14. The near-offset wavenumber vectors of the marine geometry (red) are repeated from Figure 4.13. The wider array aperture of the far offsets of the marine geometry compared to the near offsets is manifested in a better coverage of the wavenumber vector space (teal vectors). The even better coverage of the same space by the near-offset wavenumber vectors (blue vectors) of the circular/radial geometry is the result of a more even distribution of source and receiver stations although the areal coverage is comparable to the marine geometry's. The spatial images for this imaging point for all three cases can be seen in Figure 4.10 at  $(x, y) = (8.5, 8.5)$ .

To minimize computation time, we considered only single-offset imaging, the



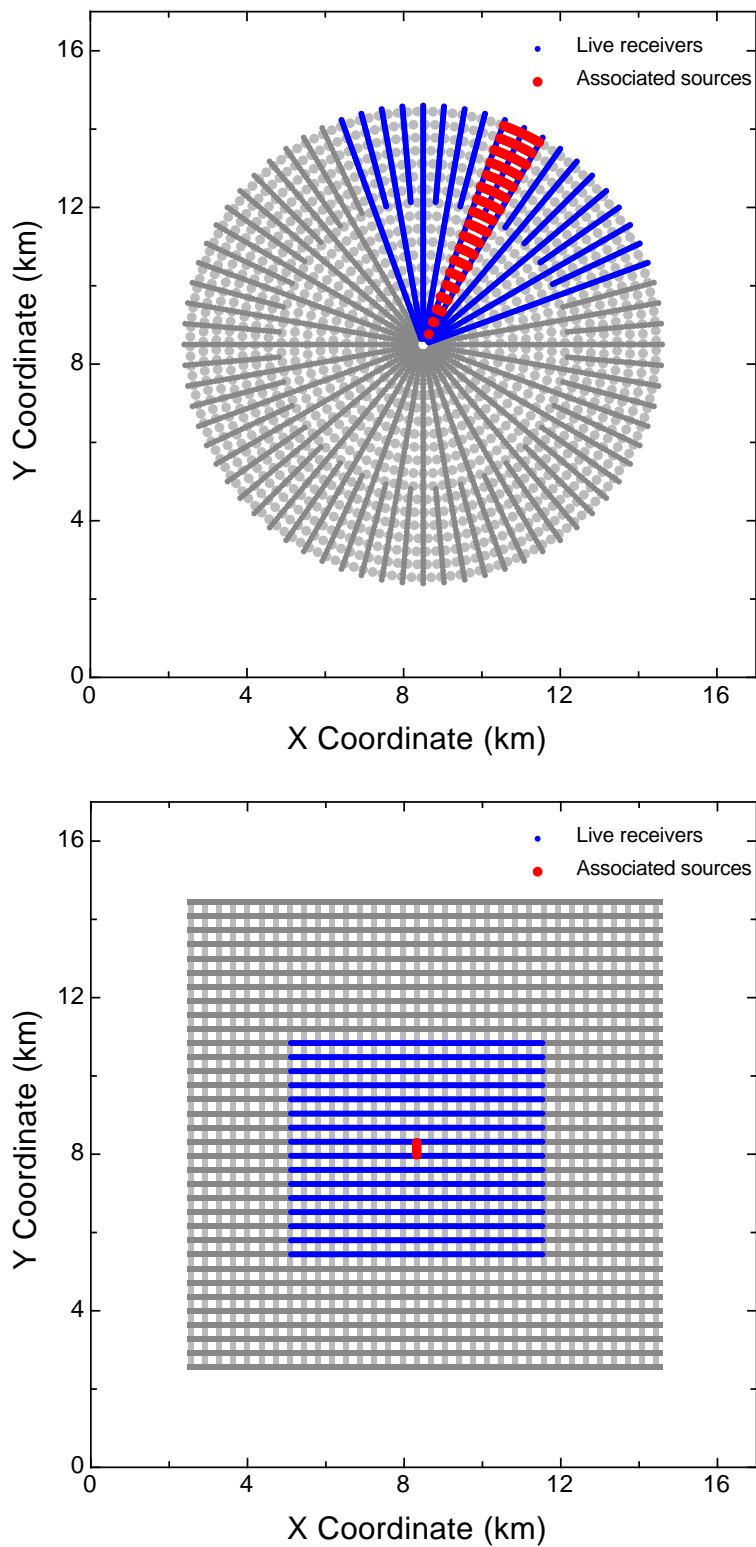


Fig. 4.9. Example of receiver patches for the circular/radial (Top) and orthogonal (Bottom) land acquisition geometries used to compute image resolution for the salt dome model (Figure 4.5). The locations of the associated sources which define these particular templates are also indicated.

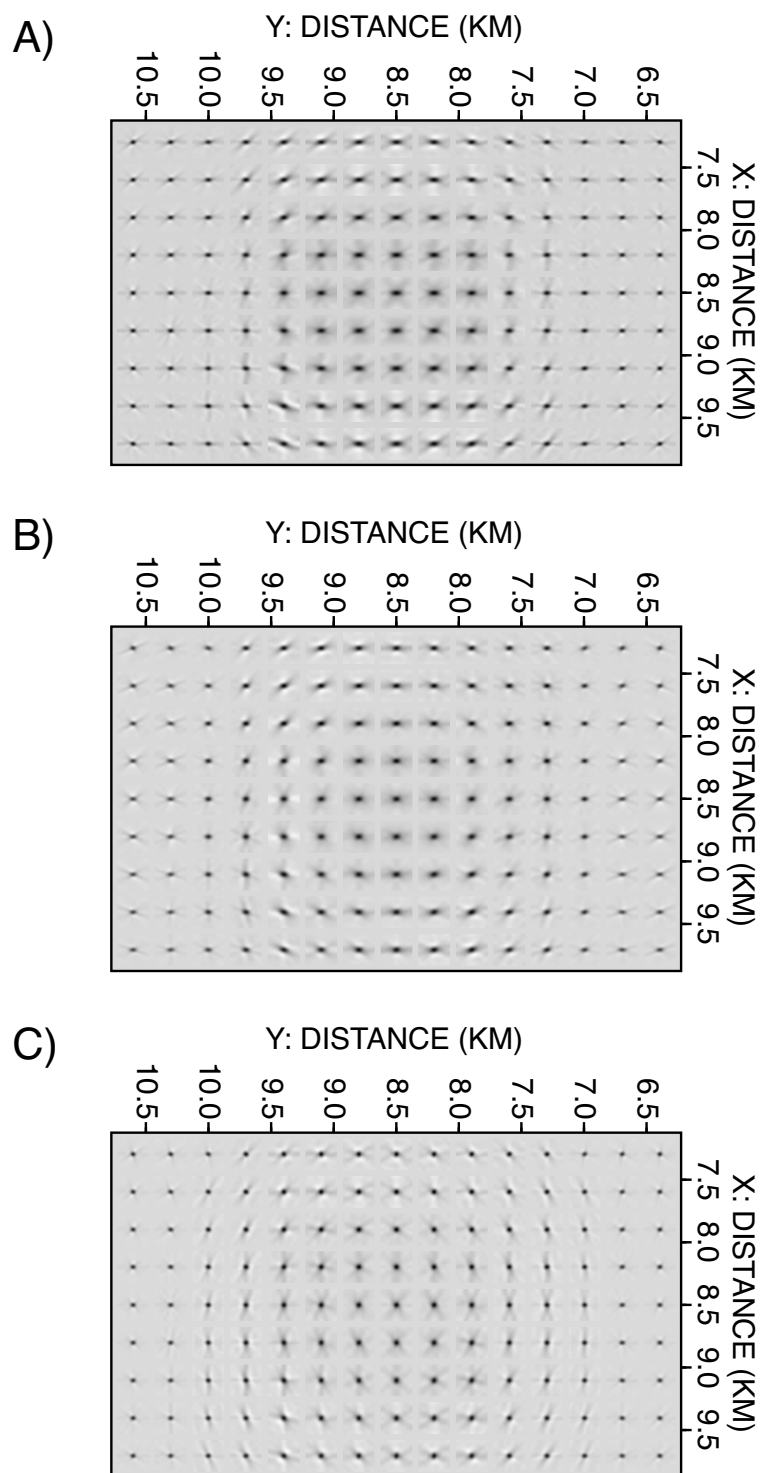


Fig. 4.10. Subsalt resolution obtained using the acquisition geometries in Figures 4.6 and 4.7. Each figure shows the point scatterer images predicted for a depth of 4 km in a region underlying the center of the salt dome. (A) Near offsets, marine acquisition geometry. (B) Far offsets, marine acquisition geometry, (C) Near offsets, circular/radial acquisition geometry.

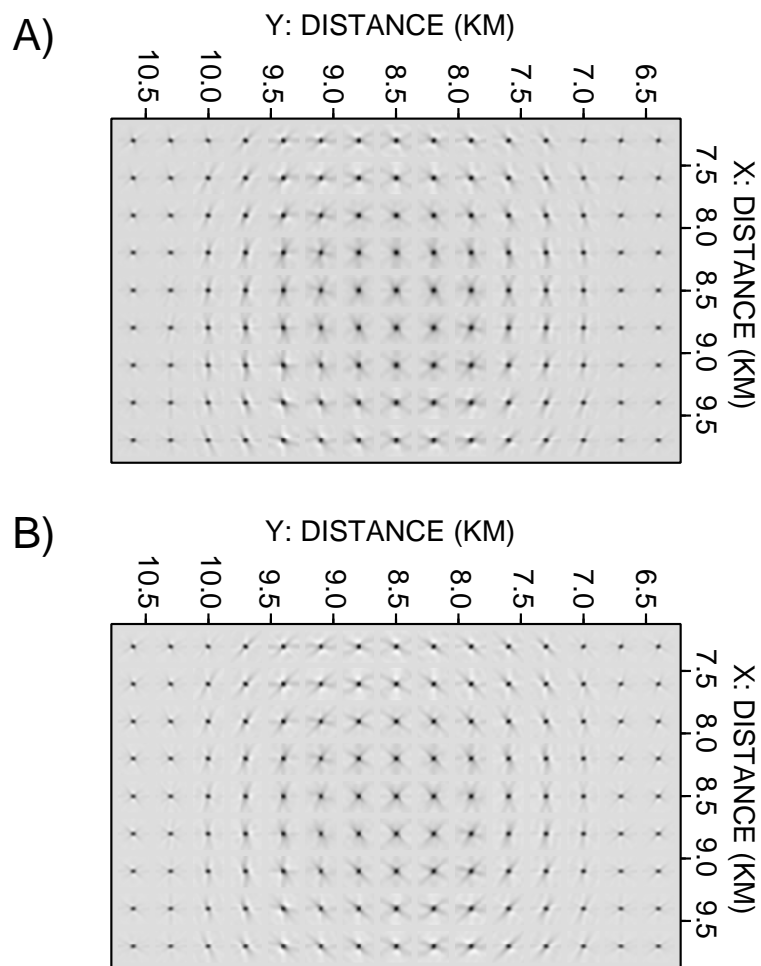


Fig. 4.11. Subsalt resolution obtained using the acquisition geometries in Figures 4.7 and 4.8. Each figure shows the point scatterer images predicted for a depth of 4 km in a region underlying the center of the salt dome. (A) Near offsets, circular/radial acquisition geometry (repeated from Figure 4.10C). (B) Near offsets, orthogonal acquisition geometry.

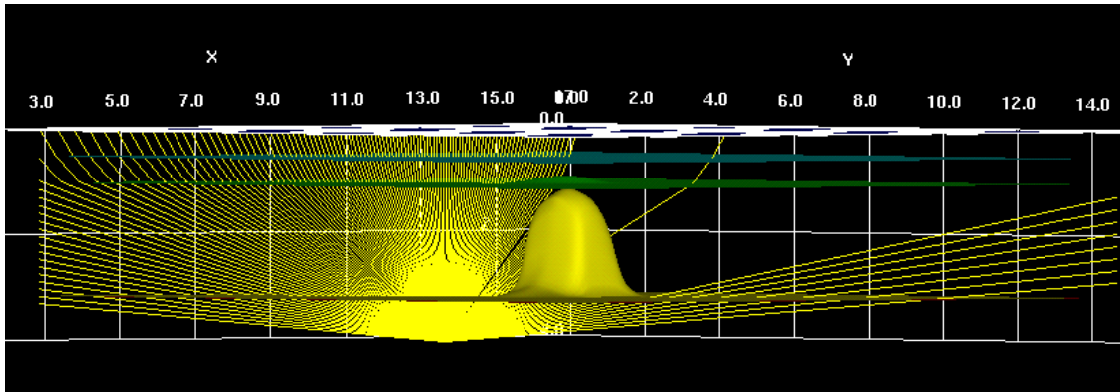


Fig. 4.12. A perspective view of the salt model at a  $45^\circ$  angle with respect to the  $x$ - and  $y$ -axes and the screening effect of the salt body on the seismic rays emanating from a subsalt imaging point. For clarity, rays only of a single azimuth value are displayed.

near- and far-offset source-receiver pairs for the marine geometry (50 and 3000 m, respectively), and the nearest-offset receiver for the land geometries (ranging from 0 to 275 m in the case of the circular/radial survey and from 42 to 153 m in the orthogonal one). In the circular/radial land geometry, it is straightforward to find the receiver that is closest to each source station, but there is no obvious way to choose the far-offset trace given the large wedges of receivers that are active for each source event. Although it would be possible to arbitrarily select the largest possible source-receiver distance, in practice there would be no logical pattern to the azimuthal offset of the receiver in this case, so we did not attempt to follow this approach. The same is also true for the orthogonal survey where the maximum offset is almost constant but the choice of azimuth is ambiguous.

These single-offset results let us make some important conclusions. First, unlike the idealized homogeneous model with the simple acquisition geometry considered above (Figures 4.1, 4.3, 4.4), the marine experiment provides better resolution for the far offsets, not the near offsets. This result can be explained by considering the ray geometries (Figure 4.15). The large-offset rays correspond to a much larger aperture at the subsalt image points, and the aperture in the wavenumber domain is also larger, producing better spatial resolution. The difference between the far- and near-offset ray (and consequently wavenumber vector) apertures is attributed to the ray bending caused by the large velocity contrast at the salt interface with the surrounding layer

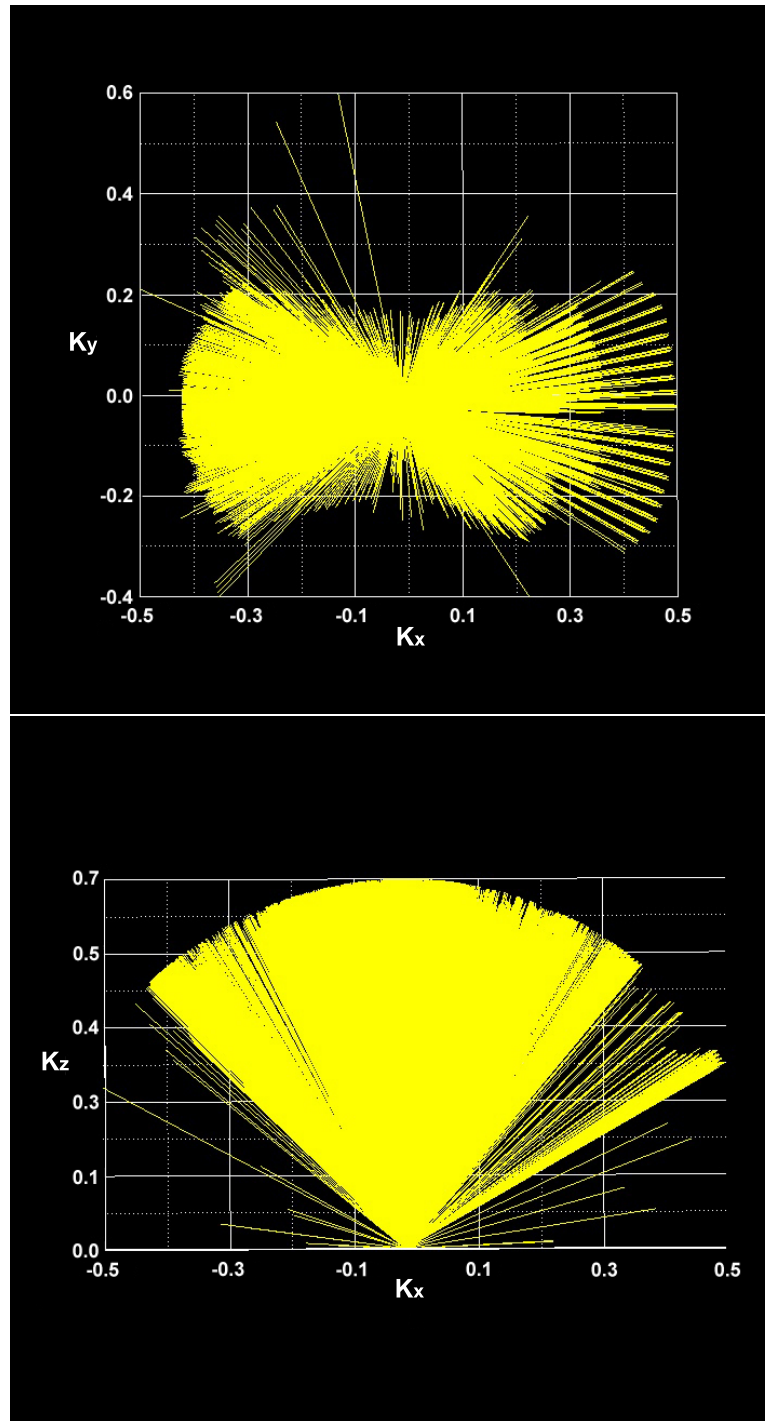


Fig. 4.13. Wavenumber vector plots for an imaging point centered beneath the salt diapir. Only the near offsets of the marine geometry were considered. The coverage of the wavenumber vector  $k_x$ - $k_y$  plane (top) reflects the acquisition geometry. The asymmetric coverage of the  $k_x$ - $k_z$  plane (bottom) is due to the feeder stock towards the negative  $k_x$ -axis.

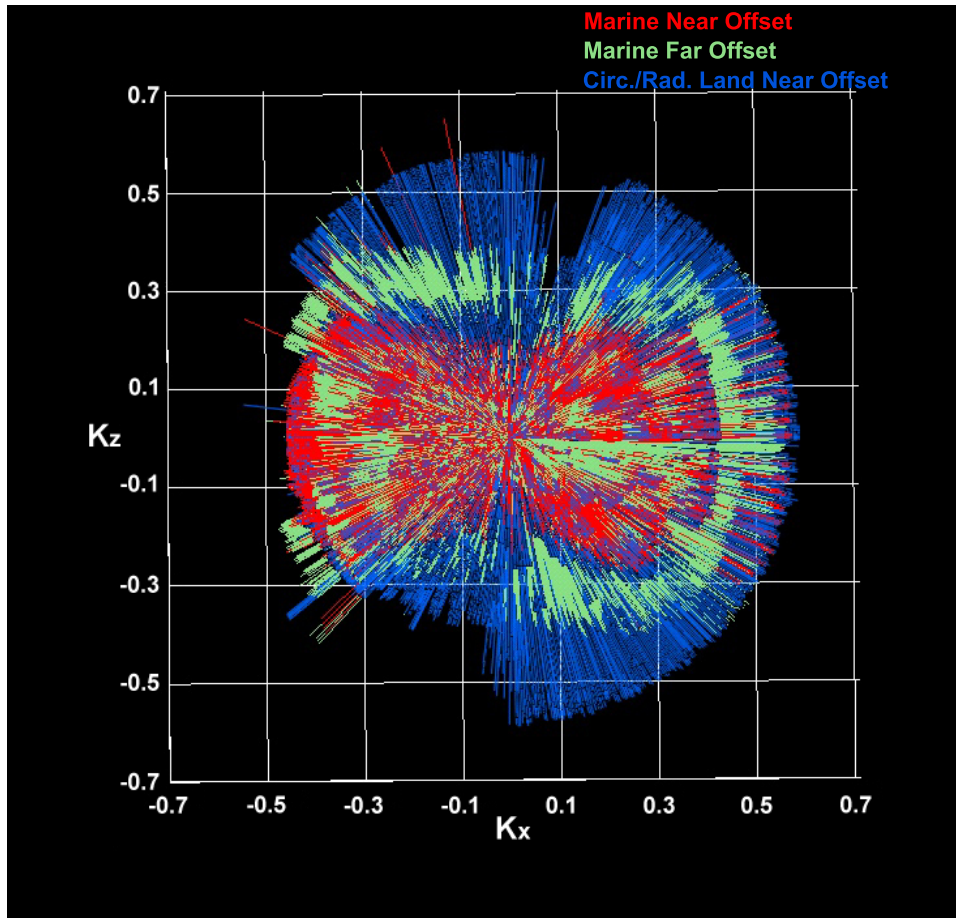


Fig. 4.14. Wavenumber vector plot for an imaging point centered beneath the salt diapir. The near offsets of the circular/radial land acquisition geometry provide a better coverage of the wavenumber vector  $k_x$ - $k_y$  plane compared to either the near- or the far-offsets of the marine geometry.

and the difference in array aperture. This array aperture difference between the near- and far-offsets is an inherent property of the towed cable marine geometry.

The single-offset calculations also allow some predictions of resolution in multi-offset migration. Since a final image produced from all offsets would essentially be an average of the results of single-offset imaging, we can infer that the result for the marine acquisition geometry would lie somewhere between the results for the images shown in Figures 4.10A and 4.10B. Since the near-offset land geometries clearly produce better resolution (Figure 4.11), we can infer that they should in fact provide a better resolved subsalt image even if resolution is somewhat worse at larger offsets. This suggests that the more complicated land geometries can be very effective.

To answer the question “which geometry provides the best resolution and to what degree?”, we resort to the image resolution measures of relative standard deviation and smoothness. Figures 4.16 and 4.17 map respectively the relative standard deviation and smoothness measures for the subsalt region. The figures show the same behavior for both measures. The two land geometries produce very similar results whereas the marine geometry consistently yields higher values (lower resolution) for both measures. It also becomes clear that the less resolved points form an annular region that lies directly beneath the perimeter of the salt body. Close examination of both ray and wavenumber vector apertures showed that they become smaller for points within this region. This is consistent with ray-tracing modeling results reported by Muerdter and Ratcliff (2001a), Muerdter et al. (2001) and Muerdter and Ratcliff (2001b) where the effects of different salt edges on the illumination of subsalt targets are extensively examined and is evident (to a different degree) in many subsalt depth migrated sections (e.g., Roden and Fagin, 2001; Roden and Gochioco, 2002).

The percent error in the relative standard deviation and smoothness measures of the marine and circular/radial geometries with respect to the orthogonal are shown in Figures 4.18 and 4.19 respectively. Once again, the similarities between the two land geometries are expressed in the small errors compared to those between the orthogonal and the marine geometries. Overall, one could state that the orthogonal geometry provides the best resolution for subsalt targets followed very closely by the circular/radial geometry. The marine geometry fails to resolve the subsalt target as well as the other two.

Another very important point is that a conventional illumination study simply counting the number of rays striking different regions of the subsalt image surface

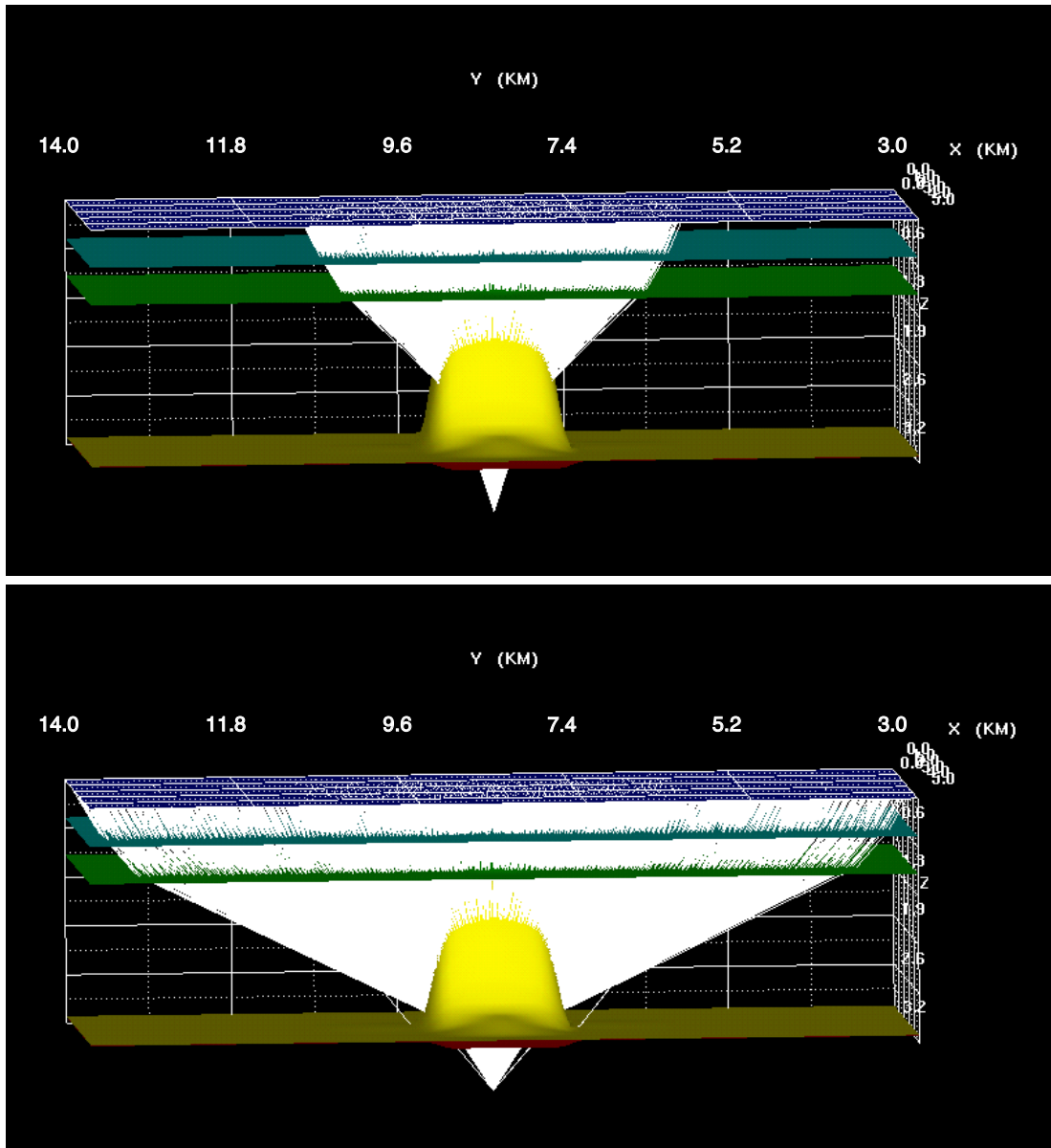


Fig. 4.15. Comparison of ray paths for near- (above) and far-offset (below) pairs in the marine acquisition geometry (Figure 4.6) for the point beneath the center of the salt dome. Only rays for several lines near the center of the survey are displayed for clarity. The predicted image resolution is better for the far-offset geometry because the wavenumber vectors include a larger aperture, as shown by the correspondingly larger ray aperture at the image point.



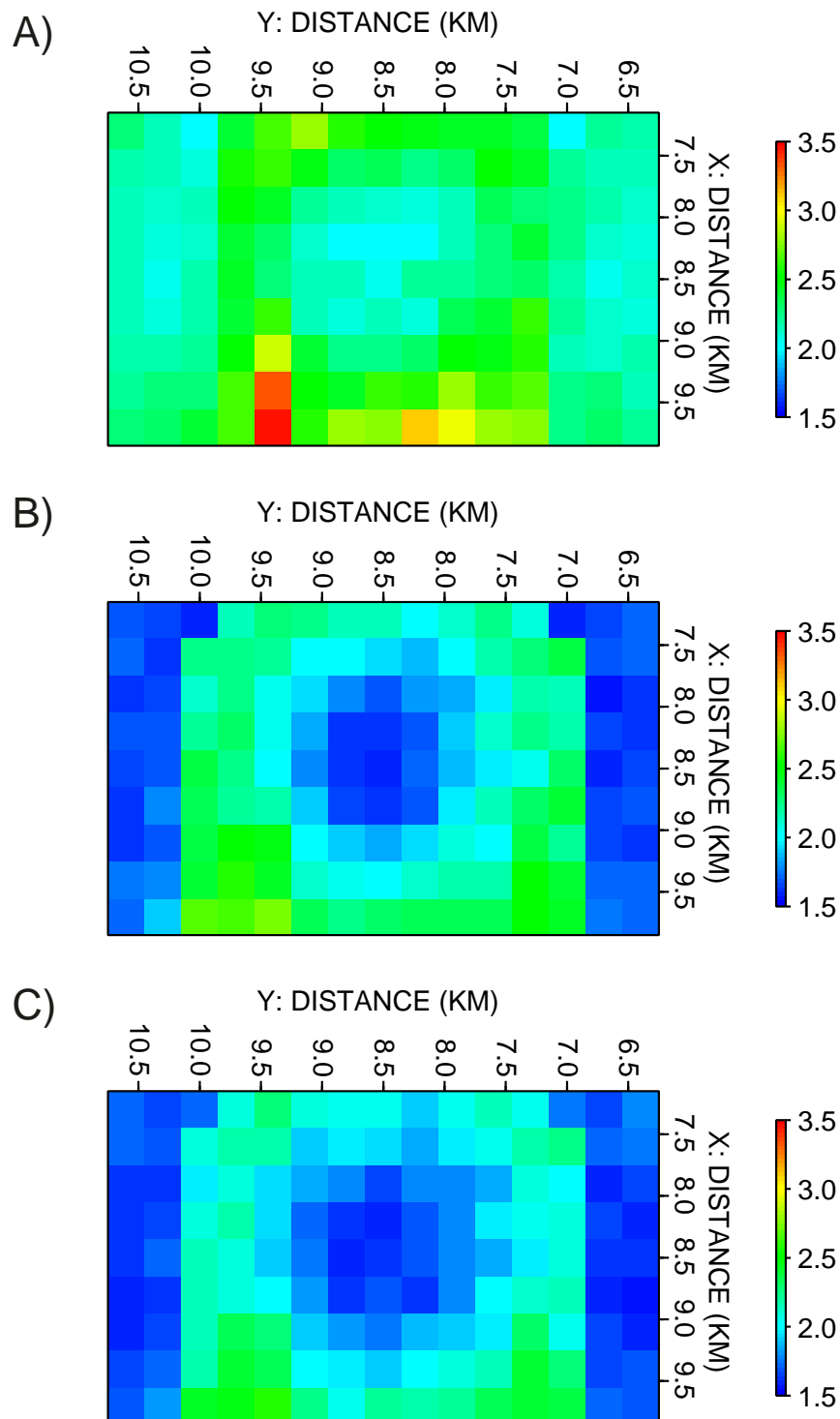


Fig. 4.16. Subsalt resolution obtained using the acquisition geometries in Figures 4.6, 4.7 and 4.8. Each figure shows the relative standard deviation measure predicted for a depth of 4 km in a region underlying the center of the salt dome. (A) Near offsets, marine acquisition geometry. (B) Near offsets, circular/radial acquisition geometry, (C) Near offsets, orthogonal acquisition geometry.

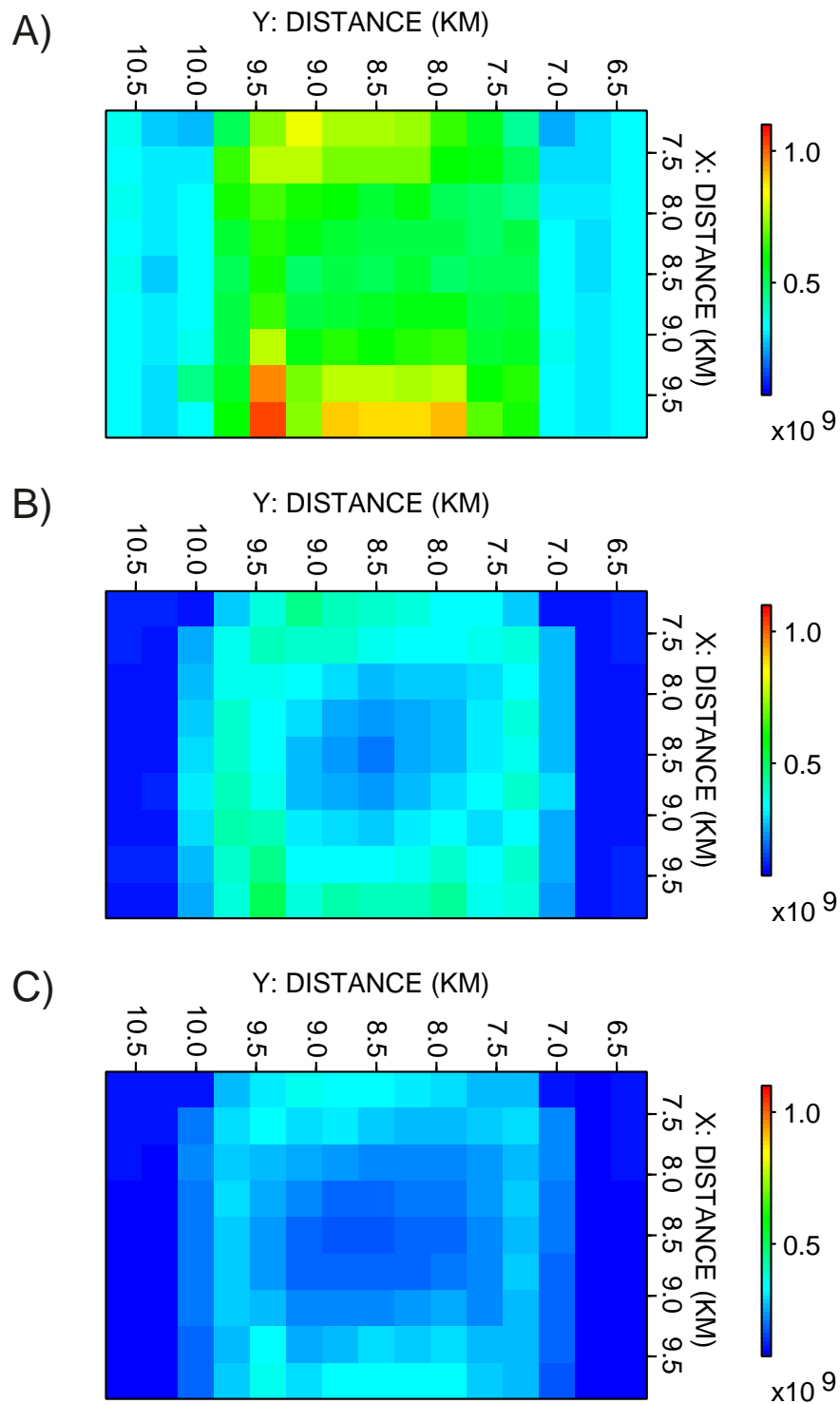


Fig. 4.17. Subsalt resolution obtained using the acquisition geometries in Figures 4.6, 4.7 and 4.8. Each figure shows the smoothness measure predicted for a depth of 4 km in a region underlying the center of the salt dome. (A) Near offsets, marine acquisition geometry. (B) Near offsets, circular/radial acquisition geometry, (C) Near offsets, orthogonal acquisition geometry.

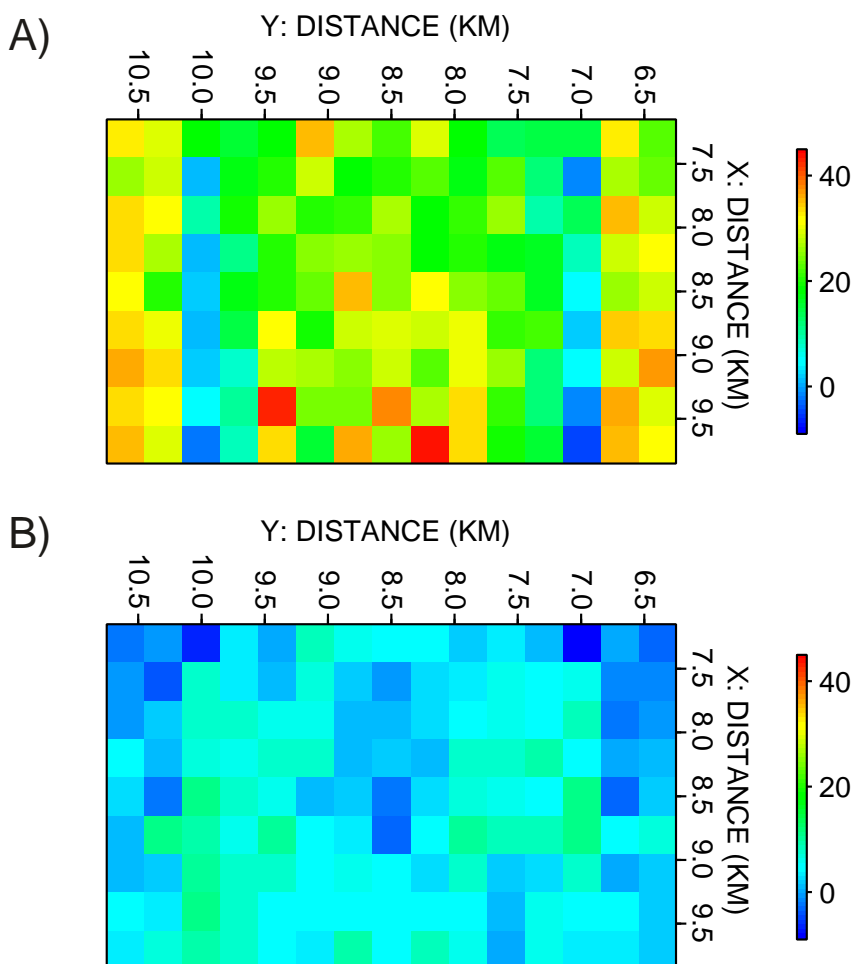


Fig. 4.18. Subsalt resolution obtained using the acquisition geometries in Figures 4.6, 4.7 and 4.8. Each figure shows the error (in %) between the relative standard deviation measures predicted by the orthogonal acquisition survey and (A) the marine acquisition geometry or (B) the circular/radial acquisition geometry. (For plots of the relative standard deviation measures, see Figure 4.16.)

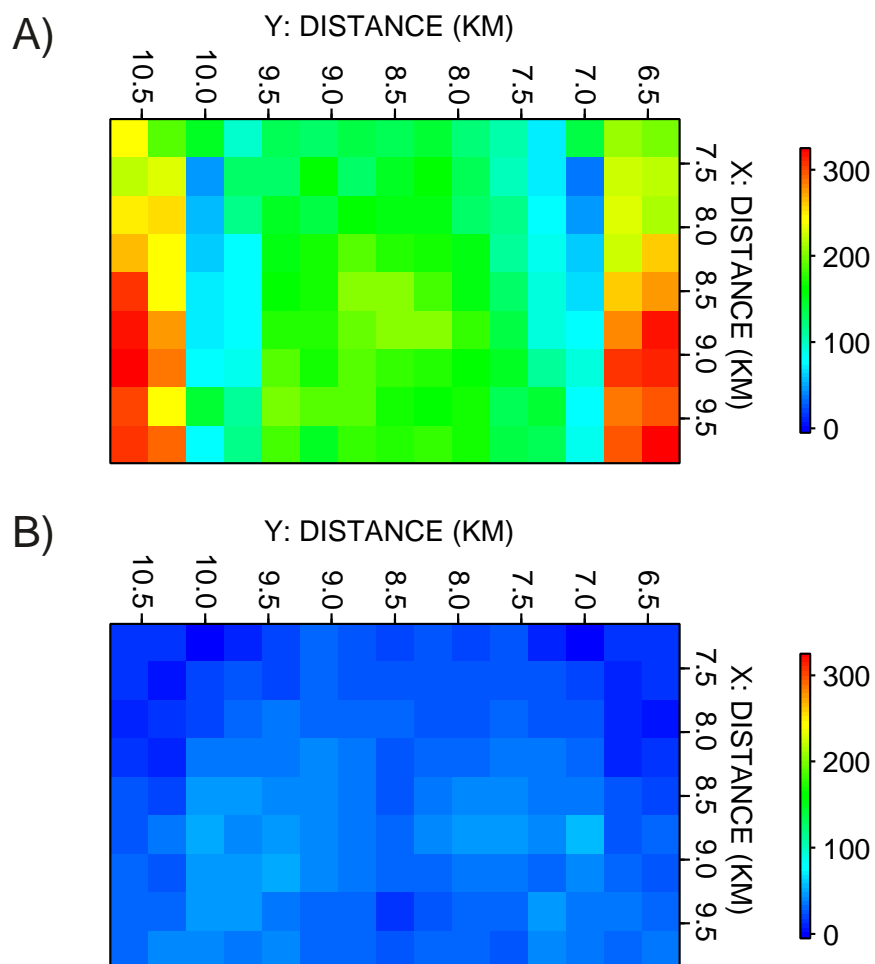


Fig. 4.19. Subsalt resolution obtained using the acquisition geometries in Figures 4.6, 4.7 and 4.8. Each figure shows the error (in %) between the smoothness measures predicted by the orthogonal acquisition survey and (A) the marine acquisition geometry or (B) the circular/radial acquisition geometry. (For plots of the smoothness measures, see Figure 4.17.)

indicates that the total number of rays does not decrease significantly in the low-resolution central region of the surface. Instead, the loss in resolution occurs because ray bending causes the largest fraction of the rays to travel in near-vertical directions. Since the corresponding wavenumber vectors will be oriented in the vertical direction as well, the horizontal resolution decreases significantly. Similar results were also reported by Muerdter et al. (2001) who show that the number of hits per common reflection point (CRP) under a salt slab are as high as away from it. Even more interesting is the case of a peak projecting from a salt slab imaged by a typical single-cable marine survey where the reported number of hits per CRP bin (60) underneath the peak is 3 times higher compared to distant areas (fold of 20) where there is no effect of the peak. This demonstrates why simple illumination analyses based solely on CRP fold count may be misleading in terms of understanding spatial resolution, although they may provide other insights.

#### **4.3.2 Subsalt imaging: Improving a problematic marine acquisition by incorporating VSP data**

In this section, we consider a narrow marine acquisition geometry (Figure 4.20) and test whether adding simultaneous acquisition of VSP data will help to improve the quality of images produced by the experiment. The survey geometry is similar to the typical single towed cable marine experiment considered in the previous section but consists of only 31 parallel lines (instead of 75) and the crossline spacing is 100 m (instead of 150 m).

A systematic test of spatial resolution at a depth of 4 km shows that the salt dome structure produces a distinct degradation in resolution (Figure 4.21). This test or blur pattern clearly indicates that a point scatterer centered beneath the dome will be approximately twice as large as one located along the edges of the test region, about 200 m long instead of 100 m. For all locations, resolution is best in the  $y$ -direction, since the seismic lines are extended in this direction, and the wavenumber vectors will have larger  $y$ -components than  $x$ -components. The near-offset image is somewhat worse than that produced using all offsets, while the far-offset image clearly resolves the points better than either of the other two scenarios, especially in the  $y$ -direction confirming the statement that considering all offsets will produce an image of “average” resolution compared to single-offset images. The far-offset acquisition

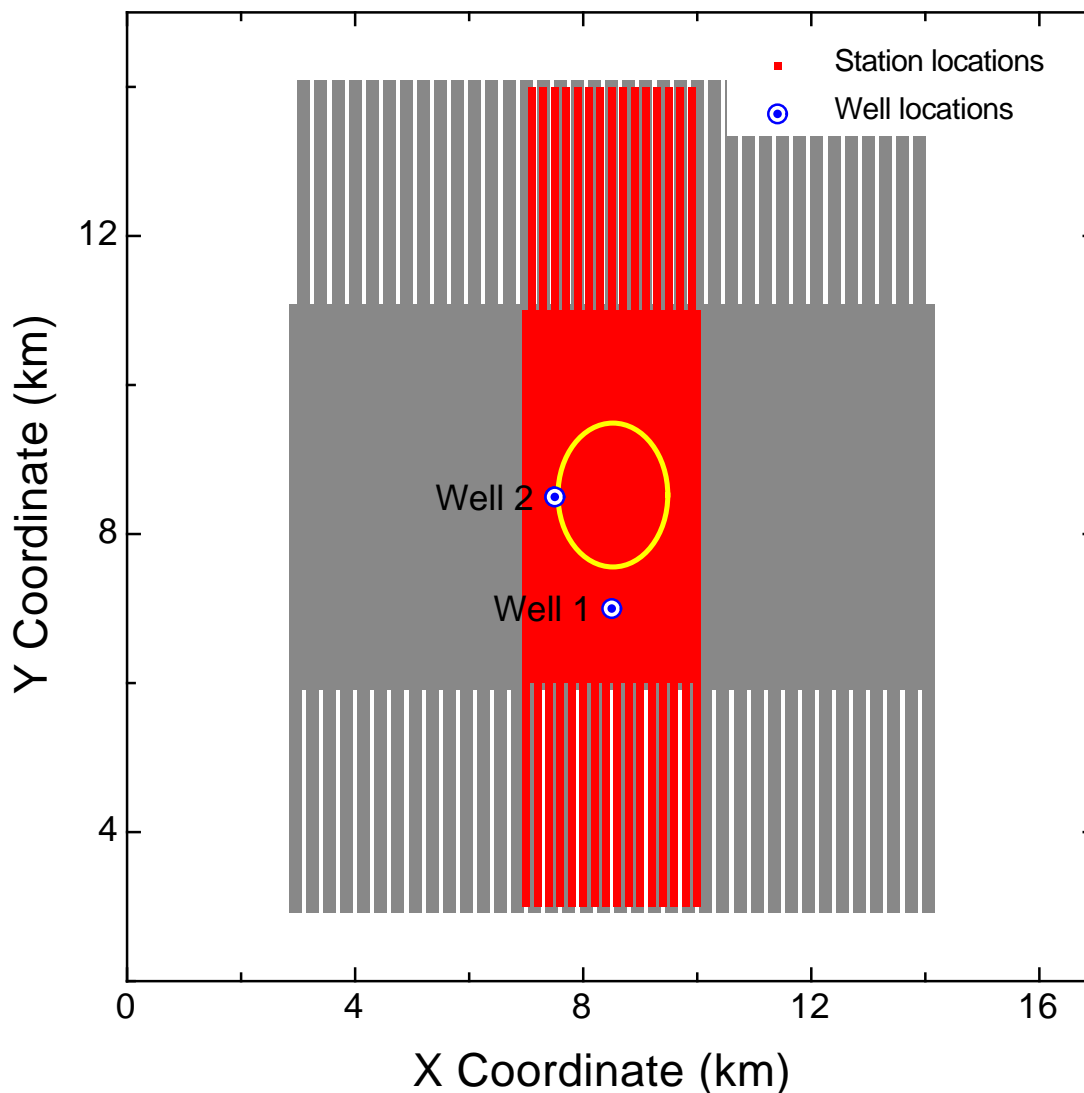


Fig. 4.20. Narrow marine acquisition geometry used to compute image resolution for the salt dome model (Figure 4.5). The elliptical outline in the center indicates the approximate location and shape of the salt structure beneath the experiment. The station locations correspond to a single-cable geometry, and the hypothetical ship sailed in the vertical direction, firing in the region from  $y = 6$  to  $y = 11$  km. Since the receivers are towed behind the boat, there are stations outside of the total source region. For comparison, the extended marine acquisition geometry of Figure 4.6 is also shown (shaded stations).

naturally utilizes rays propagating closer to horizontal, and it therefore will provide better image resolution than the previous case. This effect is exaggerated by the salt dome structure, which causes rays to arrive at angles even closer to vertical for near-offsets.

While illumination studies that count ray reflection point “fold” on subsurface targets do yield some important constraints on image quality, this is an excellent example of a case where this fold measure will be potentially misleading (Tzimeas and Gibson, Jr., 1999). Though that number would be relatively high for both near- and far-offset gathers using this Earth model, the blur patterns clearly show that inferiority of the near-offset images. The ray aperture, or wavenumber resolution vectors, must also be considered to gain a thorough understanding of the resolution that can be obtained in the final seismic image.

The blur pattern (and image resolution measures) results allow some analysis of the image quality that can be expected from the particular marine acquisition geometry that we have specified. Comparing these patterns (Figures 4.21A and 4.21B) to the equivalent ones obtained using the wide marine geometry (Figures 4.10A and 4.10B), it becomes apparent that the resolving power of the narrow marine geometry has been considerably decreased. It is therefore a direct consequence for someone to raise the question: “How could we improve on the resolution without being obliged to acquire surface data anew?”. To illustrate the application of these approaches to survey design, we consider the possibility of simultaneous VSP, or vertical cable, data acquisition. The acquisition geometry display includes two VSP borehole locations (Figure 4.20). Rather than considering the entire image surface shown in the previous examples, we will concentrate the analysis of the value of VSP data on a single image point centered beneath the salt dome, a logical approach since this is where resolution is worst with the surface-only acquisition. This also allows us to consider cross sections of the predicted image along all three coordinates planes. As a reference, we first display these three images for the marine surface array only, using the near-offset source/receiver pairs (Figure 4.22A). Since the seismic lines extend along the  $y$ -axis direction, the resolution of the point scatterer in the  $y$ - $z$  plane is fairly good, but the lack of rays along the  $x$ -axis significantly reduce resolution in the  $x$ - $z$  plane. Unlike the horizontal resolution shown in the blur pattern (Figure 4.21), the vertical resolution is fairly good. This corresponds to the ray geometries, which are mostly vertical.

Before considering the combination of VSP and surface data, we show the pre-

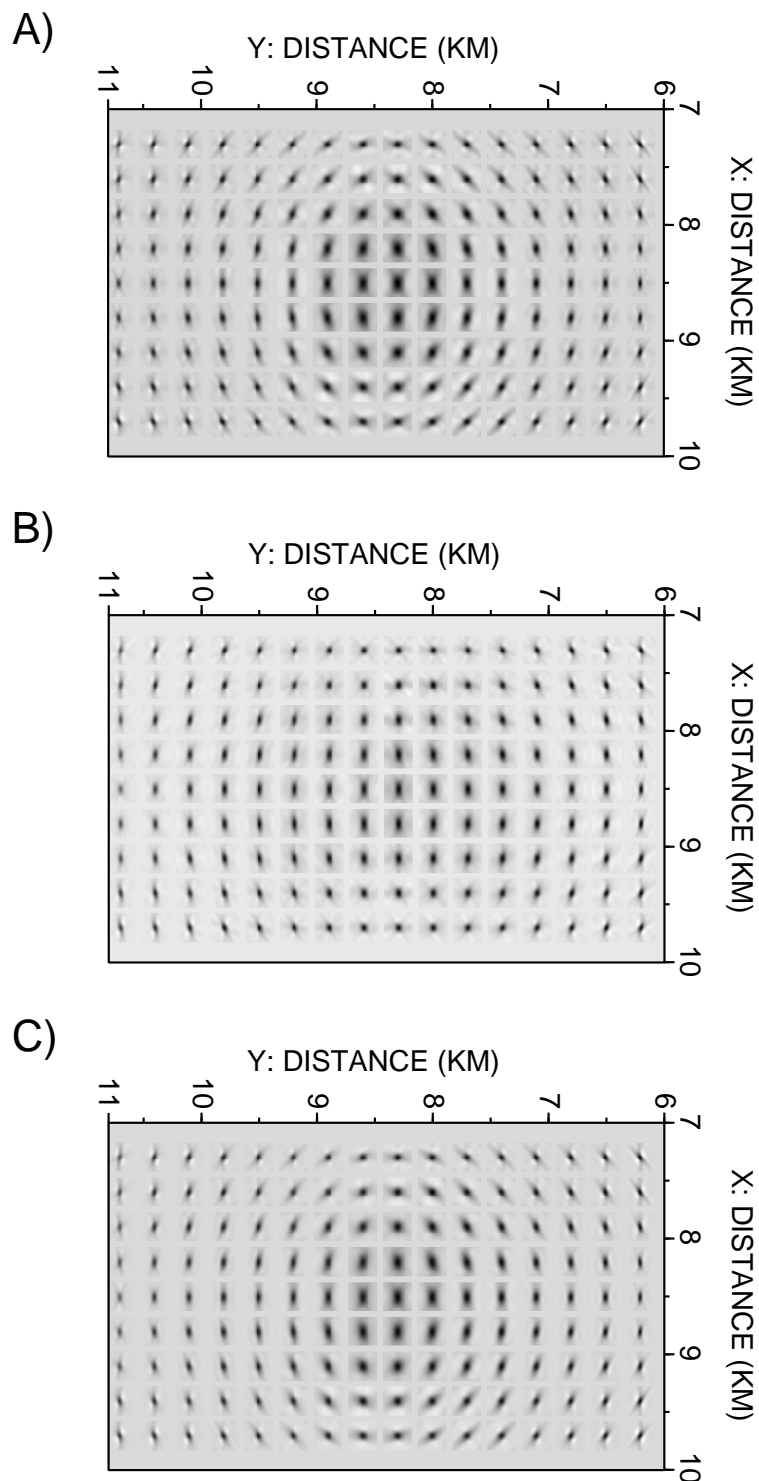


Fig. 4.21. Subsalt resolution obtained using the acquisition geometry in Figure 4.20. Each figure shows the point scatterer images predicted for a depth of 4 km in a region underlying the center of the salt dome. (A) Near offsets. (B) Far offsets. (C) All offsets.



dicted spatial resolution of the image point using only the first VSP receiver located at  $(x, y, z) = (8.5, 7.0, 2.4)$ . There is obviously only one receiver ray contributing to the calculation of wavenumber vectors in this case, and it will be contained in the  $y$ - $z$  plane. Likewise, even though the source rays will have some component in the  $x$ - $z$  plane, the majority will have much more significant lengths in the  $y$ - $z$  plane. Hence, the image point is fairly well resolved in the  $y$ - $z$  plane, but is poorly resolved in the  $x$ - $y$  and  $x$ - $z$  planes (Figure 4.22B).

On the other hand, the predicted spatial resolution of the image point using only the first receiver of the second well located at  $(x, y, z) = (7.5, 8.5, 2.4)$  reveals a different behavior. Once again, there is only one receiver ray contributing to the calculation of wavenumber vectors but now it is contained in the  $x$ - $z$  plane. The wavenumber vector distribution in this case is such that allows the image point to be better resolved in all directions (compare Figure 4.22C to 4.22B).

Combining the surface with each and both the VSP data produces an image with gradually improving resolution in all three planes (Figure 4.23). This confirms the value of adding the additional receivers to the data acquisition scheme, and shows that the larger ray aperture at the image point that is created by the deeper receivers will improve the image. There are, of course, some practical difficulties to overcome in combining such data. The VSP data will likely have higher frequency than the surface data, which would improve the image greatly. The higher frequency content of the VSP data was ignored in the preceding analysis. However, this difference in frequency content may make simultaneous imaging difficult, and imaging using VSP alone will only provide satisfactory results relatively close to the borehole. Nonetheless, the results that we show here show how to apply resolution calculations for quantitative applications in survey design.

### 4.3.3 Salt flank imaging: Surface data

The resolution predictions clearly indicate that the land geometries will yield better resolved images than the marine geometry for the subsalt target. However, the more important exploration target might be in formations adjacent to the salt dome. Figure 4.24 shows the locations of four such test locations – A, B, C, and D – all at a depth of 2 km.

Unlike the subsalt case, the near-offset imaging with the marine acquisition ge-

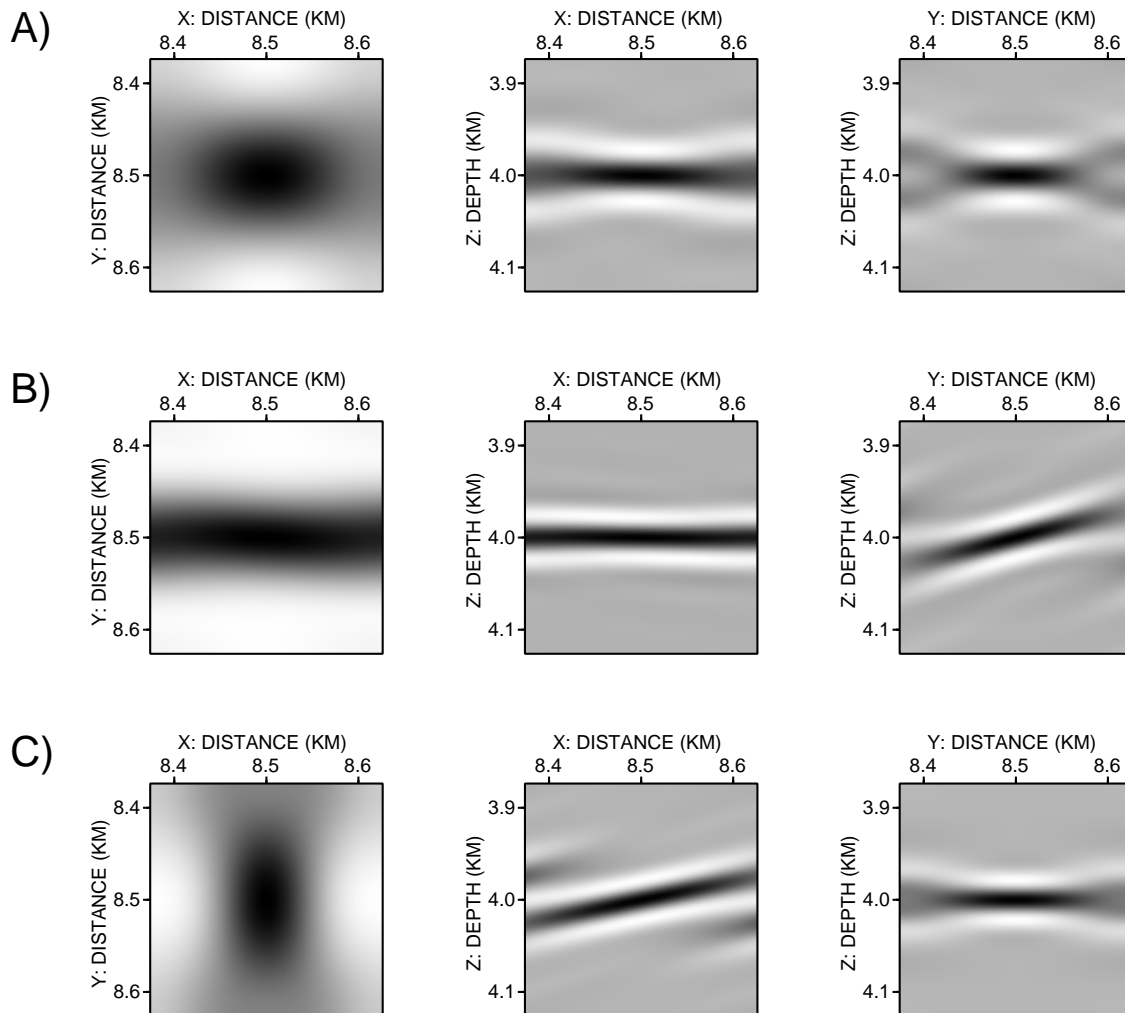


Fig. 4.22. Subsalt resolution obtained using the acquisition geometry in Figure 4.20. Each figure shows the spatial images predicted for a scatterer located directly beneath the center of the salt at the depth of 4 km. (A) Near offsets, marine acquisition geometry. (B) VSP1 (receiver in well 1). (C) VSP2 (receiver in well 2).

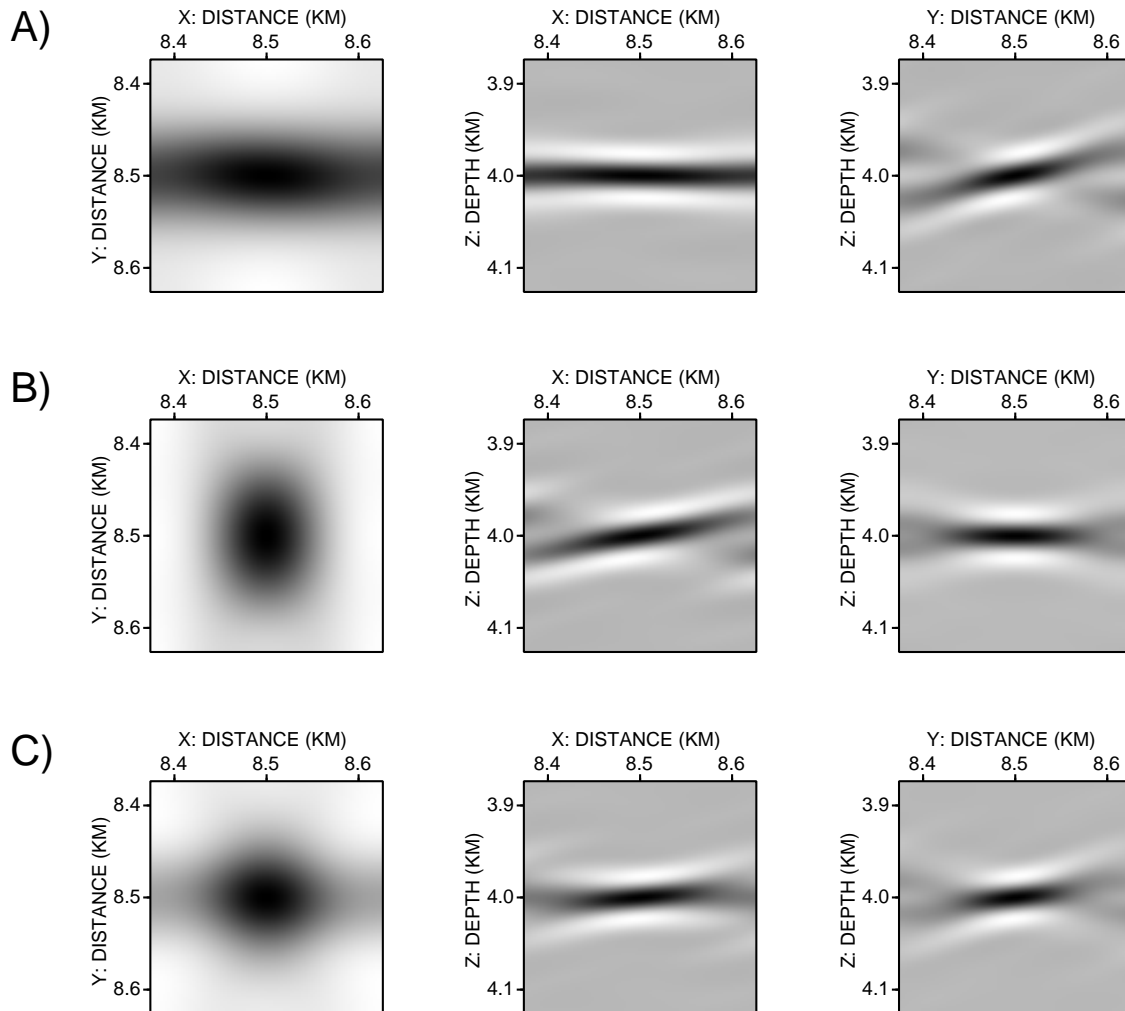


Fig. 4.23. Subsalt resolution obtained using the acquisition geometry in Figure 4.20. Each figure shows the spatial images predicted for a scatterer located directly beneath the center of the salt at the depth of 4 km. (A) Combined near offsets and VSP1. (B) Combined near offsets and VSP2. (C) Combined near offsets and both VSP's.

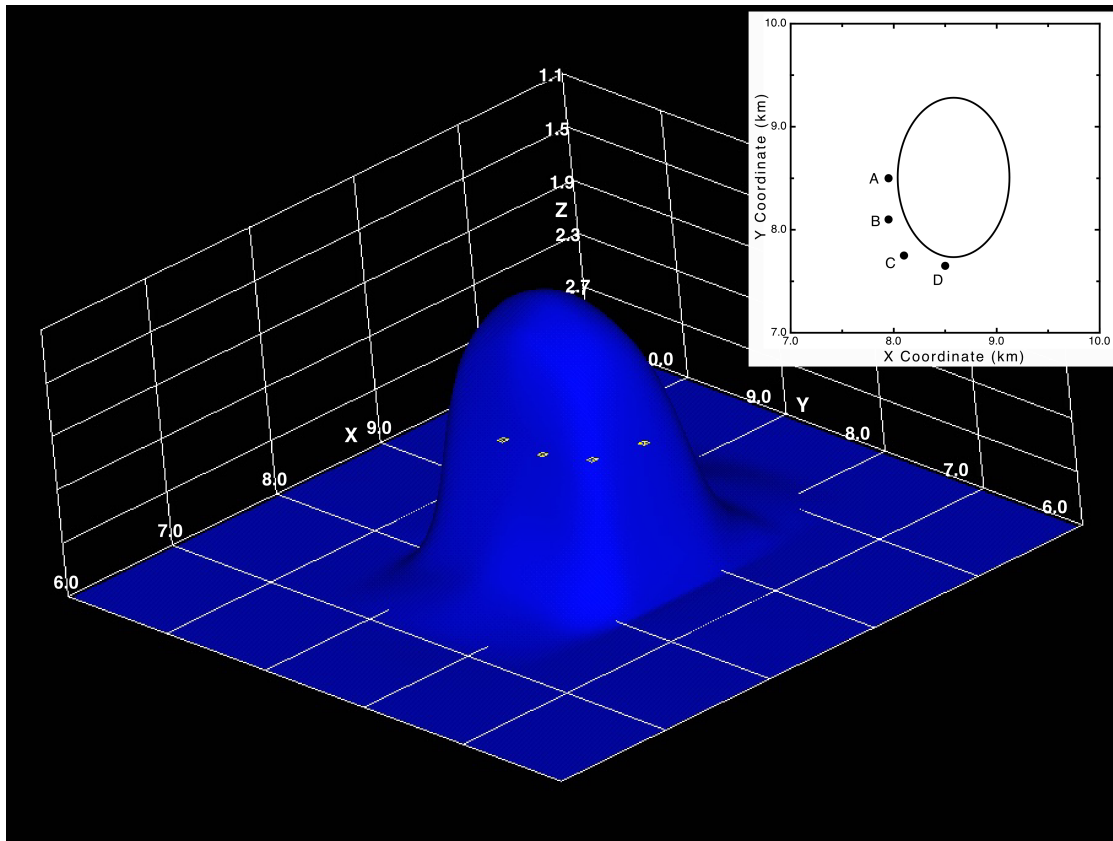


Fig. 4.24. Locations of four points located near the salt dome at a depth of 2 km. The points are used to assess salt flank imaging potential of the marine and two land acquisition geometries (Figures 4.6, 4.7 and 4.8).

ometry yields somewhat better resolution than the far-offset images, though the differences are not as obvious (Figures 4.25 and 4.26). On the other hand, the resolution of these point scatterers with the land geometries is just as good as that obtained with the near-offset marine configuration for points C and D (Figures 4.27C and 4.27D and Figures 4.28C and 4.28D) but is noticeably better for points A and B (Figures 4.27A and 4.27B and Figures 4.28A and 4.28B). The land survey designs more consistently and uniformly illuminate the image points. The important point is that both the circular and the orthogonal land geometries result in a fairly smooth azimuthal angle distribution of rays arriving at image points. On the other hand, the marine geometry, with its single towed cable, has an inferior coverage of ray directions (involving a larger concentration of raypaths near the  $y$ - $z$  plane), producing worse spatial resolution. Therefore, the land geometries should provide a more robust and reliable imaging result for this salt structure.

#### 4.3.4 Resolution and S/N ratio

All of the results presented to this point assume perfect imaging and a well-constrained model. At least some of these constraints, however, can be relaxed in a realistic manner. For example, by computing ray amplitudes as well as ray trajectories, the influence of decreasing S/N ratios can be considered. If  $A_0$  is the largest diffracted amplitude recorded by the experiment, then we can consider it to be a measure of the signal strength and define the noise level relative to it. For an S/N ratio of 4, for example, we assume that a ray with an amplitude less than  $A_0/4$  will not contribute to the imaging and we neglect its contribution to the spatial resolution calculation. This approach is not strictly correct, since the stacking procedure will tend to suppress noise during imaging, and signals weaker than noise might still contribute effectively to the final image. Because of the simplicity of this approach, we also do not attempt to account for any  $\sqrt{n}$  factor resulting from summing over traces. However, this does allow a simple way of quantitatively filtering out weaker contributions to the image and allows a straightforward analysis of how decreasing S/N ratios might reduce spatial resolution.

Application of this procedure to the salt flank image point A illustrates such a degradation in image quality (Figure 4.29). As the S/N ratio decreases from  $\infty$  to four, the images lose resolution, especially for the far-offset marine geometry at the

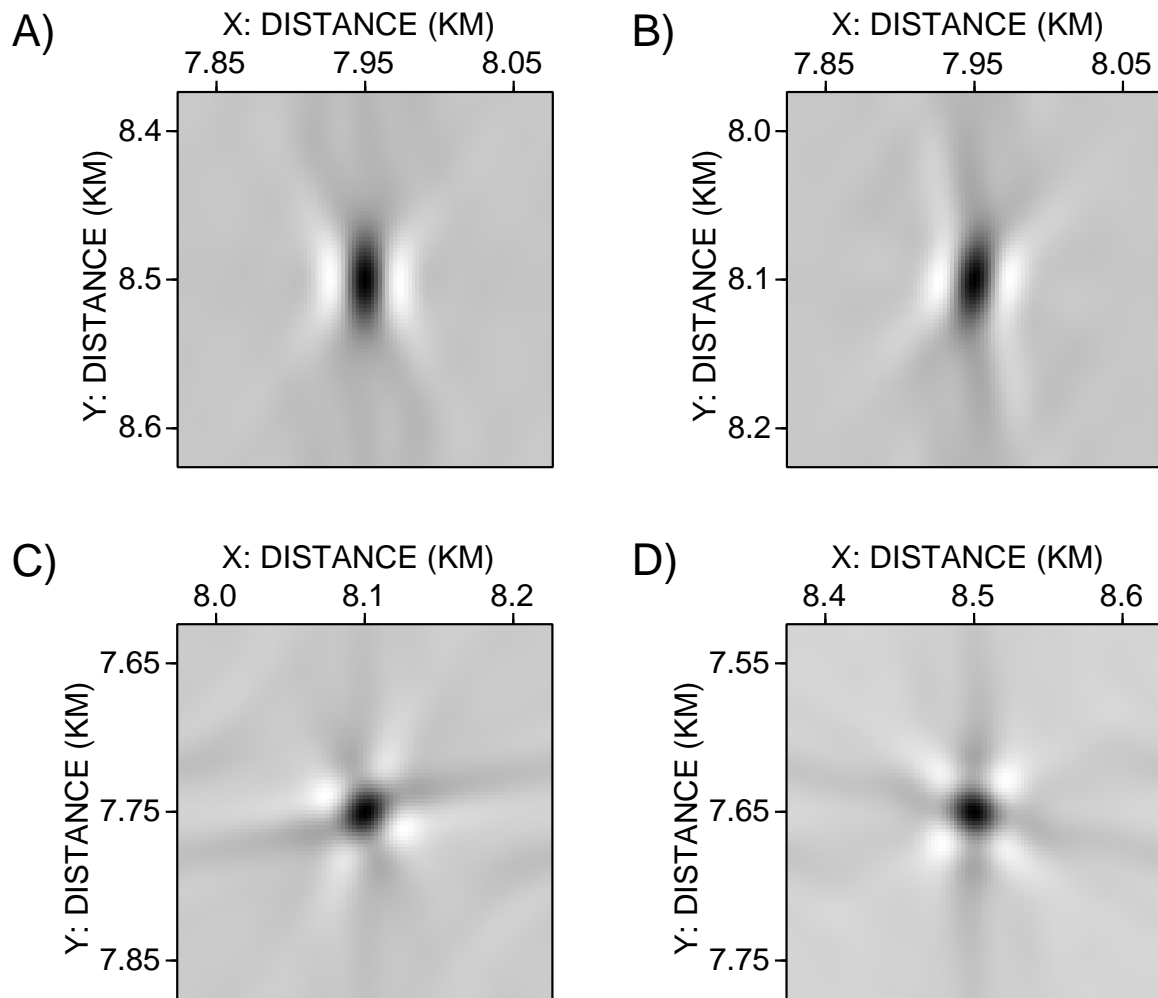


Fig. 4.25. Spatial resolution for the four salt flank image points in Figure 4.24. Only the near offsets from the marine acquisition geometry were used.

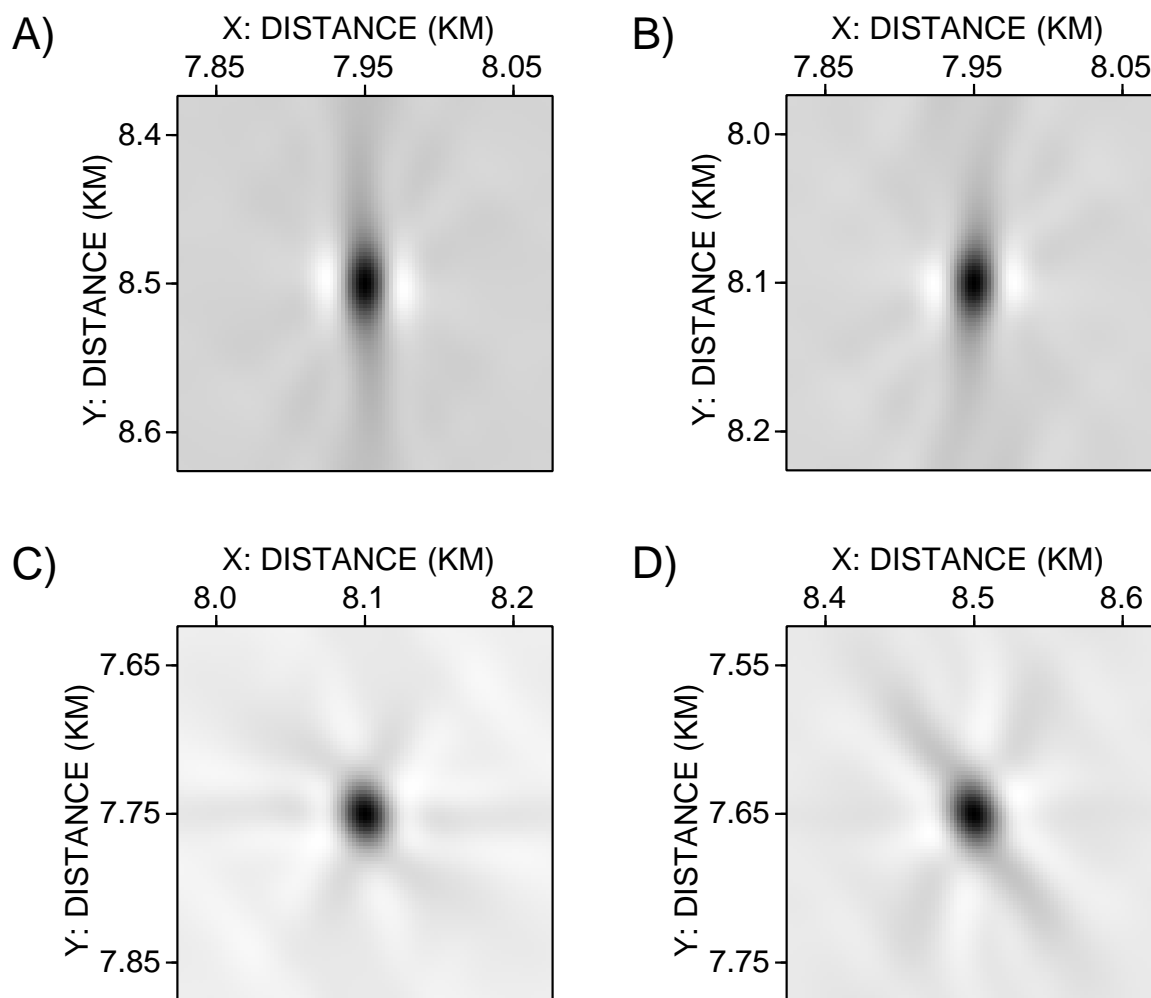


Fig. 4.26. Spatial resolution for the four salt flank image points in Figure 4.24. Only the far offsets from the marine acquisition geometry were used.

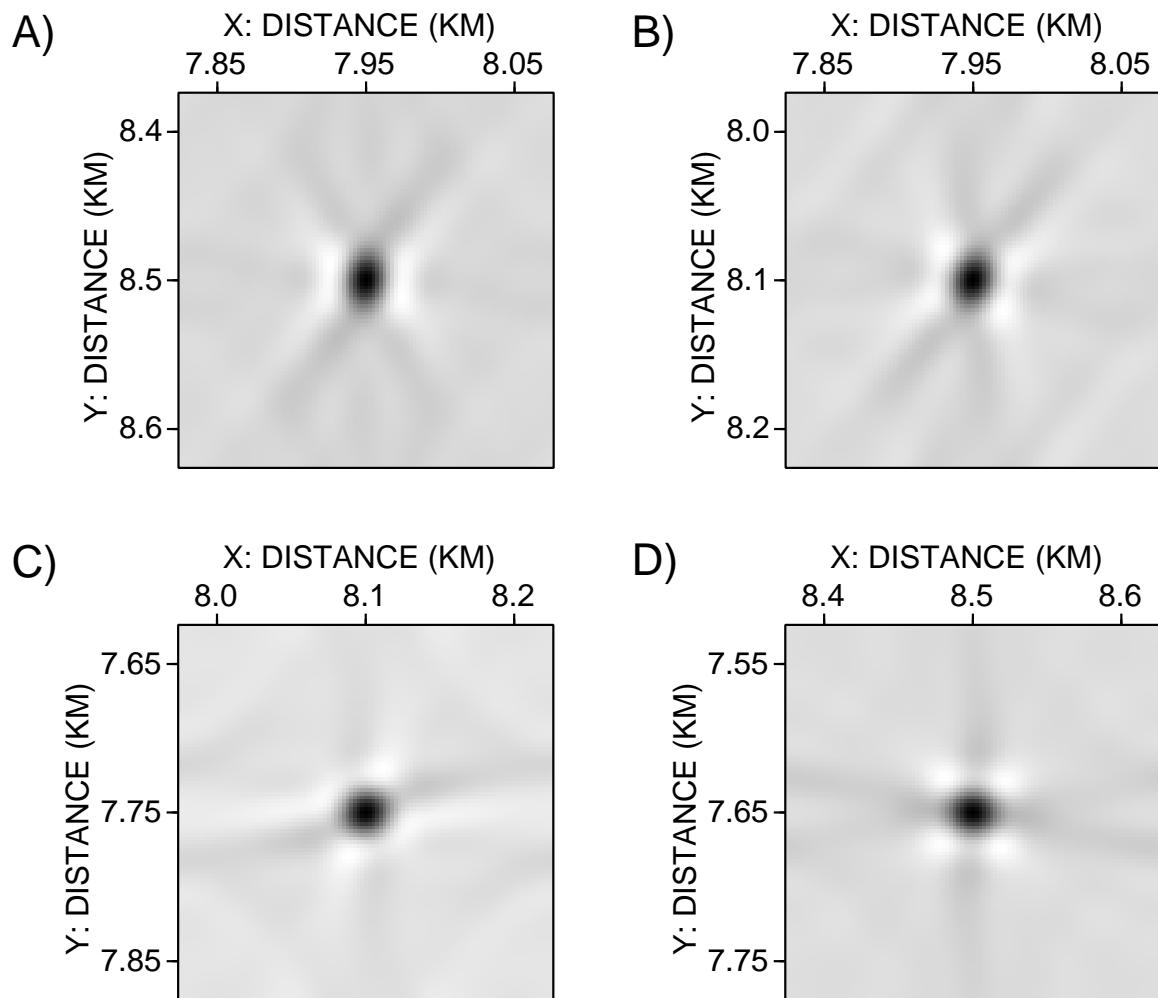


Fig. 4.27. Spatial resolution for the four salt flank image points in Figure 4.24, using the near offsets from the circular/radial land acquisition geometry.



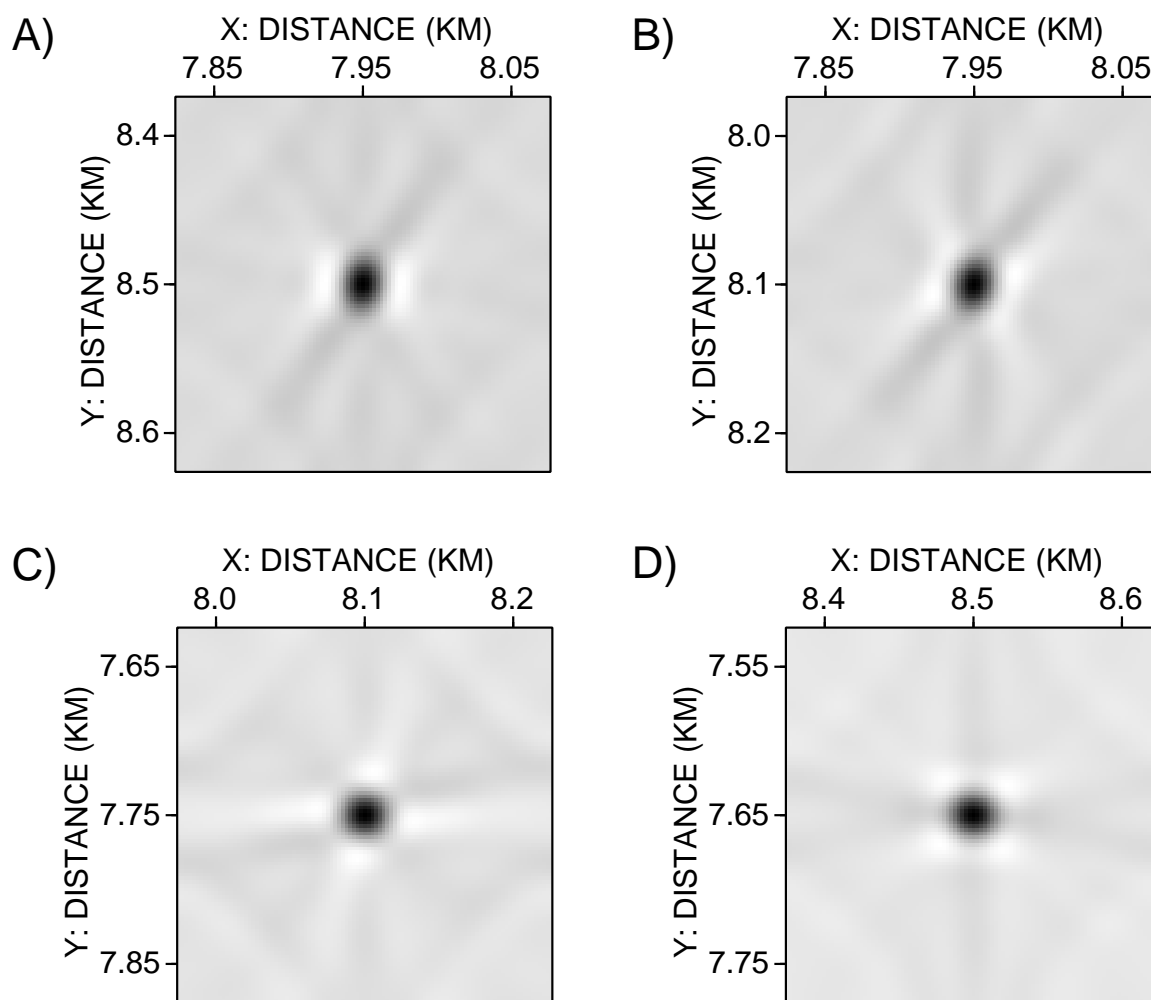


Fig. 4.28. Spatial resolution for the four salt flank image points in Figure 4.24, using the near offsets from the orthogonal land acquisition geometry.

lowest S/N ratio. In this case, it becomes clear that though the very large offsets effectively increase imaging aperture, the corresponding weak signals may be difficult to use in practical cases. Also, the land acquisition geometry is still more robust in that the image quality shows comparatively little reduction in resolution for this range of S/N ratios, though it will eventually start to decrease for lower ratio values.

#### 4.3.5 Salt flank imaging: VSP data

Since the primary goal of the field experiment was imaging structures along the flanks of the dome, we will consider this target region rather than subsalt targets for the remainder of the examples in this paper. The target point coordinates are  $(x, y, z) = (7.95, 8.5, 2.0)$  (in km). Figure 4.31 shows the spatial images of the scattering point for two signals with different frequency content. 18 sources were used for the experiment that lied on a radial line (marked “Line 135” in Figure 4.30). The proposed image resolution analysis shows the frequency dependence of the seismic resolution. In general, VSP data are of higher frequency content than surface data. Therefore, it is safe to conclude that VSP data can complement surface seismic data to improve resolution (at least, for targets close to the borehole). Consequent spatial image figures obtained by VSP geometries are generated using the higher frequency signal.

Figure 4.32 shows the spatial images of the same point obtained by using sources along two different radial source lines (marked “Line 135” and “Line 225” in Figure 4.30). A comparison of Figure 4.32A and 4.32B shows that the resolution of the scattering point is slightly different and its maximum resolution occurs at different directions. We attribute this to the fact that the wavenumber vectors are predominantly along two different directions for each line.

When we consider the imaging of the target point by all the sources along both lines (135 and 225), the resolution increases due to the fact that wavenumber vectors lying in two different directions are contributing to the imaging. However, these directions are distinct, causing the strong artifacts (edge effects) in all image planes (Figure 4.33A). Combining sources with a wide range of azimuths, all sources between lines 250 and 110, (see indicated red wedge region in Figure 4.30) to approximate the data recorded in the VSP field experiment, greatly improves the seismic image resolution (Figure 4.33B). Moreover, the amplitude of the image artifacts has been considerably decreased. Although one could argue that this is consistent with results

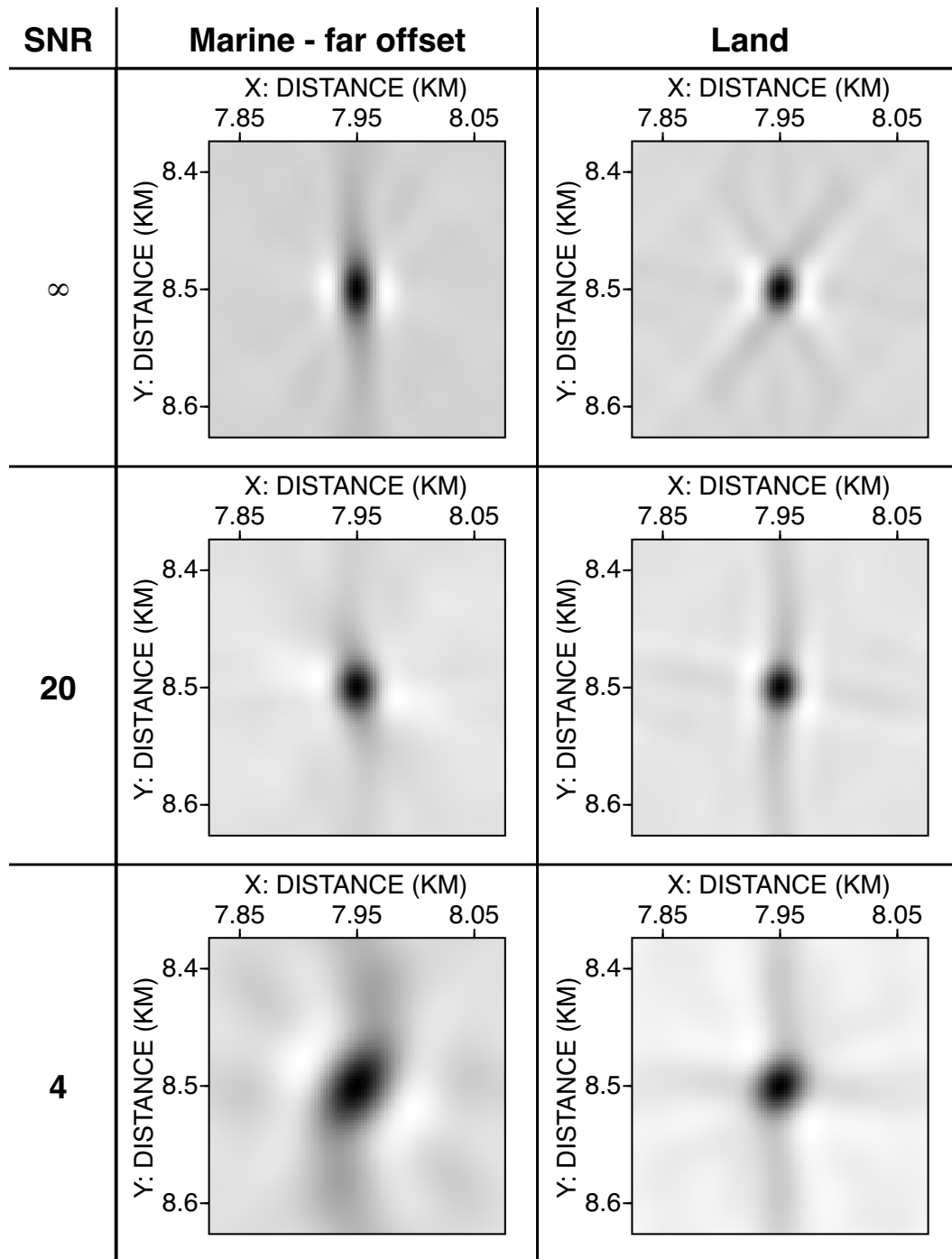


Fig. 4.29. Spatial resolution for the salt flank image point A from Figure 4.24 for different S/N ratios (SNR). The left column displays results for the far offsets from the marine geometry; the right column is for the near offsets from the circular/radial land survey. The uppermost pair of figures shows the results for perfect, noise-free data and are identical to the corresponding images in Figure 4.26 and 4.27.

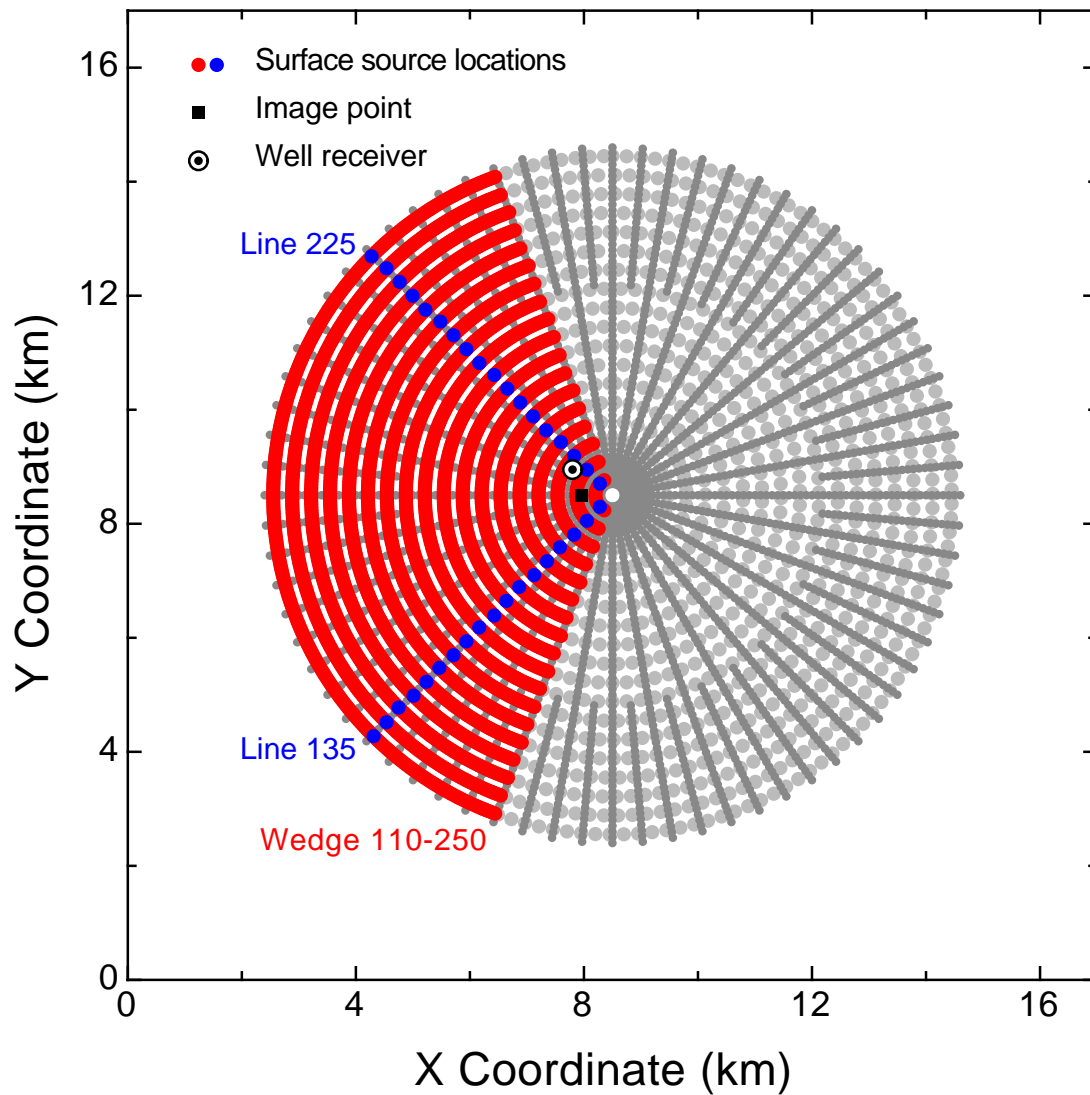


Fig. 4.30. VSP acquisition geometry used to compute image resolution for the salt dome model (Figure 4.5). For comparison, the circular/land acquisition geometry of Figure 4.7 is also shown (shaded stations).

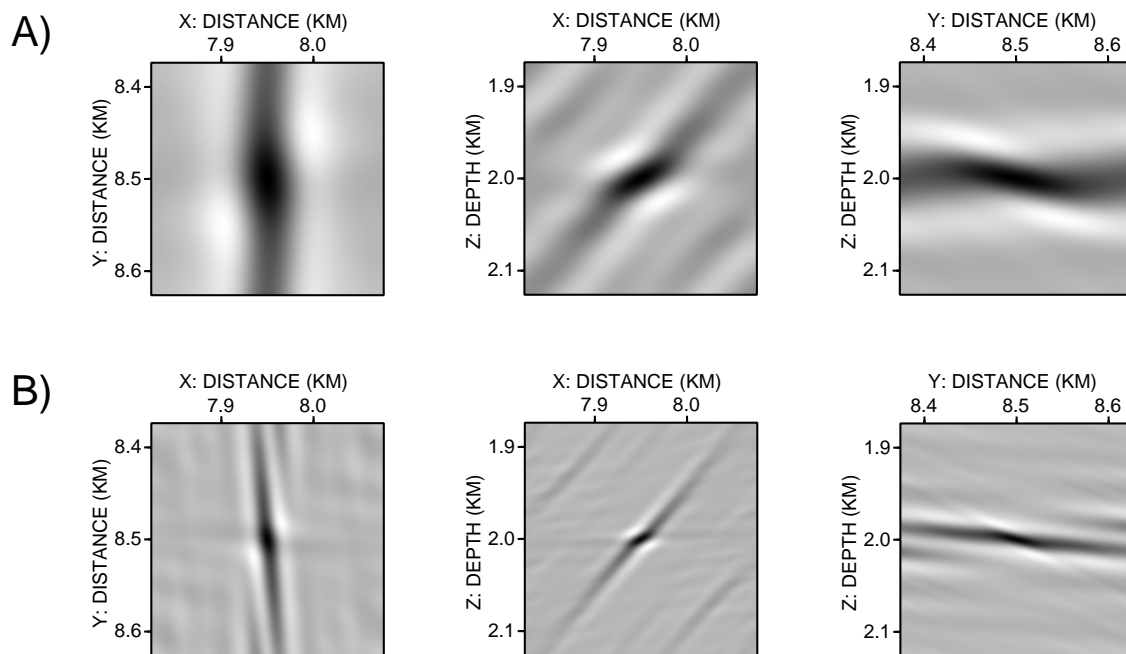


Fig. 4.31. Spatial images of the scattering point under examination using sources along line 135. (A) Dominant frequency of source signal is 30 Hz. (B) Dominant frequency of source signal is 90 Hz.

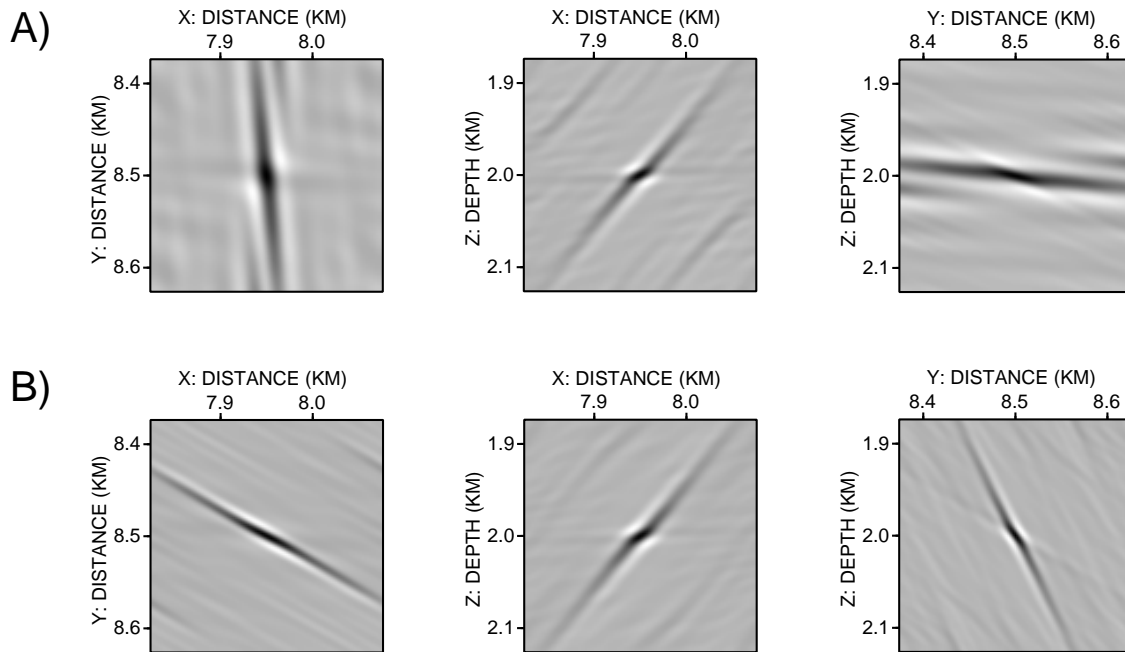


Fig. 4.32. Spatial images of the scattering point under examination. Predicted image using (A) sources along line 135 (repeated from Figure 4.31B), and (B) sources along line 225.

obtained by conventional illumination analyses that seek optimization of azimuth coverage, one should keep in mind that in this case, the salt does not interfere with the ray paths. It is therefore a simpler case than the preceding examples, where ray bending is much more significant.

#### 4.4 Discussion and conclusions

The Beylkin formula [equation 1.8] provides an important tool for analyzing variations in spatial resolution on seismic images. Since it uses only ray geometry to predict image distortion, computing hypothetical point scatterer images rapidly is relatively straightforward, especially compared to a sequence of forward modeling followed by migration. The results are also broadly applicable to a range of acquisition geometries, and converted wave imaging can be examined. Our examples for simple geometries illustrate this approach and show how resolution depends on the size of an array. Furthermore, since zero-offset source-receiver rays are coincident, the longest image

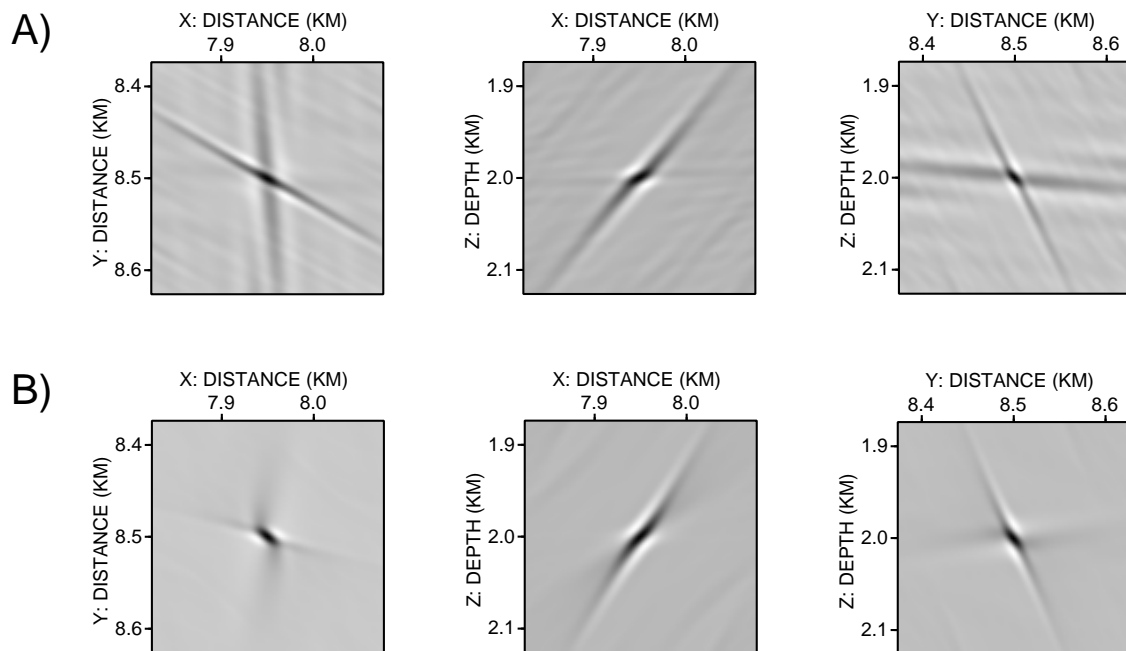


Fig. 4.33. Spatial images of the same scattering point as in Figure 4.32. Predicted image using (A) sources along both lines (135 and 225), and (B) all sources within the sector defined by lines 110 and 250.

wavenumber vectors and best image resolution are obtained with near offsets for the simple acquisition geometries. However, ray tracing modeling with more elaborate acquisition geometries and complex structures turns to be a very helpful tool in judging the validity of such statement. We also showed that multi-fold data sets produce images whose resolution is an average of all possible single-fold data sets. Therefore, if one attempts to assess the resolving capability (maximum theoretical resolution) of a particular acquisition design, it is preferable to utilize the so called “minimal data sets” (Padhi and Holley, 1997).

The comparison of land and marine survey geometries shows the value of directly considering image resolution when comparing competing designs for the more realistic, complex geometry of a salt dome structure. One point that becomes clear is that for regions with significant structural complexity associated with strong ray bending and more realistic acquisition geometries, near-offset images do not necessarily provide the best spatial resolution. The single-cable marine geometry produces better resolution for the large-offset source-receiver pairs, both because it includes rays traveling closer to horizontal and because the far-offset receivers extend a significant distance outside the region containing the shot locations. Furthermore, the number of ray reflection points is still fairly high for the near-offset experiment, emphasizing that such fold measurements would be misleading when estimating image resolution. Resolution predictions for the circular/radial survey, with its concentric rings of sources, and the orthogonal survey with its source and receiver lines running normal to each other, help to confirm that these surveys may help to improve image quality. This contradicts some previous suggestions that image resolution may not be too sensitive to acquisition geometry (von Seggern, 1994). Most likely, similar conclusions would be made from a comparison of our concentric land geometry with any other relatively narrow swath acquisition geometry like the single-cable towed array. Although the orthogonal acquisition geometry seems to have marginally better resolving capabilities, other factors may skew someone’s decision towards the circular/radial geometry. Maldonado and Hussein (1994) for example, state that the concentric-circle survey’s advantage is the increase of seismic reflection data recorded near the salt-sediment interface without suffering from non-hyperbolic paths (i.e., up- and down-going rays experience the same velocity field) as is the case with data recorded in a conventional straight line acquisition surveys or even the orthogonal surveys where because of the relative source-receiver locations, up- (or down-)going rays may travel through the



salt while down- (or up-)going rays may miss it . Another advantage is the imaging of radial faults commonly associated with salt tectonics, in their true dip direction enabling efficient collapse of associated diffractions by migration algorithms (Maldonado and Hussein, 1994). Of course, appropriate use of the circular/radial geometry presumes a fairly good a priori knowledge of the location of the tip of the salt structure in order for the survey to be centered over it.

The computations are based on a very idealized model which assumes that a migration has a perfect velocity model and noise-free seismic data. In general, any predictions must consider an optimal, best case estimate of the spatial resolution that could be obtained in practice. However, we also suggest a simple procedure allowing a straightforward assessment of the effects of varying S/N ratio to predict decreasing resolution with degradation in data quality. It is also important to realize that the predictions depend on the ray-tracing algorithm used, at least for complex media leading to multiple arrivals. Since a specific ray tracer may make an arbitrary choice of arrival or, for example, may arbitrarily choose the first arrival, a different ray geometry and wavenumber resolution vector may be computed.

Combining surface and VSP data can prove very beneficial to improving resolution of target points especially in the vicinity of the wells. The different frequency content of the surface and VSP data, however, is an obstacle that in order to overcome, we probably need a new approach to simultaneously process such data sets. Ray tracing modeling can also assist in determining which well to populate so that the VSP data will be as complimentary to the surface data as possible. This may be applicable to mature production sites where one could have several wells to choose from.

## CHAPTER V

### APPLICATION OF IMAGE RESOLUTION ANALYSIS TO VSP FIELD DATA

The area of study is located in southwestern Louisiana. A typical piercement-type salt structure of the Gulf Coast, it is a mature field with over 1100 wells drilled and over 140 MMBO ( $140 \times 10^6$  barrels of oil) produced since the early 1900's from multiple pay zones (Constance et al., 1999). In early exploration, the reservoir types were referred to as exclusively stratigraphic since early exploration was focused on reservoirs terminated against the flanks of the salt diapir. The trapping mechanisms for the oil and gas reservoirs consist of regional trend faults and local radial faulting related to the diapir, shales and depositional geometries (Constance et al., 1999). Very small (less than 200 m<sup>2</sup>) reservoir compartments are the targets of current exploration.

Although the field has been producing since the early 1900's, very little information about the geologic structure of the salt and its surrounding sediments has become publicly available. Most of our knowledge comes from two early publications that derive their conclusions from the drilled wells, unspecified electric logs and a seismic reflection survey undertaken in the early 1940's. The purpose of the recent (1998) simultaneous acquisition of three-dimensional (3-D) surface seismic data and three-component, three-dimensional Vertical Seismic Profiling (3-C, 3-D VSP) data was to improve our understanding of the structure around the salt (Constance et al., 1999). Migrated seismic sections will provide a valuable tool in delimiting the compartmentalised reservoirs.

#### 5.1 The 1998 acquisition survey

The most recent data acquisition for imaging the subsurface around the salt dome, was a simultaneous 3-D surface seismic and a 3-C, 3-D VSP survey. The seismic sources, 5.5 lb (2.5 kg) pentolite charges at depths of 15 to 27 m (49 to 89 ft), were simultaneously recorded by the surface vertical geophones and the downhole 3-C arrays in two abandoned wells (Figure 5.1). The surface acquisition geometry

is an innovative circular/radial design producing a wide range of offset and azimuth coverage. The source and surface receiver spacings as well as the active receiver patches were discussed in Chapter IV (section 4.3) where the model circular/radial land acquisition design, mimicking the real one, was introduced. The seismic sources of the northern half of the surface survey were also recorded by the two downhole 3-C arrays (Figure 5.2). The western well whose recorded VSP data we will closer examine in the following sections, was populated with 80 3-C cemented in place phones at 50 ft (15 m) intervals. The total interval covered was from 943 to 4893 ft TVD (287 to 1491 m). However, of those 80 levels, the bottom 15 were damaged during deployment rendering the active depth range from 943 to 4135 ft (287 to 1260 m). A more detailed description of the parameters and instrumentation for the surface and the two VSP data acquisitions is given by Constance et al. (1999).

One of the characteristics of this VSP survey that sets it apart from others, is the excessively large offsets. While a VSP acquisition with an offset-to-depth ratio of 1:1 is regarded and treated as large offset (Hinds et al., 1996), the survey under examination contains offset-to-depth ratios close to 5:1. Figure 5.3 shows three shot gathers with small, intermediate and large source/well offsets. The first arrivals in the near-offset shot gather consist of the direct incident wave exhibiting the familiar near-linear moveout. As the source offset increases, the pattern of the first arriving waves becomes gradually more complex eventually winding up in slightly curved, negative moveouts. Gal'perin (1974) examined similar complex wave patterns of the initial portion of the VSP records for various source offsets and velocity backgrounds and found that for large offsets, they comprised of refracted – either head waves or “curved-ray refractions” – direct and postcritically reflected waves.

The purpose of this chapter is to demonstrate the ability of the proposed method to predict the image quality obtained by the VSP acquisition geometry equally well as a conventional (and more costly) migration of the real data. Acknowledging the difficulties that the far offsets impose on the analysis, signal processing and imaging of such a data set, we will process and migrate only the near offset gathers. Only a single NW-SE line through the western well (Figures 5.2 and 5.4) was considered due to the fact that a 3-D VSP migration scheme was not available at the time. It was, therefore, the limitations of the available migration code that did not allow us to explore the full imaging potential of the 3-D VSP acquisition. Figure 5.4 depicts all the shots comprising the NW-SE line. Of those shots, only the nearest 11 (4 to

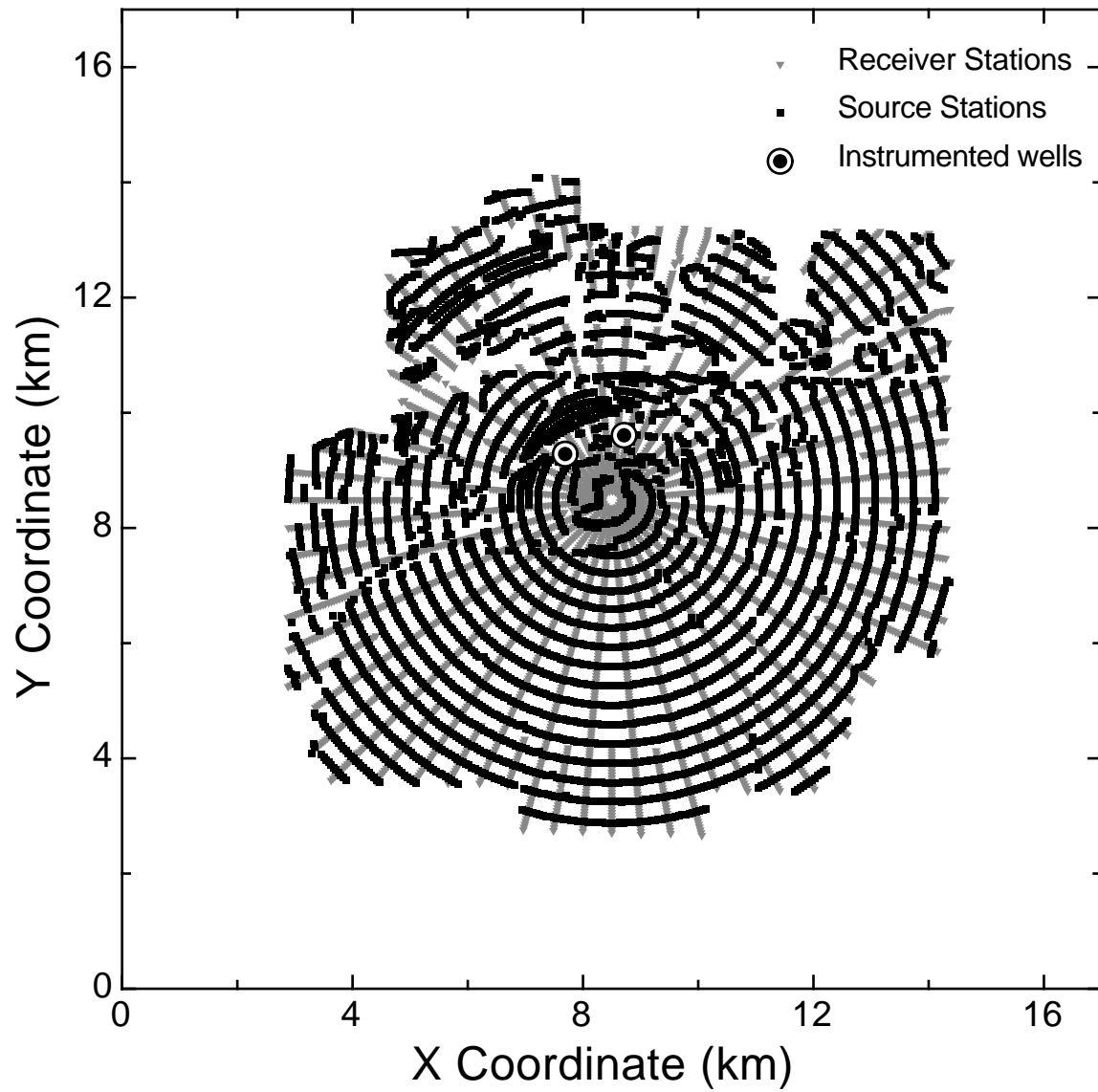


Fig. 5.1. Map view of seismic source, surface receiver and populated borehole locations used in the simultaneous surface/VSP acquisition.

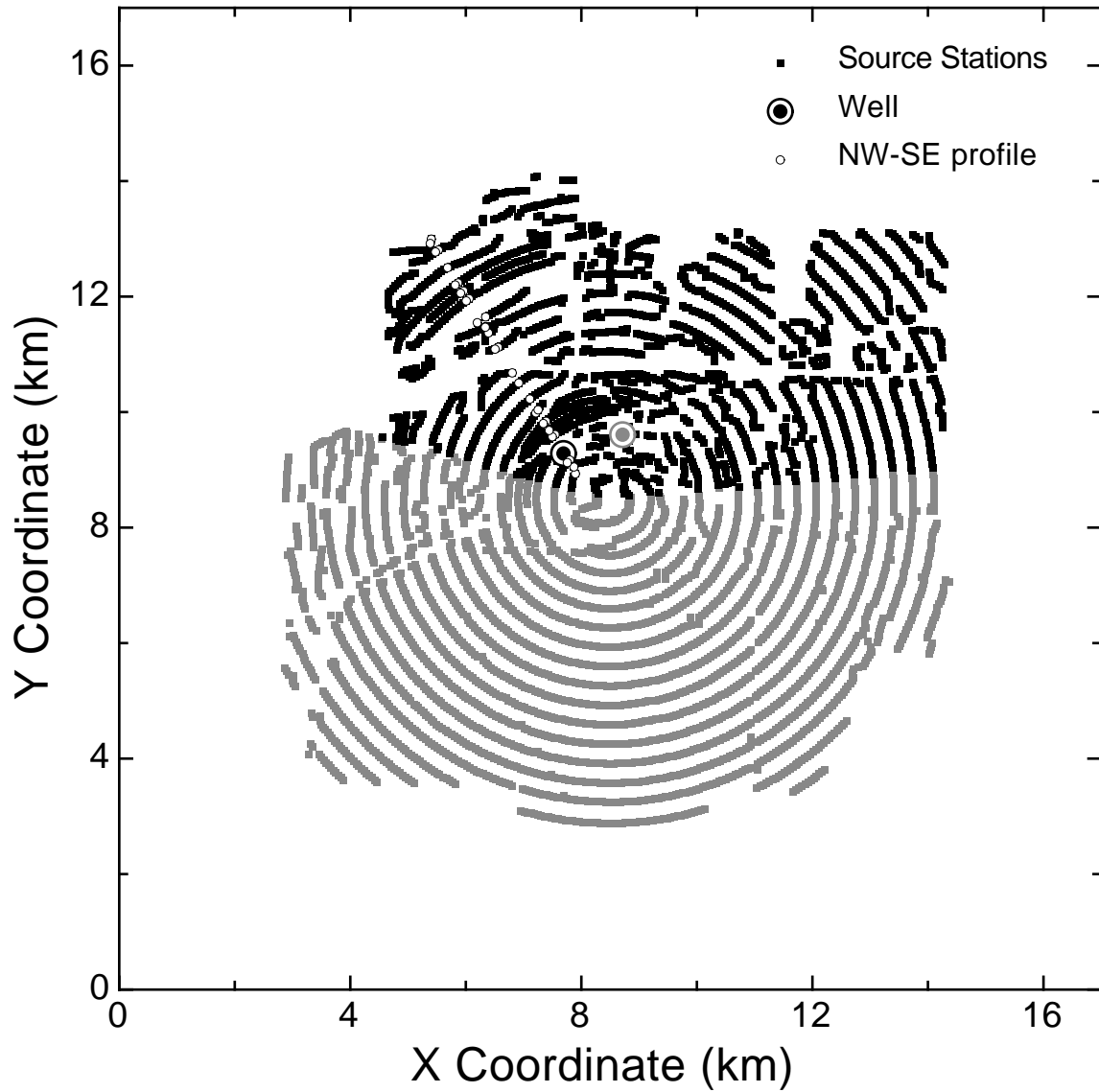


Fig. 5.2. Only the Northern half (black dots) of the total source spread of the combined surface/VSP survey was recorded by the 3-C receivers in the two wells. The open circles indicate the sources that comprised the NW-SE line under further examination (see also, Figure 5.4).

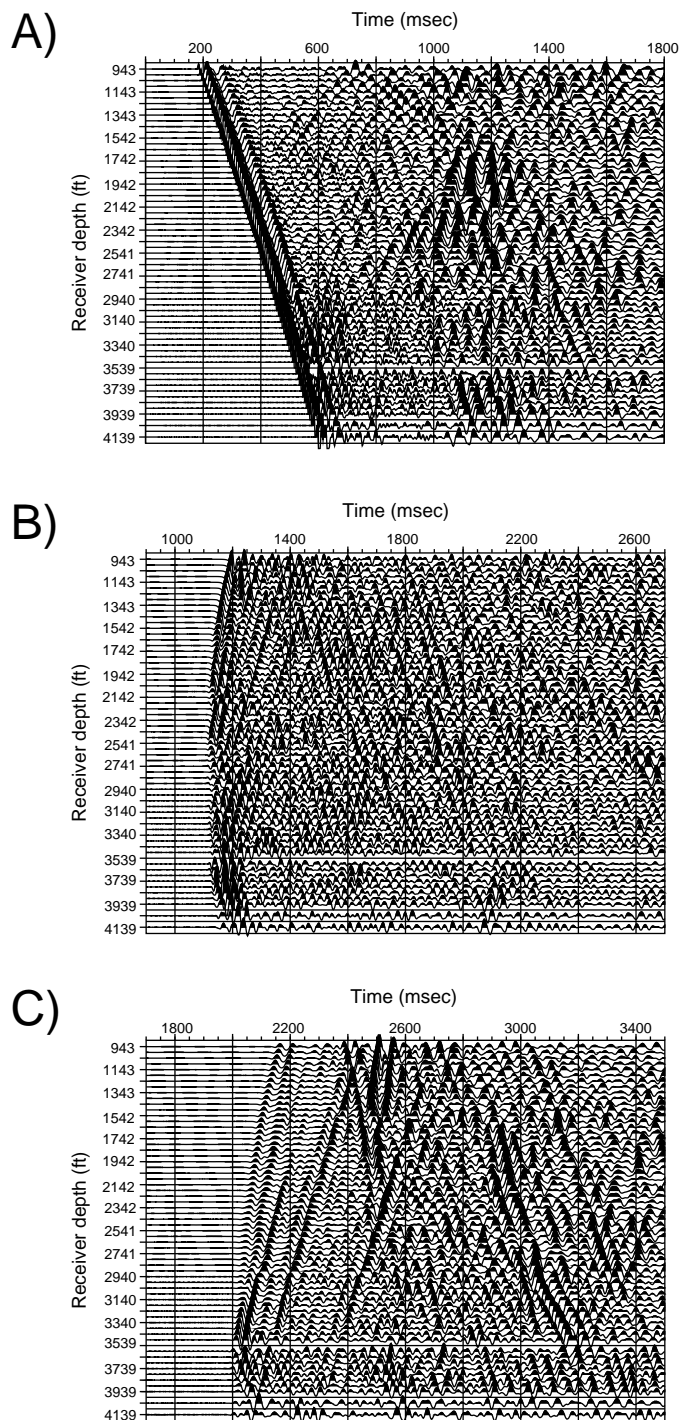


Fig. 5.3. Common shot gathers along a NW-SE line through the well (Figure 5.4). A) Near offset gather (source/well separation = 160 m). B) Mid offset gather (source/well separation = 2156 m). C) Far offset gather (source/well separation = 4356 m).

the SE and 7 to the NW of the well) were processed, migrated and compared to the results obtained by the image resolution analysis.

## 5.2 VSP data processing

### 5.2.1 Pre-processing phase

The pre-processing sequence included the initial sorting of the data in shot gathers and the application of the survey geometry to the raw data. Then, bad traces (including the records of the bottom 15 damaged receivers) were removed. Spherical divergence, transmission and absorption are responsible for amplitude losses in a time variant manner. The rate of amplitude decay of the first arrivals with depth were analyzed and corrected by applying an inverse gain function of the form:

$$\text{Spherical Divergence Gain} = T^\alpha \quad (5.1)$$

where  $T$  is the time corresponding to the trace sample on which the gain is applied and  $\alpha$  is a user defined scalar (here, an  $\alpha = 1.9$  was used).

An additional amplitude gain was subsequently applied to balance varying amplitudes from trace to trace and gather to gather. The trace balancing gain function being a time invariant function, scales the RMS amplitude of every trace to an arbitrary, user-specified RMS value. It is important to mention that both these amplitude altering functions (Spherical Divergence Gain and trace balancing) are stored in the trace headers of the output file and can be removed, if needed, at any later stage of the processing.

### 5.2.2 First arrival travel time picking

First break times provide the time-depth and velocity-depth relationships. In the case of zero offset VSP (check-shot) surveys, interval, average and RMS velocities can be accurately determined from the first arrival times. Time-depth curves can be also used to convert the depth axis to time. Furthermore, the first arrival times from a zero offset configuration are needed to static-shift the traces so that they appear as if the receivers have been recording on the surface, a useful technique to correlate VSP with surface seismic data (Cassell, 1984). In addition to the previously

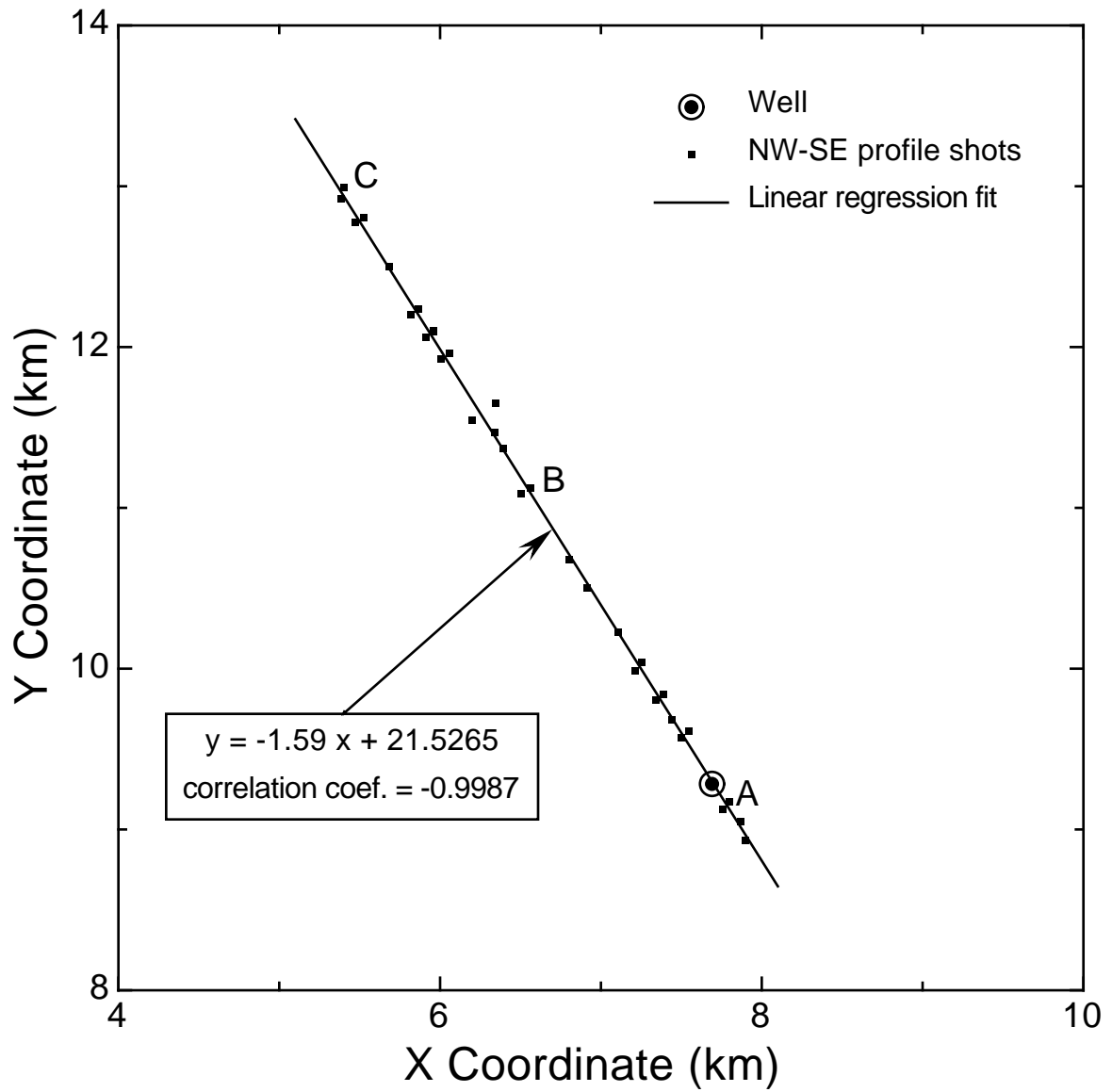


Fig. 5.4. Detailed map view of the NW-SE line sources and their position relative to the well. The labels (A,B,C) refer to the shot gathers shown in Figure 5.3.



mentioned applications, first break times are necessary in many other processing steps of VSP data (for example, median-filtering for down- and up-going wavefield separation, design of deconvolution operators from downgoing wavefields, etc.).

Consistent travel time picking can be obtained by identifying constant phases on the pulse, such as the inflection points or points of peak amplitude (Hatherly, 1982). Although traveltimes picking is a tedious task, it is usually a straightforward process which can be easily automated (Hatherly, 1982; Stewart et al., 1984 and others). However, there will always be errors associated with the picked traveltimes. Therefore, one should, at least, report an estimate of those errors. A major factor affecting our ability to pick traveltimes with confidence is the level of noise present in the seismic traces. In general, the higher the signal-to-noise ratio (SNR) is, the more accurate the traveltimes picks should be.

Since the first arrivals from a zero- (or near-)offset shot are used in VSP surveys in determining a near-well velocity field, it is useful to know the level of errors associated with the picks. Moreover, the RMS error obtained from tomographic inversion of traveltimes should be compared to the error associated with the traveltimes picks.

Here, we used a simple SNR estimate. We define SNR as:

$$SNR = \frac{RMS\_AMP_{signal}}{RMS\_AMP_{noise}} \quad (5.2)$$

The RMS amplitudes of signal and noise are computed within a user-specified window containing only those portions of the seismic traces that correspond to prior to first arrival, and the first arrival events respectively.

Both this SNR estimate and spectral analysis of the near offset gathers along the NW-SE line defined earlier (Figure 5.4) showed that the signal-to-noise ratio is high, and varies between 85 to 70 dB. Therefore, travel time picking should be performed with confidence (except in the case of a few noisy traces). A more robust way of computing the SNR is discussed by Hatton et al. (1986) provided that the traces contain the same signal and noise is uncorrelated.

Gangi and Fairborn (1968) proposed a method of determining relative time arrival time delays based on the cross-correlation of each trace of an array with a reference trace. This reference trace was obtained by summing all traces with initial crude travel times picked. In order to assess the confidence level of the traveltimes picks, cross-correlation lags of a reference trace with all traces are compared to the picked traveltimes differences between the same reference trace and all other traces. Instead

of using a sum or an average of an ensemble of traces as a reference, here a single trace was used. Therefore, waveform changes from gather to gather or even within the same gather were neglected. Nevertheless, the comparison of the cross-correlation time lags with the relative picked travel times should provide a measure of the level of the errors associated with the first arrival travel time picking. Cross-correlation lags were calculated both in integer number of samples and using quadratic interpolation between samples.

The first arrival times were picked in several different ways, namely:

- automatic pick of peak amplitude, bulk shift per shot gather to onset of first arrival
- manual pick of peak amplitude, bulk shift per shot gather to onset of first arrival
- manual pick of onset of first arrival

Comparing the picked first arrival times to the cross-correlation time lags and statistically analyzing these results, showed that the error associated with the travel time picks is in the order of 2 to 3 ms (with 2 ms being the sampling interval of the traces). Table 5.1 summarizes the statistical results for the three different travel time picking techniques. Of those three ways, trying to pick directly the travel time that corresponds to the onset of the arriving wavelet proved to be the most problematic (higher standard deviation, higher minimum to maximum range). This is expected however, because in traces with lower signal-to-noise ratio it is harder to discern the point where the arriving signal emerges than the point where it assumes its higher value. Indeed, the biggest disparities between this and the other two ways of first break picking were detected in the shot gathers with the farthest offsets where SNR is reduced. Manually picking the peak amplitude of the first arrivals and bulk shifting them to the onset of the signals was the adopted method used throughout the early processing stages.

Figure 5.5 shows the travel times for the two closest shot gathers to the NW of the well along the NW-SE line (Figure 5.4). The reported travel times are relative to the reference trace used in the cross-correlation. Although there is a good agreement between the upper portion of the picked travel times (solid lines) and the time lags resulted from the cross-correlation (solid and open circles), there is a noticeable discrepancy in the lower (deeper receivers) part of the gathers. This is attributed to the

Table 5.1. Simple descriptive statistics for the three different travel time picking approaches. All listed results are in ms.

	Automatic pick of max. amp. Bulk shift to onset	Manual pick of max. amp. Bulk shift to onset	Manual pick of onset
Mean	-0.5522	-0.2160	0.1701
Variance	5.2177	5.2114	8.2238
Stand. Deviation	2.2842	2.2828	2.8677
Median	-0.5928	-0.0046	0.1179
Maximum	8.4957	8.4560	12.5486
Minimum	-10.5466	-9.6740	-9.9919

fact that different type of receivers were used for the deeper portion of the well. Their different response is discussed in detail in the following paragraph. The open circles of the figure correspond to erroneous cross-correlation lags due to the oscillatory nature of the signal. These measurements were treated as outliers and were excluded from the statistical analysis mentioned above.

### 5.2.3 Phase matching

An additional preprocessing step applied to the data was to shape the traces corresponding to the deepest receivers to match the shallower ones. A simple visual inspection of the shot gathers was sufficient to reveal the difference in signal character between the two groups of receivers, the shallower consisting of the first 40 receivers and the deeper consisting of the rest 25 receivers (range of sequential trace number: 41 to 65). Additional supporting evidence was supplied from the cross-correlation lag curves that exhibited a “jump” in the transition from the 40th to the 41st receiver (Figure 5.5).

Figure 5.6 shows a shot gather with the first arrivals aligned. Not only is the difference in the signal character obvious, but also its effect on later events is demonstrated. The arrows point at two such events that are either misaligned along the transition from the upper to the lower receiver group or their continuity has been deteriorated.

To correct the aforementioned phase and time mis-ties, we applied a phase (and time) matching algorithm based on an algorithm proposed by Bishop and Nunns (1994). The method applies scalar corrections for both phase and time differences as these are derived from the cross-correlation function using the Hilbert transform (Taner et al., 1979). More specifically, the cross-correlation between a reference trace (can be thought of as the desired output) and a trace which we desire to shape is performed within a user specified window. Here, we used a group of several traces (usually the 5 to 6 traces closer to the transition point, i.e., sequential trace number: 35 to 40) to average and use as the reference trace. 5 to 10 of the deeper traces (sequential trace number: 41 to 46 or 50) were included in the generation of the average trace to be shaped. The cross-correlation window was designed to include the strong first arrival signal. The peak value of the envelope of the cross-correlation,  $A(\tau)$ , at  $t = \tau$ , defines the optimum time shift to be applied for the time correction.

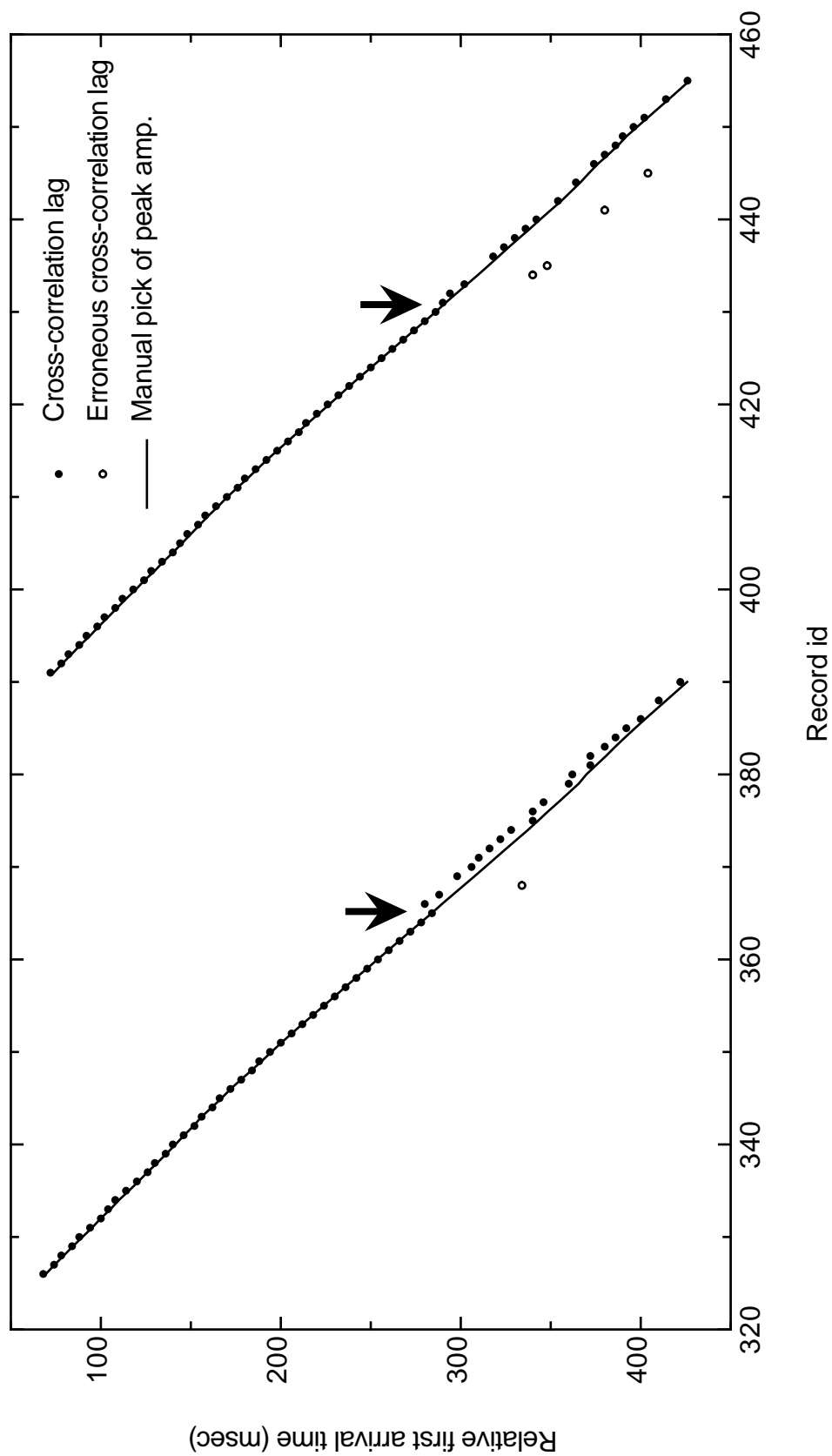


Fig. 5.5. Travel times for the two nearest offset shot gathers to the NW of the well. The discrepancies between the relative picked travel times (solid lines) and the cross-correlation time lags (circles) for the greater relative travel times are attributed to the different response of the deeper receivers. The arrows indicate the transition point between different types of receivers.

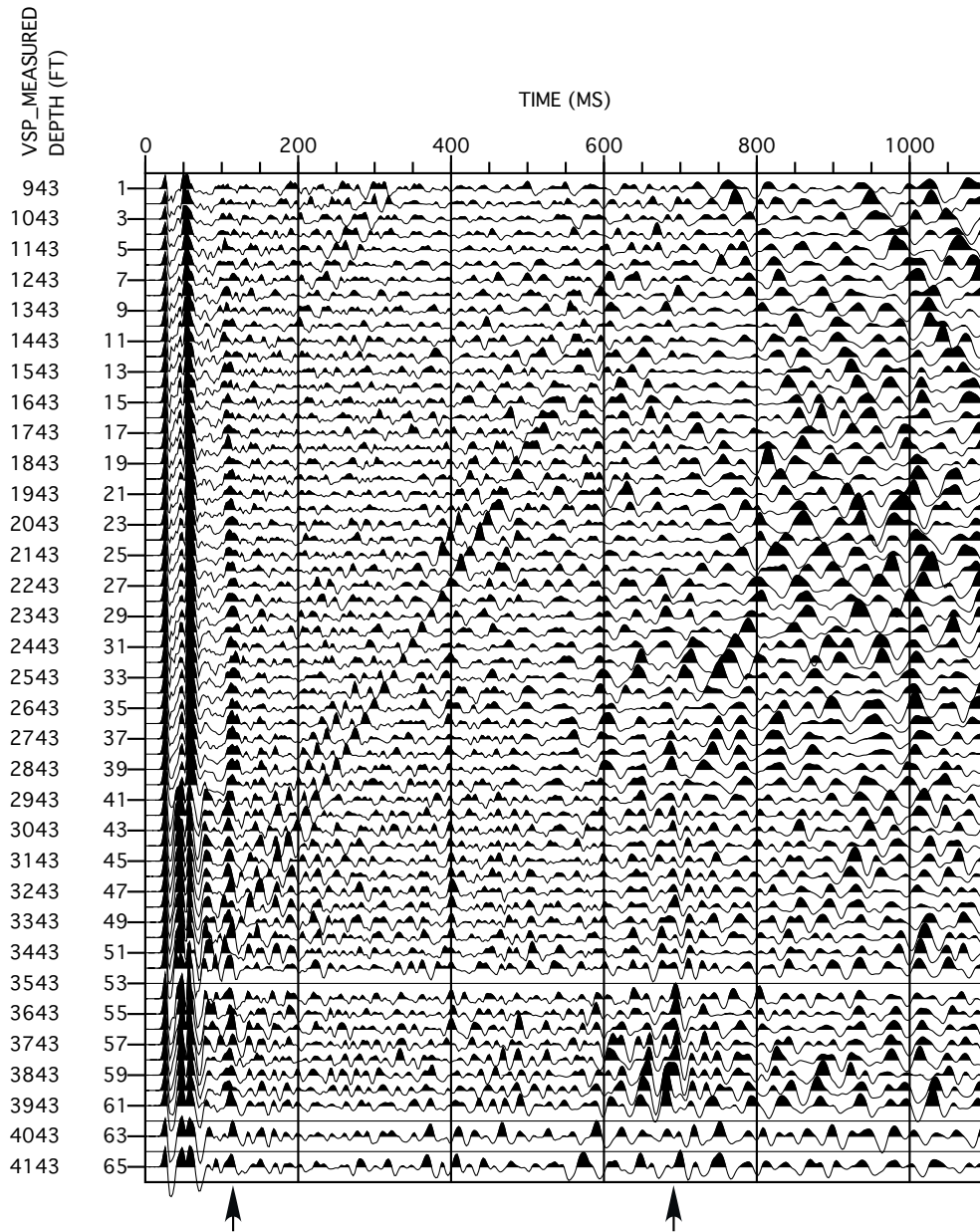


Fig. 5.6. A typical shot gather with the first arrivals aligned. The signal character change between shallow (traces 1 to 40) and deep (traces 41 to 65) receivers and its effects on later events is very clear.

The instantaneous phase,  $\phi(\tau)$ , on the other hand, determines the phase shift. The computed phase and time corrections were then applied to all of the 25 deeper traces.

The phase and time shifts computed for the 11 closest to the well shot gathers of Figure 5.4 were found to be around  $-98^\circ$  and  $-4$  ms (negative numbers meaning phase and time lead). Figure 5.7 shows the shot gather of Figure 5.6 after the phase and time correction were applied to the lower group of traces. There is a remarkable improvement of the continuity of the events along the transition point (sequential trace number: 40 to 41). An alternative way of determining the mis-tie correction would be the derivation of matching convolutional filters as proposed by Henry and Mellman (1988) and not just scalar corrections. However the computed scalar corrections were considered to be adequate.

#### 5.2.4 Velocity analysis

The velocity profile at the well location is traditionally obtained through a check-shot survey. Since a zero-offset shot was not available in this dataset, the closest (irrespective of azimuth) shot to the well was used. Its offset was 76.6 m to the south-west of the well. The observed travel time,  $t_{obs}$ , for each trace corresponding to a receiver at level  $z$  was corrected for the slant distance (source offset),  $x$ , by the factor  $z/\sqrt{z^2 + x^2}$ :

$$t = t_{obs} \cos i = t_{obs} \frac{z}{\sqrt{z^2 + x^2}} \quad (5.3)$$

where  $i$  is the angle between the source-receiver straight ray and the vertical surface projection of the receiver (Figure 5.8). The interval velocity  $V_i$  in the interval of two successive traces recorded at levels  $z_{i-1}$  and  $z_i$  is then given by the formula:

$$V_i = \frac{z_i - z_{i-1}}{t_i - t_{i-1}} \quad (5.4)$$

Figure 5.9 depicts the interval velocity profile corresponding to the nearest-offset shot after the slant time correction was applied to simulate vertical travel times. Overall, the velocity gradually increases with depth with an apparent higher increase rate in the shallower part of the section up to the depth of 0.55 km (1800 ft).

In order, however, to perform the image analysis and migration along the NW-SE line, a two-dimensional velocity field along the same orientation was needed. Different

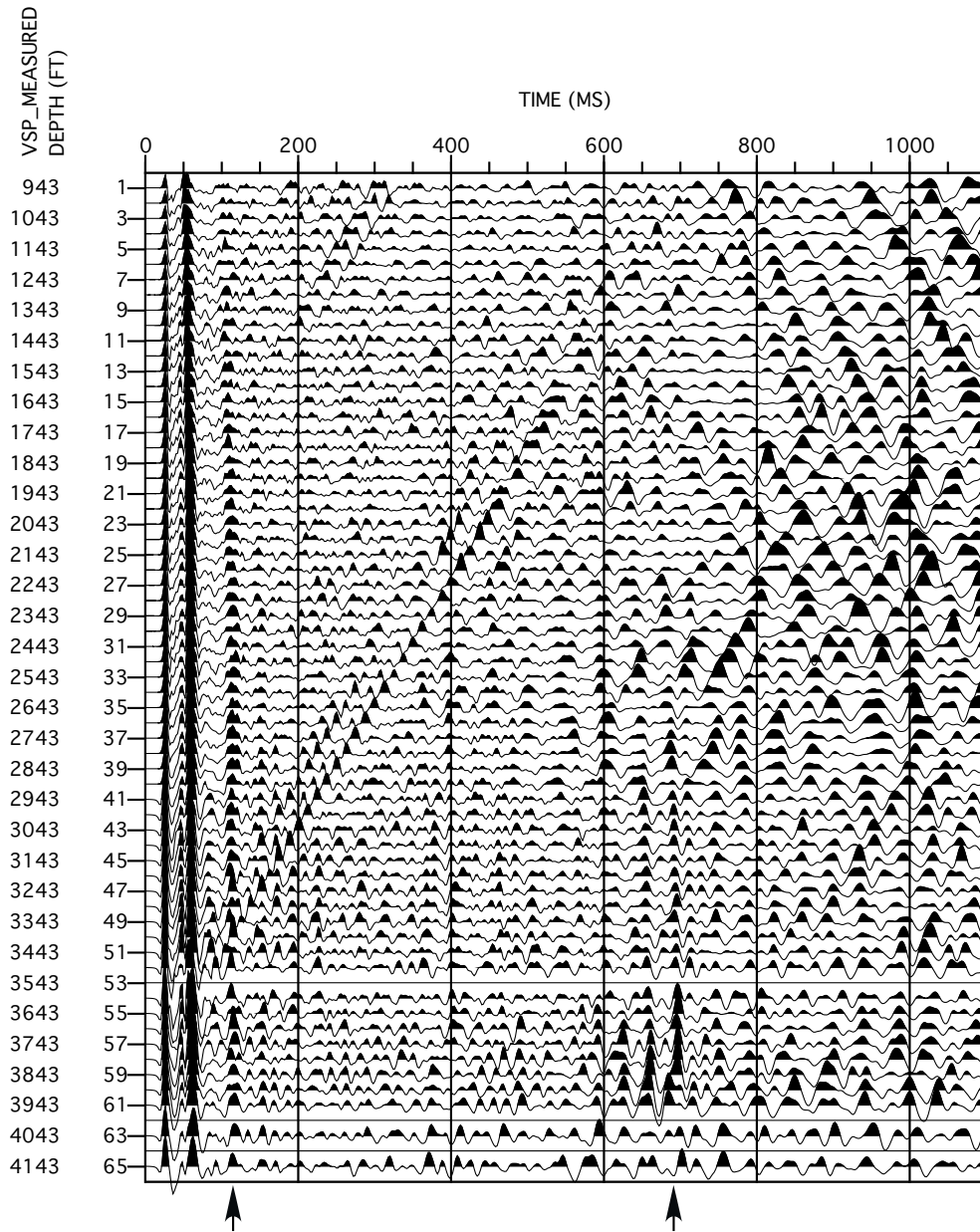


Fig. 5.7. The same shot gather as in Figure 5.6 after phase and time correction. Notice the improvement on the continuity of the two events at the time of 100 and 700 ms (marked with arrows).



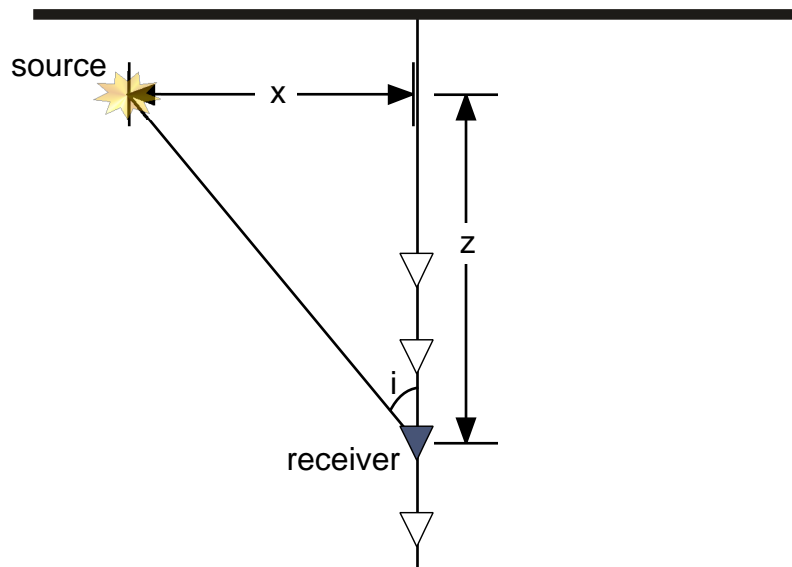


Fig. 5.8. Schematic explaining the variables involved in the correction of travel time for the source's non-zero offset. After the correction is applied, the travel times simulate a check-shot survey.

approaches to extending the computed velocity profile were tested. Forward ray tracing modeling was performed using several different velocity models. One- and two-gradient velocity models were built based on linear regression applied to the velocity profile (Figure 5.10). More specifically, for the two-gradient velocity models, the shallower gradient was slightly perturbed so that the velocity was continuous at the point where the two gradients meet (at the depth of 0.55 km) and greater than the water velocity at the surface (red lines in Figure 5.10). In addition to the flat models described above, dips of  $5^\circ$  and  $10^\circ$  towards the North-West were introduced to better simulate the assumed local geology with the salt diapir to the South-East.

Another way to build a velocity model is through the use of traveltimes tomography. TomoX, a commercial package by GeoTomo LLC was used for this purpose. The nonlinear traveltimes inversion scheme applied the Tikhonov regularization (Tikhonov and Arsenin, 1997) in order to constrain the model roughness so that the resulting models would have physical meaning (Zhang and Toksöz, 1998). Several initial velocity models ranging from simple half-space homogeneous media to more complex, two-gradient velocity models with dipping interfaces were tested. Of all initial models, a single-gradient model yielded the best fit to the observed traveltimes with an RMS

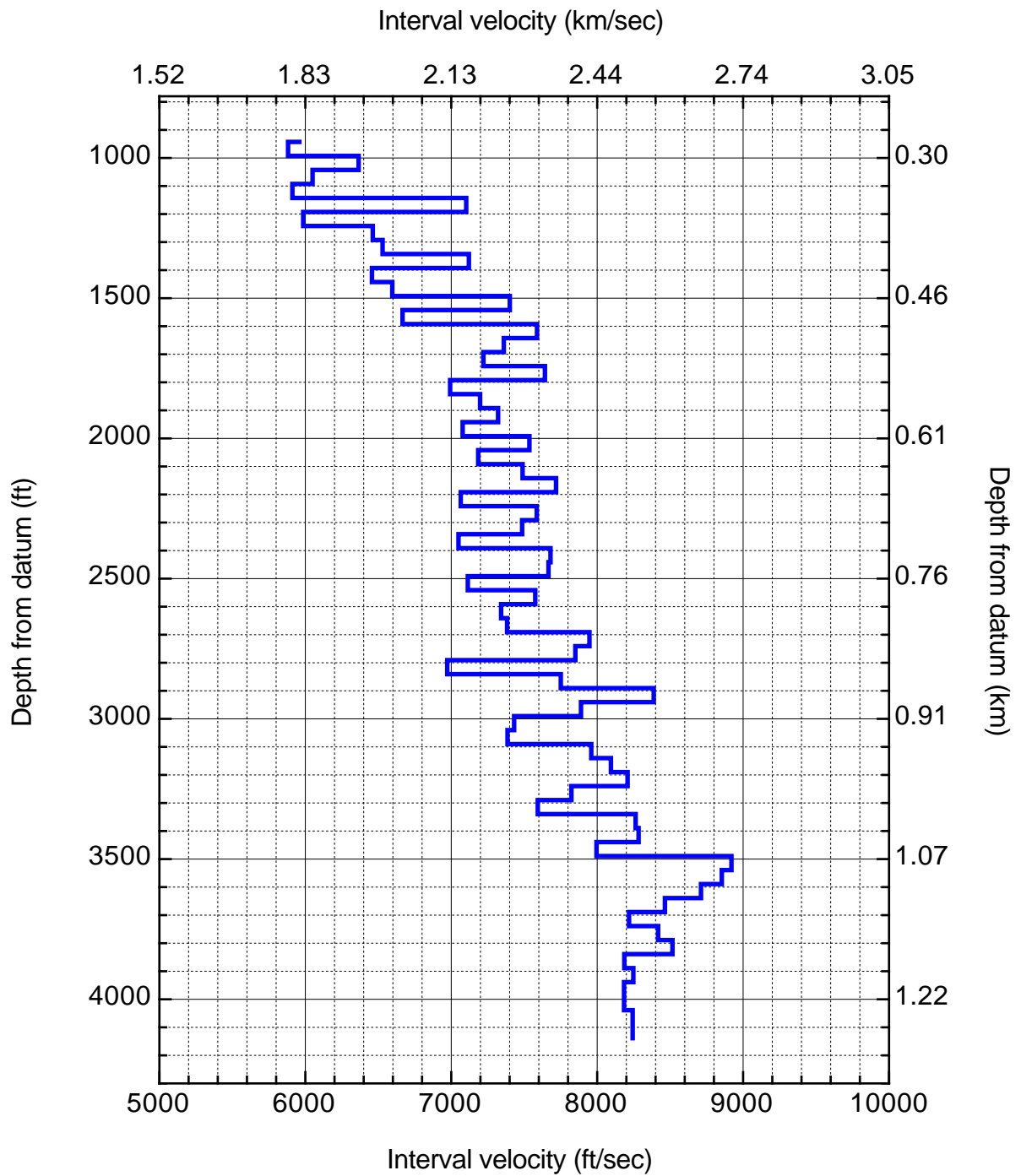


Fig. 5.9. Interval velocity graph simulating the velocity field at the well location. The one-dimensional velocity profile indicates a gradual velocity increase with depth.

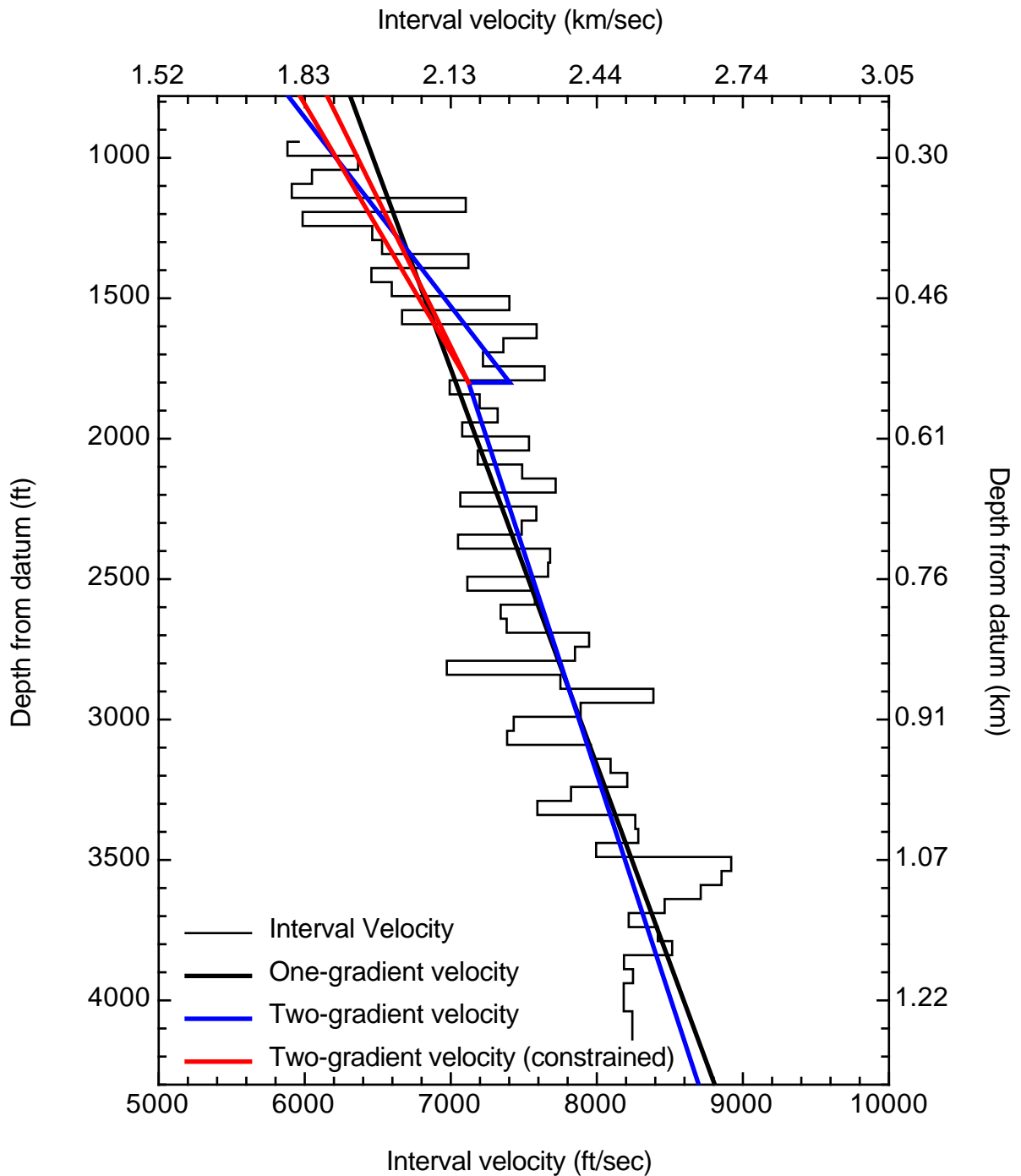


Fig. 5.10. The different gradient models as inferred from the velocity analysis of the nearest-offset shot gather (Figure 5.9). The one- and two-gradient models (black and blue lines) are the least-square fit curves to the interval velocities. For the shallower part of the model, additional constraints were applied to ensure the velocity continuity at depth and velocities greater than 1.5 km/s at the surface (red lines).

traveltime error of 6 ms. The initial velocity model was described by the equation:  $v = v_0 + \alpha z$ , where the velocity at zero depth is  $v_0 = 1.55$  km/s and the gradient  $\alpha = 0.90$  s<sup>-1</sup>. Durussel (2002) considered all 31 shot gathers along the NW-SE line (Figure 5.4) and concluded that the introduction of weak transverse anisotropy further reduces the discrepancies between the observed and computed traveltimes.

To validate the velocity model resulted by the traveltime inversion, we compared it to the velocity field along the same profile that was obtained from the velocity analysis of the surface seismic data. Figures 5.11A and 5.11B depict the velocity profiles along the NW-SE seismic line for the traveltime inversion and surface seismic data velocity analysis respectively. The source and receiver locations are also indicated for easier reference and interpretation of the results, especially for the tomography. When judging the tomographic results, one has to constrain himself in the regions transversed by seismic waves (or more appropriately, seismic rays) where traveltime results are reasonably reliable. Figure 5.12 shows the difference (in m/s) between the two computed velocity fields of Figure 5.11. The velocity difference is  $\pm 100$  m/s within the region defined by the seismic rays for the two outermost sources (except for a small area on the SE part of the profile, where the difference acquires its maximum absolute value of 160 m/s at depths of 500 m). If we consider that the velocity in this same region ranges from 1550 to 3000 m/s, the observed differences between the two approaches translate in a 5–10% error.

Finally, the velocity model obtained from the surface seismic data was used as an initial model in TomoX where the traveltime inversion yielded an RMS error of 3.7 ms after a single iteration. It was, for all practical purposes, a smoothed version of the initial model. Considering that the intrinsic error involved in traveltime picking was calculated to be in the order of 2 to 3 ms (Chapter V, section 5.2.2), it is very reasonable to assume that even the initial velocity model was a fair representation of the real local velocity.

### 5.2.5 Wavefield separation

A distinct difference between surface and VSP seismic data is that VSP data contain both down- and up-going wavefields recorded simultaneously, thus, overlaying each other. Therefore, a significant processing step of VSP data is the separation of down- and up-going wave modes. Traditionally, the objective of such separation is the

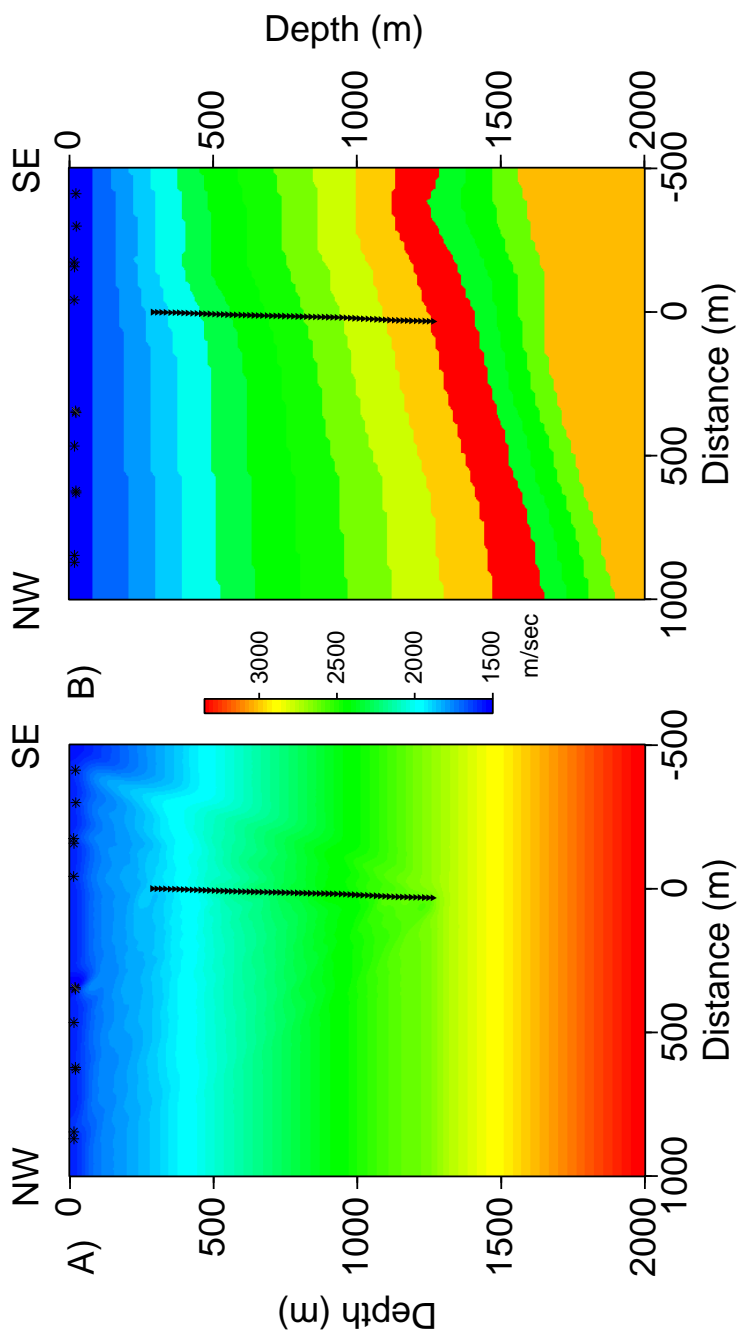


Fig. 5.11. Proposed velocity models along the NW-SE seismic line. (A) The result of traveltime inversion of a single-gradient initial velocity model. (B) Layered model resulted from the velocity analysis of the surface seismic data.

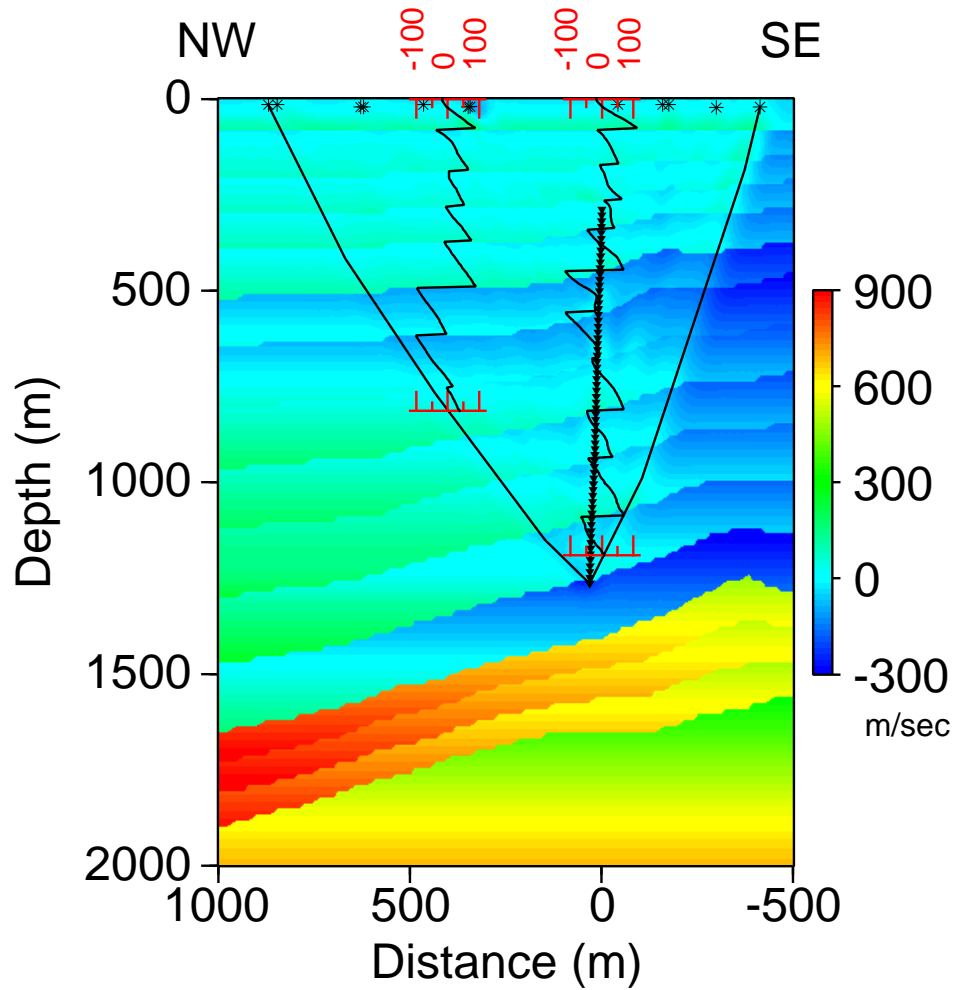


Fig. 5.12. The difference between the two velocity fields of Figure 5.11. Since tomographic results are reliable only in the area defined by the two rays (black lines) and the free surface, the “log-like” realizations of the velocity difference at the well and an arbitrary location are confined within this region.

analysis of up-going waves since a correlation to surface seismic data is then feasible. Moreover, the up-going wavefield is required as an input to many migration schemes (for example, Gibson, Jr. et al., 1994). Two different techniques were considered in order to accomplish the task of wavefield separation, namely the frequency-wavenumber ( $f-k$ ) and median filter techniques.

In VSP data, down- and up-going wavefields naturally exhibit opposite slopes. Therefore, when Fourier transformed to the  $f-k$  domain, the wavefields occupy different wavenumber half planes and their separation is readily done by rejecting the appropriate half plane. On the other hand, wavefield separation by means of median filtering is achieved in the following steps:

- Alignment of strong first arrival event (down-going), time shifting the data by an equal to the picked first arrival travetime amount.
- Application of median filter to emphasize (and smooth) down-going events which have the same slope with the first arrival. A band-pass filter is usually then applied to remove some high frequency (small amplitude) noise spikes of an otherwise smooth function (Hardage, 2000).
- Data shifted back to their original alignment.
- Subtraction of the separated down-going wavefield from the original data to obtain the desired up-going field.

Overall, the  $f-k$  filtering approach was judged to yield better results. The main reason is that while  $f-k$  filtering will allow the rejection or acceptance of events with very different dips as long as they have the same sign, median filtering will enhance (or eliminate, by subtraction from the original data) signals that exhibit a particular dip or a narrow range of dips depending on the filter's length. In general, the longer the median filter, the better its ability to reject events that are not perfectly aligned. Many shot gathers under examination exhibit down-going waves with slopes different than the first arrivals'. Such phenomenon could be explained as out-of-plane energy, possibly off the salt body which is in the vicinity of the well. In the presence of down-going events with multiple moveouts, an iterative median filtering technique could be adopted. Figures 5.13A and 5.13B show the residual signals, after the down-going wavefields have been separated by median and  $f-k$  filtering respectively and subtracted from the original, total wavefield record (Figure 5.13D). Even with a

relatively short, 5-trace median filter, the down-going events between 1000 and 1800 ms have been preserved. On the other hand,  $f$ - $k$  filtering has successfully removed all the down-going energy regardless its moveout. Figure 5.13C, the difference between Figures 5.13A and 5.13B, indicates that the main difference between the two techniques is indeed the down-going energy missed by the median filtering.

### 5.3 VSP migration and image resolution analysis

The survey under study is one of a few published 3-D, 3-C VSP surveys. Others include the Blackfoot, Alberta, Canada (Zhang et al., 1996) and the Oseberg oil and gas field in the Norwegian North Sea (Chen et al., 2000). This salt dome VSP acquisition however, is by far the largest acquired 3-D VSP data set (>700000 traces compared to the  $\approx 6500$  traces of the Blackfoot survey and  $\approx 150000$  traces of the Oseberg survey). Moreover, the recorded offsets in our case are larger than in the other surveys. Equally sparse are the references about the 3-D migration of 3-D VSP field data. Bicquart (1998) discusses the application of 3-D prestack Kirchhoff depth migration of both the Blackfoot and Oseberg field data using only the reflected (up-going) wavefields. On the other hand, Clochard et al. (1998) examine the effects of two preprocessing sequences (one consisting only of predictive and spiking deconvolution whereas the other included wavefield separation and shaping deconvolution) on a 3D/3C ray-Born imaging of the Oseberg volume.

In Chapter IV, it was demonstrated that the proposed image resolution method is applicable to 3-D acquisition design problems. Here, it is applied and compared to the migration results of the 2-D seismic line illustrated in Figure 5.4. This was done, with out the loss of generality, due to the lack of appropriate resources to migrate such a large volume of VSP data. Moreover, synthetic shot gathers were generated, processed and migrated using the field geometry and velocity model. This was deemed necessary in order to build additional confidence in comparing the predicted image resolution to the migrated images. In generating synthetics, one has complete control on the source wavelet and the level of the introduced noise (if desired so). These factors are very little known in real experiments and significantly affect the image resolution.

The data were migrated using a Kirchhoff summation algorithm provided by the ProMAX processing package (Landmark Graphics Corp.). Here, we followed the more



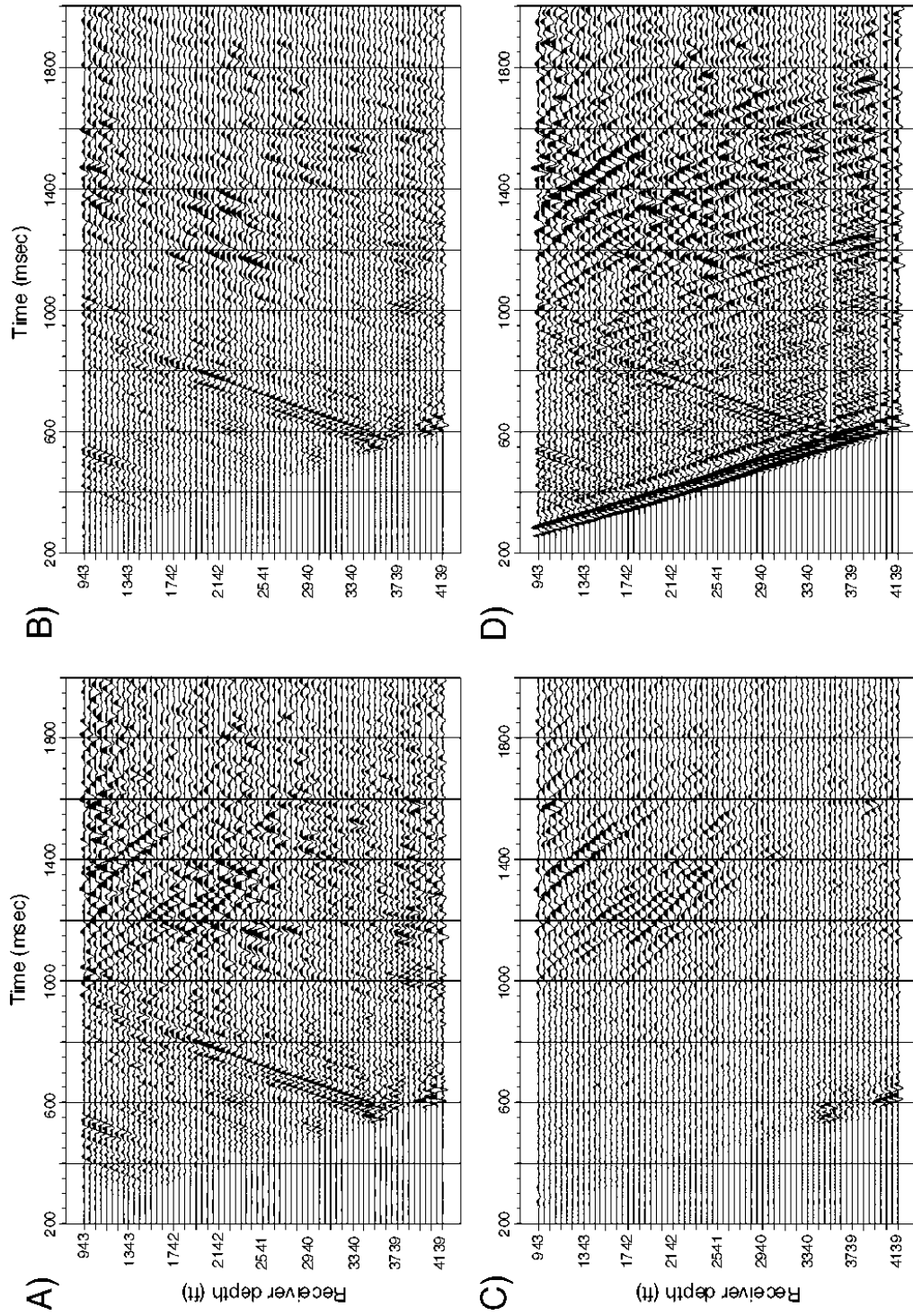


Fig. 5.13. Separated up-going wavefields using (A) median and (B)  $f-k$  filtering techniques. Observing their difference (C), it becomes readily obvious that median filtering allowed some of the down-going energy with different slope than the first arrival to “leak” into the up-going wavefield record. (D) The original shot gather data, representing the total wavefield.

elaborate preprocessing sequence where the data were separated into a upgoing and downgoing wavefields as described in the previous sections of this chapter. The input to the migration module was the separated upgoing wavefield of the nearest 11 sources to the well and the 7 closest to the well sources in the downdip direction. The velocity field obtained by the analysis of the available surface seismic data (Figure 5.11B) was used in the final comparison of the image resolution resulted from the migration to the predicted resolution by the proposed method. The reason that this velocity model was preferred over the one resulted from the traveltime inversion (Figure 5.11A) was that a layered model was required as an input to the generation of the synthetic gathers. Moreover, it was previously shown (Chapter V, section 5.2.4) that it indeed yields a good match to the observed first arrival travel times. In fact, the field data were migrated with both velocity models as well as the gradient models described in the same section (Figure 5.10). The migrated images were practically identical up to the depth of the deepest receiver ( $\approx 1.25$  km). The discrepancies at larger depths were attributed to the fact that the gradient models and the traveltime inversion model were not constrained by any field measurements thereafter, in contrast to the velocity model inferred from the surface seismic data.

### 5.3.1 Image resolution analysis

Raytracing from all 11 shots to a series of test points at several depth levels and back to the receivers was performed. The image points can be thought to be located along imaginary flat surfaces and therefore did not conform to the actual dipping reflectors. However, this fact does not subtract from the image analysis since it is based on each point being an individual scatterer.

Once the raytracing is completed, it is very easy to consider different acquisition scenarios by simply allowing only rays from particular shot (and to particular receiver) locations to contribute to the resulting spatial image of the test points. For example, it would be interesting to examine whether shooting on both sides of the well improve (and to what extent) the imaging of the reflectors. Figures 5.14 and 5.15 are examples of spatial images of a test point at the depth of 0.55 km and 200 m away from the well in the downdip direction. In Figure 5.14 only the 7 shots in the downdip direction contributed to the imaging of the point, whereas in Figure 5.15 the 4 shots in the updip direction were also considered. The distorted images of the point (due to the

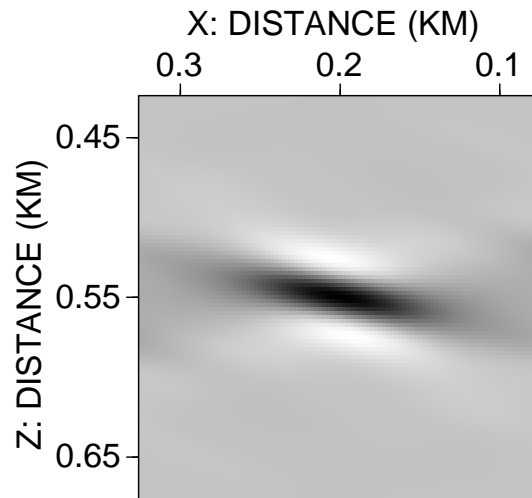


Fig. 5.14. Spatial image of a scatterer located 200 m away from the well in the downdip direction. The shot gathers that contribute to the image correspond to the 7 sources lying on the same side of the well as the test point itself.

limited temporal and spatial sampling of the wavefield) seem to be tilting towards the well (i.e., the receiver array). The obvious improvement of the overall image resolution when all 11 shots are considered is attributed to the increased recording aperture. Such tilted images also result from the migration of data from similar VSP configurations (Keho, 1984; Keho, 1986) hinting that both methods, seismic migration and the proposed image resolution analysis, are equally accurate tools for measuring image resolution. In the following subsections, we will closely examine the validity of this statement.

Figures 5.16 and 5.17 show the vertical resolution of a grid of test points that the image resolution analysis predicts when all 11 shots and only the 7 shots in the downdip direction are considered respectively. The radii of the imaged points are proportional to their predicted vertical resolution. One can easily see that in general, the closest to the well the points are, the better are resolved in the vertical direction. The shallower points' vertical resolution deteriorates faster as they get farther from the well, especially the ones located in the updip direction from the well. This is so because the sources in the updip direction are located closer to the well than the ones in the downdip direction. Therefore, a smaller distance away from the well is required in the updip direction for a test point to be associated with wavenumbers

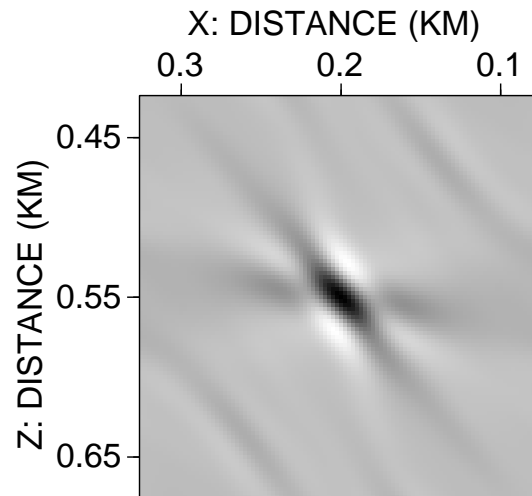


Fig. 5.15. The spatial image of the same point as in Figure 5.14. The 4 shots in the updip direction (i.e., lying on the opposite side of the well than the test point) also contributed to the imaging of the scatterer. The improvement of the spatial wavefield sampling is translated to a better resolved image of the imaging point.

that are all pointing towards the well. The wavenumber vector aperture decreases and tilts towards the horizontal wavenumber vector axis resulting in reduced vertical resolution.

Abrupt changes of resolution for nearby test points can not be fully explained by just considering the wavenumber aperture changes since in this case, random and severe ray bending is not justified by the model. Thus, the improvement of the vertical resolution (35 m) for the point just below the deepest receiver compared to the resolution of the points just above and below it, is also the result of velocity changes. Since the wavenumber vector is inversely proportional to the velocity at the scatterer, lower velocities lead to larger wavenumber vector magnitudes, better wavenumber vector domain coverage and consequently, better image resolution.

Comparing the predicted vertical resolutions of Figures 5.16 and 5.17, it becomes apparent that the points located farther on the updip direction from the well suffer the most resolution reduction than the points in the downdip direction when the 4 updip sources are excluded from the image analysis. This can, again, be explained if we consider the distribution of the wavenumber vectors (or loosely, the ray directions). By excluding the 4 updip sources, the points in the updip direction suffer a reduction in the wavenumber aperture in the neighborhood of the vertical wavenum-

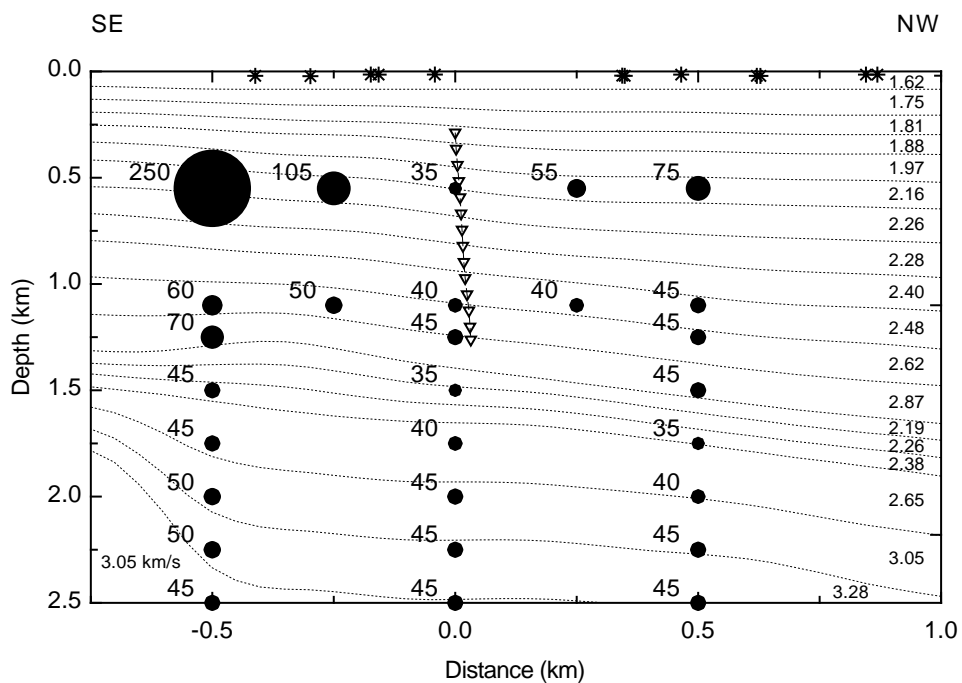


Fig. 5.16. Predicted vertical resolution (in m) of a series of test points. All 11 shots contributed in the imaging. On the far right of the model, the compressional velocities of each layer are denoted (in km/s).

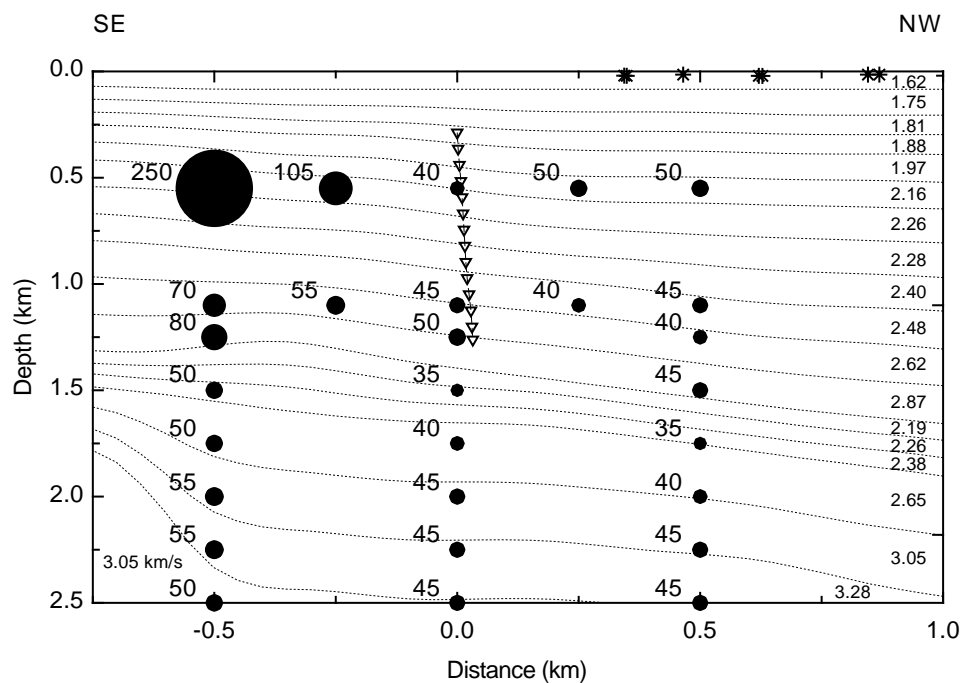


Fig. 5.17. Predicted vertical resolution (in m) of a series of test points. Only the 7 shots in the downdip direction contributed in the imaging. On the far right of the model, the compressional velocities of each layer are denoted (in km/s).

ber vector axis, resulting in vertical resolution reduction. On the other hand, the points located in the downdip direction from the well also undergo some wavenumber aperture reduction, but this is not as severe since the missing sources (and the corresponding wavenumbers) are in the direction of the receiver array anyway. Moreover, the wavenumber vectors towards the vertical axis are not affected at all. Therefore, their vertical resolution will not change at all. In fact, the shallower downdip points exhibit an increase of their resolution just because the spatial images are less tilted towards the well.

### 5.3.2 Image resolution: Migrated synthetics vs image resolution analysis

A finite difference modeling scheme was used to generate the synthetic gathers of the nearest 11 shots to the well. Whereas the exact field locations of the sources were used, the receivers were vertically aligned instead of being slightly deviated. The introduced error however, was considered very small since the maximum horizontal receiver displacement was about 30 m at the depth of 1.25 km. The source wavelet was a zero-phase Ricker wavelet. Its dominant frequency was chosen to be 30 Hz in order to simulate the frequency content of the field data. Absorbing boundaries were used on both sides and the free surface of the model. These boundaries prevented the contamination of the recorded wavefield with unwanted multiples and reflections off the sides of the model. Apart from the first arrivals, the downgoing wavefield was very weak compared to the reflected (upgoing) waves. It was therefore decided that instead of applying some wavefield separation scheme, the first arrivals be simply muted.

Prestack Kirchhoff depth migration was then applied to the synthetics. In order to examine the effect of the acquisition geometry on the vertical image resolution, all 11 shot gathers were migrated as well as only the 7 gathers of the shots lying on the downdip direction. Figures 5.18 and 5.19 show the final migrated images. The layer model used to produce the synthetics is also overlaid. Since the same velocity model was used in both the forward modeling and the migration of the synthetics, the imaged portions of the reflectors (around the well) are very accurately represent the initial model. Comparing the two figures, one notices that when all 11 shot gathers were migrated (Figure 5.18), the correctly imaged reflector portions extend further in the updip direction. However, even in the case where only the 7 shot gathers in the

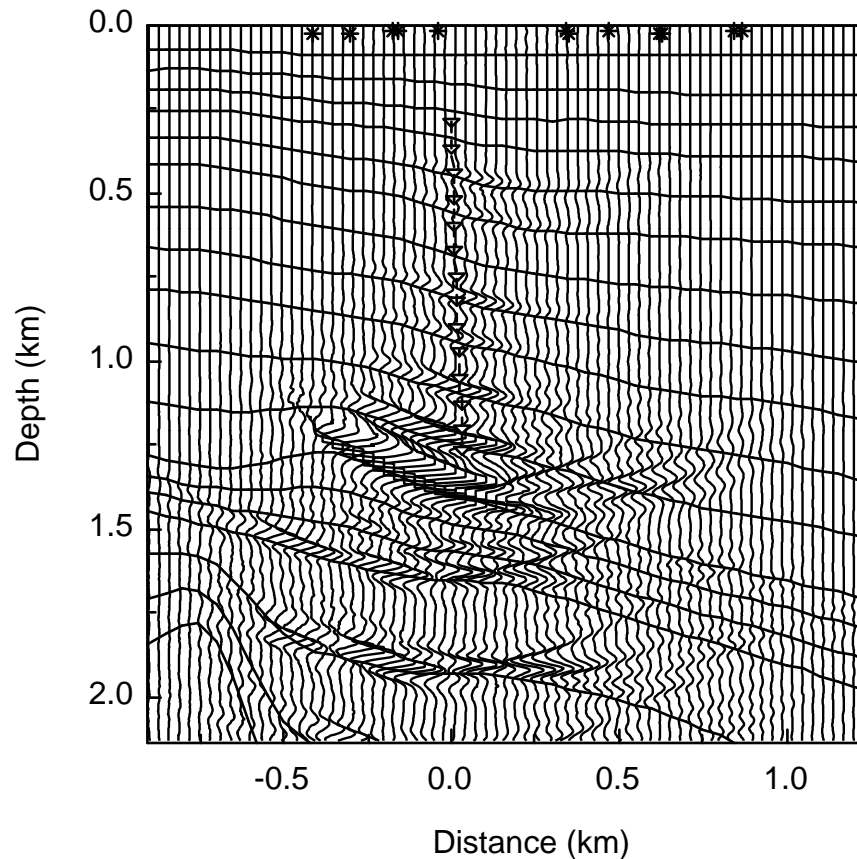


Fig. 5.18. Migrated section of all 11 synthetic gathers. The layer model used in both the forward model and the migration is overlaid for comparison reasons.

downdip direction were migrated (Figure 5.18), small updip portions of the reflectors are imaged. On the other hand, very little differences occur in the lateral extent of the imaged interfaces in the downdip direction.

The raytracing results of Figure 5.20 can give us some insight as to why the migrated sections with and without the updip gathers differ almost exclusively in the updip direction. The figure shows clearly that downdip sources are responsible for imaging the downdip portion of the reflectors as well as some of the updip portions, especially for deeper interfaces (red thick line). The updip sources do not contribute at all to the imaging of the downdip portions of the interfaces. On the other hand, they are really needed if imaging extensive portions of the reflectors in the updip direction is required (blue thick line). It is thus obvious, that neglecting these sources will mainly affect the imaging in the updip direction. Their raytracing results are



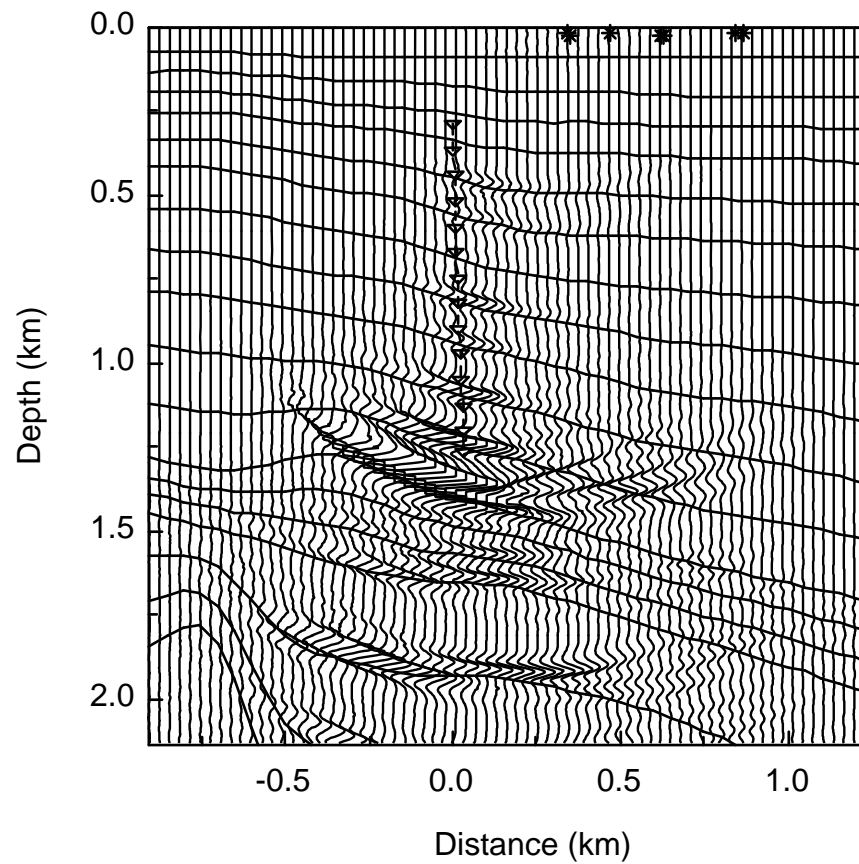


Fig. 5.19. Migrated section of only the 7 downdip synthetic gathers. Compared to Figure 5.18, it shows that neglecting the updip gathers affects mainly the updip portions of the imaged reflectors. The layer model used in both the forward model and the migration is overlaid for comparison reasons.

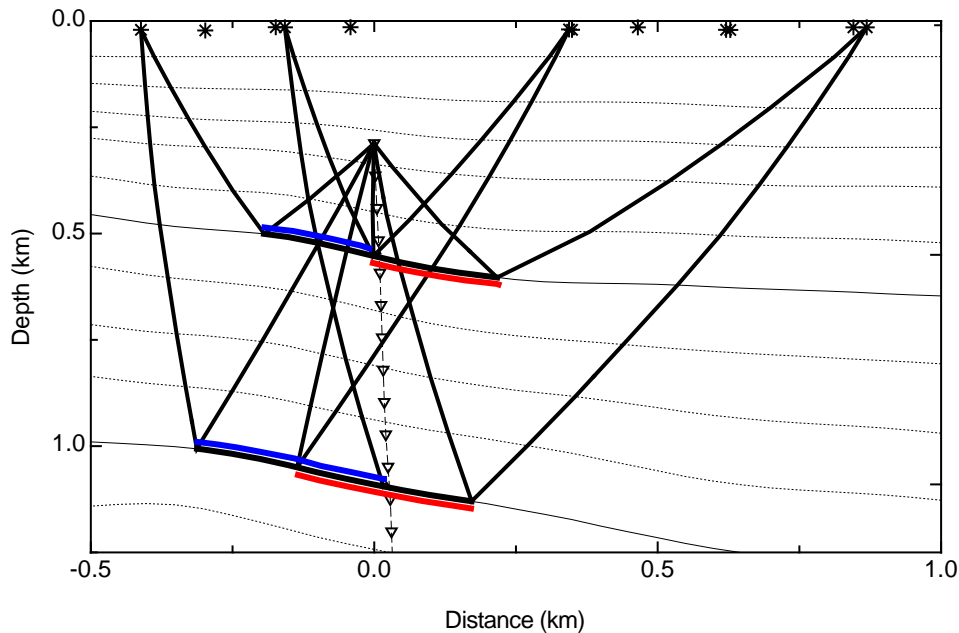


Fig. 5.20. Raytracing reveals that downdip gathers are exclusively responsible for imaging the downdip portion of the interfaces, covering some of the updip portions as well (red lines). On the other hand, updip gathers manage to image portions of the reflectors (blue lines) in the updip direction further away from the well.

therefore in total agreement with the migrated sections.

Although raytracing results are very useful in understanding what portions of the reflectors are illuminated, it is not possible to predict accurately how well they are going to be resolved. The image resolution analysis is however capable of estimating changes of resolution (horizontal and vertical) in the image space (see for example, Chapter II). Figure 5.21 compares the vertical resolution of the test points predicted by the proposed method (black circles) to the vertical resolution measured from the migrated synthetics along several interfaces (red circles). The measured vertical resolution from the migrated section is in general worse than the predicted one for the closest to scatterers. One has to bear in mind however that measuring the width of a wavelet from a migrated section is usually not a straightforward task. For example, in the case under examination, a zero-phase Ricker wavelet with a known dominant frequency (30 Hz) was the input to the forward modeling scheme used to create the synthetic gathers. Therefore, the image resolution analysis was performed with a similar wavelet (Gabor) and the same frequency content (30 Hz). However, when ex-

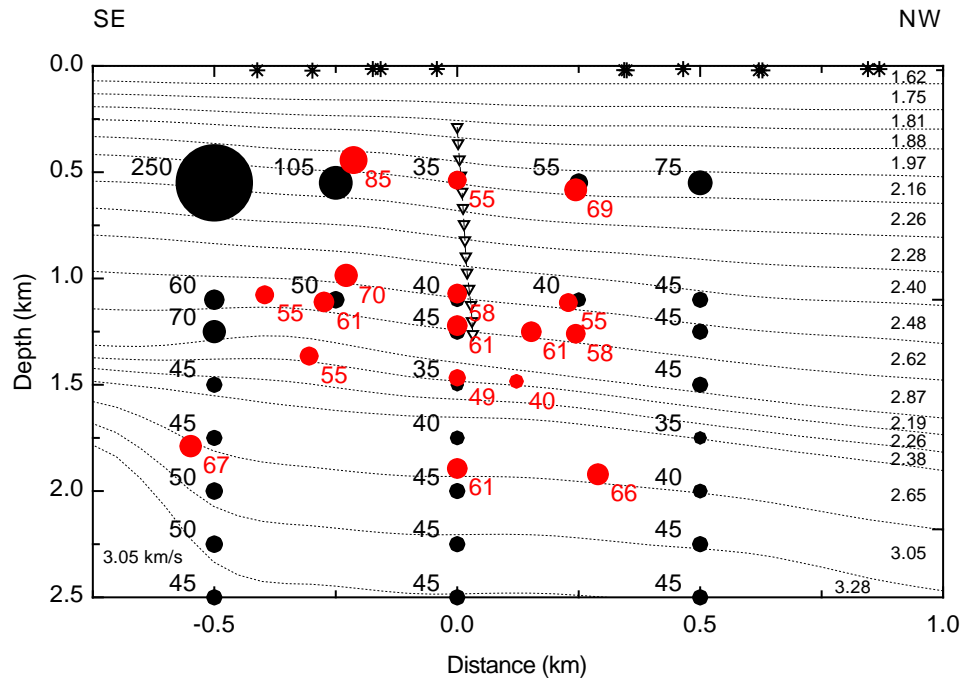


Fig. 5.21. Comparison of the predicted vertical resolution (black circles) to the measured resolution from the migrated synthetic gathers (red circles). All 11 gathers were considered in both approaches.

amined closely, the wavelet in the migrated section looked slightly distorted. Further modeling with a single interface model (to avoid interference problems) affirmed the observation. Spectral analysis also showed that the dominant frequency was 25 Hz instead of 30 Hz. These discrepancies are believed to be the results of the dispersive nature of the finite difference scheme (of second order) used in the forward modeling. Correcting for the frequency content difference, results in errors  $\approx 5$  m between the predicted and measured vertical resolutions. Overall, the changes of vertical resolution in space show the same pattern for both. For example, the decrease of velocities of the layers in the middle of the model, just below the deepest receiver, are evidenced in similar vertical resolution improvement.

### 5.3.3 Image resolution: Migrated field data vs image resolution analysis

Kirchhoff depth migration was performed to the wavefield separated field data. Similar to the synthetics, migration was applied to all 11 shot gathers and the 7 downdip

ones. However, comparing the migrated images, it was noted that they were very similar with only subtle differences in the updip section of the images. Closer examination of the actual shot gathers (the input to the migration) showed that the amplitudes of the gathers in the updip direction from the well were much smaller than the ones in the downdip direction, rendering their contribution to the imaging ineffective. On the other hand, the first arrivals prior to the wavefield separation exhibited similar amplitudes. This led us to believe that it was possible that very little energy was indeed reflected and recorded in the vertical component receivers. Assuming that the salt body is very close to the well in the updip direction, it is very likely that the sediments exhibit gradually increasing dips as they terminate against the salt. It is then possible that the waves graze along the dips of the sediments instead of being reflected back.

Figure 5.22 is the migrated section of the field data considering only the 7 shot gathers in the downdip direction from the well. It is obvious that there is no good match between the migrated section and the model (used to migrate the data) in the updip direction. The migrated image shows clear signs that the sediments are indeed getting steeper in that direction, giving convincing evidence that it is possible that this is the reason why the recorded amplitudes of the upgoing wavefield are so small. Moreover, historical evidence based on wells encountering the salt, place the cap rock in depths of 200 to 300 m. It seems therefore, that the velocity model used in the migration needs to be updated in order to accommodate these facts.

Despite the aforementioned difficulties, the vertical resolution along the imaged interfaces was measured. Figure 5.23 shows the measured resolution (red circles). The predicted vertical resolution for the same acquisition geometry (only the 7 downdip sources were considered) at several test points is overlaid for comparison reasons (black circles). Considering the facts that the wavelet is unknown, the signal-to-noise ratio although good but not infinite as in the image resolution and forward modeling applications, and the frequency content changes along the two different sets of receivers used in the field experiment, the measured vertical resolution shows similar behavior as for the predicted images: moving farther from the well, resolution deteriorates faster in the updip direction than in the downdip. Additionally, the low velocity layers exhibit better resolution.

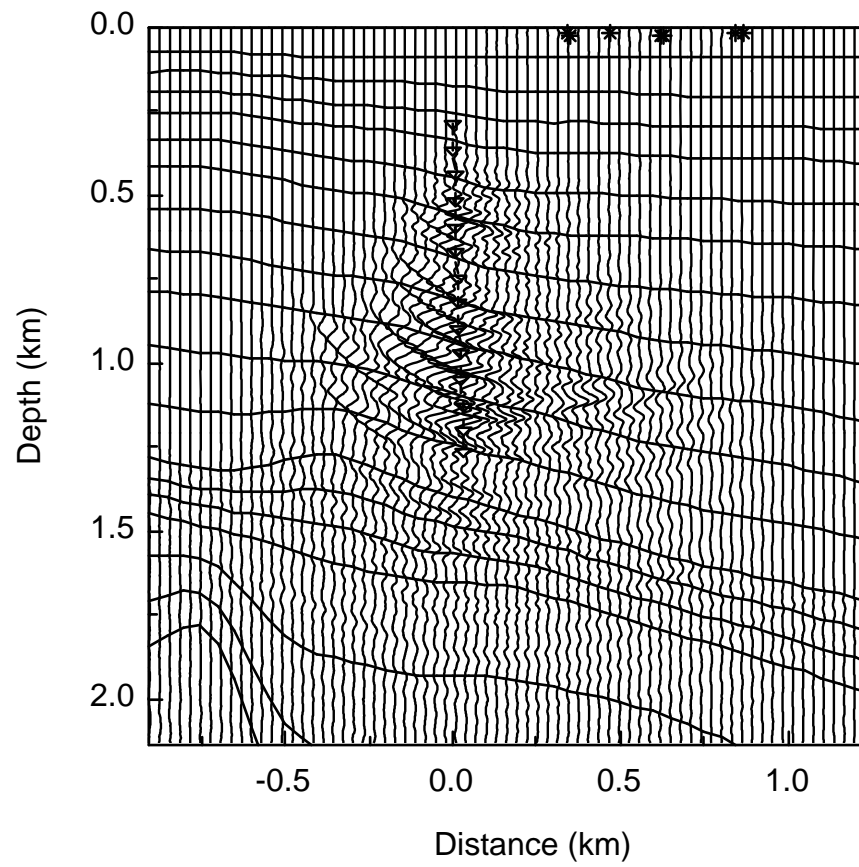


Fig. 5.22. Migrated section of only the 7 downdip shot gathers of the field data. The layer model used in the migration is overlaid for comparison reasons.

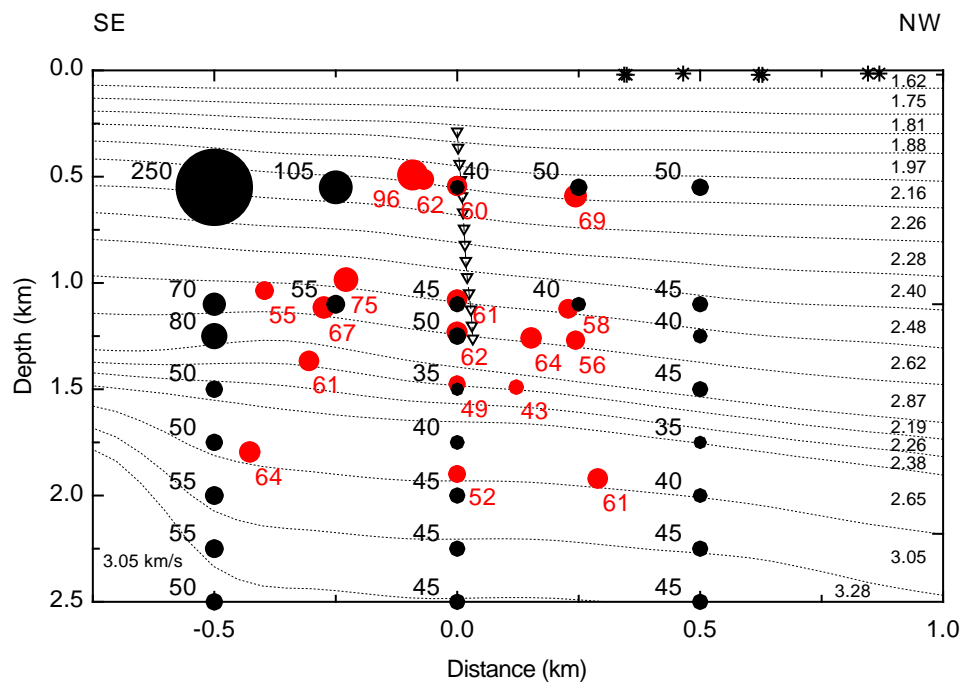


Fig. 5.23. Comparison of the predicted vertical resolution (black circles) to the measured resolution from the migrated field gathers (red circles). The 7 gathers in the downdip direction from the well were considered in both approaches.

## 5.4 Conclusions

In this chapter we considered the application of the proposed image resolution analysis to a VSP survey. Forward modeling results using a finite difference scheme, i.e., a different approach than the ray tracing technique implemented into the proposed method, were also compared to the predicted vertical resolution results.

The agreement between the measured vertical resolution from the migrated synthetic gathers and the predicted resolution based on the proposed method is judged to be very good. Changes of resolution within the illuminated portion of an interface are impossible to be assessed accurately with any of the illumination methods available to date. Even ray hit counts which, of course, require the use of a ray tracing technique, are not sufficient enough to provide a resolution measure. With a small additional burden (in terms of resources and time) of computing wavenumber vectors and performing a 3D Fourier transform, such a measure is available to help us better understand the effects of the background model and the acquisition geometry on the imaging.

Overall, the image resolution method performed reasonably well in the case of the field data given all the factors that can affect the resolution (signal-to-noise ratio, frequency content of the source wavelet) or introduce errors in measuring it (unknown wavelet signature, interference problems, etc.).

More specifically, it was shown that in this case, increasing the source recording aperture by including sources in the updip direction of the well improves the imaging of the updip portion of the reflectors. Such conclusion cannot of course be generalized; it is directly tied to this particular VSP experiment and this background structure. For example, a syncline or anticline structure would lead to different conclusions. The location of the well relative to the axis of such structures would most likely also affect the final images.

In addition to the image resolution analysis, the processing, modeling and imaging of the VSP field data also provided us with insightful information about wave propagation, the importance of building a reliable velocity model (either from the VSP data themselves or other sources such as the surface seismic data) and the uses and limitations of travelt ime inversion.

## CHAPTER VI

### CONCLUSIONS

The objectives of this work were to develop a method capable of assessing the effectiveness of competing acquisition geometries. Beylkin's equations [equations (1.7) and (1.8)], the results of a Generalized Radon Transform, provided the framework which enabled us to develop such a method. Its attractiveness lies on the fact that through simple forward computations based on a ray tracing scheme, we can evaluate the spatial resolution of a target point that a given source/receiver geometry can produce. It is a significant departure from other so called "illumination" methods which however, fail to take into account the ray geometries at the reflection points.

The main contributions of this dissertation are as follows:

- We developed a series of quantitative measures (the standard deviation, smoothness, wavenumber vector scatter plots, and spatial images) of spatial image resolution. These measures, complementary to each other, help us better understand and visualize how image resolution varies at different target areas.
- We examined the effects of factors other than the distribution of sources and receivers, on seismic image resolution. We estimated the influence of background model parameters (velocity and structure) on resolution through a suite of experiments on different models with fixed acquisition geometry. We found that in simple homogeneous half space models, the effect of seismic velocities on image quality can not only be easily predicted but also, be quantitatively assessed. In the presence of structure, as simple as a flat interface, we demonstrated that the order of the velocity changes with depth plays a dominant role on image quality. We established that models with increasing velocities with depth (especially when their values are low), favor the imaging of target points with respect to models that exhibit decreasing velocities with depth.

We formulated a method to account for different signal-to-noise ratios, deviating thus, from the calculation of the theoretically only attainable image resolution. Applying this method to the same series of models, allowed us to observe how



structure shapes affect the directions in which image resolution deteriorates with increasing noise level.

- We applied our image resolution analysis to a realistic 3D salt model, comparing three different surface acquisition geometries, a conventional single-cable marine, an orthogonal, and an innovative circular/radial geometry. We found that for structurally complex models, near-offset images do not necessarily produce the best spatial resolution. In fact, for a subsalt target area, the marine geometry provided better resolution for the far offsets, not the near offset.

Using all image resolution measures, helped us affirm that both land geometries provide higher quality subsalt images than the marine geometry, with the orthogonal judged to be slightly better than the circular/radial.

Consideration of decreasing signal-to-noise ratios in imaging target points near the salt flanks, showed that although in the case of the marine geometry the large offsets effectively increase the imaging aperture, the image resolution they provide degrades quickly with decreasing signal-to-noise ratios. On the other hand, the land geometries prove to handle the decreasing S/N ratios better since the image resolution they provide is much less affected (although, it will eventually start to decrease for lower ratio values).

Finally, combining surface and VSP data proved to improve the image resolution of target points, especially in the vicinity of the wells. Ray tracing modeling and image resolution analysis can help us resolve which well to populate so that the VSP survey be as beneficial to the final imaging of the target area as possible.

- We applied the image resolution analysis to a VSP dataset. We processed and migrated the field data. We also generated synthetic data using a finite difference scheme. The same velocity field was used to migrate the synthetics and the field data. It also provided the input model to performing the image resolution analysis. The predicted vertical image resolution of several points was compared to the measure resolution from the migrated sections of the synthetics and field data. We conclude that the proposed method performed well, showing similar vertical resolution changes as the migrated section of not only the synthetics but the field data as well.

## 6.1 Future work

- The development of Ocean Bottom Cable (OBC) technology and permanent receiver deployment allow us to acquire better and more complete seismic reflection data sets. They present us, therefore, with a chance to take advantage of not only compressional wave data but also shear wave (in land settings) or converted, C-wave, data (in marine environments). This has direct implications for a) the potential reservoir image quality we can obtain and b) our ability to better describe the petrophysical reservoir properties and their changes during production (see for example, Huffman, 2002). Relying only on the ray tracing forward modeling, image resolution analysis could readily provide estimates of the image quality that converted (P-S or, C) waves, and even S-S waves (in land) can produce compared to P-P waves. Also, it would be interesting to examine the implications of recording converted waves on the seismic acquisition geometry and compare our image analysis results to Vermeer's (2003) claims that parallel geometries are more suitable for converted-wave imaging than orthogonal geometries (see also Kommedal et al., 2002).
- In this work, we adopted the Born scattering model (see Chapter I), assuming weak scattering (no preferred directions of the scattered energy). A commonly used alternative to this approach is the "Kirchhoff" scattering model, where the backscattered energy follows certain directions, satisfying Snell's law (reflecting boundaries) (e.g., Bleistein, (1987); Jaramillo and Bleistein, (1999)). This approach requires the wavenumber vectors be restricted along the specular ray direction, i.e., normal to the reflecting boundary. Adopting this method would require minor adjustments to the existing code in order to accept only those rays (and consequently, wavenumber vectors) as an input to the image resolution analysis. The advantage of doing this is that we will be able to associate those rays with particular source/receiver locations, facilitating thus, the design of acquisition geometries capable of imaging the area of interest in the best possible way. Recently, Lu et al. (2002) proposed a similar tool to help design supplementary surveys to image initially poorly "illuminated" areas of target horizons. However, their objective is to "illuminate" the desired area of the horizon (meaning, to improve its amplitude). Unfortunately, they do not comment on the resolution of the particular area. The image resolution anal-

ysis proposed in this dissertation, could be used as an additional constraint to designing the supplementary survey.

- Seismic energy dissipation is the result of anelastic processes such as crystal defects, grain boundary processes, etc. (Kennett, 2001). A commonly used measure of the rate of energy dissipation is the loss factor  $Q(\omega)$  (where  $\omega$  the angular frequency). The frequency dependence of  $Q$  has been proposed in many different forms (e.g., Azimi et al., 1968; Jeffreys, 1958; Brennan and Smylie, 1981) and could provide the basis on which an effort should be exercised to incorporate the effects of the limiting factor of frequency attenuation into the image resolution analysis. This, in conjunction with the proposed signal-to-noise consideration, would allow us to predict the image quality in a more realistic manner.

## REFERENCES

- Aki, K., and Richards, P. G., 1980, Quantitative seismology: Theory and methods, vol. 1: W. H. Freeman and Co.
- Azimi, S., Kalinin, A. V., Kalinin, V. V., and Pivovarov, B. L., 1968, Impulse and transient characteristics of media with linear and quadratic absorption laws: *Izv. Physics of Solid Earth*, **2**, 88–93.
- Barth, N. H., and Wunsch, C., 1990, Oceanographic experiment design by simulated annealing: *J. Phys. Ocean.*, **20**, 1249–1263.
- Berkhout, A. J., 1973, On the minimum-length property of one-sided signals: *Geophysics*, **38**, 657–672.
- 1974, Related properties of minimum-phase and zero-phase time functions: *Geophysical Prospecting*, **22**, 683–709.
- Beydoun, W., and Mendes, M., 1989, Elastic ray-Born l2-migration/inversion: *Geophys. J.*, **97**, 151–160.
- Beydoun, W. B., and Tarantola, A., 1988, First Born and Rytov approximations: modeling and inversion conditions in a canonical example: *J. Acoust. Soc. Amer.*, **83**, 1045–1055.
- Beylkin, G., 1984, The inversion problem and applications of the generalized Radon transform: *Comm. Pure Appl. Math.*, **37**, 579–599.
- 1985, Imaging of discontinuities in the inverse scattering problem by inversion of a causal generalized Radon transform: *J. Math. Phys.*, **26**, 99–108.
- Beylkin, G., and Burridge, R., 1990, Linearized inverse scattering problems in acoustics and elasticity: *Wave Motion*, **12**, 15–52.
- Beylkin, G., Oristaglio, M., and Miller, D., 1985, Spatial resolution of migration algorithms, *in* Berkhout, A. J., Ridder, J., and van der Wall, L. F., Eds., *Acoustical imaging*: Plenum Press, 155–167.

- Bicquart, P., 1998, Application of Kirchhoff depth migration to 3D-VSP: 68th Ann. Mtg., Soc. Expl. Geophys., Expanded Abstracts, 389–392.
- Bishop, T. N., and Nunns, A. G., 1994, Correcting amplitude, time, and phase misties in seismic data: *Geophysics*, **59**, 946–953.
- Bleistein, N., 1987, On the imaging of reflectors in the earth: *Geophysics*, **52**, 931–942.
- 1989, Large wave number aperture-limited Fourier inversion and inverse scattering: *Wave Motion*, **11**, 113–136.
- Bracewell, R. N., 1986, *The Fourier transform and its applications*: McGraw–Hill, 2nd edition.
- Brennan, B. J., and Smylie, D. E., 1981, Linear viscoelasticity and dispersion in seismic wave propagation: *Rev. Geophys. Space, Phys.*, **19**, 233–246.
- Cassell, B. R., 1984, Vertical-seismic-profiles - an introduction: *First Break*, **2**, no. 11, 9–19.
- Chen, G., Peron, J., and Canales, C., 2000, Rapid VSP-CDP mapping of 3-D VSP data: *Geophysics*, **65**, 1631–1640.
- Clochard, V., Nicoletis, L. M., Svay-Lucas, J., Mendes, M., and Anjos, L., 1998, 3-C imaging of 3-D walk-away data in regard to preprocessing: 68th Ann. Mtg., Soc. Expl. Geophys., Expanded Abstracts, 377–380.
- Constance, P. E., Holland, M. B., and Roche, S. L., 1999, Simultaneous acquisition of 3-D surface seismic data and 3-C, 3-D VSP data: 69th Ann. Mtg., Soc. Expl. Geophys., Expanded Abstracts, 104–107.
- Cordson, A., Galbraith, M., and Peirce, J., 2000, Planning land 3-D seismic surveys: *Soc. of Expl. Geophys.*
- de Hoop, M., and Bleistein, N., 1997, Generalized radon transform inversions for reflectivity in anisotropic elastic media: *Inverse Problems*, **13**, 669–690.
- Durussel, V. B., 2002, Simulation of anisotropic wave propagation in Vertical Seismic Profiles: Master's thesis, Texas A&M University.

- Frigo, M., 1999, A fast Fourier transform compiler: SIGPLAN Conf. on Programming Language Design and Implementation, ACM.
- Frigo, M., and Johnson, S. G., 1998, FFTW: An adaptive software architecture for the FFT: Intern. Conference on Acoustics, Speech, and Signal Processing, IEEE, 1381–1384.
- Gal'perin, E. I., 1974, Vertical seismic profiling: Society of Exploration Geophysicists.
- Gangi, A. F., and Fairborn, J. W., 1968, Accurate determination of seismic-array steering delays by an adaptive computer program: *Supplemento al nuovo cimento*, **6**, 105–115.
- Gardner, G. H. F., Gardner, L. W., and Gregory, A. R., 1974, Formation velocity and density – the diagnostic basics for stratigraphic traps: *Geophysics*, **39**, 770–780.
- Gazdag, J., 1978, Wave equation migration with the phase-shift method: *Geophysics*, **43**, 1342–1351.
- Geoltrain, S., and Brac, J., 1993, Can we image complex structures with first-arrival traveltimes?: *Geophysics*, **58**, 564–575.
- Gibson, Jr., R. L., Lee, J. M., Toksöz, M. N., Dini, I., and Cameli, G. M., 1994, The application of 3-D Kirchhoff migration to VSP data from complex geological settings: 63rd Ann. Internat. Mtg., Soc. Expl. Geophys., Expanded Abstracts, 1290–1293.
- Gibson, Jr., R. L., and Stieglitz, T. C., 2001, The influence of traveltimes operators on spatial resolution in migrated images: 71st Ann. Mtg., Soc. Expl. Geophys., Expanded Abstracts, 1001–1004.
- Gibson, Jr., R. L., Toksöz, M. N., and Batini, F., 1993, Ray-Born modelling of fracture zone reflections in the Larderello geothermal field: *Geophys. J. Int.*, **114**, 81–90.
- Gonzalez, R. C., and Woods, R. E., 1992, Digital image processing: Addison–Wesley.
- Hardage, B. A., 2000, Vertical seismic profiling: Principles: Pergamon.
- Hatherly, P. J., 1982, A computer method for determining seismic first-arrival times: *Geophysics*, **47**, 1431–1436.

- Hatton, L., Worthington, M. H., and Makin, J., 1986, *Seismic data processing: Theory and practice*: Blackwell Scientific Publications.
- Henry, M., and Mellman, G. R., 1988, Linearized simultaneous inversion for source wavelet equalization and mis-tie adjustment: 58th Ann. Internat. Mtg, Soc. of Expl. Geophys., Expanded Abstracts, 953–955.
- Hinds, R. C., Anderson, N. L., and Kuzmiski, R. D., 1996, *VSP interpretive processing: Theory and practice*: Society of Exploration Geophysicists.
- Huffman, A. R., 2002, The future of pore-pressure prediction using geophysical methods: *The Leading Edge*, **21**, 199–205.
- Jaramillo, H. H., and Bleistein, N., 1999, The link of Kirchhoff migration and demigration to Kirchhoff and Born modeling: *Geophysics*, **64**, 1793–1805.
- Jeffreys, H., 1958, A modification of Lomnitz's law of creep in rocks: *Geophys. J. R. Astr. Soc.*, **1**, 92–95.
- Kallweit, R. S., and Wood, L. C., 1982, The limits of resolution of zero-phase wavelets: *Geophysics*, **47**, no. 7, 1035–1046.
- Keho, T. H., 1984, Kirchhoff migration for vertical seismic profiles: 54th Ann. Mtg., Soc. Expl. Geophys., Expanded Abstracts, 694–696.
- 1986, *The vertical seismic profile: Imaging heterogeneous media*: Ph.D. thesis, Massachusetts Institute of Technology.
- Kennett, B. L. N., 2001, *The seismic wavefield. Volume I: Introduction and theoretical development*: Cambridge University Press.
- Knapp, R. W., 1990, Vertical resolution of thick beds, thin beds, and thin-bed cyclothem: *Geophysics*, **55**, 1183–1190.
- Kommedal, J. H., Ackers, M., Folstad, P. G., Gratacos, B., and Evans, R., 2002, Processing the Hod 3D multicomponent OBS survey, comparing parallel and orthogonal acquisition geometries: *The Leading Edge*, **21**, 795–801.
- Levin, S. A., 1998, Resolution in seismic imaging: Is it all a matter of perspective?: *Geophysics*, **63**, no. 2, 743–749.

- Lu, C., Lu, R., Willen, D., and Nayvelt, L., 2002, Flower plot: A new tool for smart survey design: 72nd Ann. Mtg., Soc. Expl. Geophys., Expanded Abstracts, 45–47.
- Maldonado, B., and Hussein, H. S., 1994, A comparative study between a rectilinear 3-D seismic survey and a concentric-circle 3-D seismic survey: 64th Ann. Mtg., Soc. Expl. Geophys., Expanded Abstracts, 921–925.
- Meckel, L. D., and Nath, A. K., 1977, Geologic considerations for stratigraphic modeling and interpretation, *in* Payton, C. E., Ed., Seismic stratigraphy – Applications to hydrocarbon exploration: American Association of Petroleum Geologists, AAPG Memoir, 417–438.
- Menke, W., 1984, Geophysical data analysis: Discrete inverse theory: Academic Press, Inc.
- Miller, D., Oristaglio, M., and Beylkin, G., 1989, A new slant on seismic imaging: migration and integral geometry: *Geophysics*, **52**, 943–964.
- Moser, T. J., 1994, Migration using the shortest-path method: *Geophysics*, **59**, 1110–1120.
- Muerdter, D., Kelly, M., and Ratcliff, D., 2001, Understanding subsalt illumination through ray-trace modeling, Part 2: Dipping salt bodies, salt peaks, and nonreciprocity of subsalt amplitude response: *The Leading Edge*, **20**, 688–697.
- Muerdter, D., and Ratcliff, D., 2001a, Understanding subsalt illumination through ray-trace modeling, Part 1: Simple 2-D salt models: *The Leading Edge*, **20**, 578–595.
- 2001b, Understanding subsalt illumination through ray-trace modeling, Part 3: Salt ridges and furrows, and the impact of acquisition orientation: *The Leading Edge*, **20**, 803–816.
- Nichols, D. E., Farmer, P., and Palacharla, G. K., 1998, Improving prestack imaging by using a new ray selection method: 68th Ann. Mtg., Soc. of Expl. Geophys., Expanded Abstracts, 1546–1549.
- Padhi, T., and Holley, T. K., 1997, Wide azimuths - why not?: *The Leading Edge*, **16**, 175–177.



- Ricker, N., 1953, Wavelet contraction, wavelet expansion and the control of seismic resolution: *Geophysics*, **18**, 769–792.
- Roden, R., and Fagin, S., 2001, An introduction to this special section: Prestack Depth Migration: *The Leading Edge*, **20**, 485.
- Roden, R., and Gochioco, L. M., 2002, Introduction – PSDM 2: The sequel: *The Leading Edge*, **21**, 1204.
- Schoenberger, M., 1974, Resolution comparison of minimum-phase and zero-phase signals: *Geophysics*, **39**, no. 6, 826–833.
- Sheriff, R. E., and Geldart, L. P., 1995, *Exploration seismology*: Cambridge University Press, 2nd edition.
- Shi, Y. Q., and Huifang, S., 2000, *Image and video compression for multimedia engineering*: CRC Press.
- Slawson, S. E., Grove, K. D., and Fisher, G. W., 1994, Model-based 3-D seismic acquisition design: 64th Ann. Mtg., Soc. Expl. Geophys., Expanded Abstracts, 919–920.
- Slawson, S. E., Grove, K. D., and Monk, D. J., 1995, Model-based 3-D seismic survey design: 57th Ann. Internat. Mtg., Europ. Assoc. Geosc. Engin., Expanded Abstracts, B009.
- Stewart, R. R., Huddleston, P. D., and Kan, T. K., 1984, Seismic versus sonic velocities: A vertical seismic profiling study: *Geophysics*, **49**, 1153–1168.
- Stieglitz, T. C., 2001, A new approach to travelttime selection for Kirchhoff migration: Ph.D. thesis, Rice University.
- Taner, M. T., Koehler, F., and Sheriff, R. E., 1979, Complex seismic trace analysis: *Geophysics*, **44**, 1041–1063.
- Thierry, P., Operto, S., and Lambaré, G., 1999, Fast 2-D ray+Born migration/inversion in complex media: *Geophysics*, **64**, 162–181.
- Tikhonov, A. N., and Arsenin, V. Y., 1997, *Solutions of ill-posed problems*: W. H. Winston and Sons.

- Tzimeas, C., and Gibson, Jr., R. L., 1999, Enhanced spatial resolution measures: An alternative to conventional illumination analysis: 69th Ann. Mtg., Soc. Expl. Geophys., Expanded Abstracts, 657–660.
- van Trier, J., and Symes, W. W., 1991, Upwind finite-difference calculation of traveltimes: *Geophysics*, **56**, 812–821.
- Vermeer, G. J. O., 1999, Factors affecting spatial resolution: *Geophysics*, **64**, 942–953.
- 2003, Responses to wide-azimuth acquisition special section: *The Leading Edge*, **22**, 26–30.
- Versteeg, R., and Grau, G., 1991, The marmousi experience: Proceedings of the 1990 EAEG workshop on practical aspects of seismic data inversion: *Eur. Assn. of Expl. Geophys.*
- Vidale, J. E., 1988, Finite-difference calculation of traveltimes: *Bull. Seis. Soc of Am.*, **78**, 2062–2076.
- 1990, Finite-difference calculations of traveltimes in three dimensions: *Geophysics*, **55**, 521–526.
- von Seggern, D., 1991, Spatial resolution of acoustic imaging with the Born approximation: *Geophysics*, **56**, 1185–1201.
- 1994, Depth-imaging resolution of 3-d seismic recording patterns: *Geophysics*, **59**, 564–576.
- Widess, M. B., 1973, How thin is a thin bed?: *Geophysics*, **38**, 1176–1180.
- Yilmaz, Ö., 1987, *Seismic data processing*: Soc. of Expl. Geophys.
- Zhang, J., and Toksöz, N., 1998, Nonlinear refraction traveltime tomography: *Geophysics*, **63**, 1726–1737.
- Zhang, Q., Stewart, R. R., Parkin, J. M., and Sun, Z., 1996, Analysis of the Blackfoot 3C-3D VSP survey: CREWES Research Report, **8**, 40.1–40.26.

**VITA****Constantinos Tzimeas**

Department of Geology and Geophysics  
Texas A&M University  
College Station, Texas 77843  
(979) 458-1169

**Education**

Ph.D., May 2004, Texas A&M University, College Station, Texas

M.S., December 1992, University of Leeds, Leeds, U.K.

B.S., September 1991, Aristotle University of Thessaloniki, Thessaloniki, Greece

**Permanent address**

9 Kesarias, N. Votsi  
Kalamaria  
Thessaloniki, 55134  
Greece  
phone: 01130 2310 434-221  
email: [costas@nyssa.tamu.edu](mailto:costas@nyssa.tamu.edu)